The University of
Nottingham

Shakedown Analysis and Design of Flexible Road Pavements under Moving Surface Loads

by

Juan Wang *BEng, MSc*

GEORGE GREEN LIBRARY OF
SCIENCE AND ENGINEERING

Thesis submitted to the University of Nottingham for
the degree of Doctor of Philosophy

January 2011

ABSTRACT

Flexible road pavements often fail due to excessive rutting as a result of cumulative vertical permanent deformation under repeated traffic loads. The currently used analytical approach to flexible pavement design evaluates the pavement life in terms of critical elastic strain at the top of the subgrade. Hence, the plastic pavement behaviour is not properly considered. Shakedown analysis can take into account the material plasticity and guarantee structure stability under repeated loads. It provides a more rational design criterion for flexible road pavements.

Finite element analyses using the Tresca and Mohr-Coulomb yield criteria are performed to examine the responses of soil half-space when subjected to different loading levels. Both shakedown and surface ratchetting phenomena are observed and the residual stresses are found to be fully-developed after a limited number of load passes. The finite element results are then used to validate the solutions from shakedown analysis.

The main focus of current research is concerned with new solutions for static (i.e. lower-bound) shakedown load limits of road pavements under both two-dimensional and three-dimensional moving surface loads. Solutions are derived by limiting the total stresses at any point (i.e. residual stresses plus loading induced elastic stresses) to satisfy the Mohr-Coulomb yield criterion. Previous analytical shakedown solution has been derived based on a residual stress field that may not satisfy equilibrium for certain cases. In this study, a rigorous lower-bound shakedown solution has been derived by imposing the equilibrium condition of residual stresses.

The newly developed shakedown solutions have been applied to one-layered and multi-layered pavements. It was found that the rigorous lower-bound solution based on the self-equilibrated residual stress field is lower than the analytical shakedown solution for cases when the critical point lies on the surface or at the base of the first pavement layer. The results showed that the theoretical predictions of pavement shakedown load limit generally agree with the finite element and experimental observations for pavement behaviours.

The shakedown solution has been further extended to study the influence of the shape of contact load area for pavements under three-dimensional Hertz loads. It was found that the shakedown load limit can be increased by changing the load contact shape from a circle area to an elliptical one. A new pavement design approach against excessive rutting has been proposed. The pavement design is suggested by plotting thickness design charts using the direct shakedown solutions and choosing the thickness combination based on the design traffic load.

ACKNOWLEDGEMENTS

I would like to express my deepest gratitude to my supervisor, Professor Hai-Sui Yu, for the golden opportunity provided by him to conduct research of interest and for his excellent guidance, generous support and encouragement over the years.

Sincere thanks are due to Dr. Huaxiang Li who helped me to overcome difficulties and provided me with valuable advice for this research.

I would also like to thank all my colleagues and friends for their help and suggestions during my thesis writing and also for the pleasant time we spent together.

In addition, I would like to acknowledge the financial support provided by the China Scholarship Council and the University of Nottingham.

Finally, I would like to thank my family for their constant encouragement and endless love.

CONTENTS

LIST OF FIGURES

LIST OF TABLES

NOTATION

A	contact area
a	half contact width for two-dimensional surface loads and radius of circular contact area for three-dimensional surface loads
AASHO	American Association of State Highway Officials
AASHTO	American Association of State Highway and Transportation Officials
c	cohesion
c_n	cohesion of nth layer
CBR	California Bearing Ratio
D	full contact width for two-dimensional surface loads and diameter of circular contact area for three-dimensional surface loads
E	Young's modulus
E_n	Young's modulus of nth layer
FE	finite element
f	yield condition

G	shear modulus
H	height
h_n	thickness of *n*th layer
k	shear resistance for Von Mises material
$k_{\max}$	normalised analytical shakedown limit
$k'_{\max}$	normalised lower-bound shakedown limit
L	length
N_f	number of load application to failure
P	total normal load
PSI	Present Serviceability Index
PTF	Pavement Test Facility
p	normal contact pressure
p_0	maximum normal contact pressure
p_{0_i}	external loads
p_0^*	maximum contact pressure in experiment
$\overline{p}$	uniform contact pressure
Q	total shear load

q	shear contact stress
q_0	maximum shear contact stress
STF	Slab Test Facility
U	surface displacement
$\dot{u}_i$	displacement velocity
x, y, z	global coordinates
x', z'	local coordinates
ΔU_1	increment of horizontal surface displacement per load pass
ΔU_2	increment of vertical surface displacement per load pass
$\Delta\varepsilon_{ij}^p$	plastic strain increment per load pass
ε_{xz}	shear strain
ε_t	tensile strain
ε_z	subgrade strain
ε_{ij}^p	plastic strain tensor
$\dot{\varepsilon}_{ij}^k$	kinematically admissible plastic strain rate cycle
λ	dimensionless load parameter

λ_{sd}	analytical shakedown limit parameter
λ'_{sd}	lower-bound shakedown limit parameter
λ^n_{sd}	analytical shakedown limit parameter for *n*th layer
λ'^n_{sd}	lower-bound shakedown limit parameter for *n*th layer
μ	surface frictional coefficient
σ_{ij}	total stress tensor
σ_t	tensile stress
σ_0	yield strength for Von Mises material
σ^e_{ij}	elastic stress tensor
σ^k_{ij}	stress tensor on the yield surface
σ^r_{ij}	residual stress tensor
$\left(\sigma^e_{ij}\right)_p$	elastic stress tensor due to normal load
$\left(\sigma^e_{ij}\right)_q$	elastic stress tensor due to shear load
ϕ	friction angle
ϕ_n	friction angle of *n*th layer
ψ	dilation angle

ψ_n	dilation angle of *n*th layer
υ	Poisson's ratio
υ_n	Poisson's ratio of *n*th layer
2D	two-dimensional
3D	three-dimensional

CHAPTER 1

INTRODUCTION

1.1 Background

Road pavements such as track road, driveway, motorway, airport runway and taxiway are daily-used civil engineering structures built over soil subgrade for the purpose of sustaining vehicular traffic safely and economically. The analysis and design of road pavements under moving traffic loads is an important but complex problem. Over the last three decades, there has been a positive evolution in philosophy and practice from a wholly empirical approach to pavement design towards the use of a theoretical framework for design (e.g. AASHTO, 2002; Austroads, 1992; Highway, 2006, 2009). However, a major limitation of this theoretical framework is that elasticity theory is of fundamental concern and no consideration is given to strength and plasticity of pavement material.

Plasticity theory has been used for stability problems of foundations, embankments and slopes in the field of geotechnical engineering. These problems usually deal with static loads which may increase gradually to such a limit that the soil cannot withstand the current stress state and fails due to instantaneous collapse. In these cases, limit analysis can provide a proper measure for structure safety design. However, when the soil structure is subjected to repeated or cyclic loads, such as road pavements under vehicular traffic, the design load provided by limit analysis is by no means sufficient to prevent structure failure. Although the applied repeated loads may not cause instantaneous collapse of the structure, they possibly induce plastic deformation in every load cycle and finally results in structural failure either from alternating plasticity or from unlimited incremental plasticity (ratchetting). Shakedown analysis is thus introduced to determine the critical load limit (termed as 'shakedown limit') that will prevent structure failure under cyclic load conditions.

The determination of the shakedown limit, as an essential part in the application of shakedown concept, usually can be achieved either by numerical elastic-plastic analysis or by two classical shakedown theorems. Compared to numerical elastic-plastic approach, where the full history of stress-strain curve is calculated, the shakedown theorems allow a direct calculation of the shakedown limit through searching the critical failure point, thus is drawn lots of attention by engineering researchers. According to König (1987), the static shakedown theorem was proved by Bleich (1932) using a system of beams of ideal *I*-corss-sections. Later, it was Melan (1938), who established a foundation stone for static shakedown theorem for the general case of continuum, giving a lower bound to the shakedown limit. In 1960, Koiter formulated a general kinematical shakedown theorem which can provide an upper bound to the shakedown limit.

The fundamental shakedown theorems have been applied to study behaviours of elastic-plastic structures subjected to repeated or cyclic loads (e.g. Johnson, 1985; König, 1987). In the field of geotechnical engineering, their applications in pavement structures under traffic loads are particularly useful as the shakedown limit is able to provide a more rational design criterion (Yu, 2006).

The possibility of using shakedown limit as an appropriate load parameter for the pavement design was firstly recognised by Sharp and Booker (1984) who studied the AASHO road test records. Brett (1987) examined the variation of roughness of a number of road sections in New South Wales, Australia. The results also suggested the stable roughness condition was attributed to shakedown of pavement. Over the years, many researchers have studied the shakedown condition of pavements using the fundamental shakedown theorems. However, due to the difficulties in optimisation and numerical calculation, particularly for the three-dimensional pavement problems, the true shakedown load limit has not yet been well determined. Compared to the upper-bound shakedown solution, the lower-bound shakedown solution gives conservative estimation to the true shakedown load limits. It is potentially more useful in the design of pavement structures.

1.2 Aims and objectives

The overall purpose of the research is to provide practical methods and solutions for shakedown analysis of flexible pavements under repeated traffic loads.

The research objectives include:

- To gain better understanding of the static shakedown theorem and the shakedown and non-shakedown phenomena of soil half-space under moving surface loads.
- To examine residual stress fields in pavements induced by repeated moving surface loads.
- To develop theoretical solutions for shakedown load limit so that numerical shakedown results can be benchmarked.
- To study the influence of load contact shape on the shakedown load limit.
- To derive shakedown limits of layered pavements and study parameters that might affect the shakedown limit.
- To highlight the difference between the two-dimensional and three-dimensional pavement models.
- To check the validity of the shakedown solution by comparing it with the results obtained from laboratory tests.
- To propose a design procedure for flexible pavements using the shakedown solutions.

1.3 Thesis outline

This thesis is divided into six chapters. A brief outline is given below:

Chapter 1 introduces the necessary background and key objectives of the current research on the analysis and design of pavements using shakedown theory.

Chapter 2 contains comprehensive literature reviews including shakedown concept and theorems, principles of flexible pavements, shakedown phenomena in pavements, shakedown analyses in pavement applications and plastic deformation in rolling and sliding contact.

Chapter 3 presents finite element analysis of soil half-space subjected to moving surface loads. The shakedown and non-shakedown phenomena as well as the development of plastic strains and residual stresses are examined. Shakedown status of the soil half-space is also checked by using Melan's lower-bound shakedown theorem.

Chapter 4 develops analytical solutions for shakedown of single-layered pavements. Both two-dimensional and three-dimensional pavement models are considered. The shakedown solutions are also extended to cases with elliptical contact area.

Chapter 5 gives shakedown solutions for multi-layered pavements. The influences of layer thickness and material properties on the shakedown limit are examined. Results are also compared with other author's solutions and experimental data. Finally, a simple pavement design procedure with the use of the present shakedown approach is proposed.

Chapter 6 summarises the major findings of this research and proposes suggestions for further research.

CHAPTER 2

LITERATURE REVIEW

2.1 Introduction

This Chapter starts with an introduction to the basic shakedown concept and classical shakedown theorems. Then, flexible road pavements are described in several aspects including components and materials, distress modes, contact loads and design approaches. Following that, a literature review concerning experimental observations of pavement shakedown phenomena and recent studies on pavement shakedown analysis is presented. Finally, a review of elastic-plastic half-space responses in rolling-sliding contact is given.

2.2 Notion of shakedown

As shown in Figure 2.1, when an elastic-plastic structure is subjected to cyclic or repeated loads, four distinctive situations may occur due to different levels of load magnitudes (Yu, 2006).

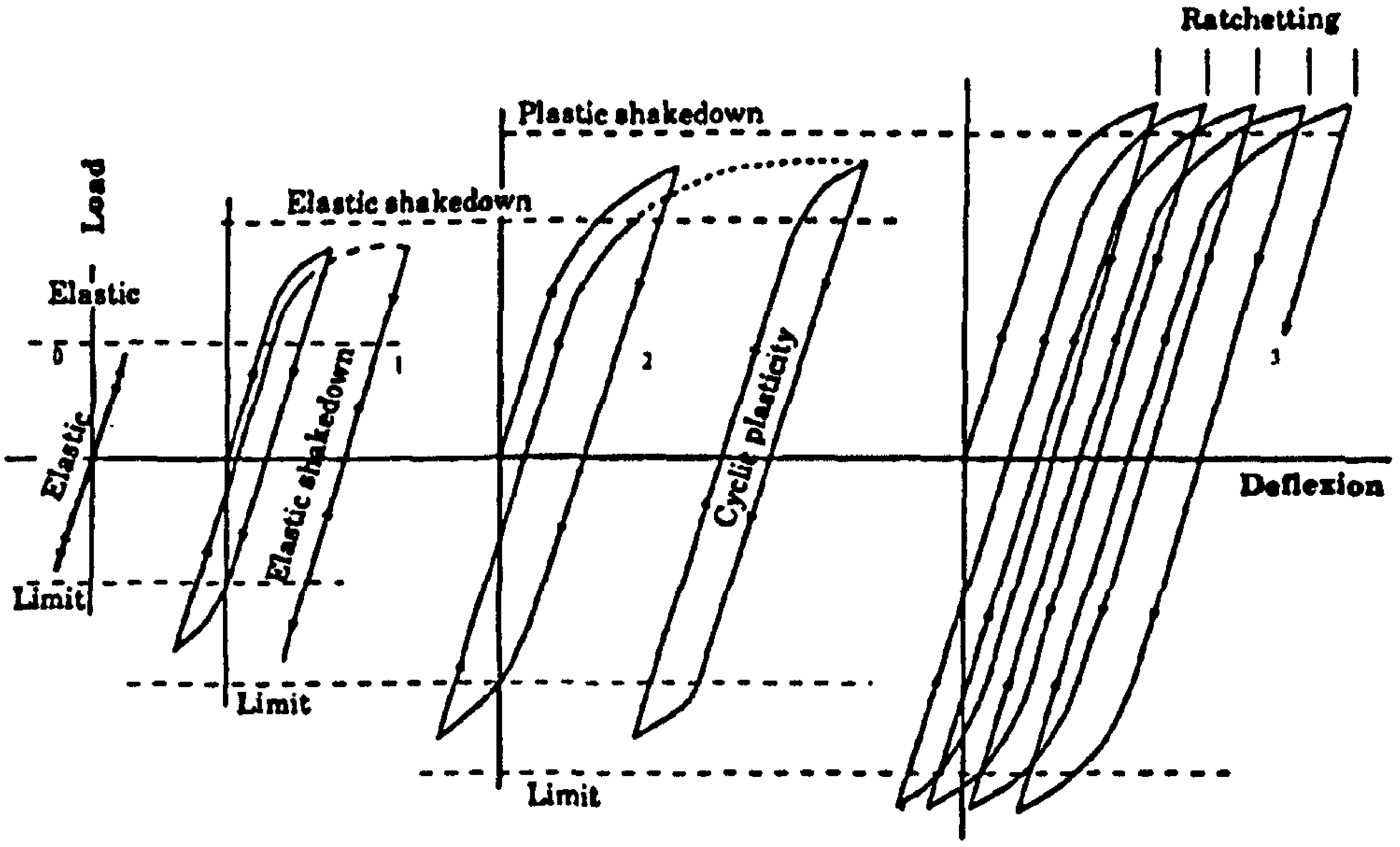

Figure 2.1. Elastic/plastic behaviour of structure under cyclic loads (Collins et al., 1993b)

Firstly, if the applied load is sufficiently small, purely elasticity can be recognised, so that the strain is fully recoverable and nowhere in the structure experiences plastic deformation.

Then, with an increase in load level, stress states of some points exceed the material yield surface, and therefore the structure deforms plastically. However, after a number of load cycles, it is likely that the structure adapts itself to the cyclic loads and finally it responds purely elastically to the subsequent load cycles. This phenomenon is termed as 'shakedown' and the critical load limit below which shakedown can occur is regarded as the 'shakedown limit'.

Thirdly, if the load level is higher than the shakedown limit and the plastic deformation changes in sign in every load cycle, a closed cycle of alternating plasticity may take place. This situation is called cyclic plasticity or plastic shakedown. In this situation, although the total plastic deformation remains small, the structure at the most stressed points may fail due to alternating plastic collapse.

Finally, when the loading level is high and there is always some plastic deformation added in every load cycle, the structure may undergo unlimited incremental plasticity and finally fail due to excessive plastic deformation. This phenomenon is known as ratchetting.

The purpose of shakedown analysis is to find the load limit between the shakedown case and the latter two non-shakedown cases in the prevention of structure collapse due to unlimited plastic deformation.

2.3 Shakedown theorems

2.3.1 Melan's static shakedown theorem

Melan's static or lower-bound shakedown theorem (Melan, 1938) states that an elastic-perfectly plastic structure will shakedown under repeated or cyclic loads if the yield condition at any point is not violated by a total stress field which combines the self-equilibrated residual stress field with the elastic stress field produced by the applied load. If the applied load is denoted by λp_0 (where p_0 may be conveniently set as the unit pressure in the actual calculation and λ is a dimensionless scale parameter), then all the induced elastic stress components are also proportional to λ. Melan's lower-bound shakedown theorem hence demands that:

$$f\left(\lambda\sigma_{ij}^{e}+\sigma_{ij}^{r}\right)\leq 0, \qquad (2.1)$$

where

$\lambda\sigma_{ij}^{e}$: elastic stress field due to the applied pressure λp_0,

σ_{ij}^{r}: self-equilibrated residual stress field,

$f\left(\sigma_{ij}\right)=0$: yield condition for the material.

The largest value of λ obtained by searching all possible self-equilibrated residual stress fields will give the actual shakedown load limit $p_{sd}=\lambda_{sd}p_0$ in which λ_{sd} is the shakedown limit parameter.

2.3.2 Koiter's kinematic shakedown theorem

Koiter's kinematic or upper bound theorem (Koiter, 1960) states that an elastic-perfectly plastic structure will not shakedown under repeated or cyclic loads if any kinematically admissible plastic strain rate cycle $\dot{\varepsilon}_{ij}^{k}$ and any external loads p_{0i} within the prescribed limits can be found for which:

$$\int_0 dt \iint_S p_{0i}\dot{u}_i dS > \int_0 dt \iiint_V \sigma_{ij}^{k}\dot{\varepsilon}_{ij}^{k} dV, \qquad (2.2)$$

where

$\dot{u}_i$: displacement velocity,

S: structure surface where traction are specified,

σ_{ij}^k : stresses on the yield surface,

V: structure volume.

Alternatively, the upper bound theorem can be formulated as follows:

$$\lambda_{sd} \int_0 dt \iint_S p_{0i} \dot{u}_i dS \leq \int_0 dt \iiint_V \sigma_{ij}^k \dot{\varepsilon}_{ij}^k dV, \tag{2.3}$$

which provides an upper bound to the shakedown load parameter λ_{sd}.

2.4 Flexible road pavements

2.4.1 Road pavement components and materials

Road pavements are layered structures (see Figure 2.2) positioned over the natural soil to support wheel loads of different magnitudes, speeds and intervals. Generally speaking, road pavements can be classified into two types: flexible and rigid. A flexible road pavement consists of unbound materials (i.e. they have no binder) and asphalt, while a rigid road pavement has a concrete slab as the main structure layer.

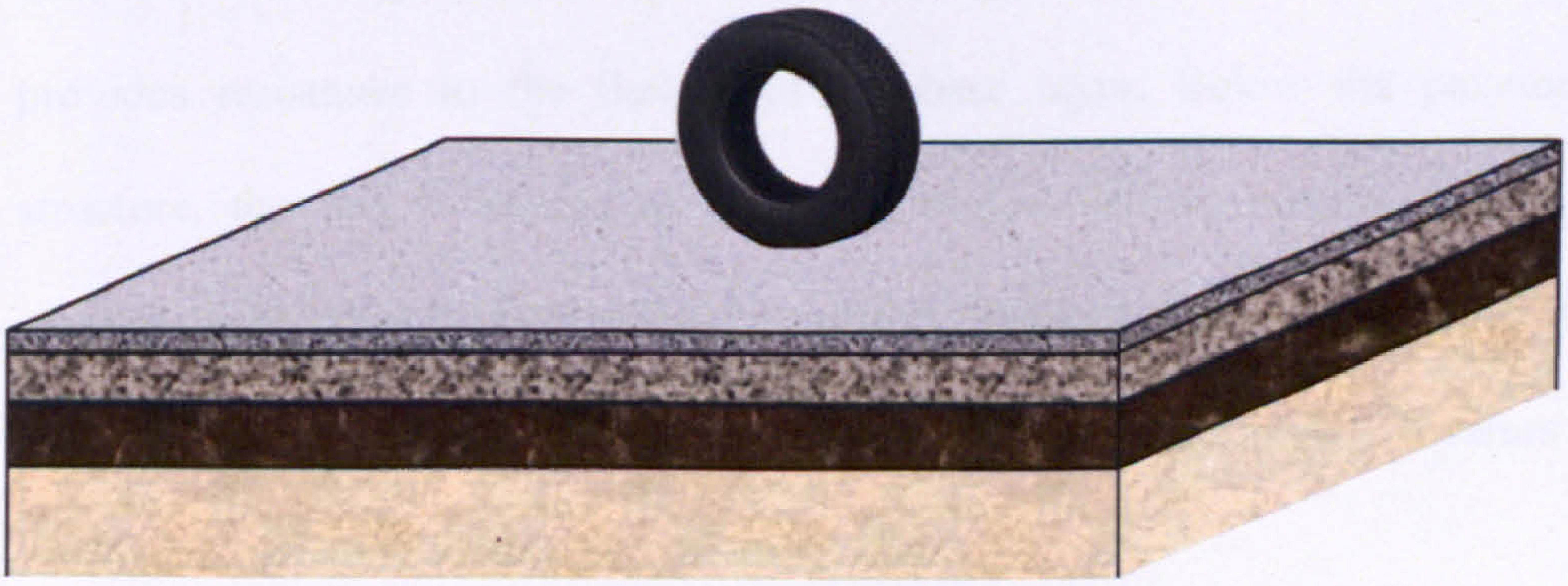

Figure 2.2. A pavement under a wheel

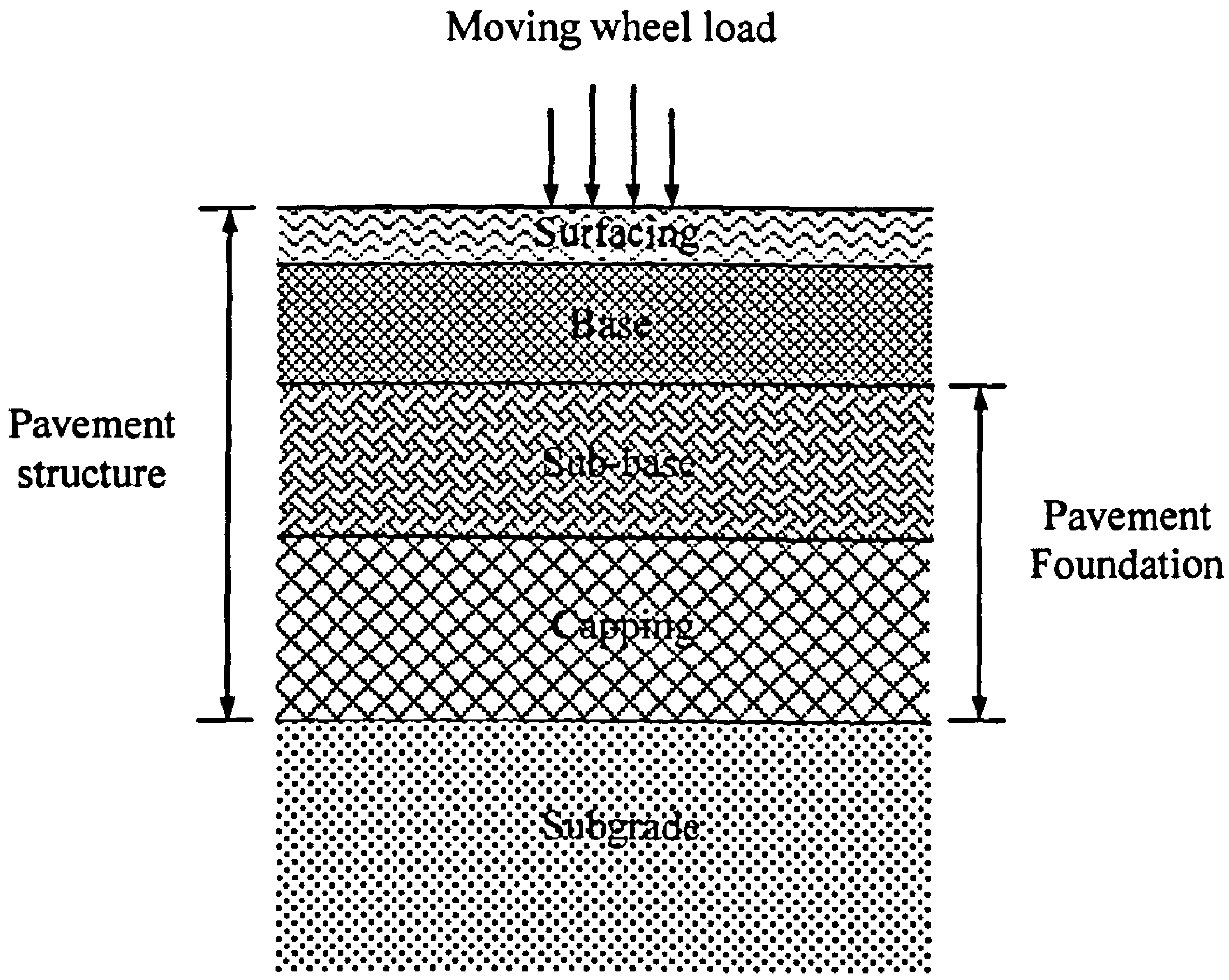

Figure 2.3. Typical structures of flexible pavements

As shown in Figure 2.3, flexible pavement structures usually consist of several main layers: surfacing, base, sub-base and capping. The surfacing is usually of high quality, tough enough to withstand direct loading and to provide good ride quality; however, it has a relatively small structure influence. The base gives the pavement most of its strength and has a relatively large thickness. The sub-base works in conjunction with the base to support the wheel loads and also provides resistance to the flexure of the base layer. Below the pavement structure, the soil is termed as subgrade, and is seldom strong enough to support the load application alone. Capping is usually a cheap, locally available material, and is only used for weak subgrade. Pavement foundation refers to the layers between the base and the subgrade.

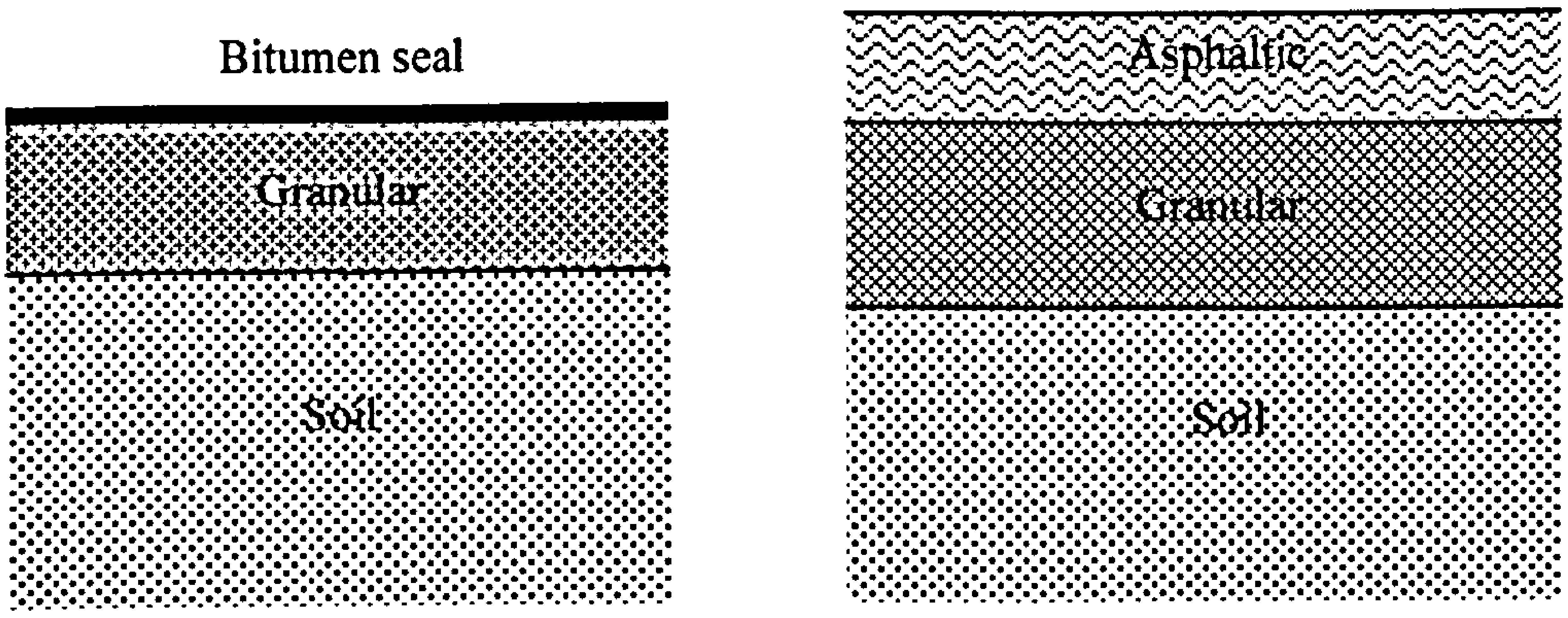

(a) Sealed granular road (b) Asphalt pavement

Figure 2.4. Typical material layouts of flexible pavements

Figure 2.4 shows two typical material layouts of flexible road pavements. One feature common to them is the placement of one or more layers of granular materials over the subgrade soil. The typically used granular materials include gravels or crushed rocks which are able to be compacted and exhibit the ability to withstand shear but not tension. The surface material can be either bitumen or asphalt. The bitumen, which is basically a residue from the distillation of heavy crude oil, is to provide a waterproof covering and a smooth riding surface here. Its primary mechanical property is viscosity, which is sensitive to temperature. The asphalt, which is a mixture of unbound granular material and bitumen, deforms as in the case of granular material and has significant tensile strength due to the added bitumen (Thom, 2008). The asphalt usually has much higher stiffness and strength than the granular materials and its properties are dependent on temperature and loading frequency.

2.4.2 Road pavement failure modes

There are two principle structural failure modes of flexible road pavements: rutting and cracking. They are of most concern to pavement engineers.

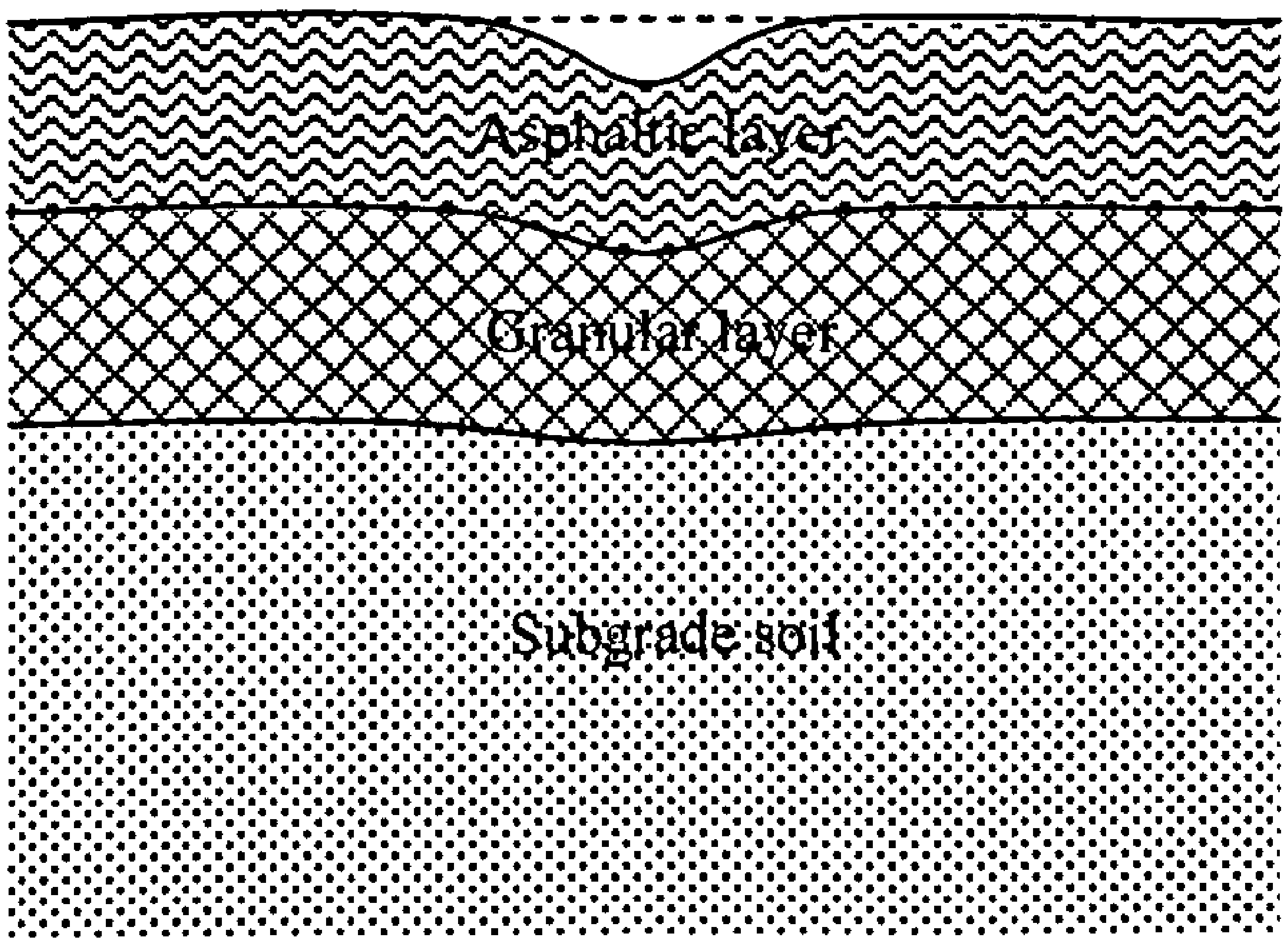

Figure 2.5. Rutting in road pavements

As shown in Figure 2.5, rutting is recognised as a surface downward deformation on the wheel track from the original level of pavement. It arises due to an accumulation of permanent deformation in the pavement structure (including the asphaltic layer and granular layer) and the subgrade when they are subjected to moving wheel loads, as illustrated in Figure 2.6. According to Brown (1996), the surface rutting usually arises from the surface layer for thick asphalt pavement; however, it is mainly attributed to the granular layers and subgrade for thinly sealed pavement. In Britain, a maximum deformation of 25 mm in the wheel tracks has been defined as the failure condition and a maximum deformation of 15 to 20 mm is regarded as the optimum condition for remedial work, such as the provision of an overlay or replacement of the surfacing (Croney and Croney, 1991).

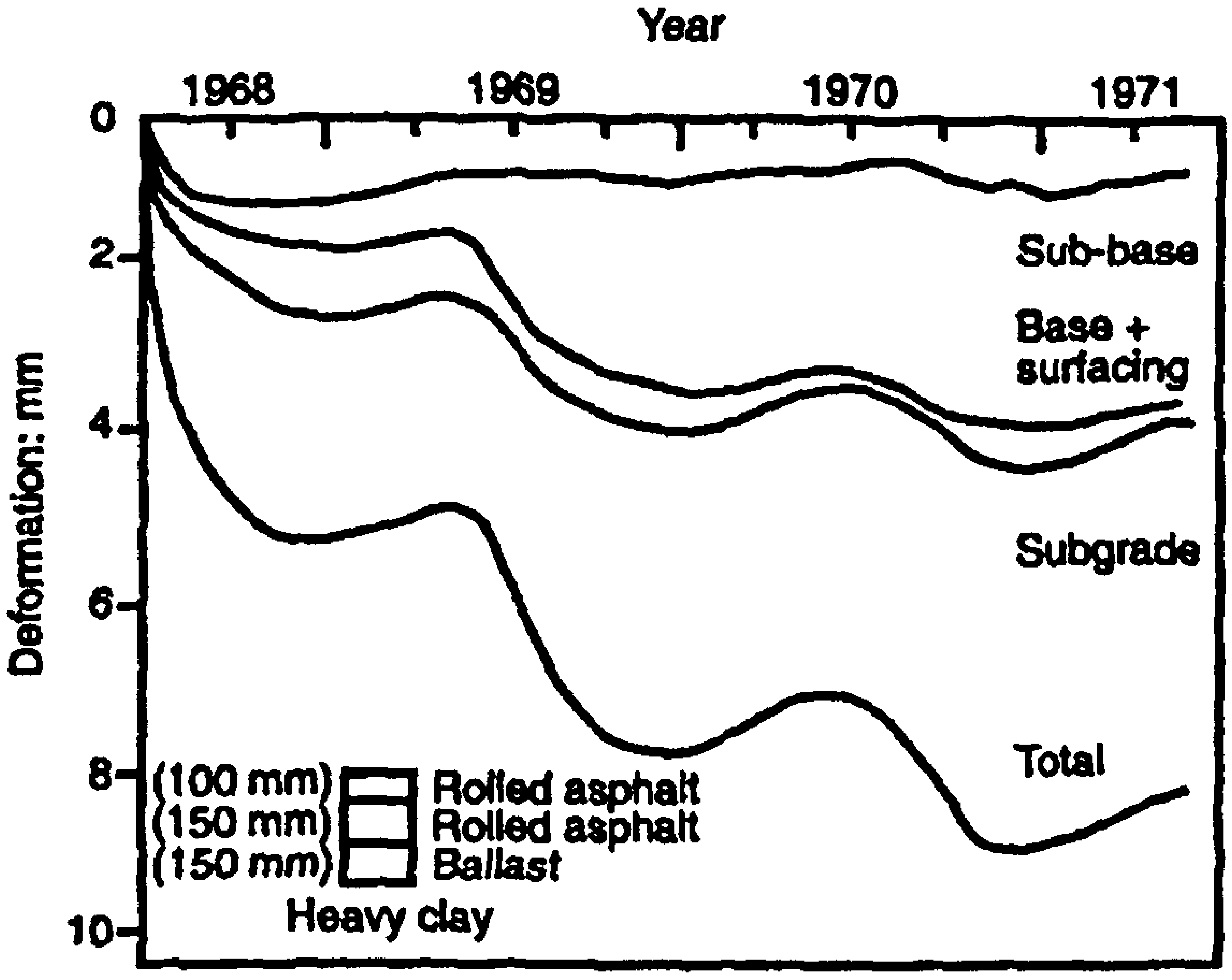

Figure 2.6. Development of permanent deformation in Transport Research Laboratory experiments at Alconbury Hill (Lister, 1972)

Cracking of flexible pavements under the influence of repeated wheel loads is a fatigue phenomenon caused by flexure of pavement as a result of small resistance in the lower region (Brown, 1996). As shown in Figure 2.7, the fatigue cracking may occur at the surface outside the loaded area or at the bottom of the asphaltic layer directly under the load, where the tensile stress or strain is highest. The surface cracking is apparent particularly for the thin surfacing pavement, while the thicker asphalt layer tends to introduce more tensile stresses at the bottom of the layer rather than at the surface. Under repeated load applications, the cracks propagate, connect, and form one or more longitudinal parallel cracks at the surface, as shown in Figure 2.8 (Huang, 1993).

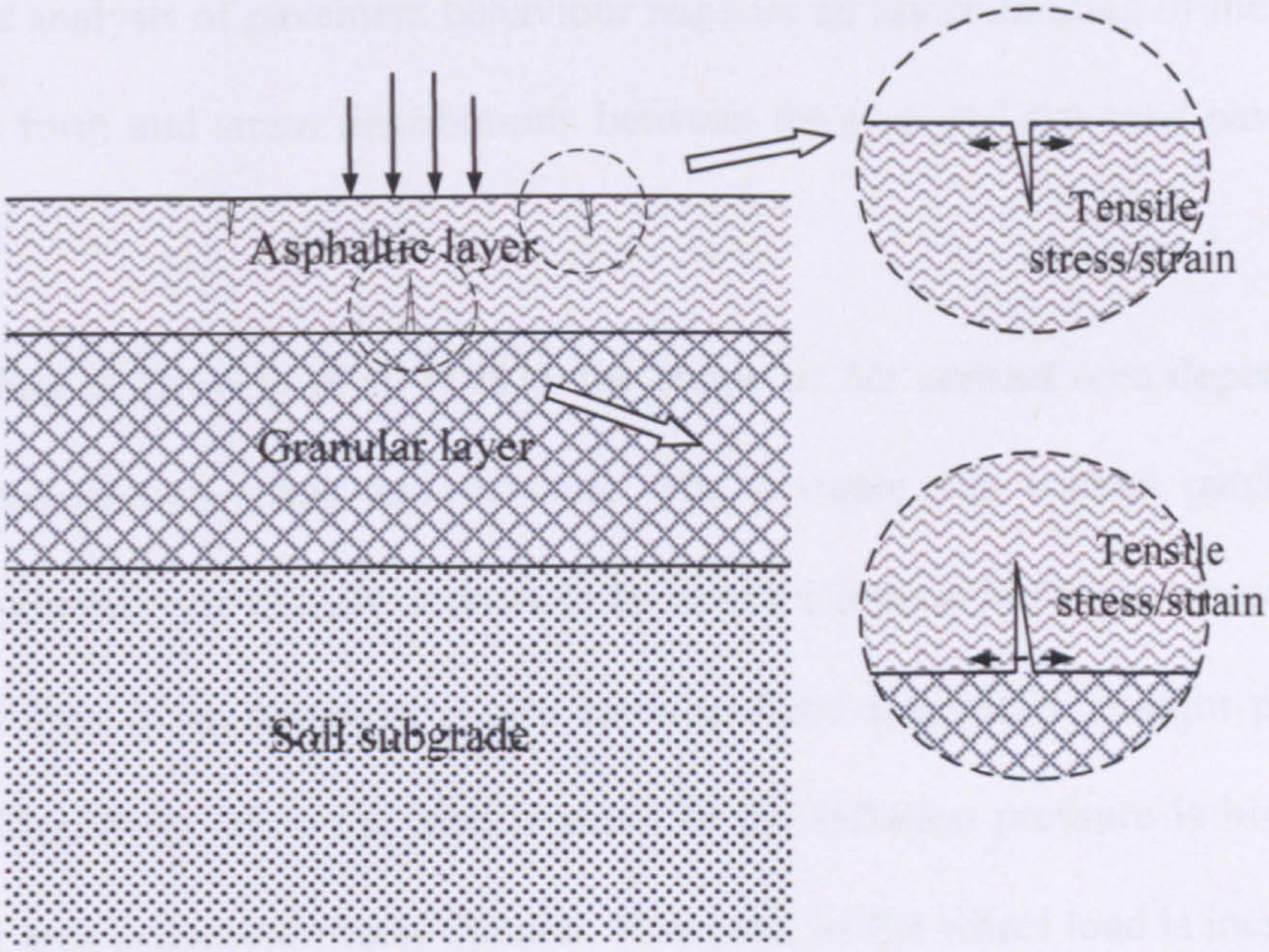

Figure 2.7. Tensile strains in asphalt layer under wheel loading

Figure 2.8. Fatigue cracking in wheel paths

2.4.3 Contact area and load distributions

The wheel load is transmitted through the tyre to the road pavement surface. A realistic analysis of pavement behaviour requires an understanding of the likely contact form and stress distributions between the tyre and the road pavement surface.

According to Browne et al. (1981), the shape of the contact area depends on tyre cross-section shape and structure. For example, the contact patch of a typical aircraft tyre usually appears to be nearly elliptical in shape, whereas the contact area of an automotive tyre tends to have essentially straight parallel sides. Moreover, when the load is small or the inflation pressure is high, the contact area is approximately circular. However, as the wheel load is increased, the contact patch becomes increasing elongated in the direction of travel, as shown in Figure 2.9. Nevertheless, a circular loaded area is usually considered by researchers in pavement engineering (Browne et al., 1981; Croney and Croney, 1991; Huang, 1993; Werkmeister et al., 2004).

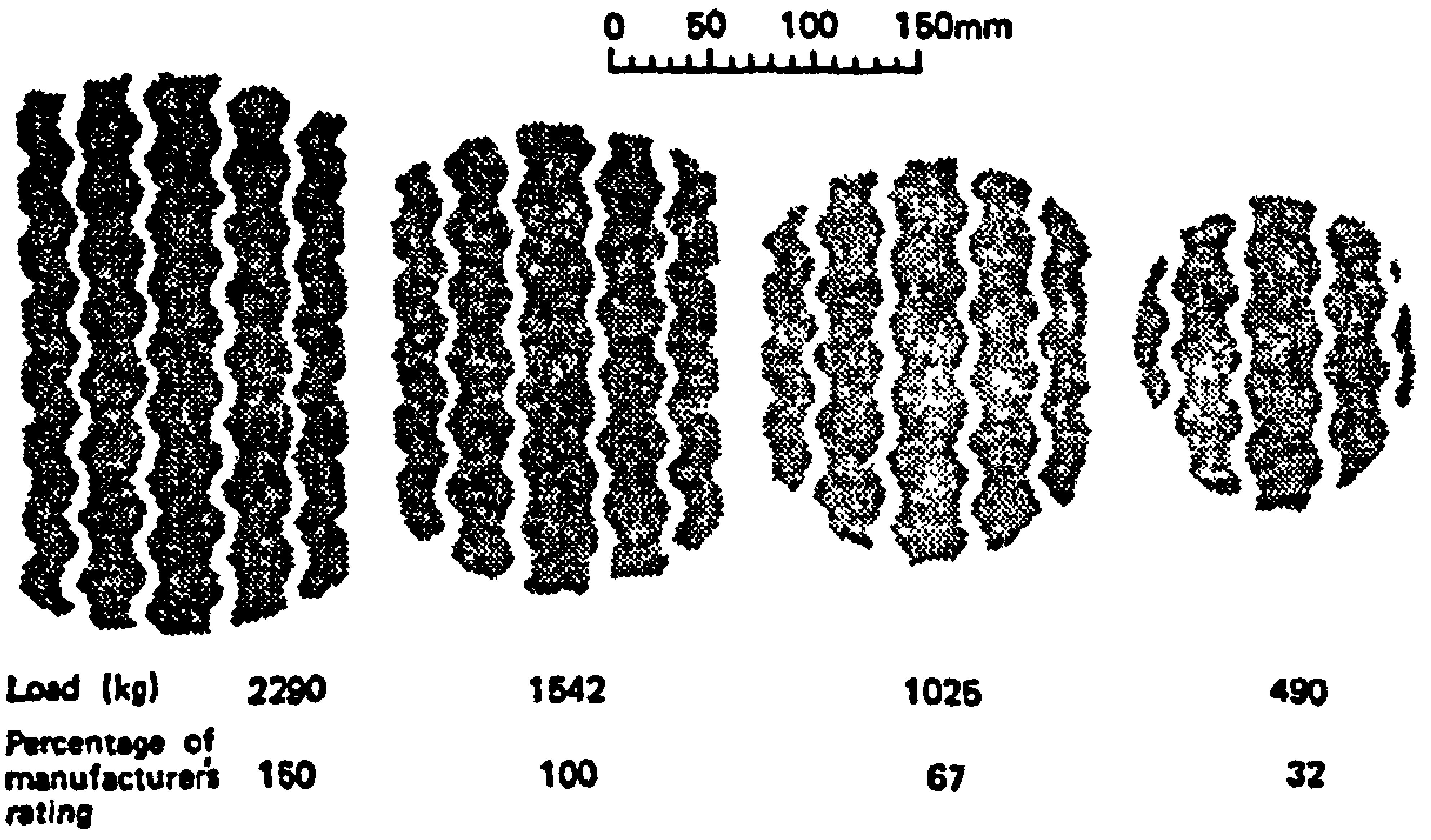

Figure 2.9. Contact patches (Croney and Croney, 1991)

The loading acting on the pavement can be expressed as two components: one perpendicular to the contact surface, called 'normal load', and one tangential to the contact surface, called 'tangential load'. The tangential load may be further decomposed into a longitudinal component, parallel to the central plane of the tyre, and a transverse component, perpendicular to the central plane.

Experimental measurements on the load distributions between the tyre and the road pavement have been conducted by a number of authors. It has been found that the load distributions are highly non-uniform (Freitag and Green, 1962; De Beer et al., 2005). According to Browne et al. (1981) and Huhtala et al. (1989), the normal pressure distribution is influenced by the tyre structure, tyre inflation pressure, driving forces (driving or carrying), and so on. For example, Huhtala et al. (1989) have reported that the contact pressure is greatest in the centre for truck tyres, whereas it is greatest on the tyre edge for personal cars. The normal load distribution is nearly independent of speed (Bonse and Kuhn, 1959; Himeno et al., 1997), but acceleration and deceleration have a significant effect on the longitudinal force component (Bonse and Kuhn, 1959). The major part of the longitudinal force component is in the rear of the contact patch due to the braking or traction forces, and its direction is also dependent on these forces (Browne et al., 1981). Bonse and Kuhn (1959) have found that the distribution of the transverse force component is influenced by deviation from the central plane and tyre characteristics, and is zero at the centre line of the tyre tread. Moreover, its direction is always towards the centre line of the tyre tread.

2.4.4 Road pavement design approaches

Flexible road pavement design approaches can be broadly classified as empirical and analytical. The empirical design approaches tend to rely more on experience and observations gained from experimental pavements and in-service roads and use index-value-based characterisation of material properties (e.g. California Bearing Ratio (CBR), layer coefficient, etc.). The analytical approaches use a theoretical framework that relates the critical elastic stress/strain to pavement overall performance.

The most commonly used empirical approaches are based on the CBR test, which was initially developed by O.J. Porter in the 1930s. The CBR test is a penetration test that gives a ratio of the load on a testing material to the load on a standard crushed rock material with an equal achievement of penetration which is defined as failure. By using the CBR test, an empirical relationship between the CBR values and the required pavement thickness can be evaluated. Britain has adopted the CBR method for flexible pavement design since 1946. The British pavement design standard of the Highways Agency (2009) provided guidance to pavement foundation design in which the subgrade CBR values are converted into stiffness moduli in relation to the thickness and foundation stiffness. The Highways Agency (2006) also presented guidance to flexible pavement base and surfacing design in which the layer thicknesses are in relation to material types and traffic intensities.

Between 1958 and 1960, one of the most significant pavement tests of the twentieth century was conducted by the American Association of State

Highway Officials (AASHO). Its results then contributed to the pavement design guides of the American Association of State Highway and Transportation Officials (AASHTO) presented afterwards. The AASHO road test interpreted how well the pavement serves the user as pavement serviceability. The pavement serviceability concept is then defined in terms of Present Serviceability Index (PSI) in the following AASHTO design guides. The PSI, together with layer coefficient and reliability factors, formed an empirical equation for flexible pavement design in the 1986 AASHTO guide.

Over the last three decades, there has been a positive transition from wholly empirical approaches to pavement design towards the use of analytical approaches (e.g. Powell et al., 1984; Brown et al., 1985; Seeds, 2000; Nunn, 2004). In Britain, the analytical pavement design procedure is included in the Highways Agency (2006, 2009). The design flow of this approach can be summarised as Figure 2.10. On the one hand, the traffic loads are converted into the number of standard axles (design life). On the other hand, a multi-layer linear elastic analysis package is used to calculate the load-induced elastic stresses and strains in pavements. Two critical stresses/strains are considered: excessive horizontal tensile stress/strain at the bottom of the base layer causing fatigue cracking, and excessive vertical compressive strain at the top of the subgrade producing permanent deformation at the pavement surface, as shown in Figure 2.11. The 1992 Austroads guide and the 2002 AASHTO guide also utilise similar theoretical framework for pavement design.

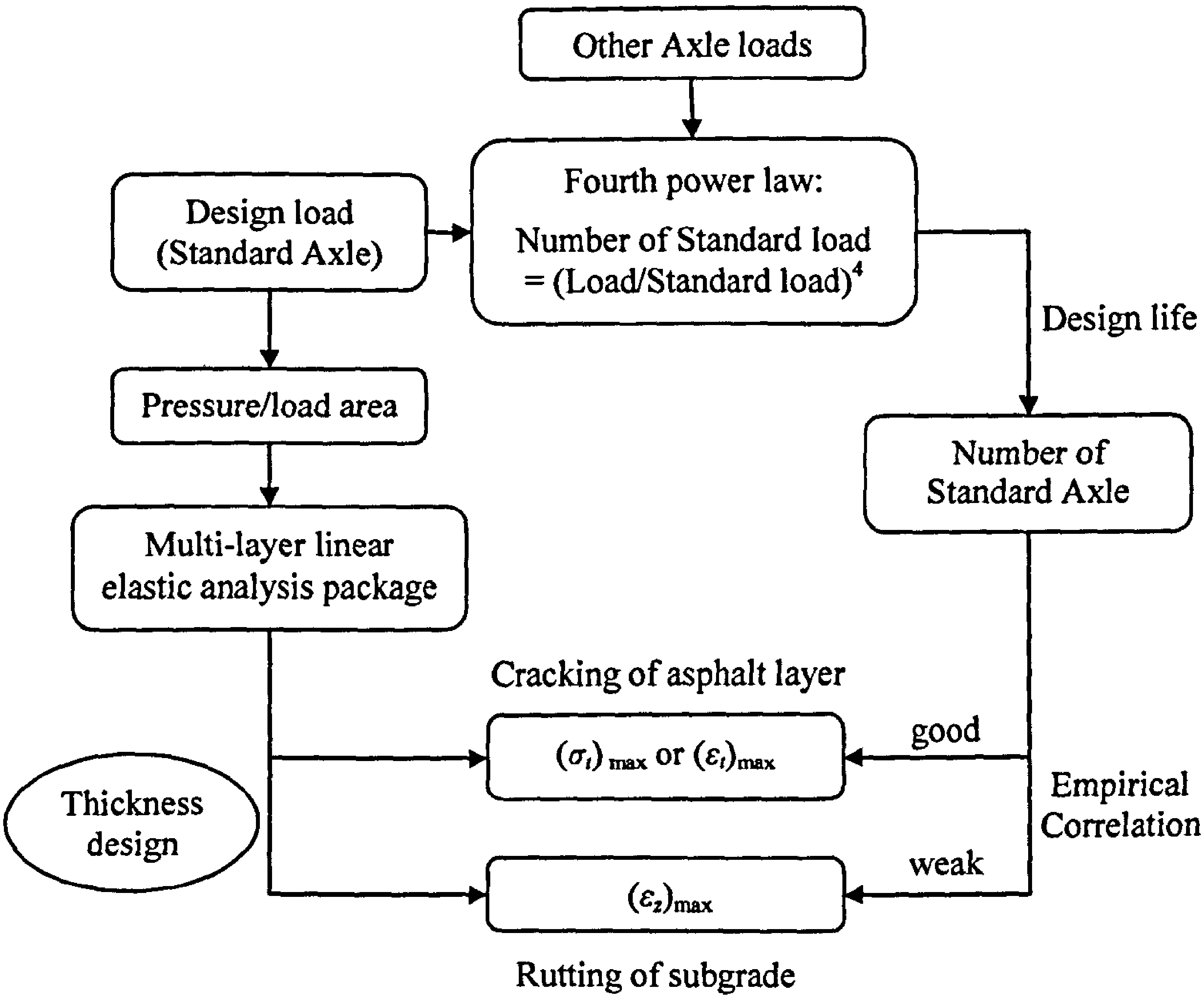

Figure 2.10. Design flow for mechanics-empirical approach (Yu, 2011)

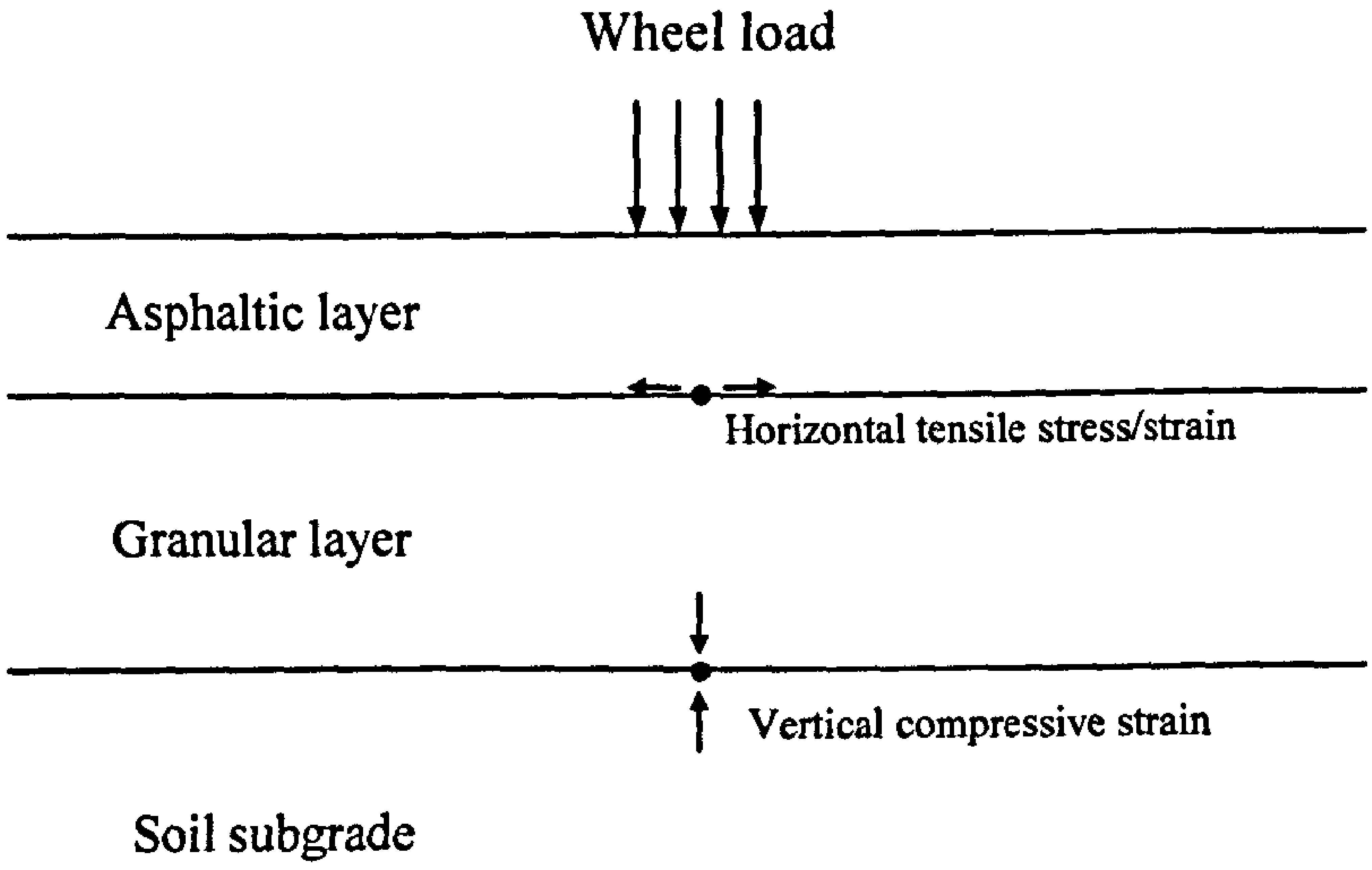

Figure 2.11. Critical stresses and strains in a flexible pavement

The relationships between the pavement life and the critical stresses/strains are usually expressed as empirical equations which were derived based on real evidence of pavement performance. For example, the equation proposed by Powell et al. (1984) in the UK Transport Research Laboratory is likely to be approximately suitable for roads on UK clay soils, as shown in Equation (2.4) for the prevention of excessive rutting.

$$N_f = 3.09 \times 10^{10} \varepsilon_z^{-3.95}, \tag{2.4}$$

where N_f is the number of load applications to failure in millions, ε_z is the subgrade strain (microstrain),

Brown and Brunton (1986) also suggested a design criterion to prevent fatigue cracking as shown in Equation (2.5).

$$N_f = C\left[\frac{1}{\varepsilon_t}\right]^m, \tag{2.5}$$

where ε_t is the tensile strain at the bottom of the asphaltic layer, C and m are constants which depend on volumetric proportion of binder and its initial softening point.

The analytical approach provides a means of evaluating and comparing different design alternatives in an attempt to maximise the pavement's whole life value. However, it should be noted that this approach is mainly based on the elasticity theory. Although empirical equations have been introduced to predict pavement life, the relationship between the subgrade elastic strain and the pavement rutting is weak (see Figure 2.10). Therefore, any attempt at utilising plasticity theory in the prediction of pavement failure is a clear advance in the pavement design process.

2.5 Shakedown phenomena in road pavements

Observations from repeated load tests and full-scale road experiments have both shown the existence of shakedown phenomena.

2.5.1 Repeated load tests

A flexible road pavement, particularly when unsurfaced or thinly surfaced, can be broadly described as one or more layers of granular material placed over the subgrade soil. The overall performance of the pavement structure is then primarily dependent on the behaviour of granular layers.

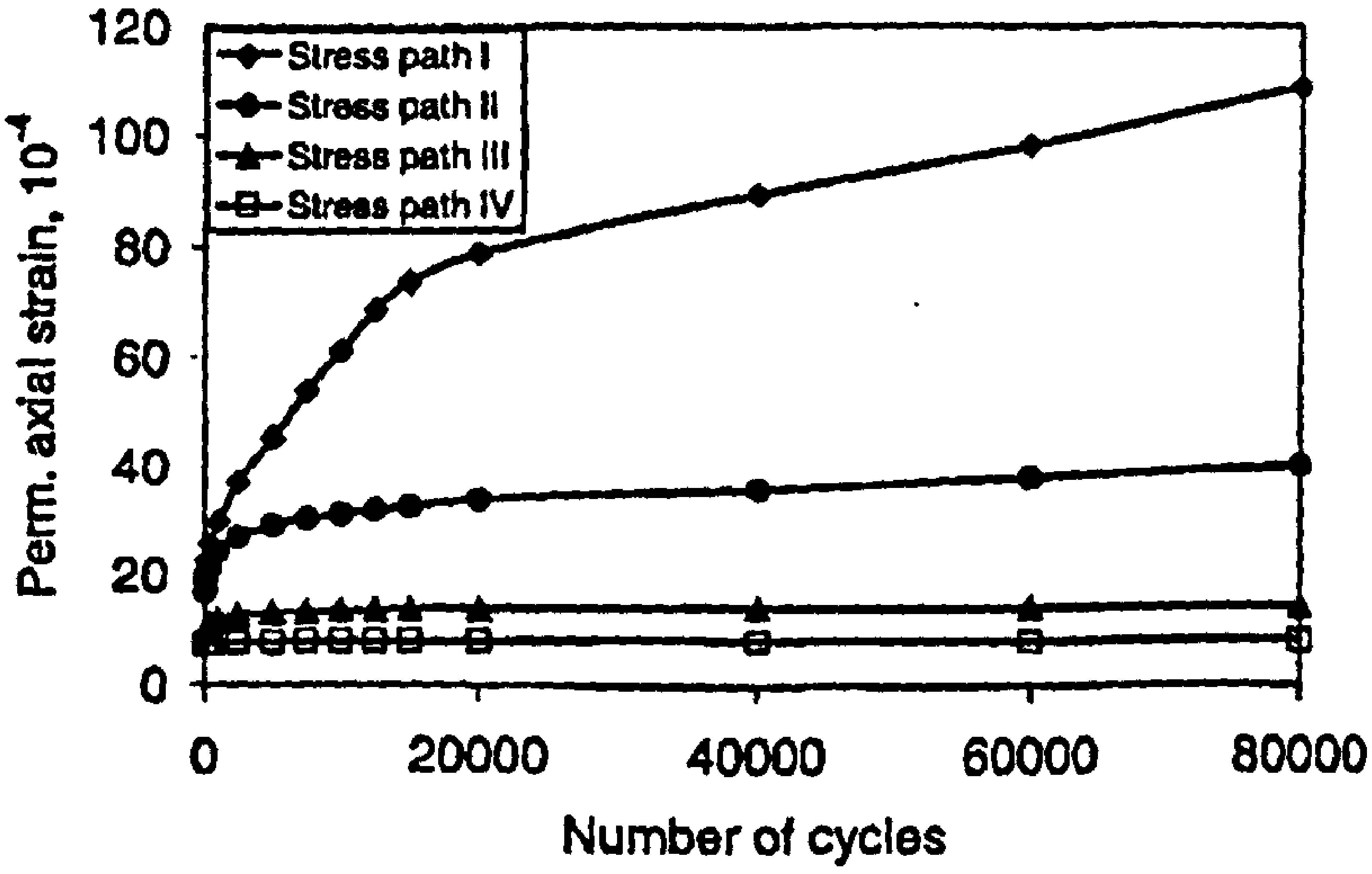

Figure 2.12. Effect of number of cycles and stresses on permanent axial strain (Lekarp and Dawson, 1998)

Lekarp et al. (1996) performed repeated load tests in triaxial apparatus and hollow cylinder apparatus to study the long-term behaviours of granular materials. Five different aggregates were selected, four of which were placed in the Triaxial Apparatus subjected to cyclic deviator and confining pressures, while the last aggregate was tested in the Hollow Cylinder Apparatus with variable deviator stress. The cumulative permanent axial strain was plotted against the number of load cycles (see Figure 2.12) and it was then pointed out by Lekarp and Dawson (1998) that high levels of stress ratios q'/p' (q' is deviator stress, p' is mean stress) cause gradual collapse of the material while low stress ratios ultimately result in an equilibrium state, in similarity with the shakedown concept. Similar results were also reported by several other authors (e.g. Chan, 1990; Gidel et al., 2001; Arnold et al., 2003; Habiballah and Chazallon, 2005). Lekarp et al. (2000) carried out an extensive review of the permanent strain response of unbound aggregates and pointed out that the applied stress level is one of the most significant factors affecting this response and the resulting permanent strain would eventually reach an equilibrium condition at low levels of stress.

Werkmeister et al. (2001, 2004, 2005) did a series of triaxial tests on Granodiorite and sandy gravel by varying vertical stress (deviator stress) while keeping a constant confining pressure. The results were reported by plotting cumulative vertical permanent strain against vertical permanent strain rate (see Figure 2.13). Based on the plots, the responses of the granular materials were categorised as plastic shakedown (Range A), plastic creep (Range B) and incremental collapse (Range C).

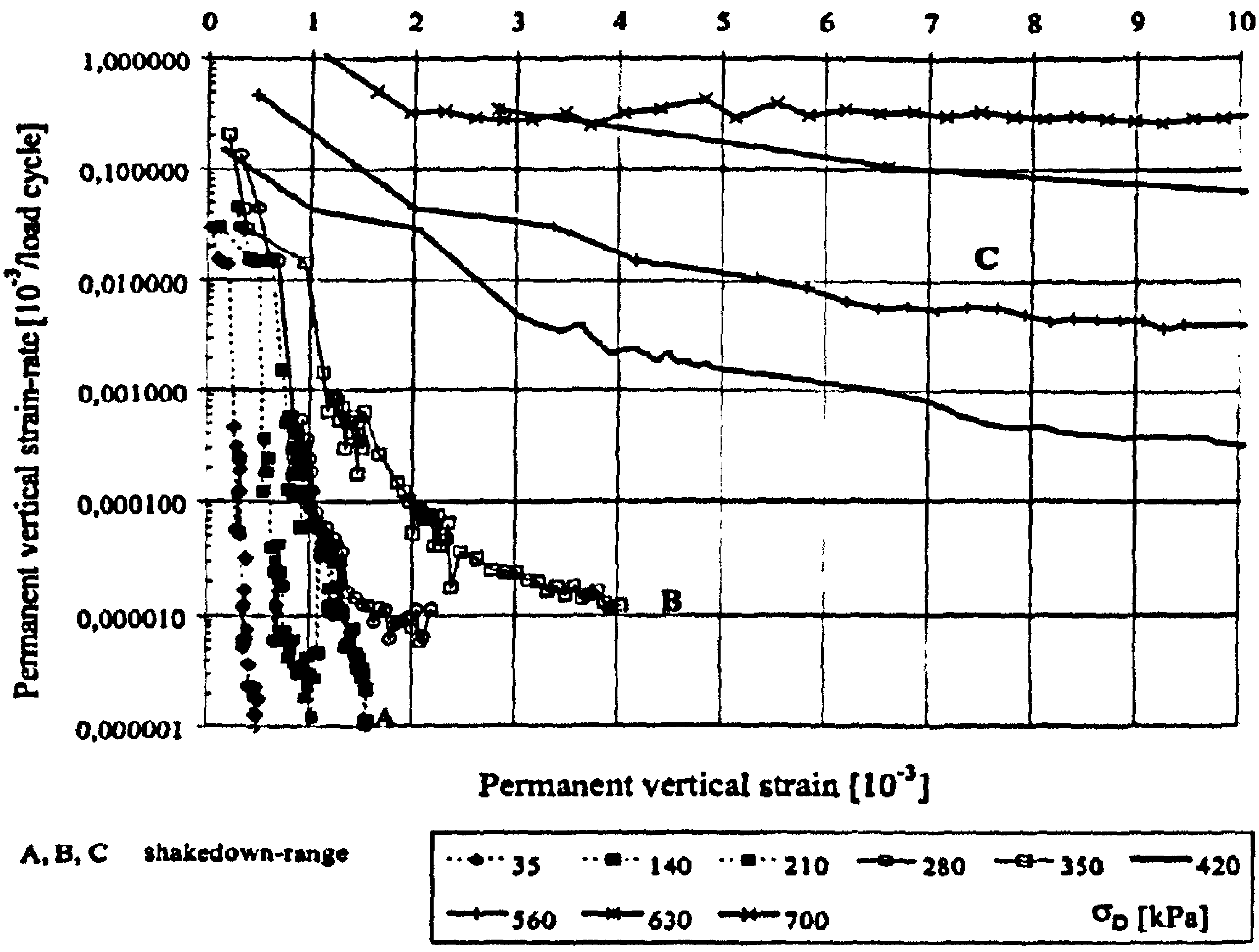

Figure 2.13. Permanent vertical strain against permanent vertical strain rate of Granodiorite, with confining pressure = 70 kPa (Werkmeister et al., 2001)

A number of undrained triaxial tests were also conducted on natrual soil. Sangrey et al. (1969) varied the axial compression with an axial strain rate of about 0.0002% per mininute to enable satisfactory measurements of pore water pressure. It was found that the specimen may reach a non-failure equilibrium condition in which closed stress-strain and pore pressure-strain hysteresis loops are measured, otherwise a pore pressure buildup will bring the soil to the effective stress failure envelope. Muhanna et al. (1998) and Yang and Huang (2007) tried to define the shakedown status and examined the effect of water content on the shakedown limit. It was found that an increase in moisture content can decrease the soil's resistance to load.

2.5.2 Full scale road tests

Shakedown phenomena were also directly observed in full-scale road tests. As early as 1984, Sharp and Booker studied the AASHO test data and pointed out the possibility that a shakedown limit may exsit below which the PSI can be controlled in a satisfactory range (see Figure 2.14).

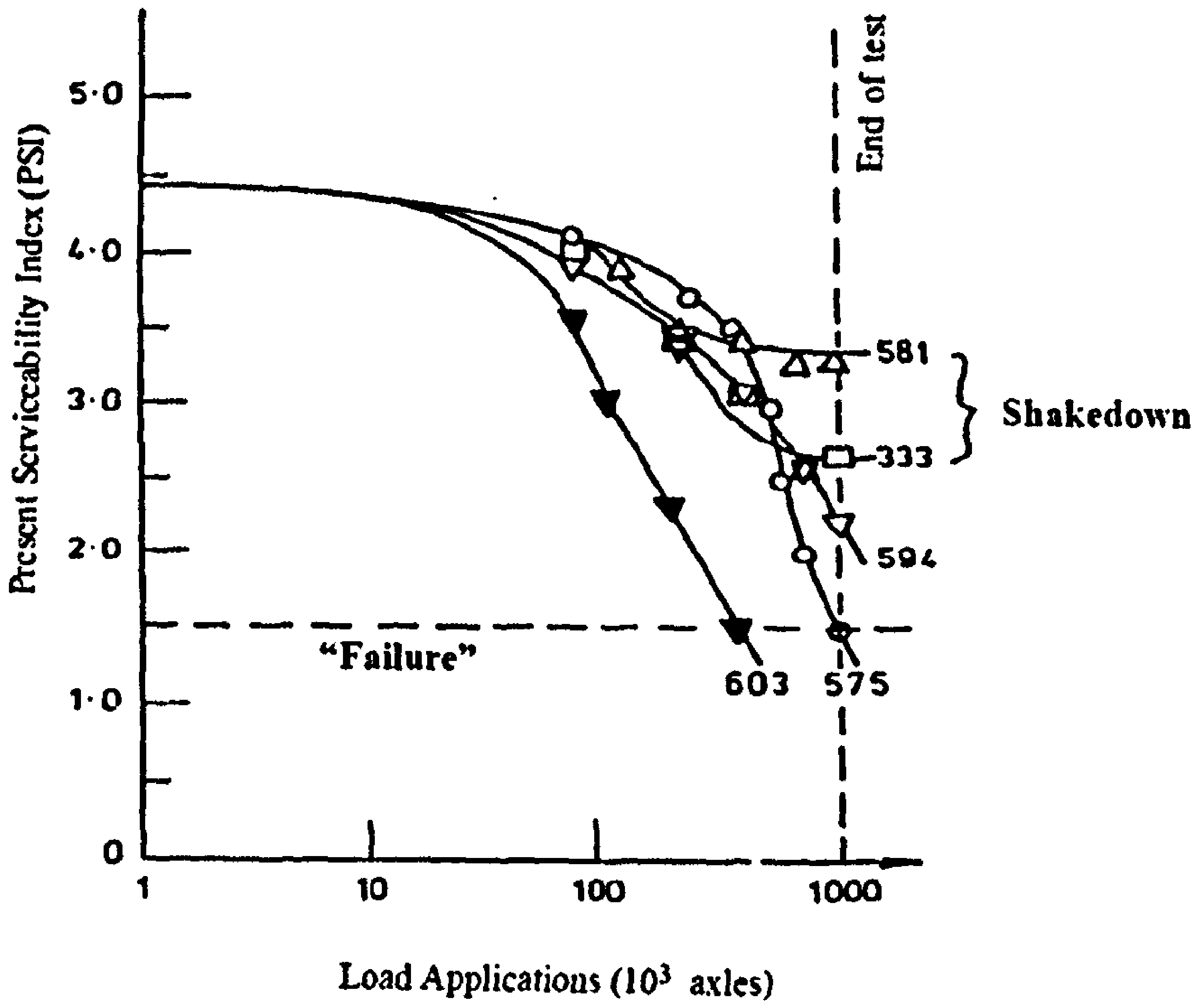

Figure 2.14. Typical performance trends (Sharp and Booker, 1986)

Juspi (2007) performed a series of wheel tracking tests in the University of Nottingham using various wheel loads with up to 100,000 wheel passes. The permanent vertical deformation was plotted against the number of passes for different contact pressures, as shown in Figure 2.15. It was found that the development of vertical permanent deformation depends directly on the applied load levels. These curves were then categorised into three types (see Figure 2.15): Type 1 showing a stabilized permanent deformation after 5000 passes, was clearly a shakedown situation; Type 2, showing a gradually increase of permanent deformation throughout the loading period; Type 3, showing a rapid development of permanent deformation, was clearly in excess of shakedown. As a result, the experimental shakedown load limit should be between 229 kPa and 339 kPa for this particular case. More details of these tests will be presented in Chapter 5.

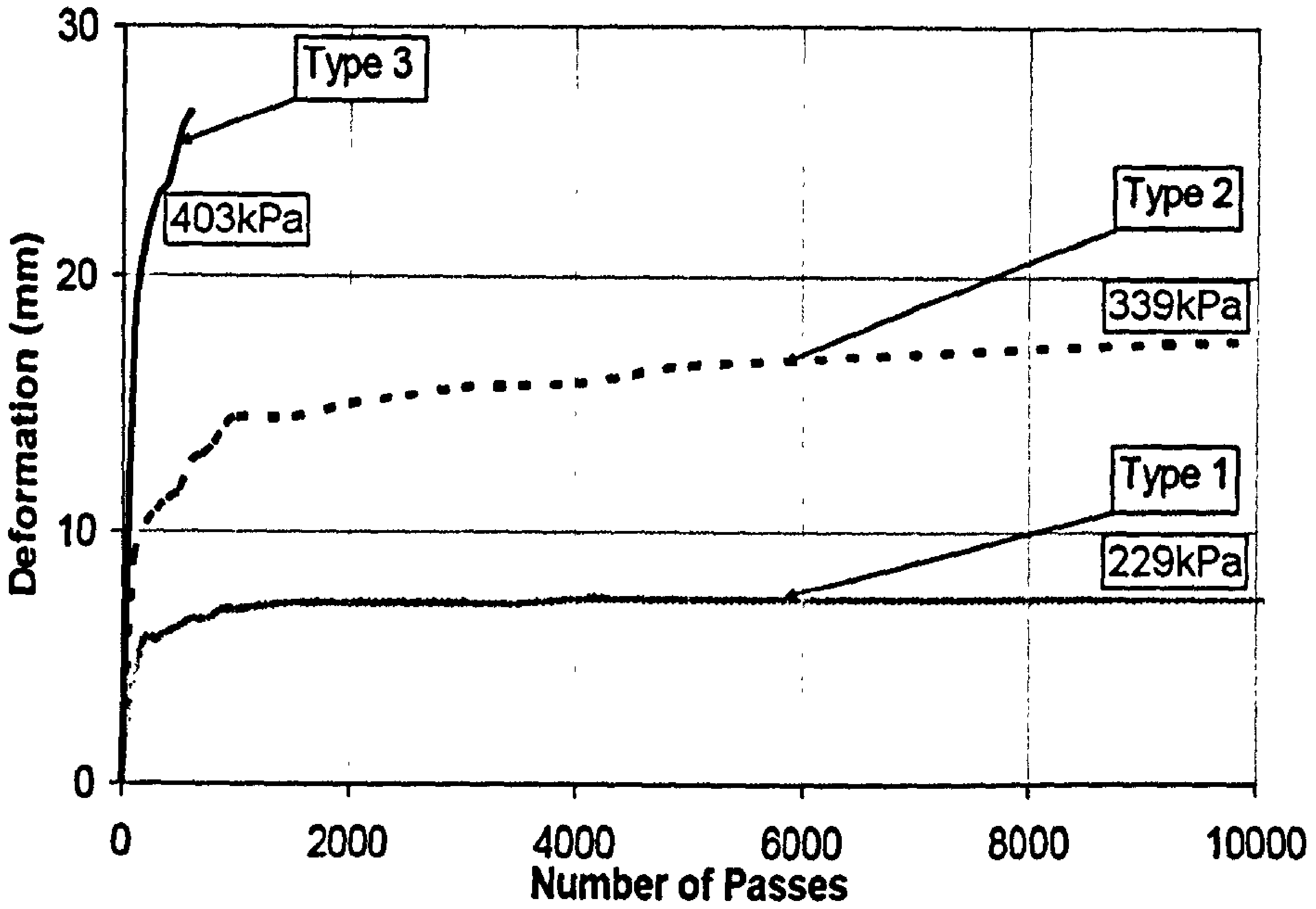

Figure 2.15. Variation in vertical deformation with number of load passes (Juspi, 2007)

Ravindra (2008) and Ravindra and Small (2008) conducted pavement tests using the Sydney University Pavement Testing Facility to investigate the shakedown behaviour of road pavements. The test pavements consisted of a recycled crushed concrete base layer and a sand subgrade layer. The wheel load was kept the same, but the thickness of the base layer was ranging from 50 mm to 350mm (i.e. pavement shakedown load limit varies). It was found that when the shakedown load limit is smaller than the wheel load, there is a rapid increase in vertical surface deformation as shown in Figure 2.16.

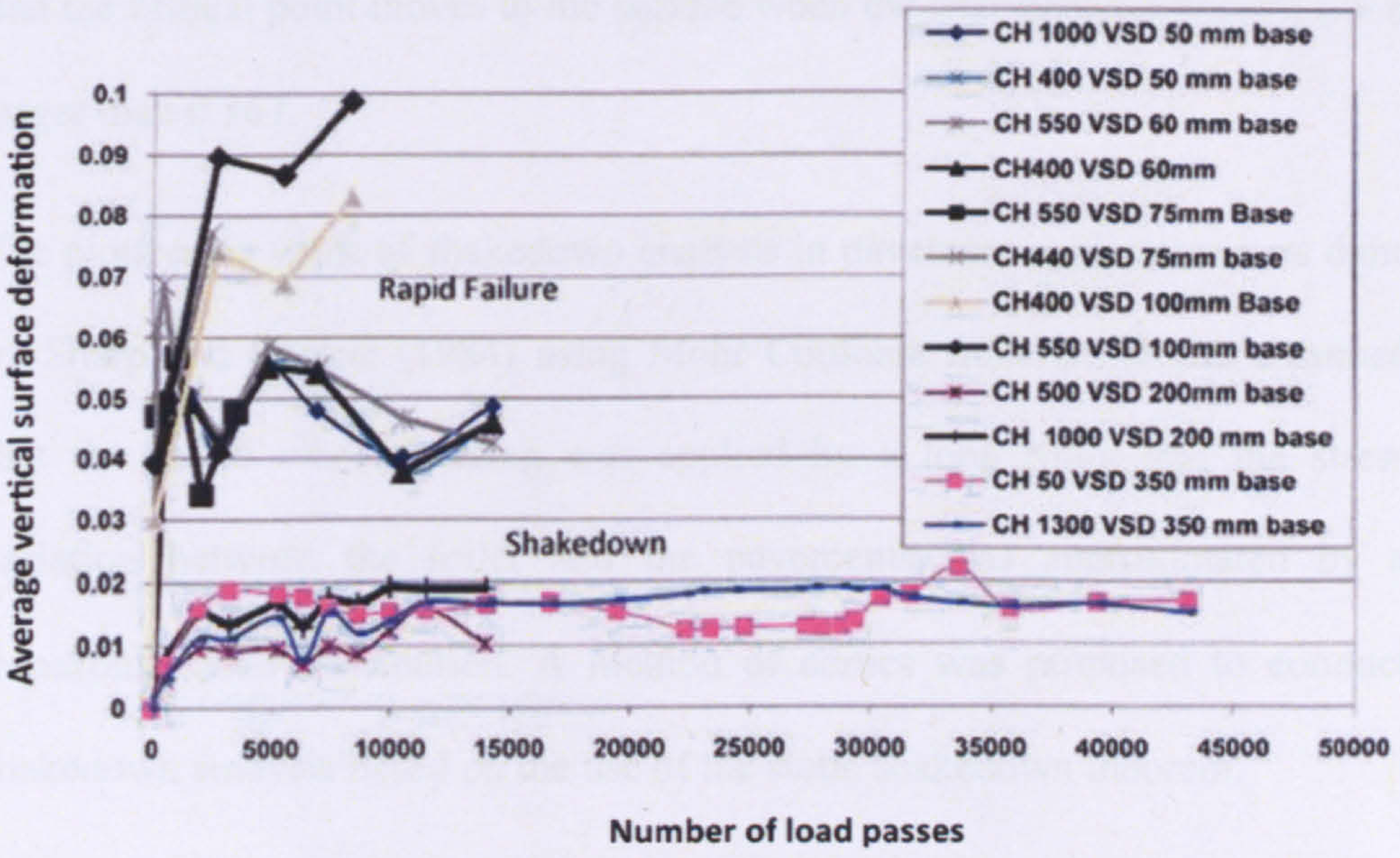

Figure 2.16. Average vertical surface deformation (laser reading) of particular cross sections against number of load passes (Ravindra, 2008)

2.6 Shakedown analyses in pavement engineering

Shakedown analyses for pavements under traffic loads usually utilise the classical shakedown theorems: either Melan's static shakedown theorem or Koiter's kinematic shakedown theorem.

In 1962, Johnson had utilised the line rolling contact assumption to examine the shakedown condition of an isotropic, elastic-perfectly plastic Tresca half-space. Using the Hertz load distribution, the shakedown limit was found as $p_0 = 4.0c$ at the critical points ($\pm 0.87a$, $0.50a$), and the corresponding residual stresses at these points are $-0.134p_0$ (i.e. $-0.536c$). Johnson and Jefferies (1963) then extended this analysis to the rolling and sliding contact problem and found that the critical point moves to the surface when the frictional coefficient q/p is larger than 0.367.

The pioneering work of shakedown analysis in pavement application was done by Sharp and Booker (1984) using Mohr Coulomb material. It was assumed that the actual wheel loading was applied by a long roller and the stress variation between the roller and the pavements was approximated by a trapezoidal load distribution. A method of conics was proposed to conduct shakedown analysis based on the use of the static shakedown theorem.

Raad et al (1988) proposed a numerical shakedown approach using finite element formulation coupled with an optimisation technique. The influences of thickness and material characterisation of the granular layer and the asphalt concrete layer on the shakedown behaviour were examined in detail in their following papers (Raad et al., 1989a, 1989b; Raad and Weichert, 1995; Boulbibane et al., 2000).

Radovsky and Murashina (1996) presented an analytical approach to shakedown analysis of a plane strain pavement model. Experimental studies were also conducted to determine the general form of a horizontal residual stress field in soil. As shown in Figure 2.17(a), pressure cells were installed at various lateral and vertical positions of the experimental road section. The soil had 10% sand, 77% silt and 13% clay. The roller wheel had five tyres with a contact width $2a$ = 27 cm. It was found that the residual stresses ceased to increase after 12 rolling passes. Figure 2.17(b) shows the measured residual stresses against the depth. The peak residual stress occurs at z = 7 cm (i.e. z/a = 0.52).

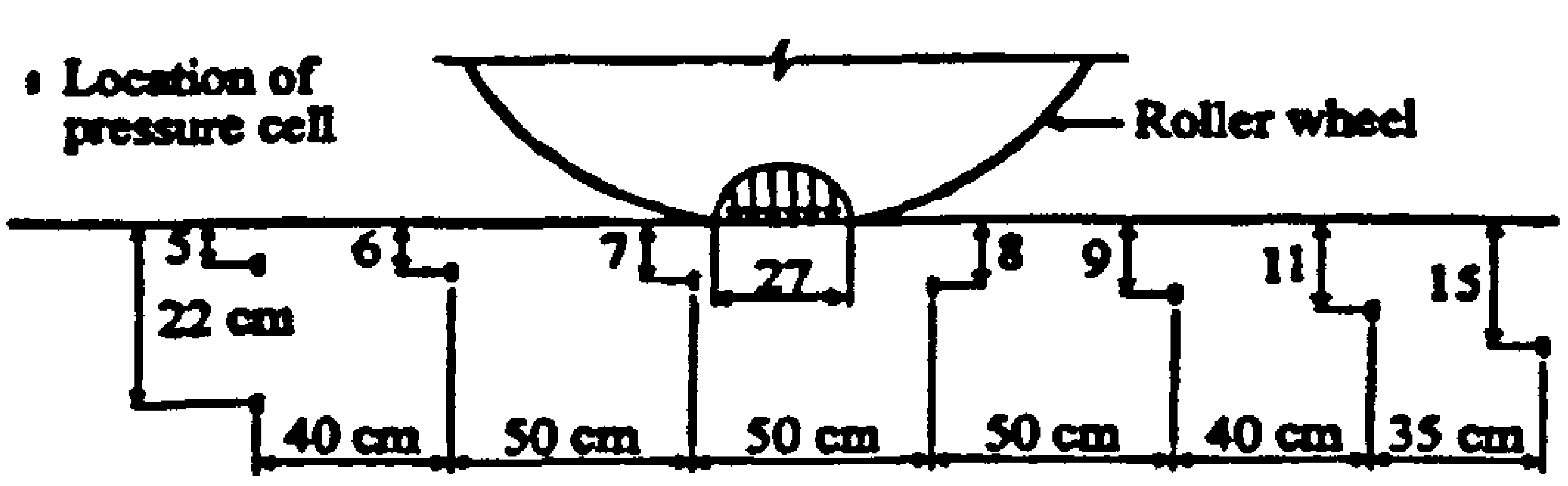

(a) Location of pressure cell

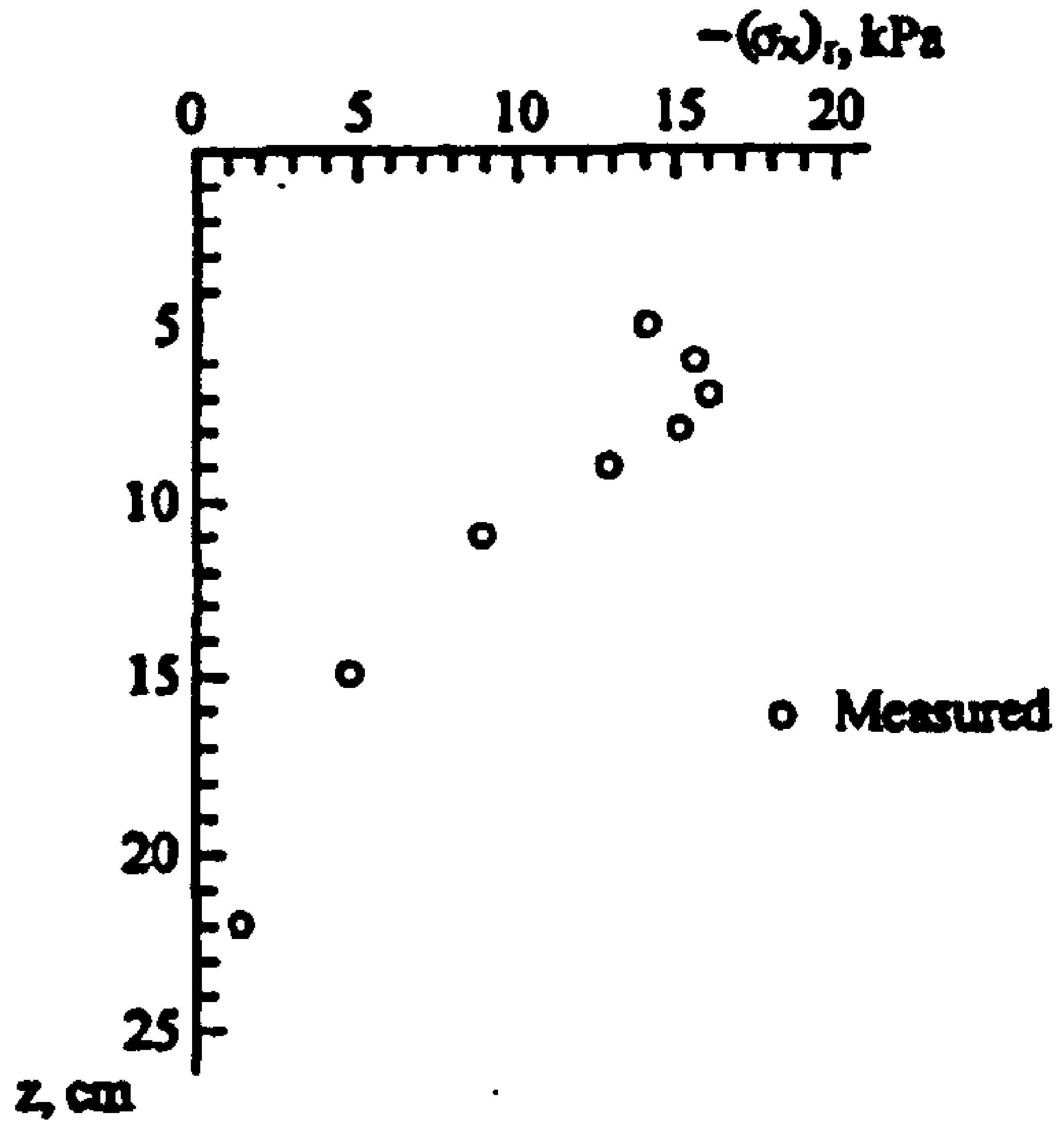

(b) Measured residual stresses

Figure 2.17. Measured residual stresses in soil after rolling passes (Radovsky and Murashina, 1996)

Yu and Hossain (1998) developed a lower-bound shakedown formulation using finite element technique and linear approximations. The optimum residual stress field was found by using stress-based finite elements. The shakedown problem was finally solved as a linear programming problem. Shiau and Yu (2000) investigated the influences of material properties on the shakedown limit of layered pavement by using the lower-bound shakedown formulation and developed a displacement bounding method for estimating the pavement permanent deformation at shakedown state. Shiau (2001) also extended the formulation to shakedown analysis of three-dimensional pavements. However, the size of the linear programming problem became prohibitively large when finer mesh was applied.

Yu (2005) proposed an analytical solution for shakedown of cohesive-frictional half-space under moving Hertz loads using Melan's static shakedown theorem. This solution provides the same two-dimensional shakedown limits as those in Collins and Cliffe (1987). In the case of cohesive material, the obtained shakedown limits are also close to the three-dimensional upper bound shakedown solution of Ponter et al. (1985).

Krabbenhøft et al. (2007) and Zhao et al. (2008) suggested a scanning line method to find the lower-bound shakedown limits of plane strain half-space under moving surface loads. The influences of different load distributions on the shakedown limits were examined.

Meanwhile, based on the kinematic shakedown theorem, Collins and Cliffe (1987) and Collins et al. (1993a, 1993b) obtained an upper bound shakedown solution by assuming a failure mechanism of subsurface slip, which was parallel to the shakedown solution of Ponter et al. (1985) for a pure cohesive material under three-dimensional moving loads. The solution was then developed by introducing a rut failure mechanism at the cross-section perpendicular to the direction of travel, providing more realistic shakedown limits (Collins and Boulbibane, 1998; Boulbibane and Collins, 2000; Collins and Boulbibane, 2000; Boulbibane et al., 2005).

Li and Yu (2006) developed a numerical approach to kinematic shakedown analysis of frictional materials by making use of finite element technique and nonlinear mathematical programming. The potential difficulty of integration along a deformation path is removed by using König's technique (König, 1987). This approach was then extended to materials following non-associated plastic flow (Li, 2010). It was found that the shakedown limit with non-associated plastic flow is smaller than that with associated plastic flow.

A linear matching method, originally proposed for limit and shakedown analyses of metal structures under static or cyclic load (Ponter and Engelhardt, 2000; Chen and Ponter, 2001, 2005; Ponter et al., 2006), has been applied to the pavement shakedown problem using the Drucker-Prager yield criterion (Boulbibane and Ponter, 2005). According to Boulbibane and Ponter (2006), the basic idea of this method is that the stress and strain fields for non-linear material behaviour may be simulated by the solution of linear problems where the linear moduli vary with time and space.

2.7 Plastic deformation and shakedown of half-space in rolling and sliding contact

According to Johnson (1985), rolling is defined as a relative angular motion between two bodies in contact about an axis *y* (see Figure 2.18). If the peripheral velocities of two surfaces at point *O*, V_1 and V_2, are equal, the motion is a pure rolling; otherwise it is accompanied by sliding. The contact stresses are normal to the contact plane *x*-*y* for the pure rolling contact. And the sliding will introduce a surface shear force parallel to the contact plane.

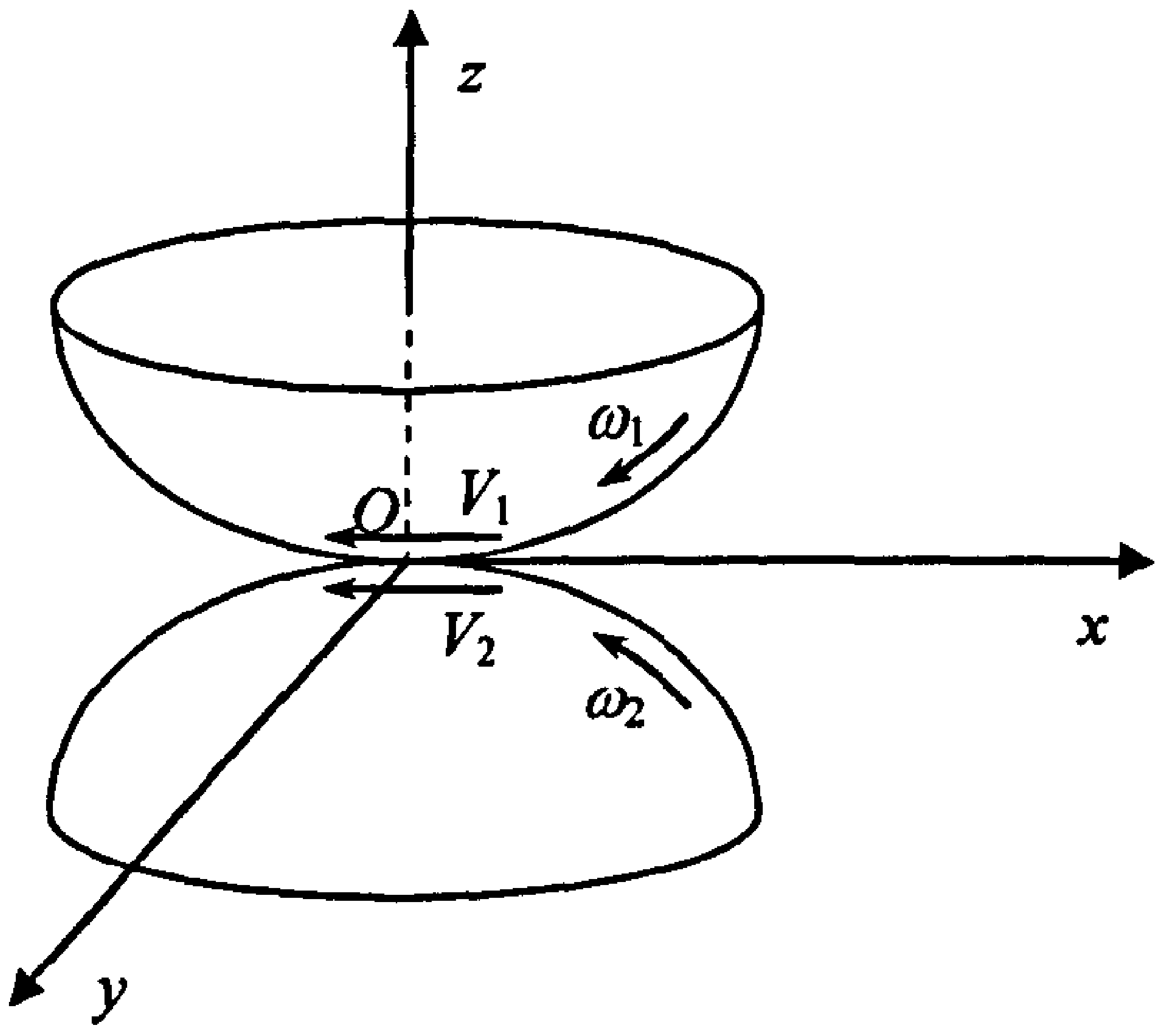

Figure 2.18. Two bodies in contact at *O*

Several engineering problems are concerned with repeated rolling and sliding contact, such as roller bearings, railway track and road pavements. In these cases, the dimensions of the contact area are quite small compared with the dimensions of the bodies.

2.7.1 Hertz load distribution

The contact stresses on the solid surface due to the rolling and sliding contact are usually assumed to be in Hertz load distribution (Johnson, 1962, 1985). For a line contact problem which considers a long cylinder rolling over a half-space with a contact width $2a$ and a maximum pressure p_0 at the load centre, the contact pressure p can be written as Equation (2.6). For a point contact problem which considers a ball rolling on a surface with an elliptical contact area, the normal pressure distribution can be written as Equation (2.7) where a and b are semi-axes of the elliptical contact area.

$$p = p_0\left(1 - \frac{x^2}{a^2}\right)^{1/2}, \tag{2.6}$$

$$p = p_0\left(1 - \frac{x^2}{a^2} - \frac{y^2}{b^2}\right)^{1/2}. \tag{2.7}$$

The surface contact shear stress q is usually expressed in an analogical form (Equation (2.8) for the line contact and Equation (2.9) for the point contact), linked with the normal pressure by a frictional coefficient $\mu = q/p$.

$$q = q_0\left(1 - \frac{x^2}{a^2}\right)^{1/2}, \tag{2.8}$$

$$q = q_0\left(1 - \frac{x^2}{a^2} - \frac{y^2}{b^2}\right)^{1/2}. \tag{2.9}$$

2.7.2 Plastic deformation and residual stresses

Rolling and sliding line contact

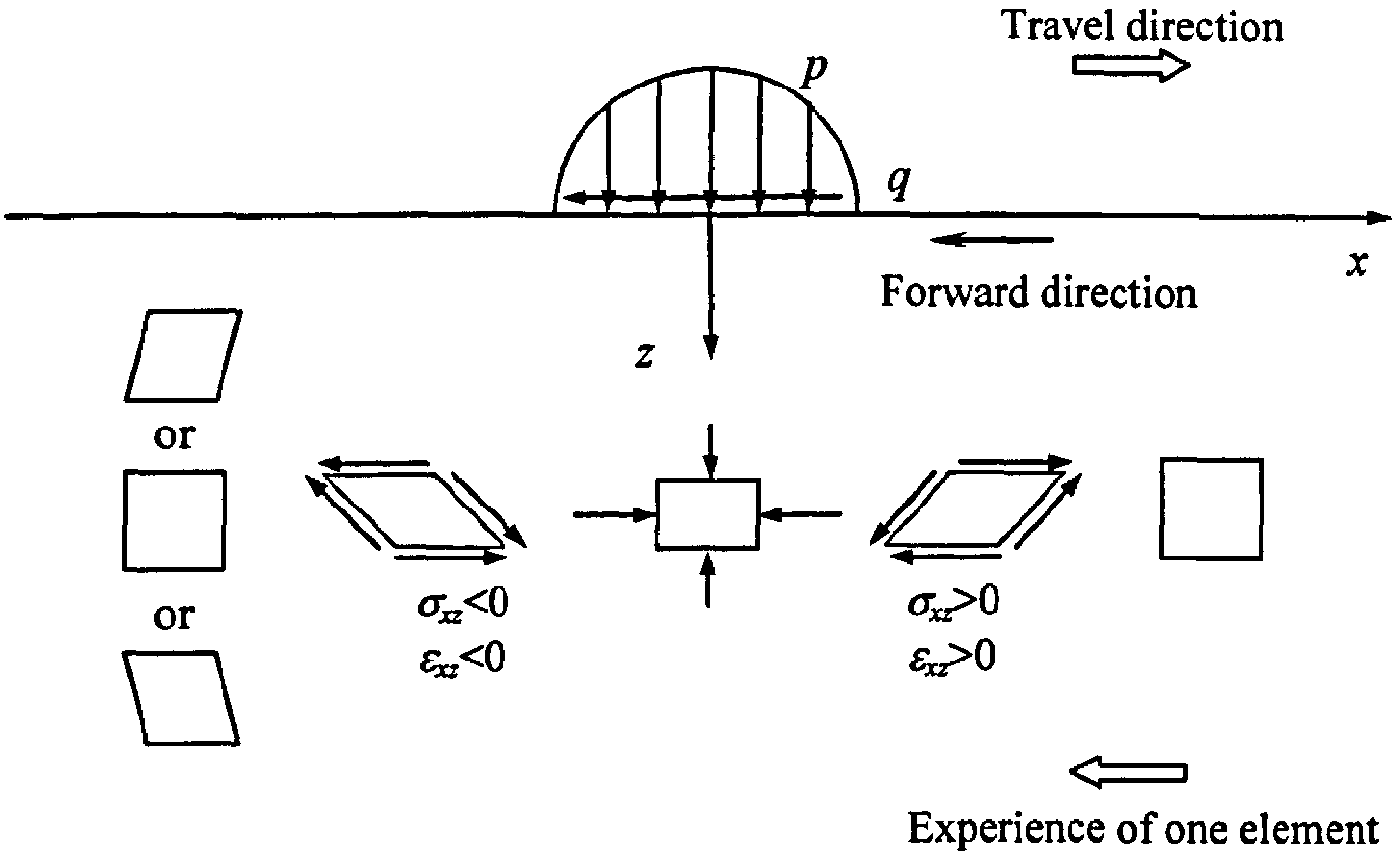

Figure 2.19. Experience of one element in line contact

When the rolling and sliding contact travels over a semi-infinite half-space in the x direction (see Figure 2.19), any element at the same depth z experiences the same stress and strain history. As shown in Figure 2.19, an element of material is subjected to a cycle of reverse shear during one contact pass. If the stress state exceeds the yield limit, some plastic shear strains ε_{xz}^{p} will occur. One element may experience both positive and negative plastic shear strain, and it is the combination of them that gives rise to net plastic shear strain after one contact pass. These net plastic shear strains, whether in positive or in negative, are only dependent on depth z and they form a plastic shear band in the half-space parallel to the surface. While the negative plastic shear strain produces a forward plastic flow, the positive plastic shear strain produces a backward plastic flow (the forward direction refers to Figure 2.19). The overall plastic shear strain in the half-space manifests itself as a tangential displacement of the surface (Merwin and Johnson, 1963). When the load is above the shakedown limit, the half-space will either experience tangential surface ratchetting due to cumulative net plastic shear strains, or undergo continuous cyclic plasticity due to full reversal of plastic shear in each contact pass. It should be noted that different material models may give rise to different half-space responses (which will be discussed in Section 2.7.3).

Directly under the contact, an element of material is compressed normal to the surface and a small amount of compressive plastic strains ε_{zz}^{p} may occur. Under the plane strain condition, the element then attempts to expand in the x direction. Since all elements at the same depth deform plastically in the same way in turn, their lateral expansion must be annulled by the development of compressive residual stresses σ_{xx}^{r} acting parallel to the surface (Johnson, 1985). When the load is at or below the shakedown limit, these residual stresses generally help the material to resist further development of plastic deformation. When the load is above the shakedown limit, as the load magnitude is increased further, the residual stresses will spread into a thicker layer but will be incapable of preventing continuing plastic deformation.

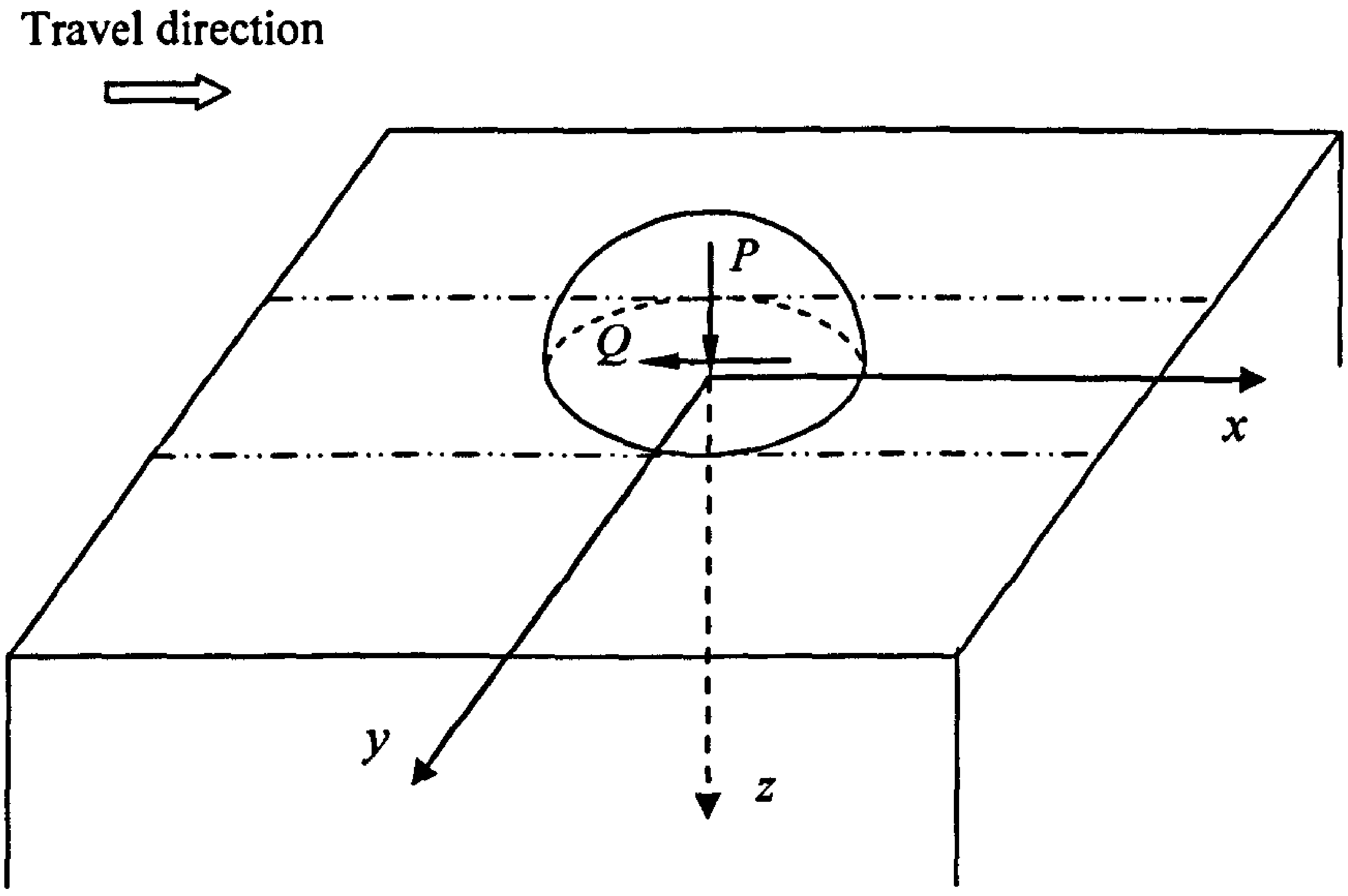

Figure 2.20. Rolling and sliding point contact

According to Ponter et al. (1985), the point contact problem has two different modes of continuing plastic deformation: plastic displacements in the direction of travel, which is similar to that found in the line contact, and a groove of steadily increasing depth produced by a thin wheel. In the first mode, the surface displacement is associated with plastic shear strains ε_{xz}^{p} and ε_{xy}^{p}. In the second mode, the material directly below the contact is compressed in the z direction and moves in the y direction. The material compression is associated with plastic normal strains ε_{zz}^{p} and ε_{yy}^{p}, while the material lateral movement is attributed to the presence of plastic shear strain ε_{yz}^{p} (Kulkarni et al., 1990, 1991; Jiang et al., 2002). In addition, all six components of residual stresses are possible and, indeed, they are independent of x.

2.7.3 Historical development

There have been consecutive analytical and numerical works on the investigation of metal half-space responses in repeated rolling or rolling and sliding contact.

In the early studies, elastic-perfectly plastic Von Mises material was usually adopted. Merwin and Johnson (1963) developed an approximate method to investigate the plastic flows and residual stresses by assuming that the total strain cycle was the same as the elastic strain cycle. It was found that the surface is displaced in the forward direction in the pure rolling line contact. This finding agrees with experimental observations (e.g. Crook, 1957; Hamilton, 1963; Hahn and Huang, 1986). When the load is above the shakedown limit, the surface tangential displacement accumulates at a constant rate with the number of load passes. Johnson and Jefferis (1963) then extended this method to the rolling and sliding contact problem. However, one limitation of this approximate method is that the equilibrium condition is not satisfied during the rolling contact process.

The pure rolling contact problem was also solved by a finite element method of Bhargava et al. (1985a, 1985b) which fulfils the equilibrium and compatibility requirements. This method obtains similar peak residual stresses to those reported by Merwin and Johnson (1963). Both backward and forward plastic flows were observed in the half-space. However, consecutive cycles only produce increases in the forward plastic flow. Consequently, the surface displacement is dominated by the relatively larger forward plastic flow. The finite element method also found that Merwin and Johnson (1963) severely underestimates the rate of increase in surface displacement by a factor of about five.

Hearle and Johnson (1987) then used a distributed dislocation technique to avoid the simplifying assumption of Merwin and Johnson (1963), and the obtained surface displacement agrees with Bhargava et al. (1985b), as shown in Figure 2.21. For the rolling and sliding contact, Hearle and Johnson (1987) showed higher surface displacement than that obtained by Johnson and Jefferis (1963).

Based on the finite element model of Bhargava et al. (1985a, 1985b), Ham et al. (1988) conducted finite element analysis for the rolling and sliding contact. The obtained forward surface displacement is much higher than that predicted by Johnson and Jefferis (1963) and Hearle and Johnson (1987). Ham et al. (1989) then introduced a linear kinematic hardening plasticity model and predicted a much smaller value than that for the elastic-perfectly plastic material.

Bower and Johnson (1989) modifed the technique of Hearle and Johnson (1987) by using a nonlinear kinematic hardening plasticity model proposed by Bower (1989). Their rate of increase in surface dispacement for the pure rolling contact generally agrees with the observations in experiments, as shown in Figure 2.21. For rolling with significant sliding contact, Bower and Johnson (1989) noticed that the suface displacement is dominated by the behaviour of surface elements. They then assumed that the elastic stress field within the thin surface layer provides a good approximation to the true stress field and excluded the plastic deformation in the axial direction to perform integration. Compared to the experimental work, the obtained surface displacement becomes asymptotically correct as the shakedown limit is approached.

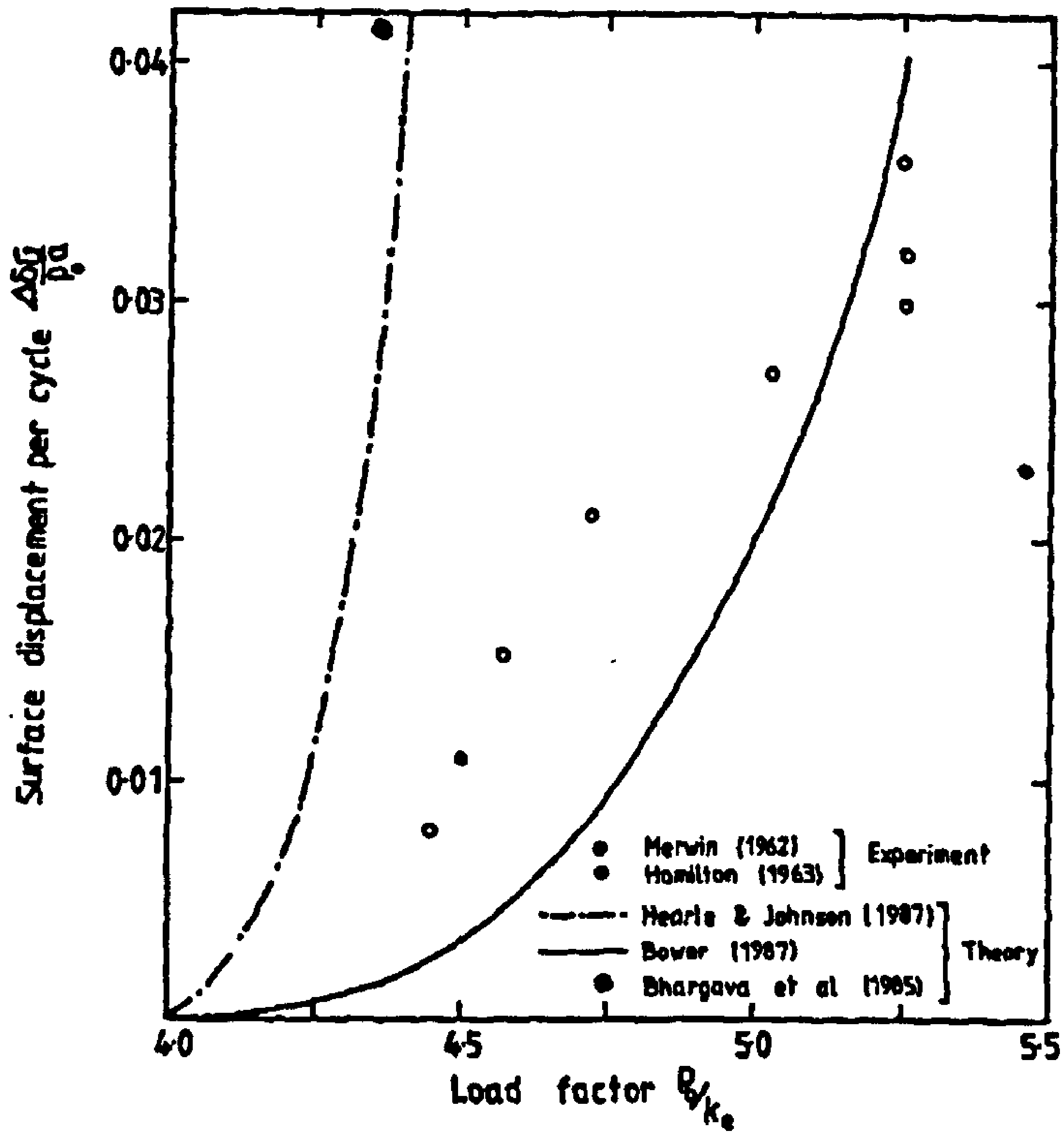

Figure 2.21. Rate of increase in surface displacement for pure line rolling (Bower and Johnson, 1989)

More studies have shown that the material model dramatically affects the half-space responses. For example, the non-linear kinematic hardening models can account for the cumulative plastic deformation (Bower and Johnson, 1989, 1991; McDowell and Moyar, 1991; Howell et al., 1995; Jiang and Sehitoglu, 1996; Sakae and Keer, 1997; Xu and Jiang, 2002), while the linear kinematic hardening models enforce fully reversed plastic cycles and therefore exclude the possibility of ratchetting (Ham et al., 1989; Kulkarni et al., 1990, 1991; Yu et al., 1993; Jiang and Sehitoglu, 1994). Bower and Johnson (1989) also noted that isotropic hardening material will always shakedown to an elastic state in one half cycle. Moreover, Bower's model (Bower, 1989; Bower and Johnson, 1989) predicted a constant rate of surface movement while Jiang's model (Jiang and Sehitoglu, 1996; Jiang et al., 2001; Xu and Jiang, 2002) showed a decay of the surface displacement rate as the number of rolling contacts increased.

In the present study, the elastic-perfectly plastic Mohr Coulomb model was adopted for finite element analysis of soil half-space under moving surface loads (see Chapter 3).

2.8 Summary

Flexible road pavements subjected to repeated traffic loads may fail due to the fact that irrecoverable strain accumulates at each load application, leading to excessive vertical permanent deformation after a number of load applications. Alternatively, if the pavement ceases to experience any further plastic strain after a number of load cycles, a shakedown status is achieved. Shakedown analysis is mainly concerned with the calculation of the shakedown load limit below which the pavement can shake down, so that the pavement permanent deformation will be very small even under a very large number of load applications. Generally speaking, one can determine the shakedown limit by using either the shakedown theorem or elastic-plastic analysis.

CHAPTER 3

FINITE ELEMENT ANALYSIS OF SOIL HALF-SPACE UNDER MOVING SURFACE LOADS

3.1 Introduction

In this chapter, the finite element (FE) method is used to simulate the responses of plain strain soil half-space subjected to repeated moving surface loads. These responses including the developments of residual stresses, plastic strains and permanent deformations cannot be predicted by using the classical shakedown theorems.

The Tresca and Mohr Coulomb yield criteria are used to model the plastic flow of the soil. Both associated plastic flow rule and non-associated plastic flow rule are considered. The surface loads, assumed in two-dimensional Hertz load distribution, are applied using different loading levels around the shakedown limit in order to capture the shakedown and non-shakedown phenomena of the soil half-space. The influence of the residual stress distribution on the half-space shakedown status is highlighted by using Melan's static shakedown theorem. The FE calculated residual stress fields will also be used in the next chapter for the purpose of comparison.

3.2 FE model

3.2.1 ABAQUS

The FE method is a numerical approach that solves the governing differential equations of a system through a discretisation process. Its development can be traced back to the work done by Hrennikoff (1941) and Courant (1943). By the early 1970s, the FE software was only used on large main-frame computers. However, since then there has been a transition to 'workstations' and then desktop personal computers. Nowadays, the FE software has been widely used in engineering applications.

ABAQUS is a commercial FE software package developed by SIMULIA. It can solve problems ranging from relatively simple linear analyses to the most challenging nonlinear simulations. ABAQUS also offers portals for user material, user elements, user output etc. Its ability to incorporate a FORTRAN subroutine into the calculation is exceptionally useful. The present FE analyses were conducted using the user subroutine DLOAD, which can define the variation of the distributed load magnitude as a function of position, time, element number, load integration point number, etc.

ABAQUS has an extensive library of elements that can be used for a wide range of applications, such as continuous elements, rigid elements, contact elements etc. The choice of element type has important consequences regarding the accuracy and efficiency of the simulation. The standard continuous elements were selected for the present study. According to the ABAQUS manual, the continuous elements are provided with first-order (linear) and second-order (quadratic) interpolation. The interpolation order is usually determined by the number of nodes used in the element. The linear elements have nodes only at their corners, such as Figure 3.1, while the quadratic elements have one more node in the middle on each side, such as Figure 3.2. The quadratic elements provide higher accuracy than the linear elements for smooth problems that do not involve complex contact conditions or severe element distortions.

(a) Fully integration (b) Reduced integration

Figure 3.1. Two-dimensional linear elements

(a) Fully integration (b) Reduced integration

Figure 3.2. Two-dimensional quadratic elements

ABAQUS evaluates the material response at each integration point (Gauss point) in each element and a choice between full and reduced integration can have a significant effect on the accuracy of results for a given problem. The expression 'full-integration' refers to the number of integration points required to integrate the polynomial terms in an element's stiffness matrix exactly when the element has a regular shape. As shown in Figure 3.1(a) and Figure 3.2(a), the fully-integrated, linear element has two integration points in each direction while the fully-integrated, quadratic element has three integration points in each direction. The reduced-integrated elements use one fewer integration point in each direction than the fully-integrated elements, as shown in Figure 3.1(b) and Figure 3.2(b). The ABAQUS manual suggests that the second-order reduced-integrated element in ABAQUS/Standard generally yield more accurate results than the corresponding fully-integrated elements. As a result, the eight-noded, reduced-integrated, quadrilateral elements (CPE8R) were adopted in the present study to model the soil half-space in the plane strain condition.

3.2.2 FE model

Figure 3.3 shows the FE model of plane strain half-space under moving Hertz load distribution. There is a restraint on horizontal movement at the vertical boundaries, and there is a restraint on vertical movement at the bottom boundary. This model tries to simulate the idealised line contact problem (refers to Section 2.7) by using a long travelling distance. The size of the simulated region ($84a$ long × $30a$ high) was selected through sensitive studies in which further extension of length or width or change of boundary condition (e.g. spring boundary condition) has a negligible effect on the half-space responses.

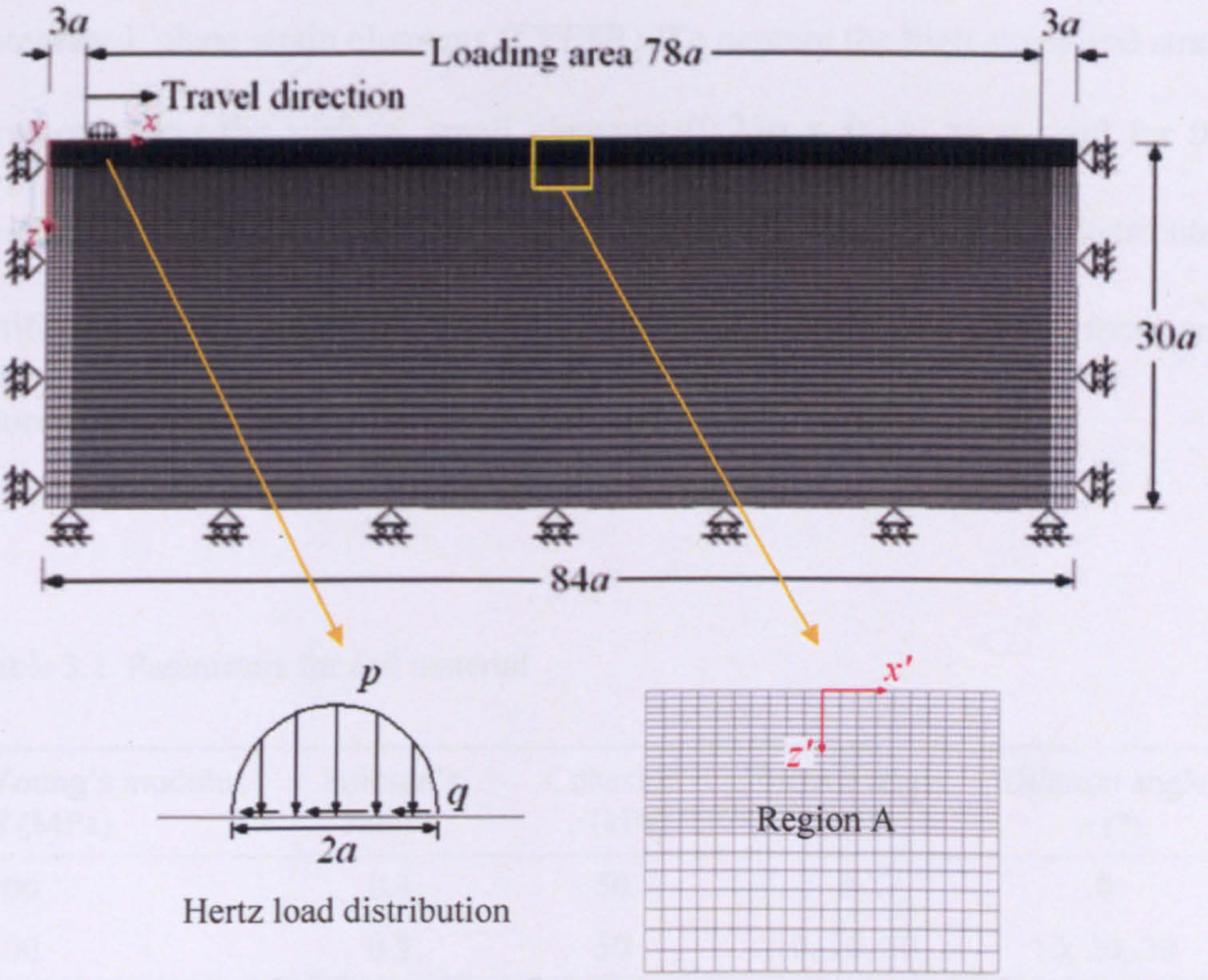

Figure 3.3. FE model of plane strain half-space under moving surface loads

At the top surface of the half-space, the Hertz load, including normal pressure p and surface traction q (refers to Equations (2.6) – (2.9)), is moving along a loading area (78*a*). A user-subroutine DLOAD was utilised to control the load applications. In every load pass, the Hertz load distribution was first applied gradually at the start point. It then translated incrementally in the x direction over a distance of 76*a*. Automatic increment size was selected in the ABAQUS, so that sufficiently small increments can be taken to obtain the results in a reasonable accuracy. Loads were completely removed at the end of each pass, so that the residual stresses and the plastic strains can be obtained.

The simulated region was discretised by 22,960 eight-noded, reduced-integrated, plane strain elements (CPE8R). To capture the high stress and strain gradients near the surface, small elements ($0.25a \times 0.1a$) were used for the region near the loading area ($z \leq 2a$) and the elements were distributed uniformly along $2a \leq x \leq 82a$. Away from $z = 2a$, the mesh becomes more and more coarse.

Table 3.1. Parameters for soil material

Young's modulus E (MPa)	Poisson's ratio υ	Cohesion c (kPa)	Friction angle ϕ (°)	Dilation angle ψ (°)
100	0.4	50	0	0
100	0.3	50	10, 20, 30	10, 20, 30

Material of the FE model is assumed to be elastic-perfectly plastic using the standard linear elastic parameters (Young's modulus E and Poisson's ratio υ) and Mohr Coulomb yield criterion parameters (cohesion c, friction angle ϕ and dilation angle ψ). The material is also assumed be homogeneous and isotropic. As summarised in Table 3.1, Poisson's ratio was given as a relatively high value 0.4 in the case of Tresca-type soil (i.e. $\phi = \psi = 0$), while it was chosen as a lower value 0.3 for frictional soil. In addition, the problem was analysed using stress and strain measures that account for geometry changes, to capture material rearrangement due to possible large deformation. It should be noted that in the present study and the following chapters, compressive stresses and strains are always taken as negative.

3.2.3 Model verification

A number of semi-analytical methods (Merwin and Johnson, 1963; Hearle and Johnson, 1987) and FE methods (Bhargava et al., 1985a, 1985b) have been used for analyses of Von Mises half-space under moving surface loads, as reviewed in Section 2.7. In the present study, FE analyses were first undertaken using Von Mises elastic-perfectly material so that the validity of the proposed FE model can be proved.

The material properties were selected the same as those used in Bhargava et al. (1985a, 1985b): Young's modulus $E = 207$ GPa, Poisson's ratio $\upsilon = 0.3$, shear resistance $k = \sigma_0 / \sqrt{3} = 227$ MPa (σ_0 is the yield strength). A pure rolling condition (i.e. only normal loads) was considered and the Hertz load distribution had a maximum pressure $p_0/k = 4.35$ in the centre.

Figure 3.4 shows the residual stress σ^r_{xx} and plastic strain ε^p_{xz} distributions in the Region A (refers to Figure 3.3) upon the removal of load applications. As can be seen, the stress and strain distributions are independent of the travel direction. This suggests that the results taken from the Region A are representative for the line contact problem.

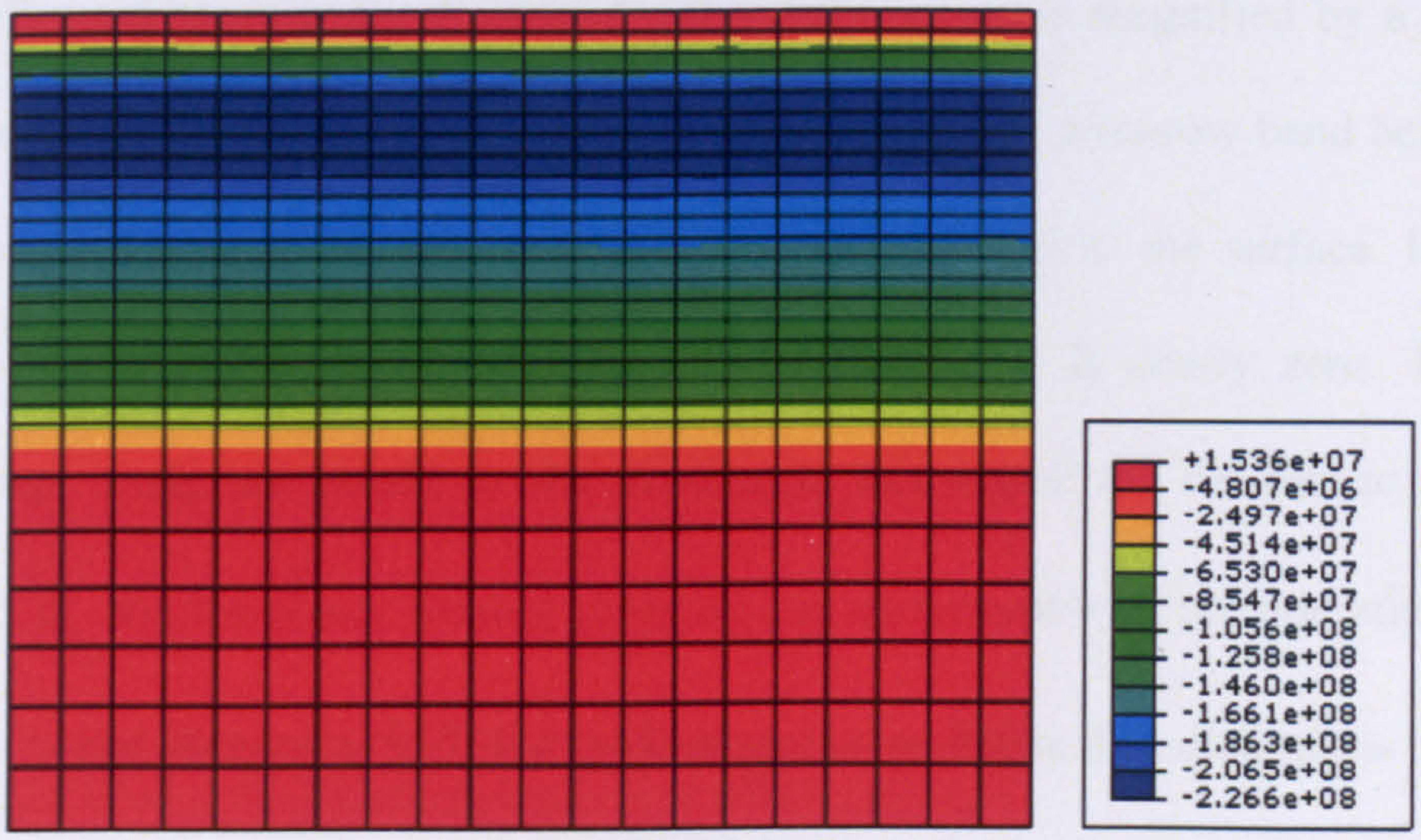

(a) Horizontal residual stress σ^r_{xx}

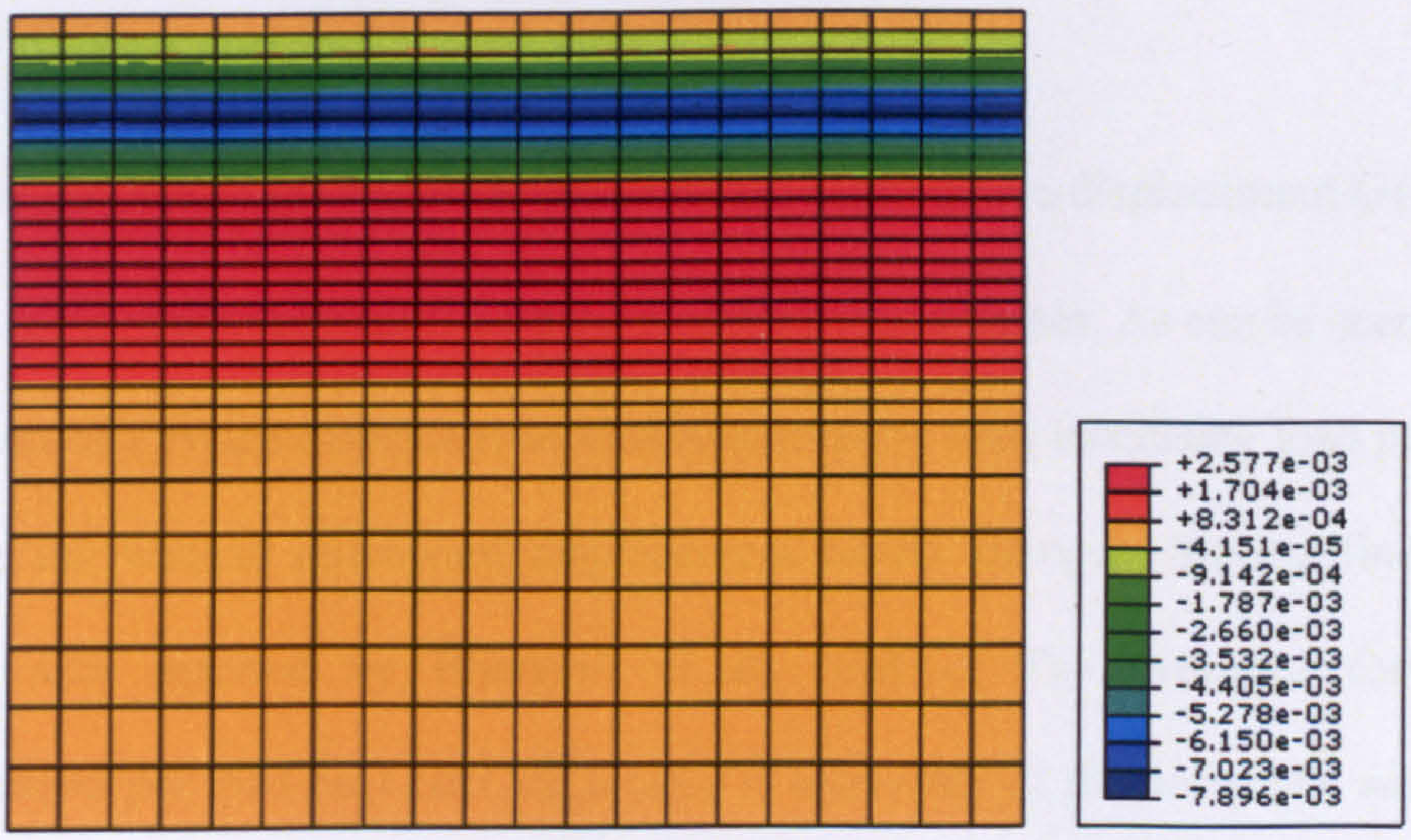

(b) Plastic shear strain ε^p_{xz}

Figure 3.4. Residual stress and plastic strain fields in the Region A after five load passes

Figure 3.5 compares the deformed mesh after five load passes with the undeformed mesh in the Region A. The deformation is magnified by a scale factor 100. There are obvious shear deformation within a narrow band beneath the surface and small compressive deformation normal to the surface. In the travel direction, horizontal deformation of Region A is nearly zero. These findings imply the plastic strains existing in this region are the plastic shear strain ε_{xz}^{p} and the plastic normal strain ε_{yy}^{p}, in agreement with considerations in Merwin and Johnson (1963) for the line contact problem. The distortions of the vertical lines represent the forward and backward plastic flow. The forward plastic flow occurs at smaller depths due to the negative plastic shear strain while the backward flow occurs at deeper depths due to the positive plastic shear strain.

Figure 3.6 shows the variation of the normalised surface displacement GU/p_0a (U is surface displacement) with the number of load passes. As can be seen, the amount of forward displacement increases linearly with increasing load passes while the vertical downward displacement barely changes. Similar findings were also reported by Bhargava et al. (1985b). The averaged forward movement per load pass $G\Delta U_1/p_0a$ (ΔU_1 is increment of the horizontal surface displacement) is 0.043, in agreement with the results of Bhargava et al. (1985b) and Hearle and Johnson (1987) which were shown in Figure 2.21.

Figure 3.7 shows that the residual stress distributions at the middle section in the present study are close to those in Merwin and Johnson (1963) and Bhargava et al. (1985b).

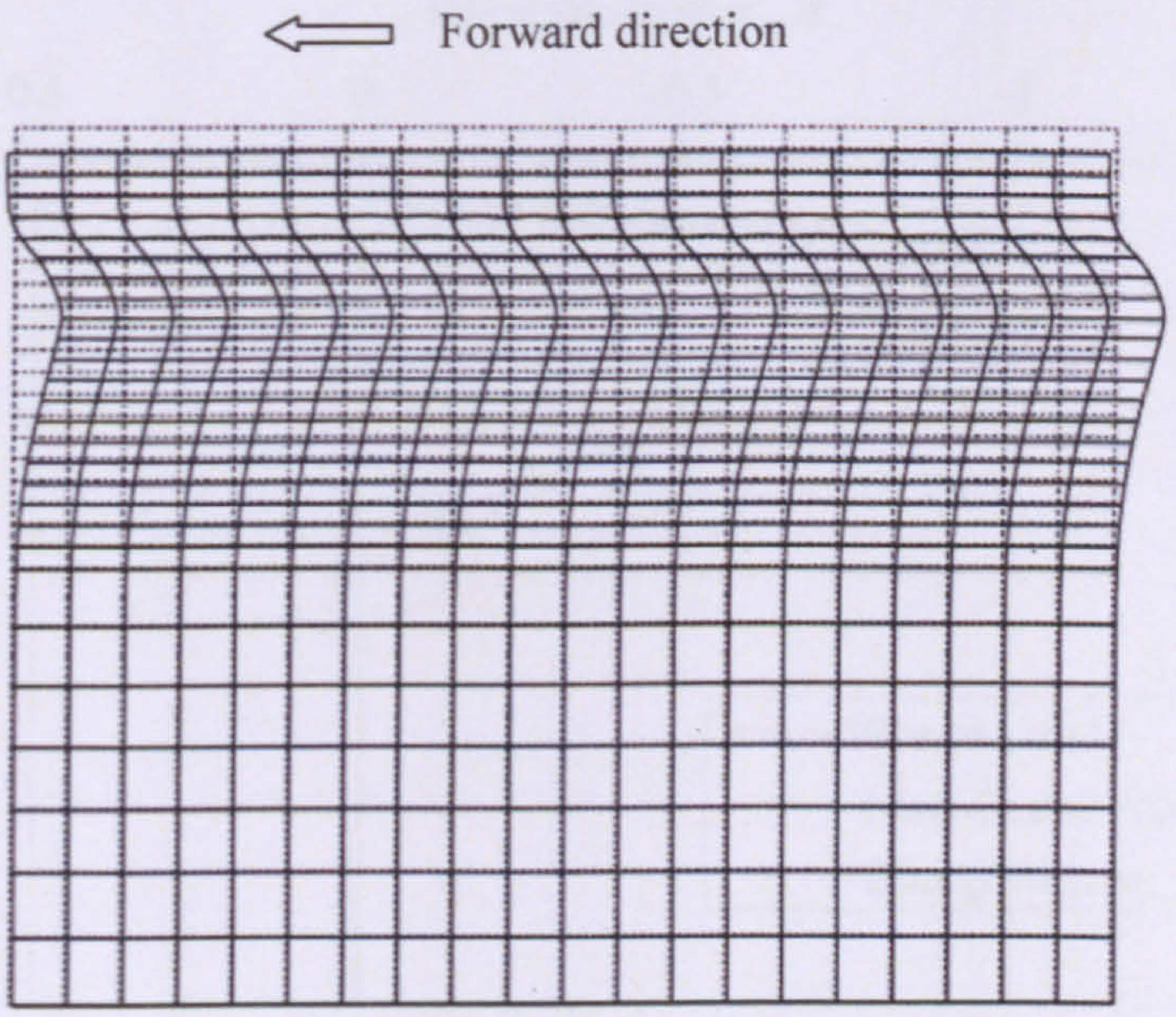

Figure 3.5. Deformed mesh in the Region A after five passes (scale factor: 100)

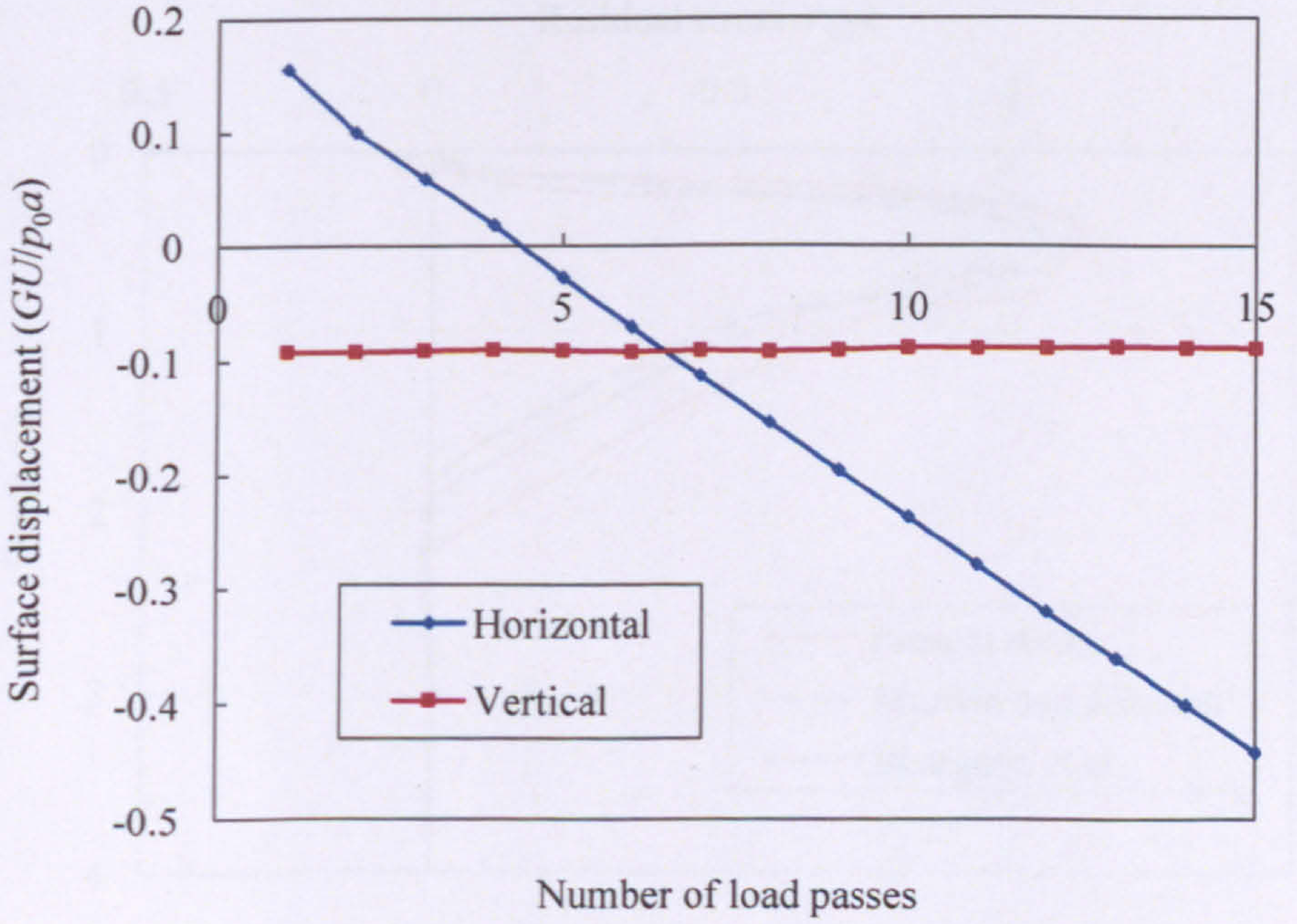

Figure 3.6. Surface displacement against number of load passes for Von Mises half-space when $p_0 = 4.35c$

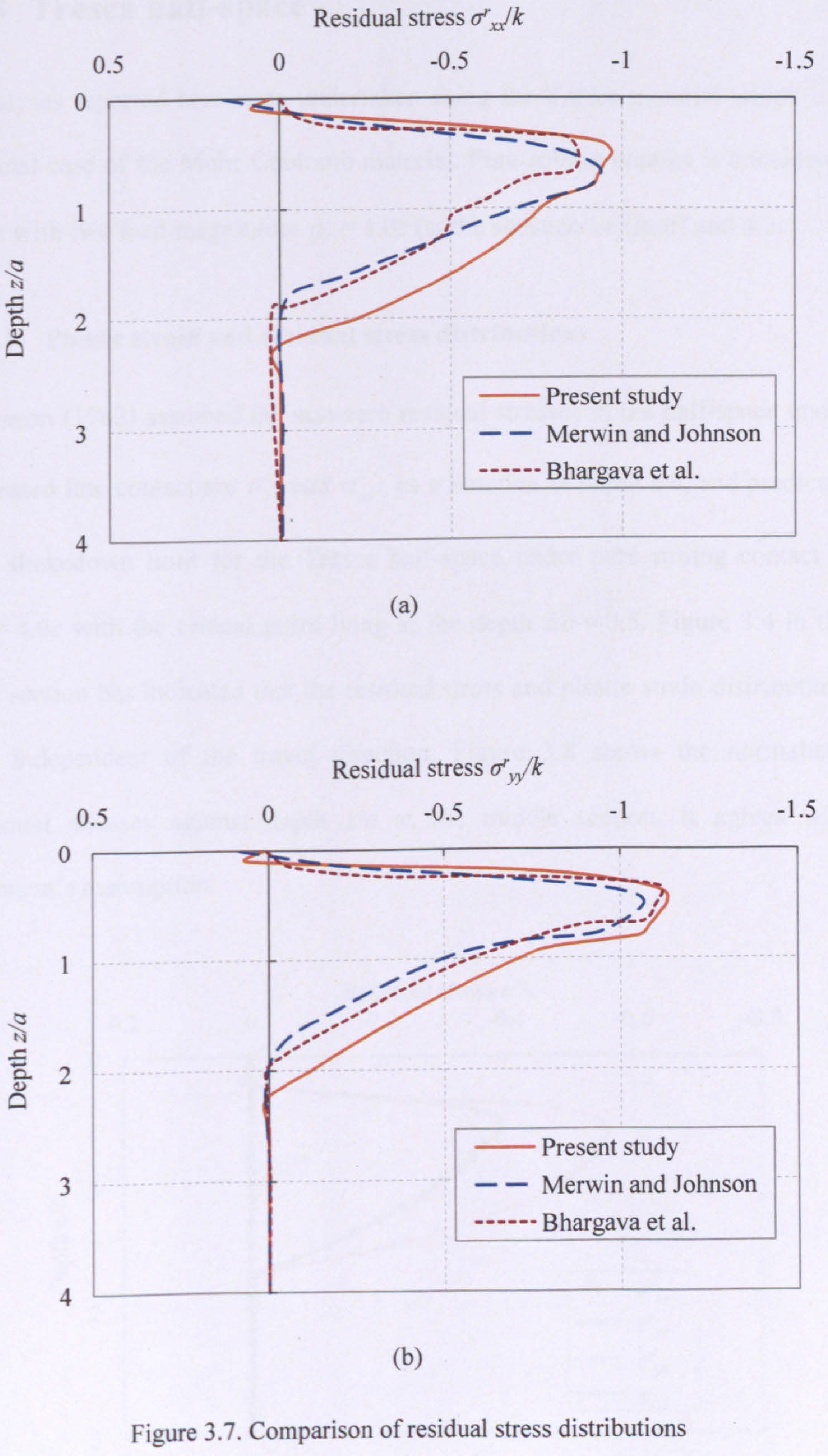

Figure 3.7. Comparison of residual stress distributions

3.3 Tresca half-space

Analyses reported here were undertaken using the Tresca material which is a special case of the Mohr Coulomb material. Pure rolling contact is considered first with two load magnitudes $p_0 = 4.0c$ (at the shakedown limit) and $4.2c$.

3.3.1 Plastic strain and residual stress distributions

Johnson (1962) assumed the non-zero residual stresses in the half-space under repeated line contact are σ^r_{xx} and σ^r_{yy}, as a function of depth z/a, and predicted the shakedown limit for the Tresca half-space under pure rolling contact is $p_0 = 4.0c$ with the critical point lying at the depth $z/a = 0.5$. Figure 3.4 in the last section has indicated that the residual stress and plastic strain distributions are independent of the travel direction. Figure 3.8 shows the normalised residual stresses against depth z/a at the middle section. It agrees with Johnson's assumption.

Figure 3.8. Residual stress fields after three load passes when $p_0 = 4.0c$

Figure 3.9 and Figure 3.10 show the distributions of the plastic strains (ε^p_{xz} and ε^p_{zz}) and residual stresses (σ^r_{xx} and σ^r_{yy}) at the middle section of Region A after different numbers of load passes. The residual stresses are normalised with respect to the soil cohesion c, and the depth z is normalised by the half contact width a. As can be seen, the residual stresses σ^r_{xx} and σ^r_{yy} and the plastic normal strain ε^p_{zz} are usually negative (i.e. in compression), while the plastic shear strain ε^p_{xz} varies from negative to positive.

After the first pass of $p_0 = 4.0c$, the half-space shows some plastic strains and residual stresses below the surface: $0.1 \leq z/a \leq 1.8$ (see Figure 3.9). However, further load applications do not have any obvious effect on the existing plastic strains and residual stresses. Therefore, the half-space is in a steady state.

When $p_0 = 4.2c$ (Figure 3.10), the plastic zone is $0.1 \leq z/a \leq 2$, larger than that in Figure 3.9. With the increase of load passes, the plastic shear strains in the repeatedly deformed zone $0.3 \leq z/a \leq 0.8$ decrease continuously with the number of load passes, and therefore the forward plastic flow (negative plastic shear strain) outweighs the backward plastic flow after a few load passes. In addition, during the repeated load applications, the peak point of negative ε^p_{xz} moves towards $z/a = 0.5$ which is the most critical depth in the half-space according to Johnson (1962). The plastic normal strain only changes slightly in the repeated deformed zone. The residual stresses in the repeated deformed zone generally decrease with increasing load passes, and they reach steady states after four load passes. Therefore, the development of residual stresses is attributed to the compressive ε_{zz}^{p} rather than ε_{xz}^{p}.

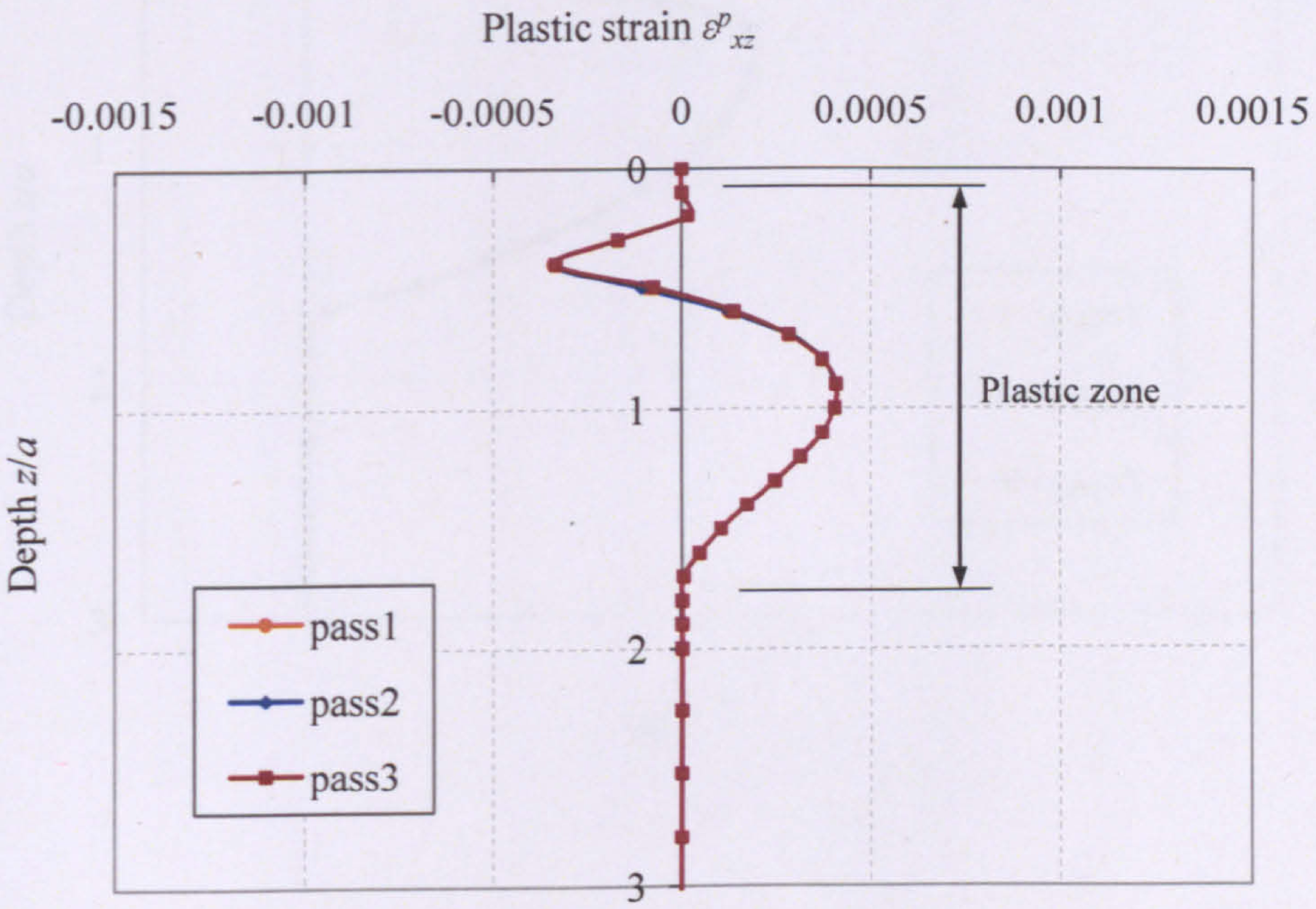

(a)

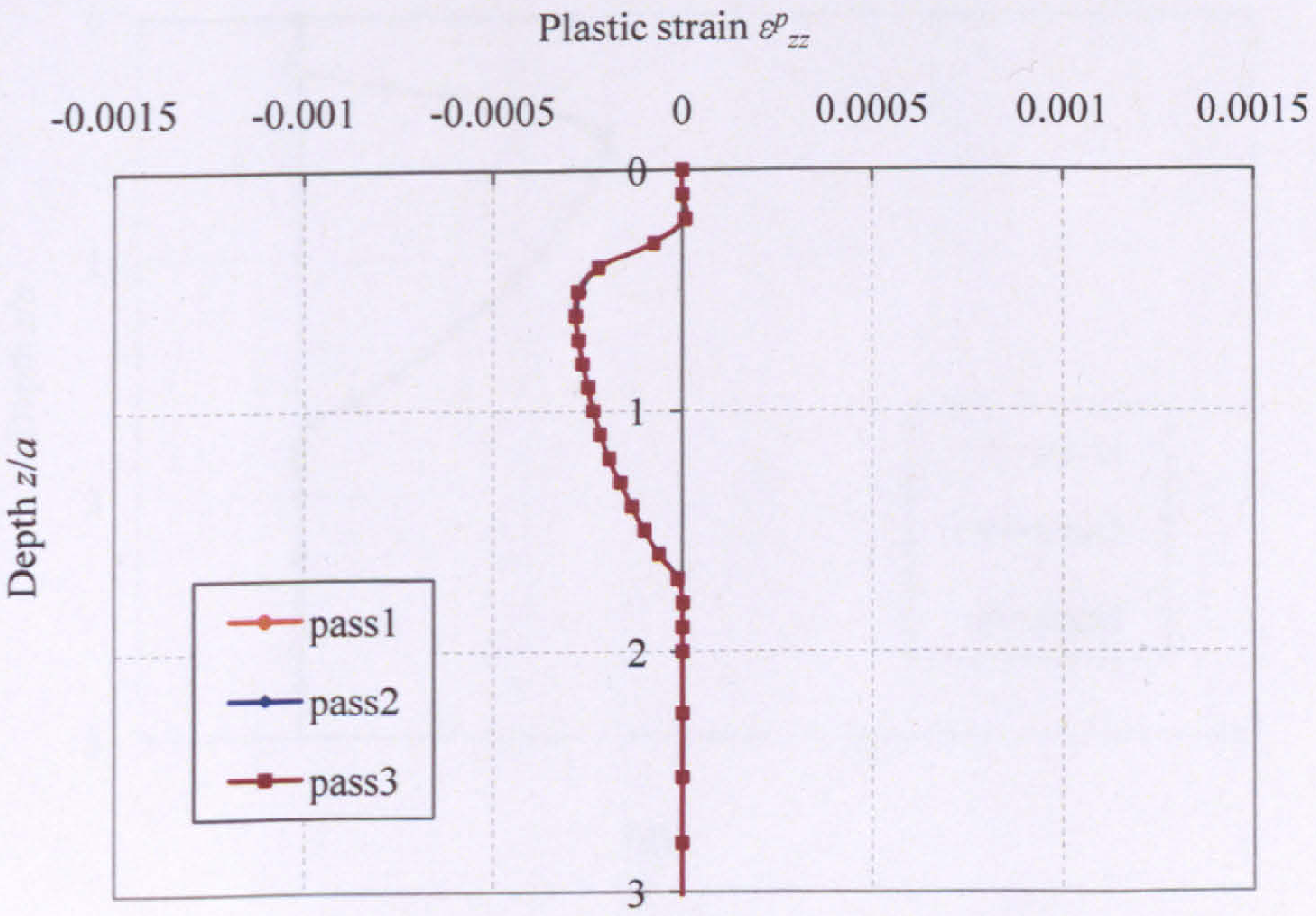

(b)

Figure 3.9 continued on following page

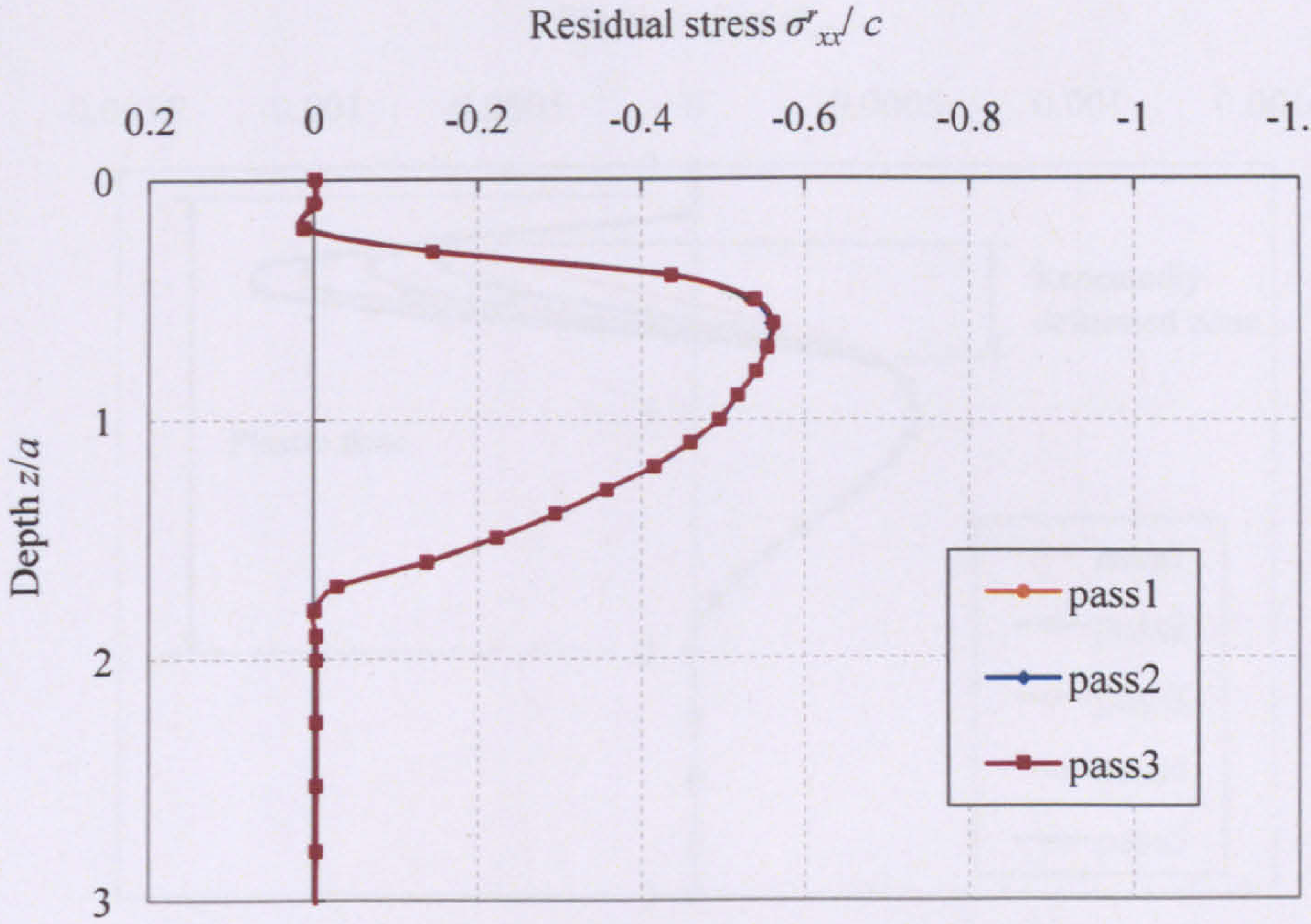

(c)

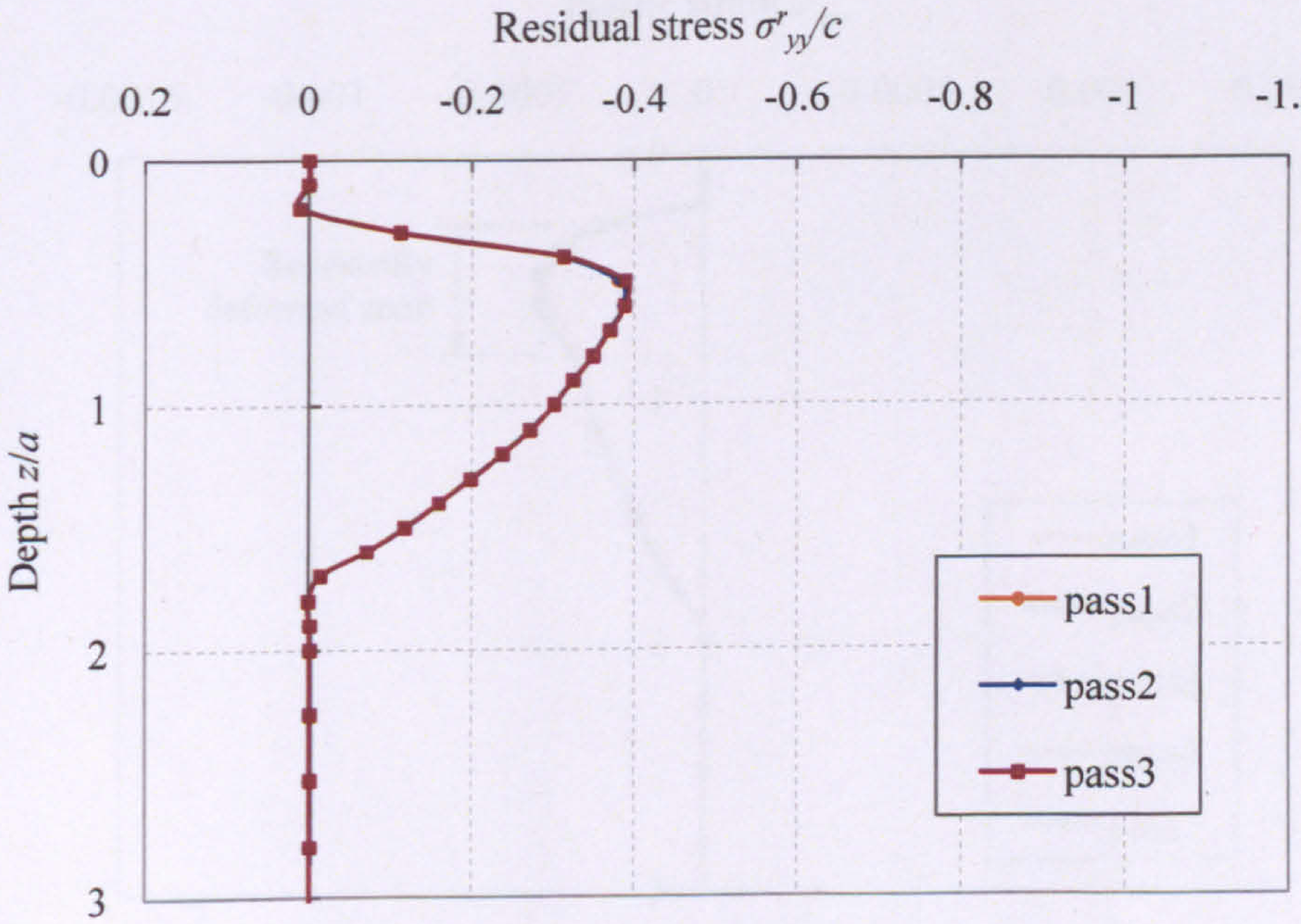

(d)

Figure 3.9. Distributions of plastic strains and residual stresses when $p_0 = 4.0c$

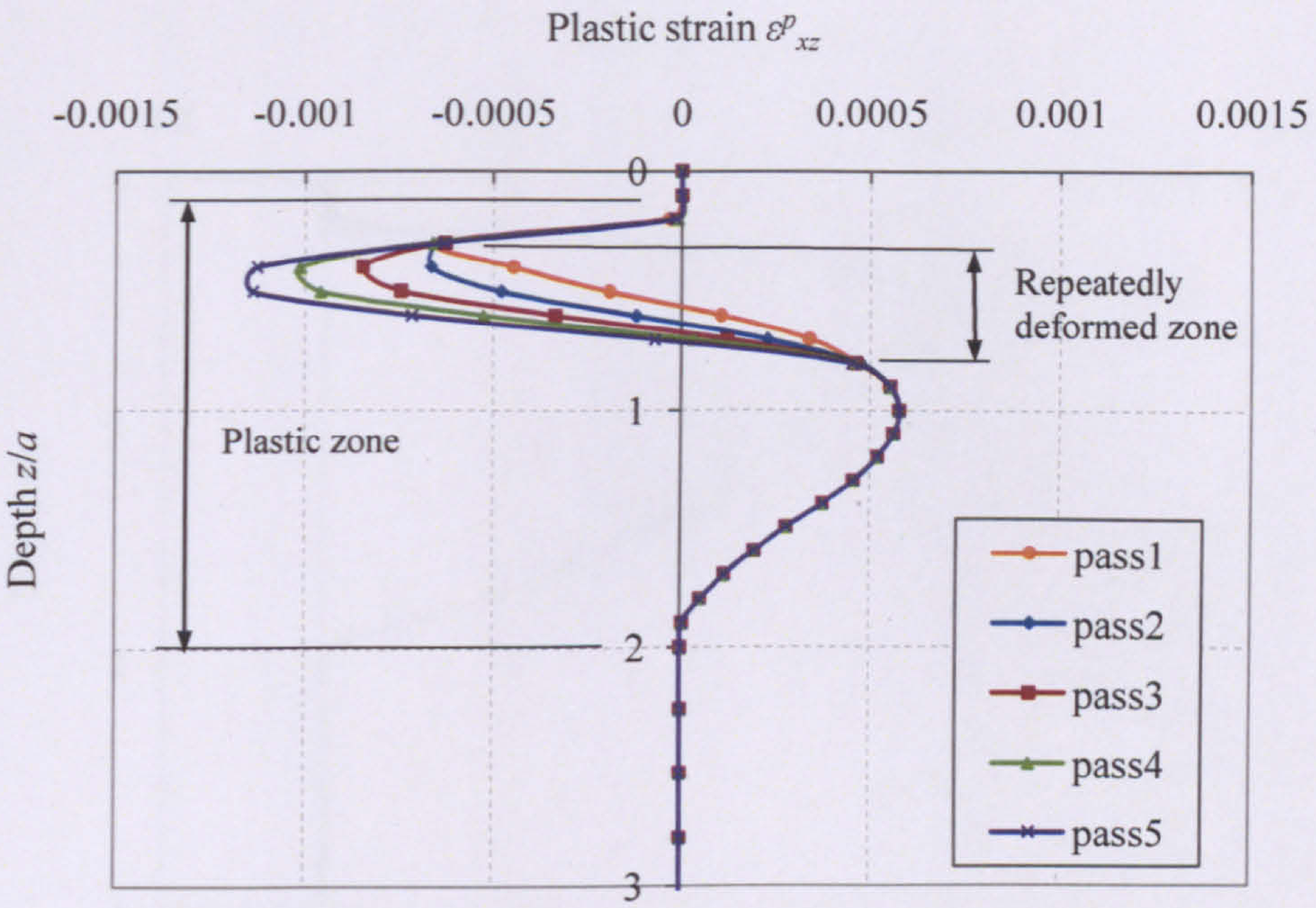

(a)

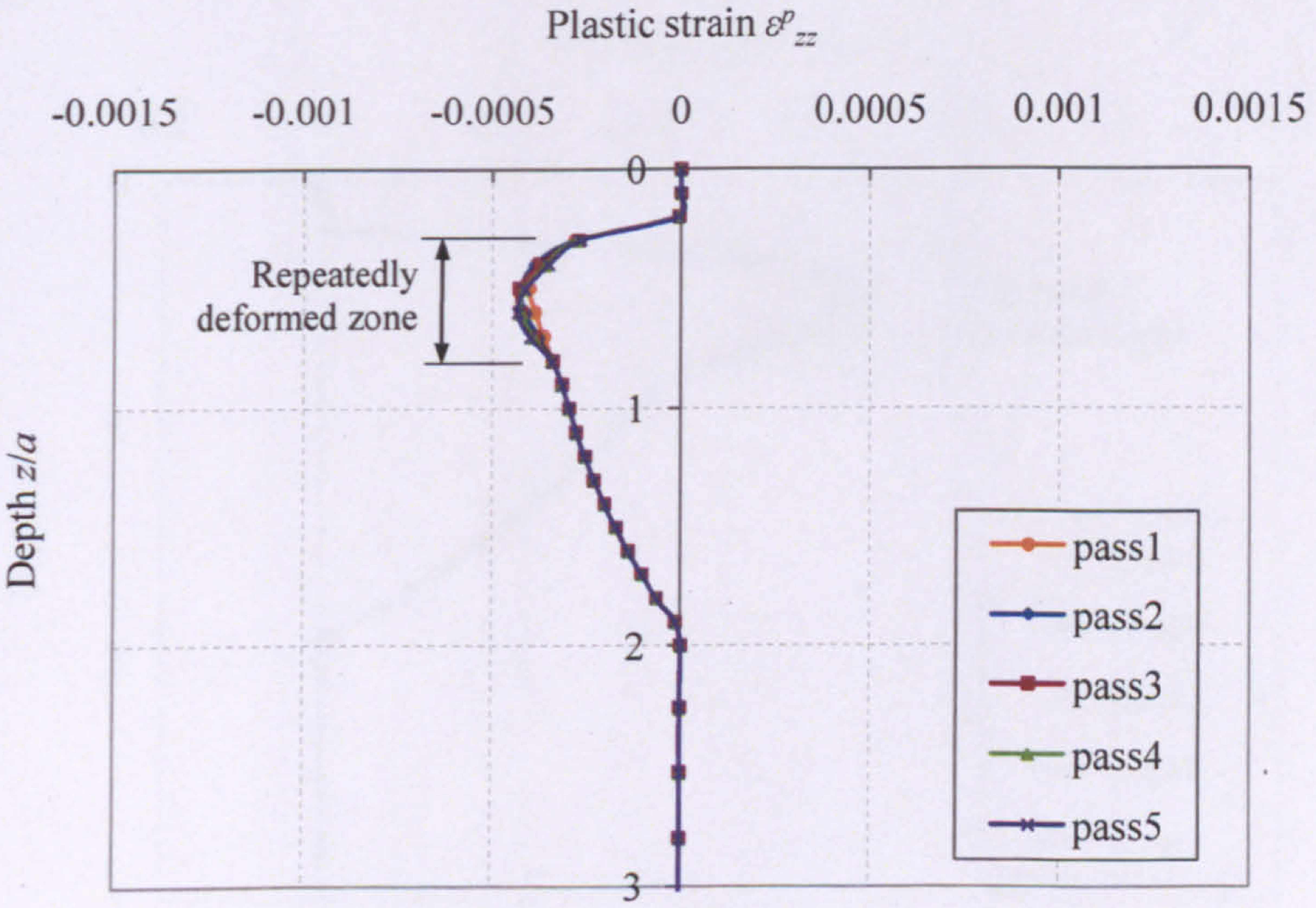

(b)

Figure 3.10 continued on following page

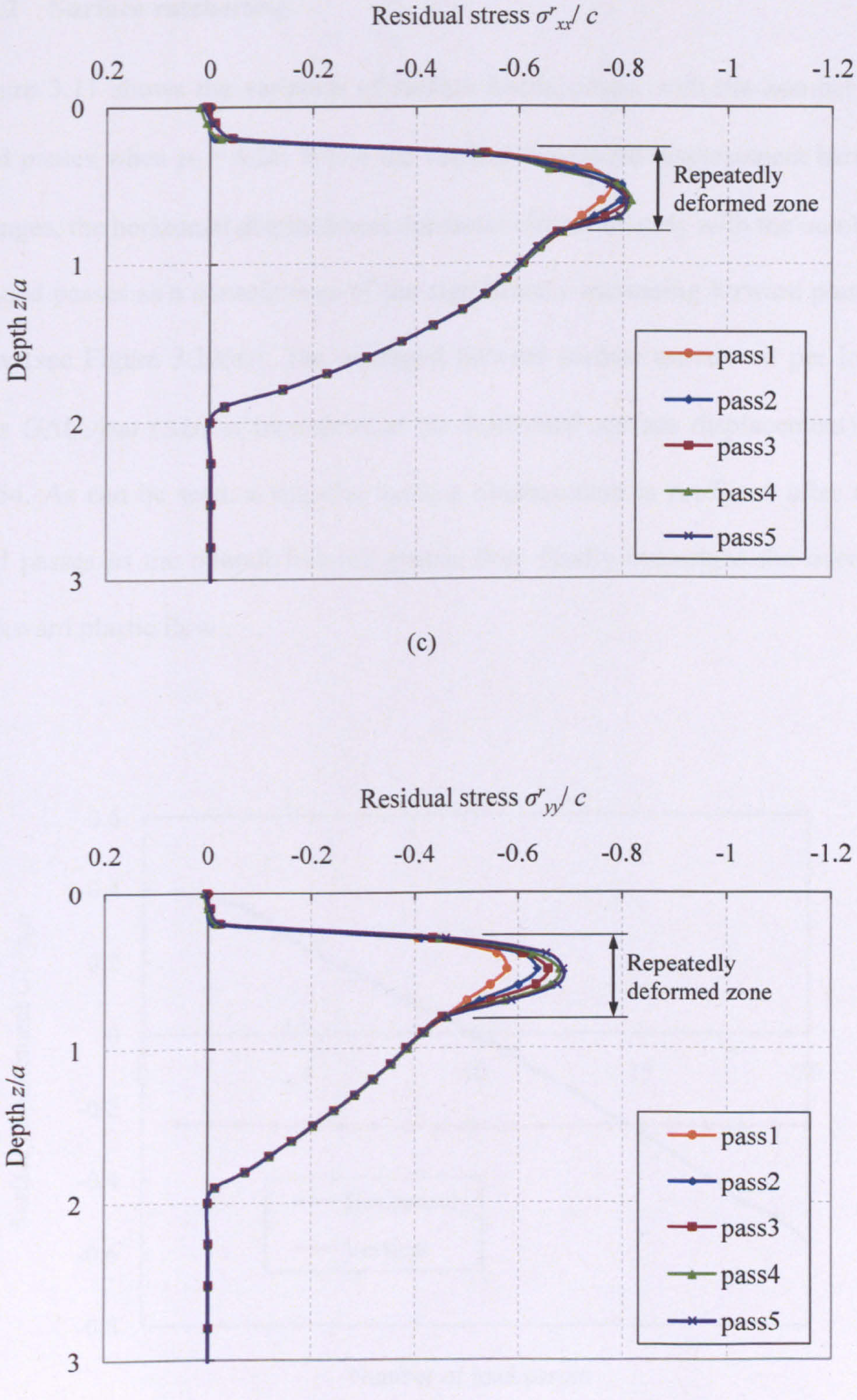

(c)

(d)

Figure 3.10. Distributions of plastic strains and residual stresses when $p_0 = 4.2c$

3.3.2 Surface ratchetting

Figure 3.11 shows the variation of surface displacement with the number of load passes when $p_0 = 4.2c$. While the vertical downward displacement barely changes, the horizontal displacement decreases almost linearly with the number of load passes as a consequence of the significantly increasing forward plastic flow (see Figure 3.10(a)). The averaged forward surface movement per load pass $G\Delta U_1/p_0a$ (ΔU_1 is increment of the horizontal surface displacement) is 0.054. As can be seen, a negative surface displacement is predicted after ten load passes as the overall forward plastic flow finally outweighs the overall backward plastic flow.

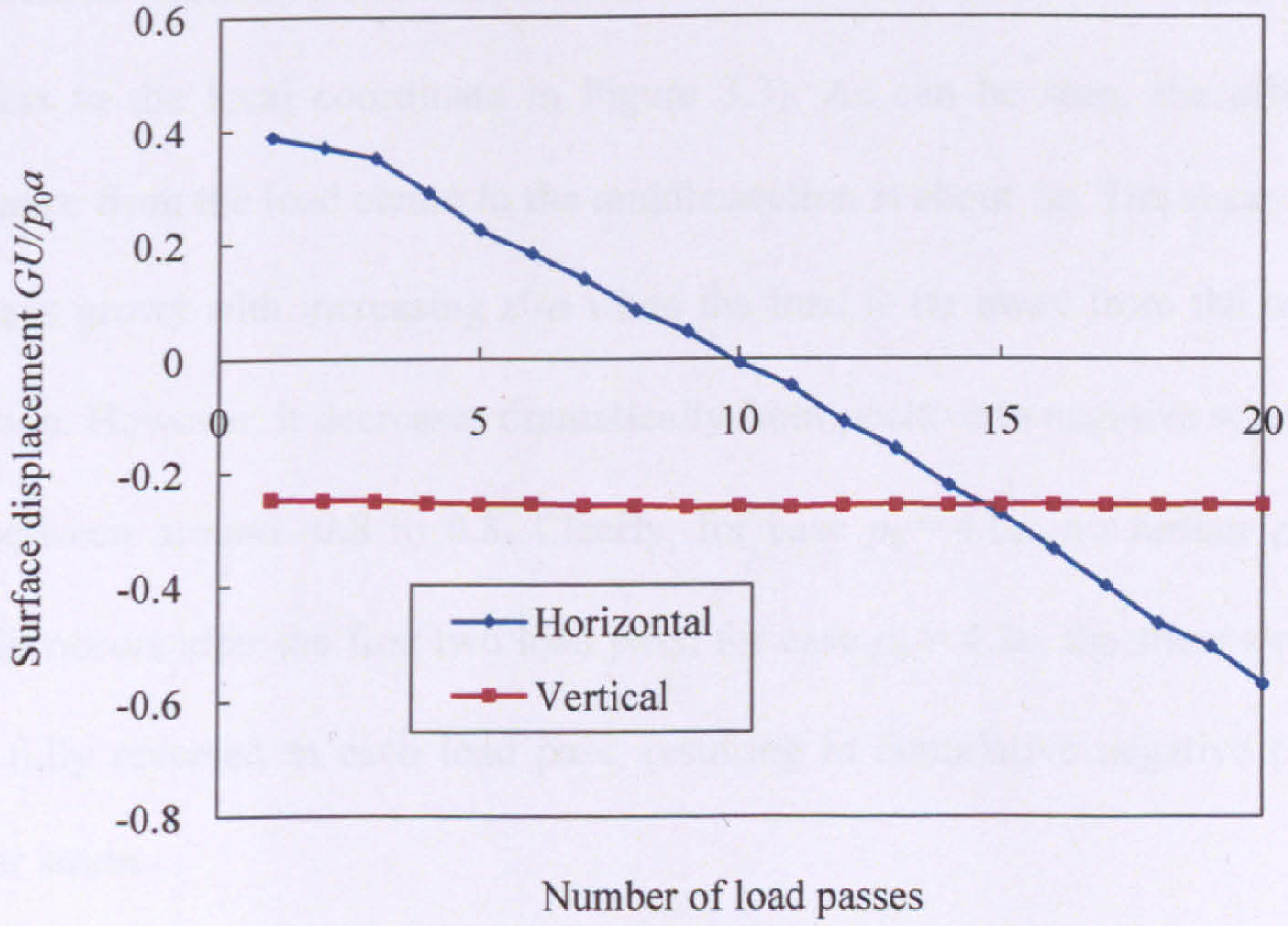

Figure 3.11. Surface displacement against number of load passes when $p_0 = 4.2c$

3.3.3 Stress-strain response

Permanent deformation of the Tresca half-space is mainly attributed to the plastic shear strain. Figure 3.12 shows typical shear stress-strain responses at the critical depth (i.e. $z/a = 0.5$) for $p_0 = 4.0c$ and $4.2c$ respectively. The shear stress is normalised by the soil cohesion. As can be seen, the shear stress-strain cycles are evident due to the reverse of shear stress from positive to negative during each load pass. When $p_0 = 4.0c$, the stress-strain response becomes pure elastic after two load cycles. When $p_0 = 4.2c$, the shear stress-strain cycle moves towards the left since the amount of negative plastic shear strain outweighs that of positive plastic shear strain in each load cycle.

Figure 3.13 exhibits shear strain history at the critical depth in the middle section, in which x' is the current horizontal coordinate of the Hertz load centre (refers to the local coordinate in Figure 3.3). As can be seen, the effective distance from the load centre to the middle section is about $5a$. The shear strain always grows with increasing x'/a when the load is far away from the middle section. However, it decreases dramatically from positive to negative when x'/a is between around -0.8 to 0.8. Clearly, for case $p_0 = 4.0c$, no further plastic strain occurs after the first two load pass; for case $p_0 = 4.2c$, the shear strain is not fully reversed in each load pass, resulting in cumulative negative plastic shear strain.

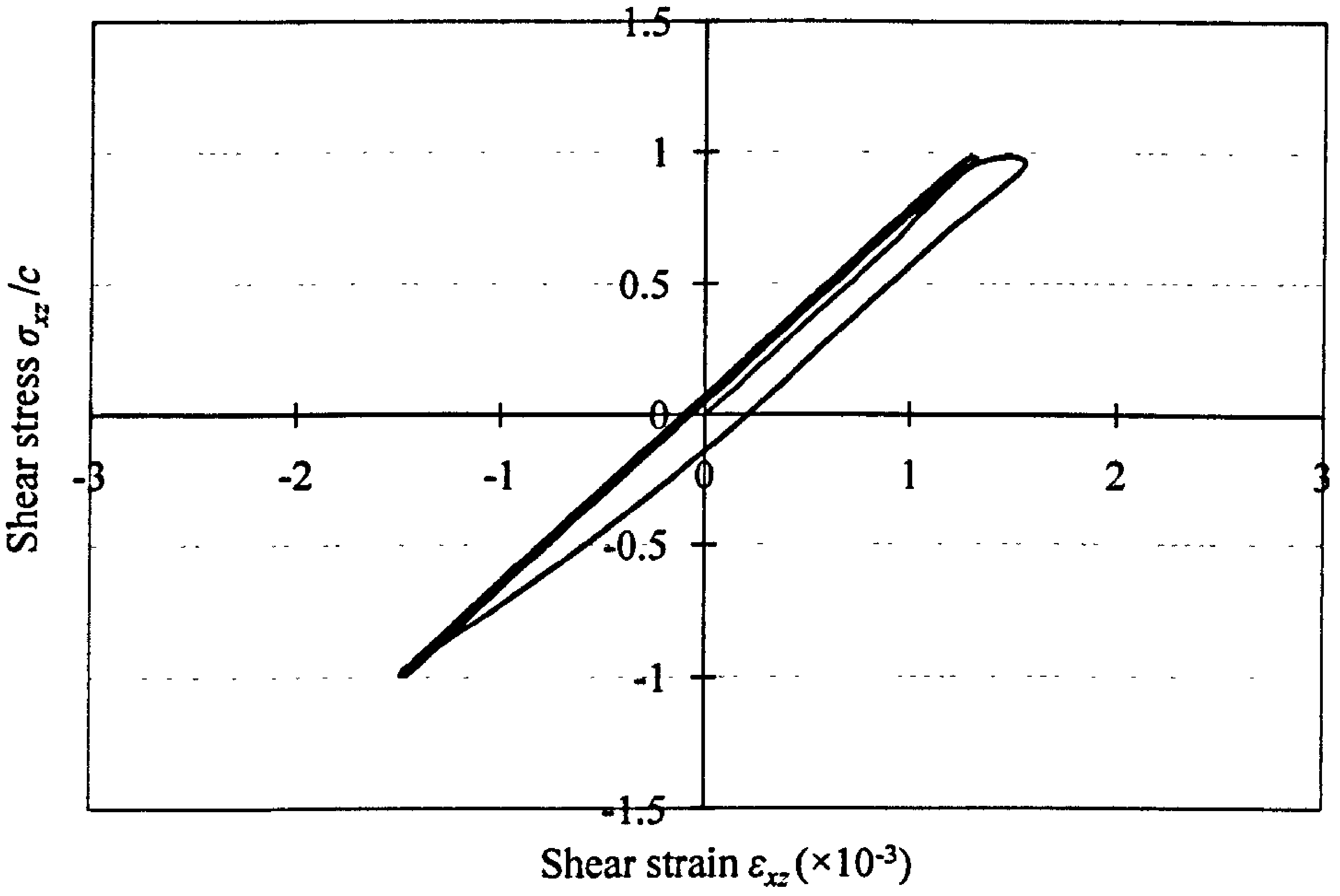

(a) $p_0 = 4.0c$

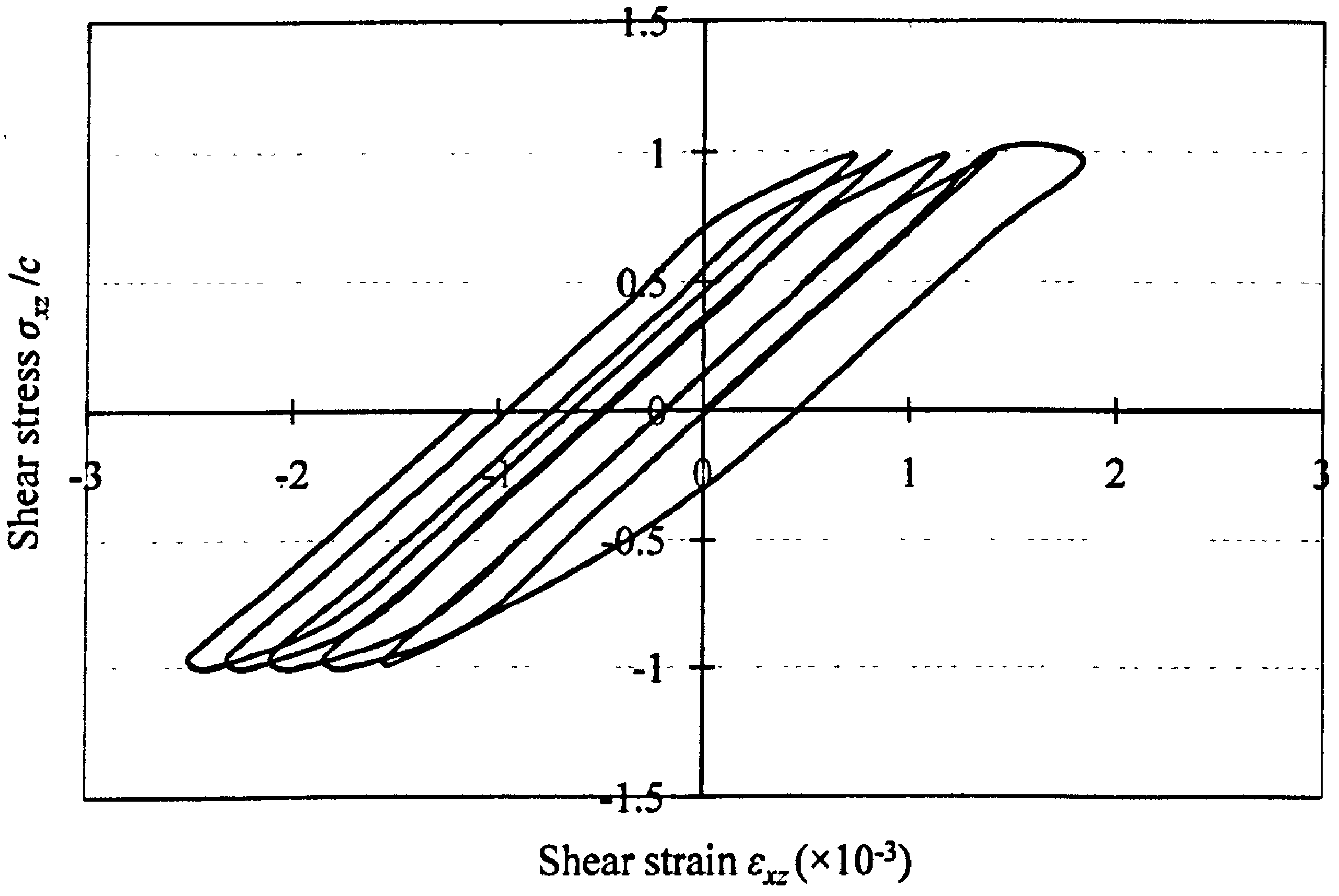

(b) $p_0 = 4.2c$

Figure 3.12. Shear stress-strain cycles at depth $z/a = 0.5$ in the middle section during the passage of the load

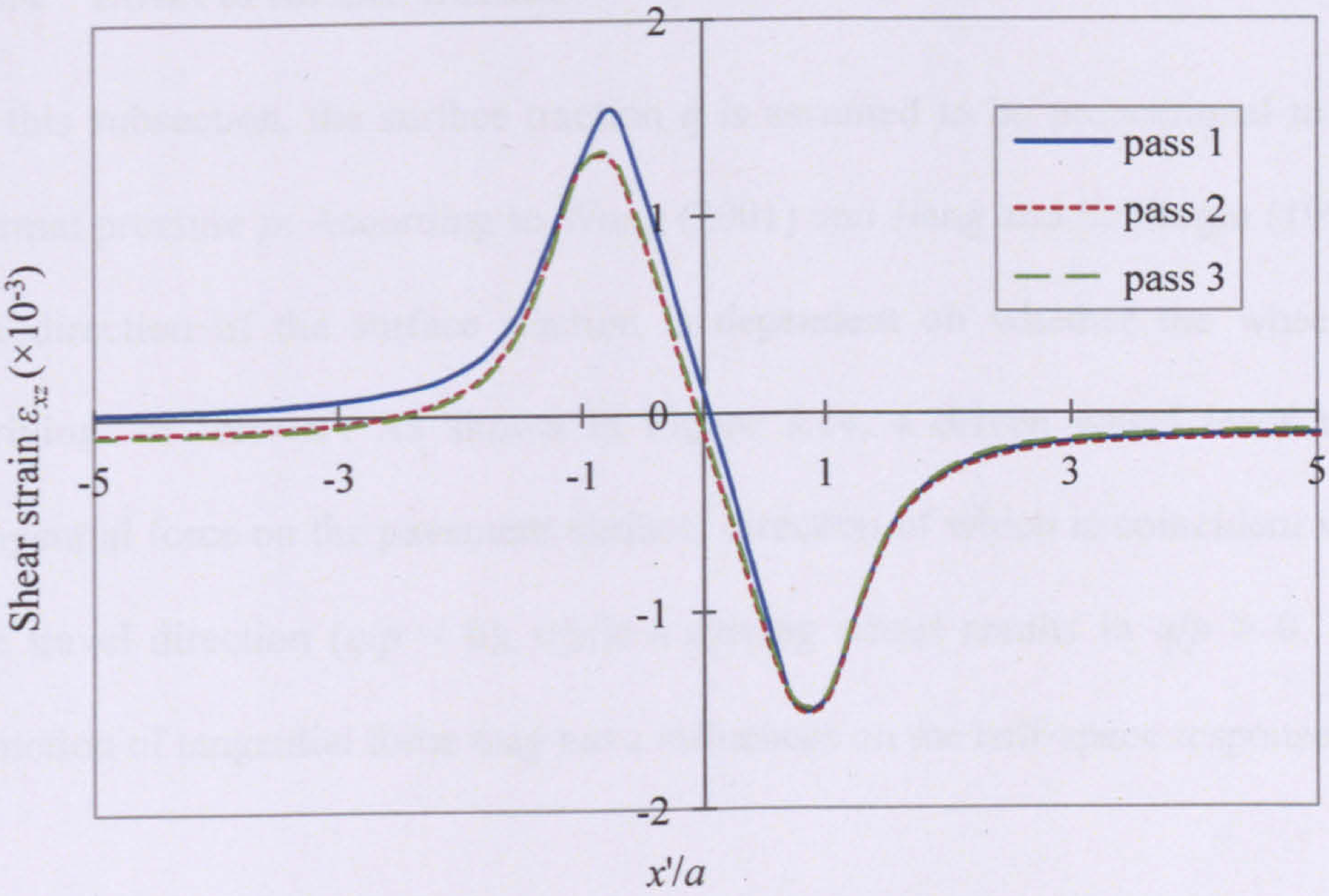

(a) $p_0 = 4.0c$

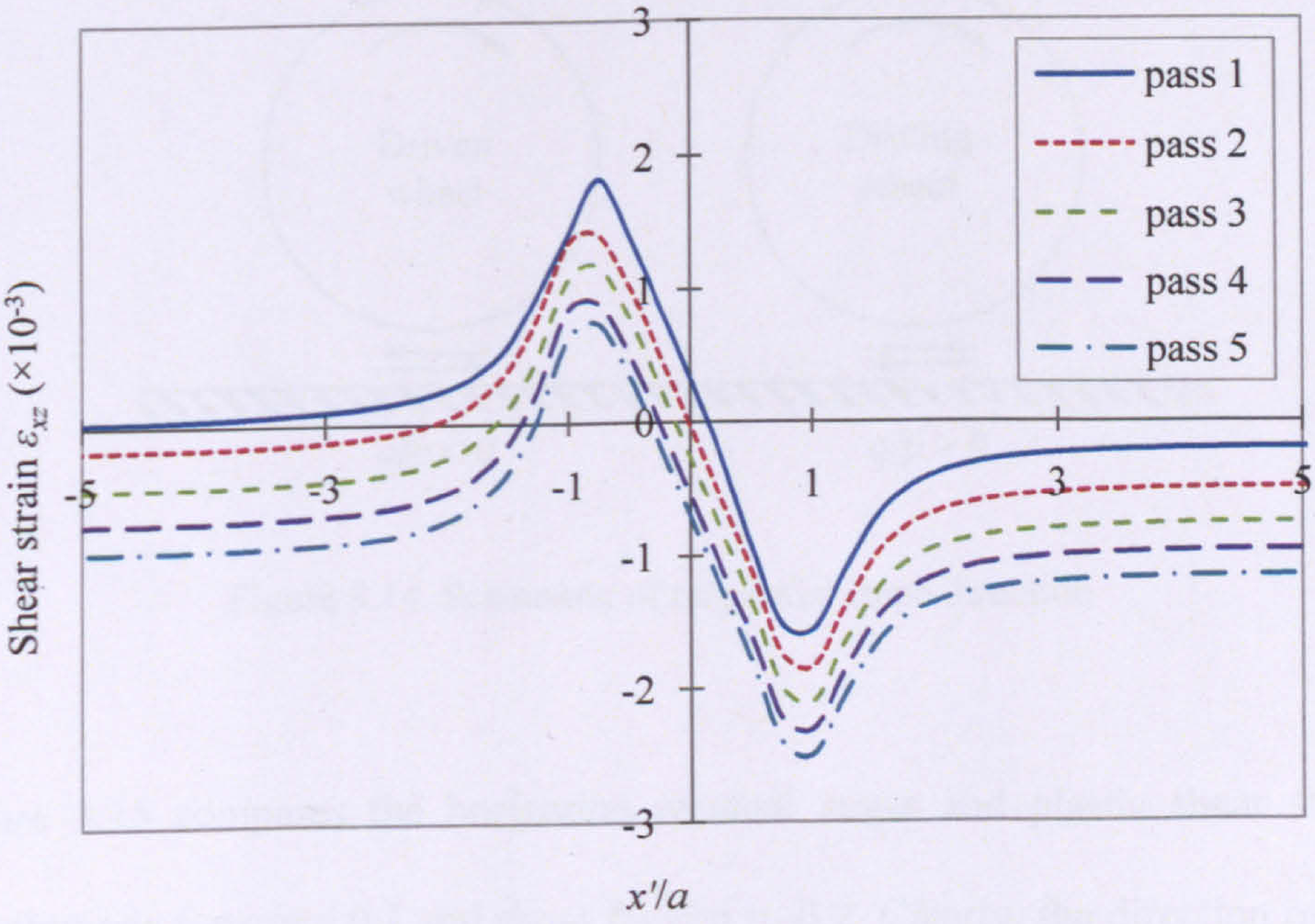

(b) $p_0 = 4.2c$

Figure 3.13. Shear strain history at depth $z/a = 0.5$ in the middle section during the passage of the load

3.3.4 Effect of surface traction

In this subsection, the surface traction q is assumed to be proportional to the normal pressure p. According to Wong (2001) and Jiang and Sehitoglu (1996), the direction of the surface traction is dependent on whether the wheel is 'driving' or 'driven'. As shown in Figure 3.14, a driven wheel leads to a tangential force on the pavement surface, direction of which is coincident with the travel direction ($q/p < 0$), while a driving wheel results in $q/p > 0$. The direction of tangential force may have influences on the half-space responses.

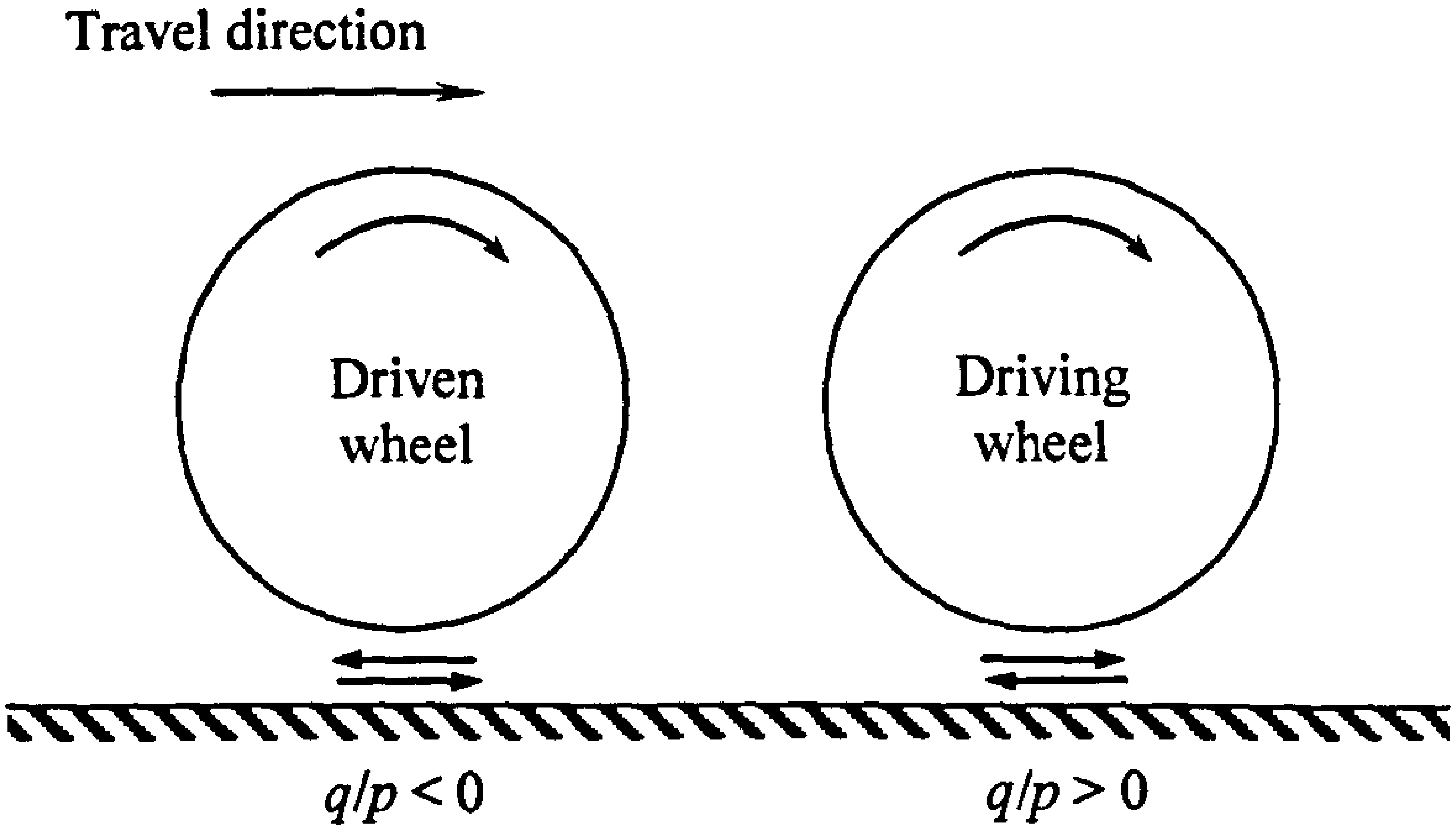

Figure 3.14. Schematic of tangential force direction

Figure 3.15 compares the horizontal residual stress and plastic shear strain distributions for $q/p = 0.2$ and those for $q/p = -0.2$. Clearly, the direction of the surface traction directly affects the sign of plastic shear strain. Moreover, the negative q/p produces larger amounts of plastic shear strains and horizontal residual stresses than the positive q/p.

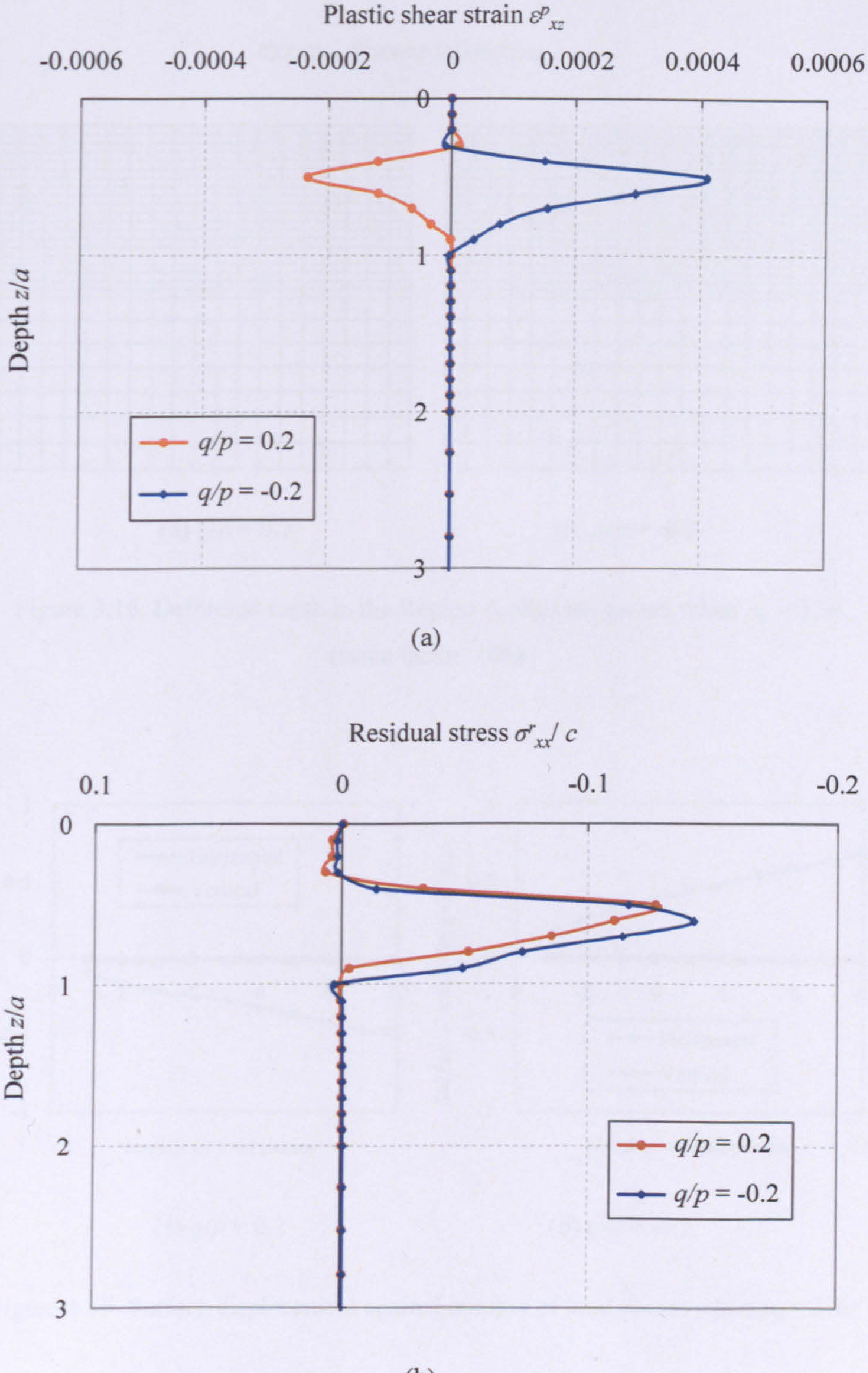

(a)

(b)

Figure 3.15. Influences of tangential force direction on plastic strain and residual stress distributions when $p_0 = 3.2c$

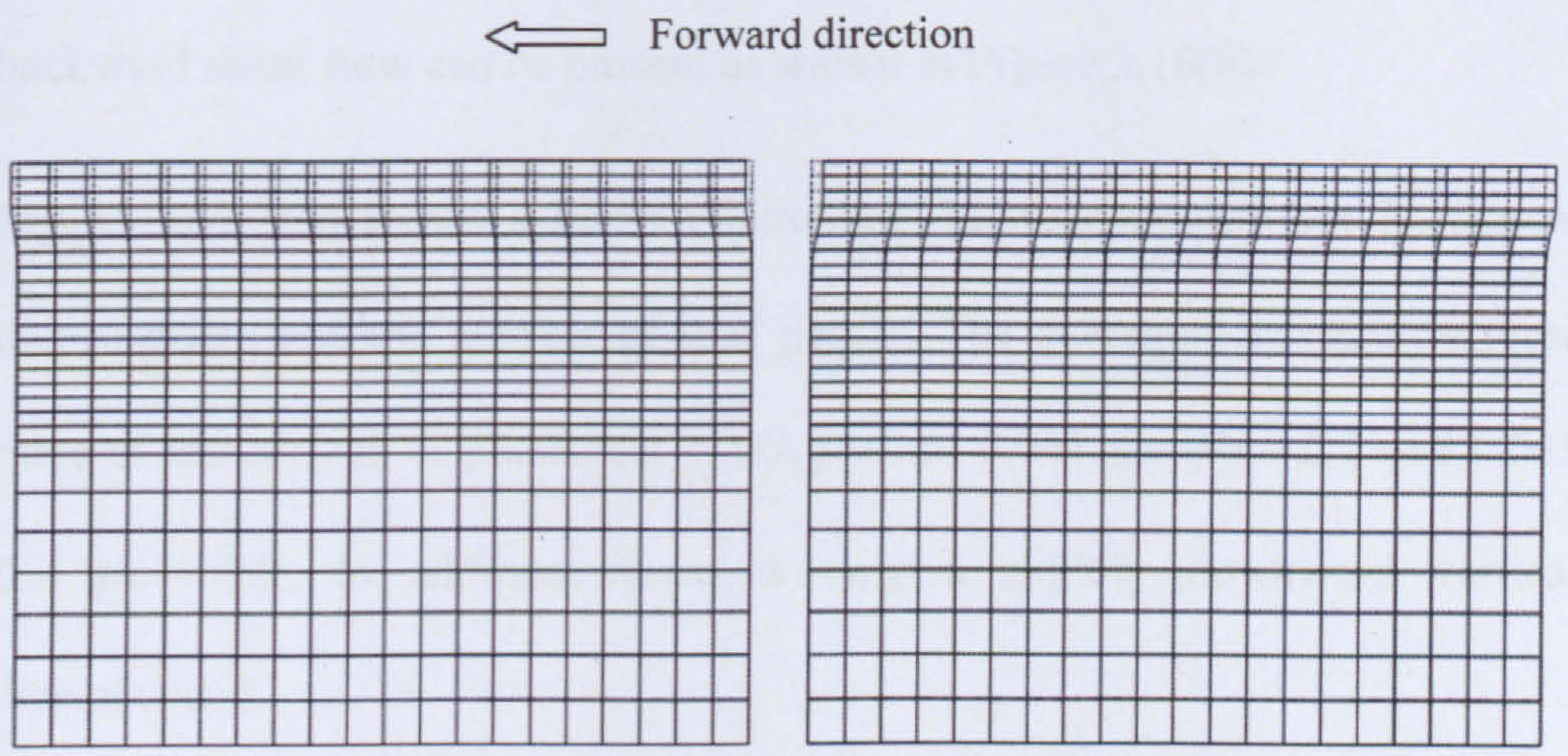

(a) $q/p = 0.2$ (b) $q/p = -0.2$

Figure 3.16. Deformed mesh in the Region A after ten passes when $p_0 = 3.3c$ (scale factor: 100)

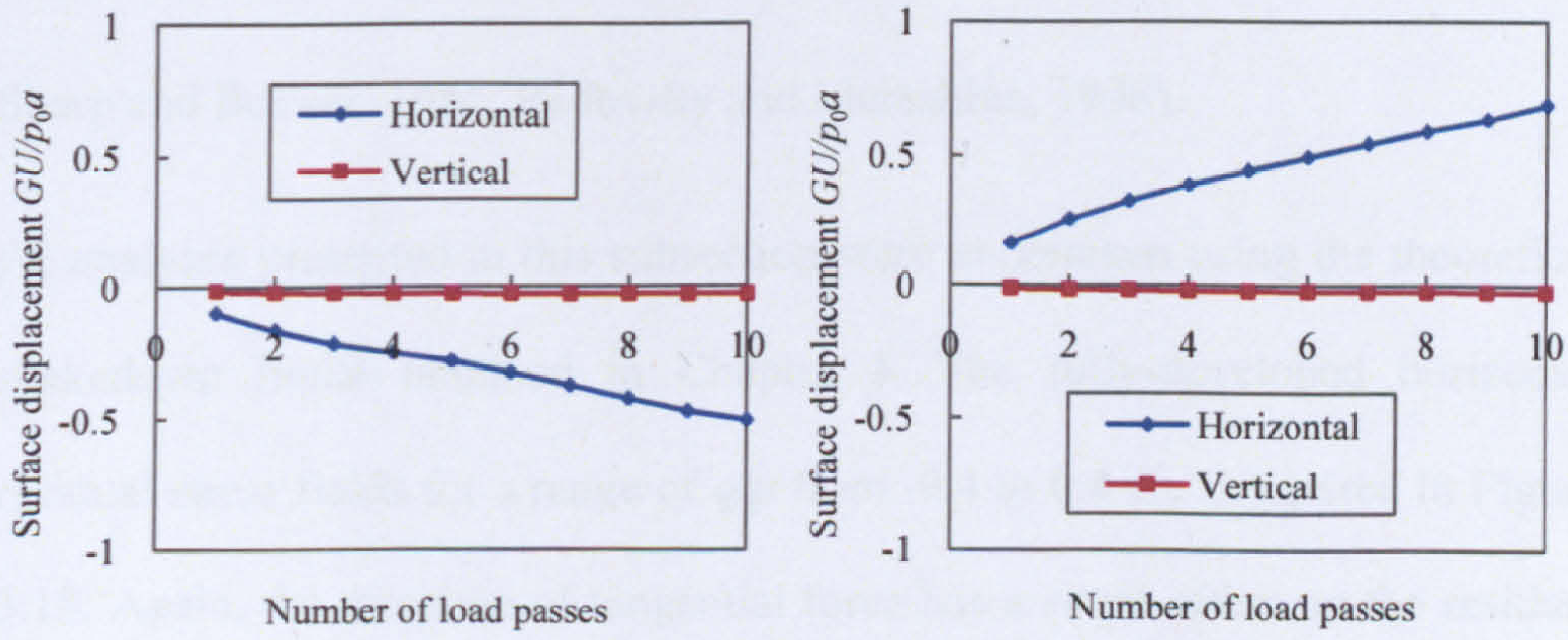

(a) $q/p = 0.2$ (b) $q/p = -0.2$

Figure 3.17. Surface displacement against number of load passes when $p_0 = 3.3c$

Figure 3.16 shows the deformed and undeformed mesh in the Region A after ten load passes when $p_0 = 3.3c$ and $q/p = \pm 0.2$ (the theoretical shakedown limit is $3.2c$). Only forward shear flow is observed in Figure 3.16(a) due to the presence of surface traction in the forward direction. When q/p = -0.2, only backward shear flow can be present as shown in Figure 3.16(b).

Figure 3.17 also shows a linear relationship between the surface horizontal displacement and the number of load passes. The averaged increase/decrease rates of the surface displacement $G\Delta U_1/p_0a$ are 0.041 for $q/p = 0.2$ and 0.052 for $q/p = -0.2$. In addition, there is only a slightly downward vertical displacement.

3.3.5 Residual stress field at the shakedown limit

Residual stress field is a key component in Melan's static shakedown theorem. For the two-dimensional pavement problem, the distribution of horizontal residual stresses σ_{xx}^r affects the pavement shakedown limit (Johnson, 1962; Sharp and Booker, 1984; Radovsky and Murashina, 1996).

FE analyses presented in this subsection were undertaken using the theoretical shakedown limits obtained in Chapter 4. The fully-developed horizontal residual stress fields for a range of q/p from -0.4 to 0.4 are compared in Figure 3.18. Again, the direction of tangential force has a slight effect on the residual stresses. When q/p varies from -0.3 to 0.3, the residual stresses are mainly compressive and the peak compressive residual stresses are beneath the surface. The plastic region decreases markedly with increasing q/p. When $q/p = \pm 0.4$, there are only very small residual stresses at the surface of the half-space.

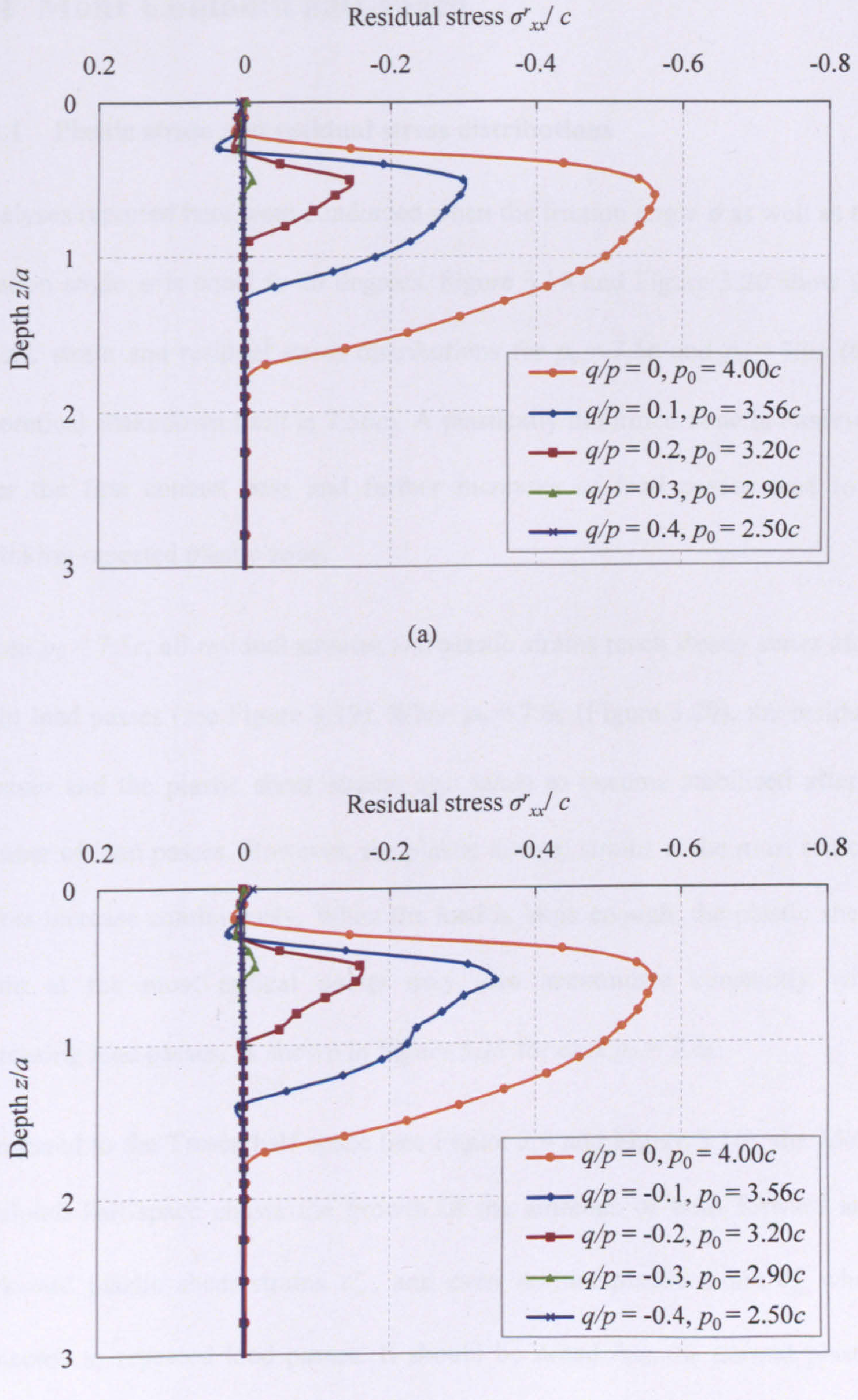

(a)

(b)

Figure 3.18. Residual stress fields for different values of q/p

3.4 Mohr Coulomb half-space

3.4.1 Plastic strain and residual stress distributions

Analyses reported here were conducted when the friction angle ϕ as well as the dilation angle ψ is equal to 20 degrees. Figure 3.19 and Figure 3.20 show the plastic strain and residual stress distributions for $p_0 = 7.5c$ and $p_0 = 7.6c$ (the theoretical shakedown limit is $7.56c$). A plastically deformed zone is observed after the first contact pass and further increases of load passes lead to a shrinking repeated plastic zone.

When $p_0 = 7.5c$, all residual stresses and plastic strains reach steady states after eight load passes (see Figure 3.19). When $p_0 = 7.6c$ (Figure 3.20), the residual stresses and the plastic shear strains also tends to become stabilised after a number of load passes. However, the plastic normal strains at the most critical points increase continuously. When the load is large enough, the plastic shear strain at the most critical points may also accumulate constantly with increasing load passes, as shown in Figure 3.21 for case $p_0 = 7.8c$.

Compared to the Tresca half-space (see Figure 3.9 and Figure 3.10), the Mohr Coulomb half-space shows the growth of the amounts of both forward and backward plastic shear strains ε_{xz}^{p}, and even normal plastic strain ε_{zz}^{p} when subjected to repeated load passes. It should be noted that the normal plastic strains in the half-space are attributed to both soil compression and dilatancy.

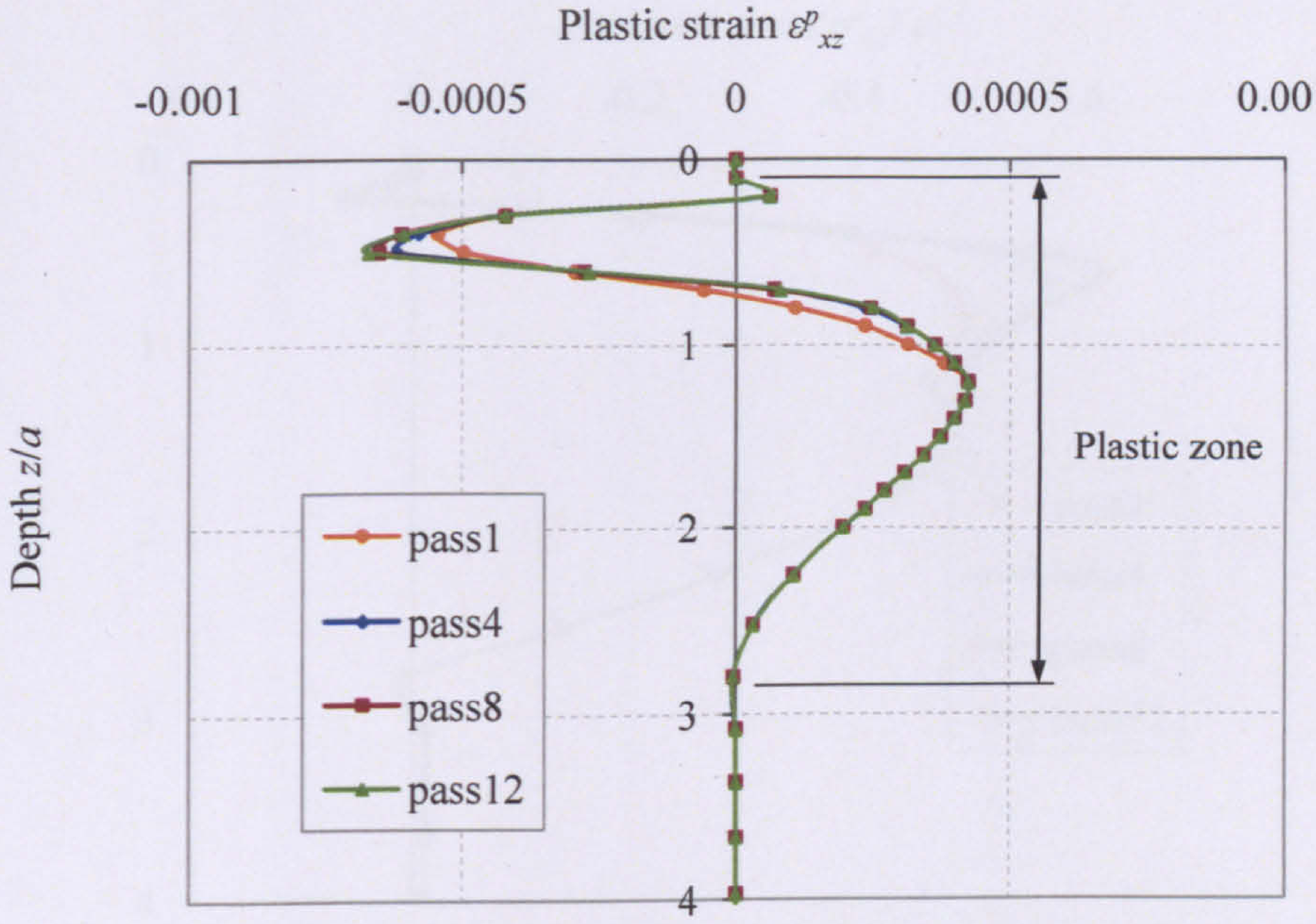

(a)

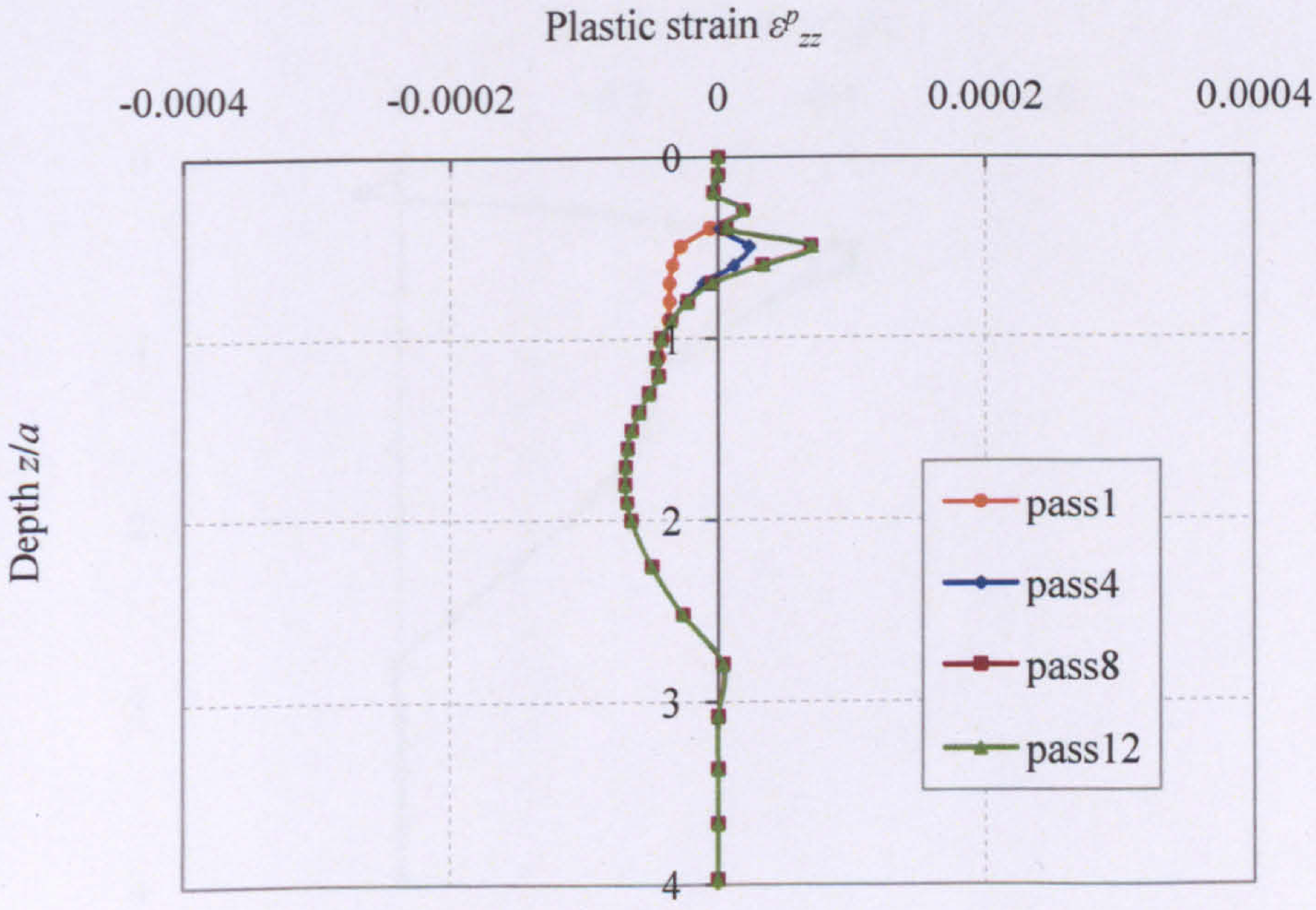

(b)

Figure 3.19 continued on following page

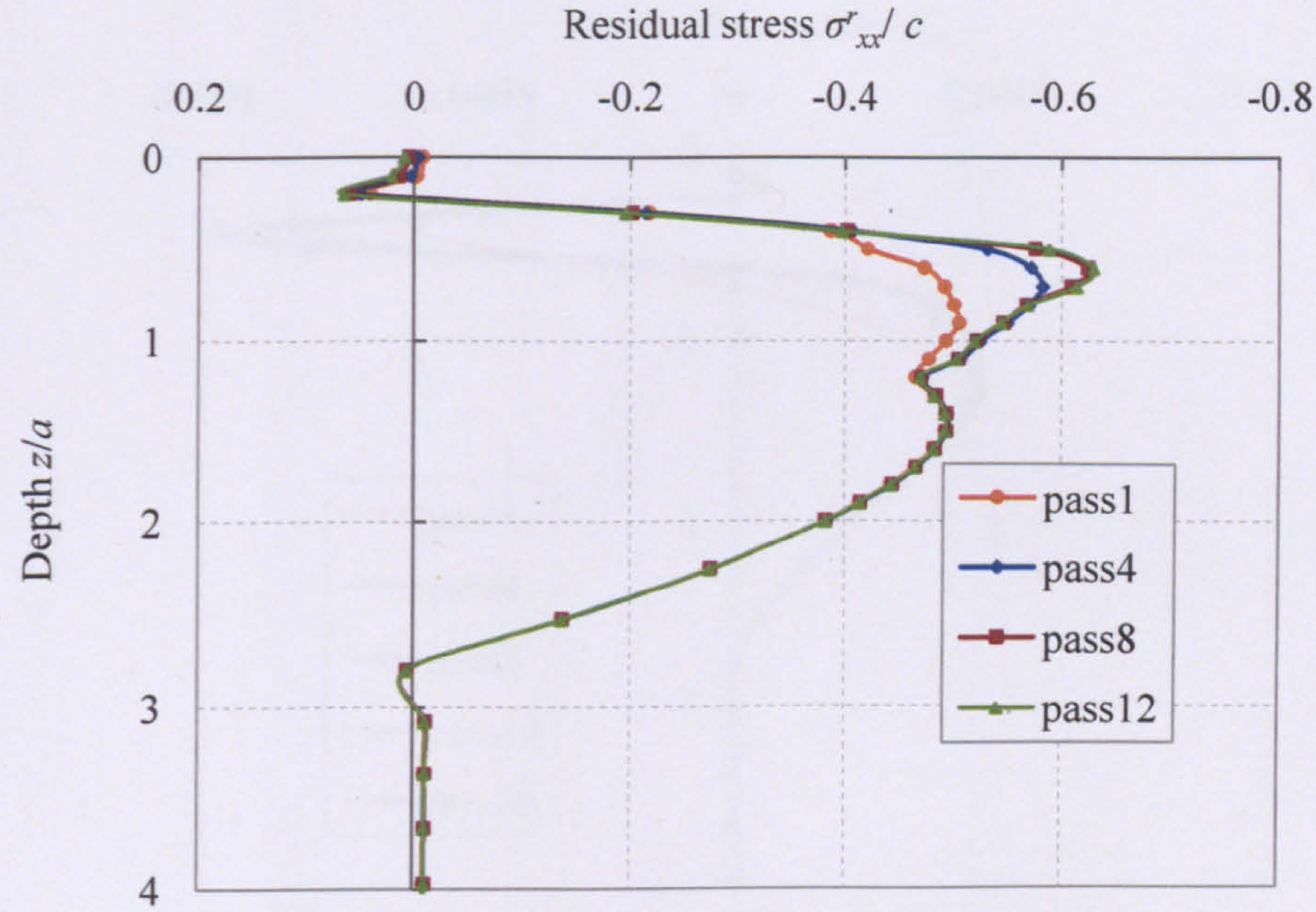

(c)

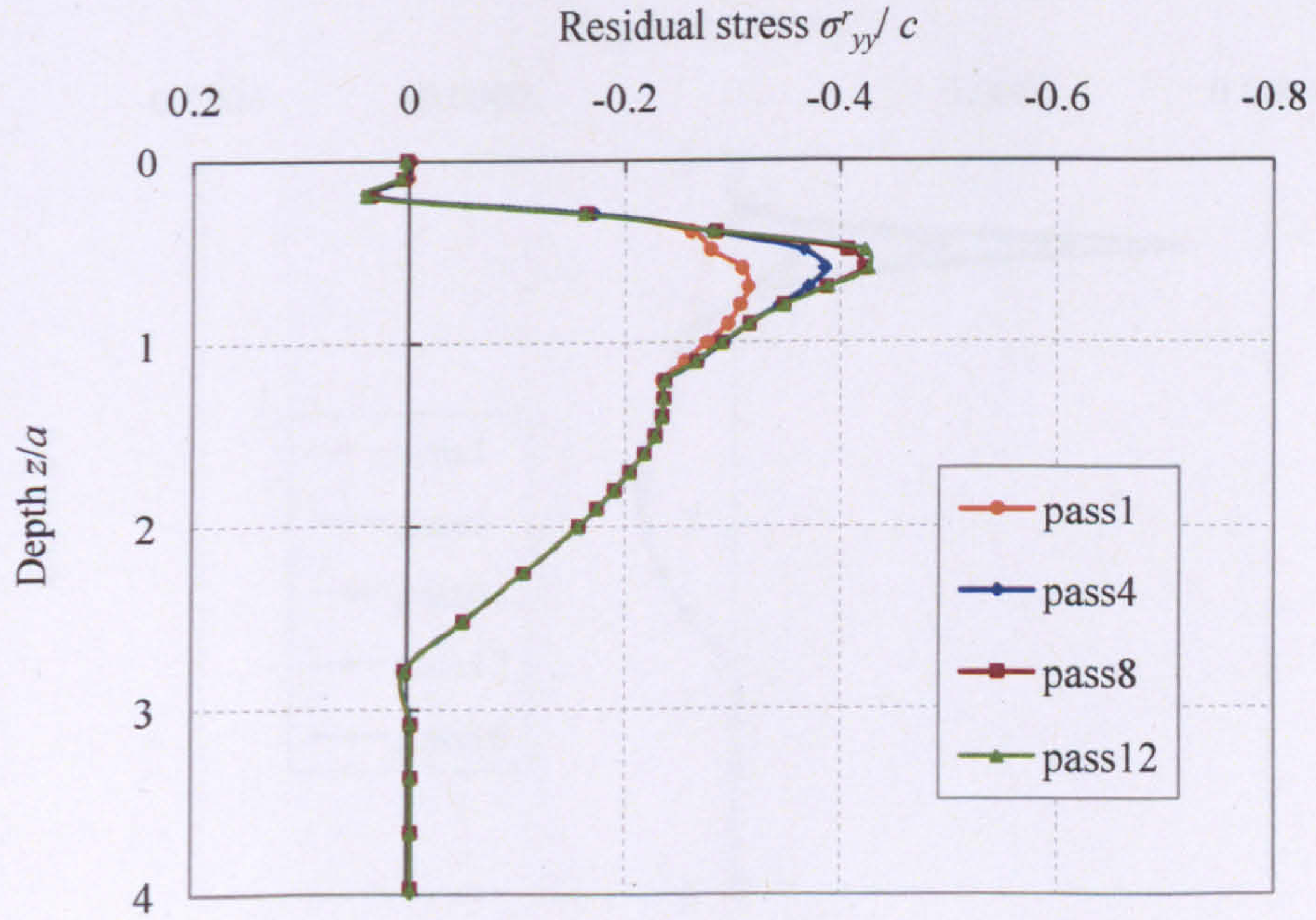

(d)

Figure 3.19. Distributions of plastic strains and residual stresses when $\phi = \psi = 20°$ and $p_0 = 7.5c$

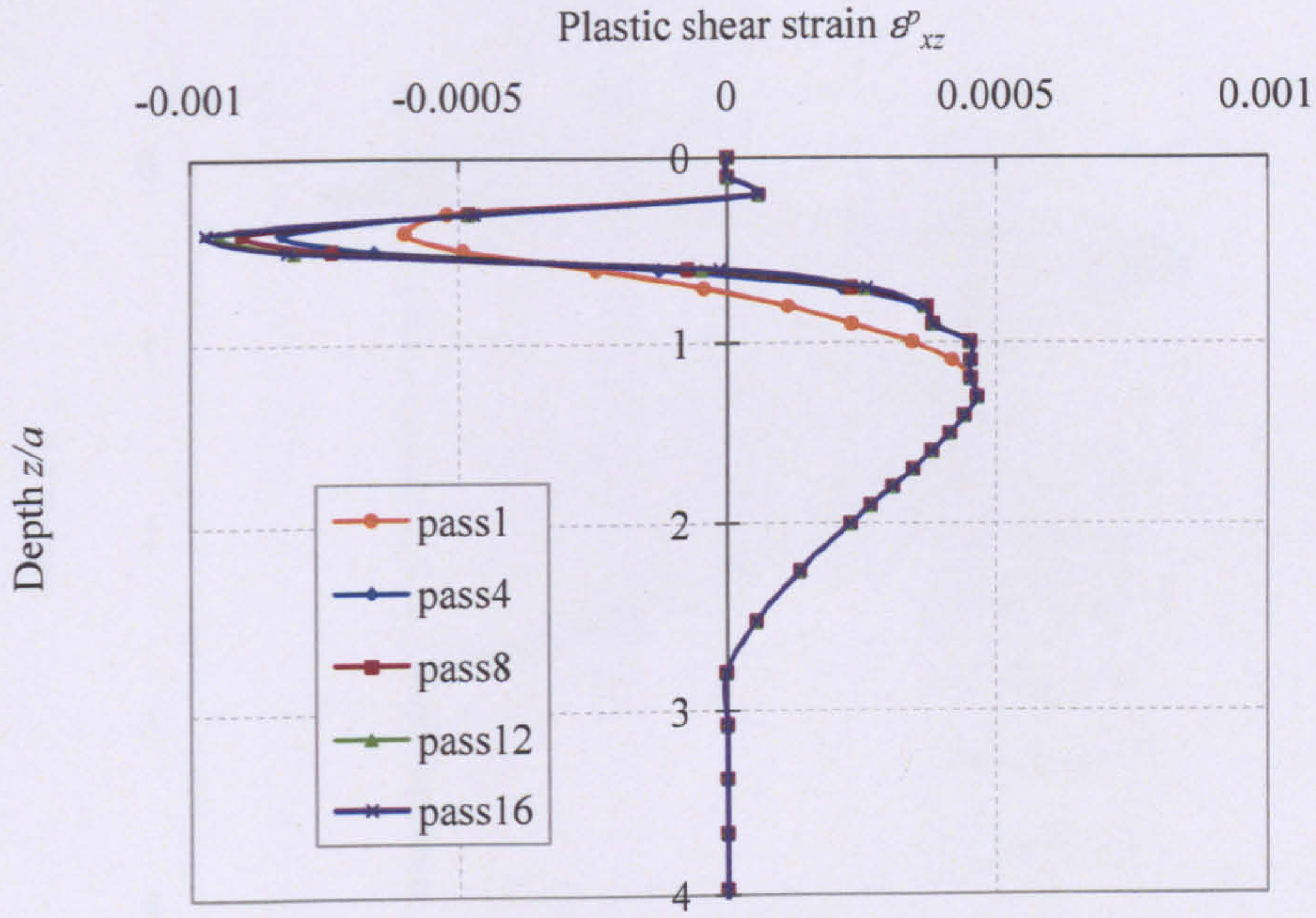

(a)

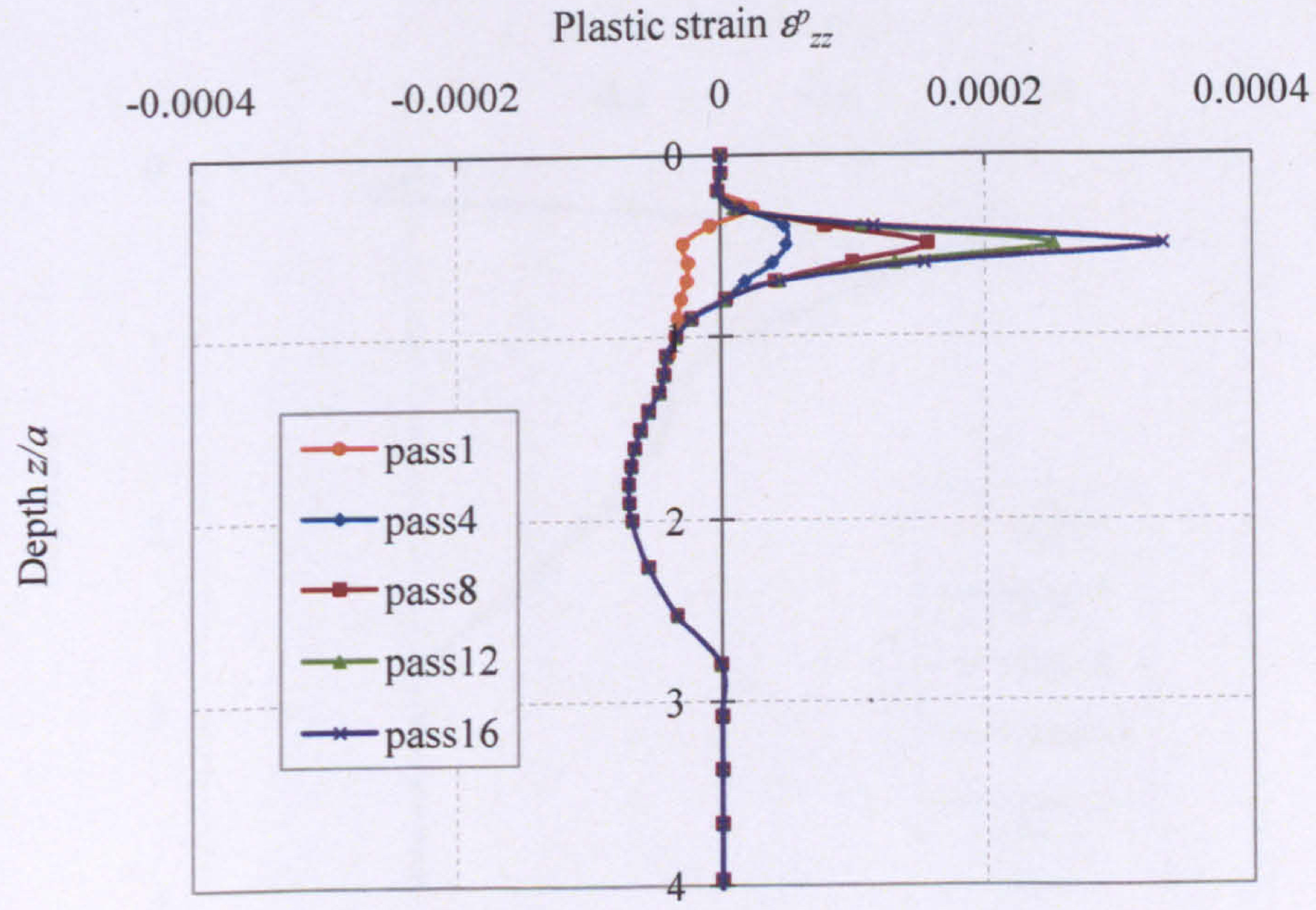

(b)

Figure 3.20 continued on following page

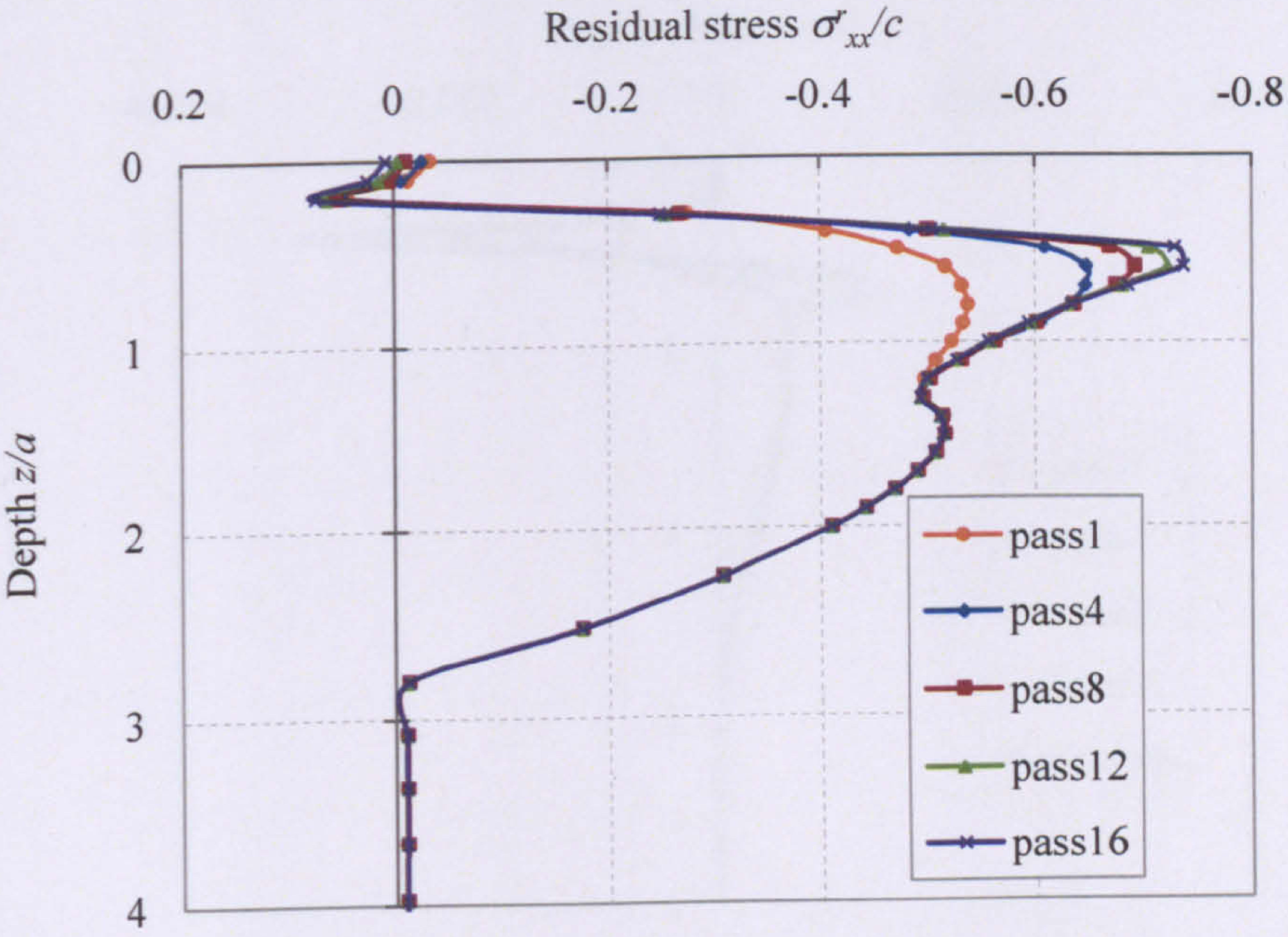

(c)

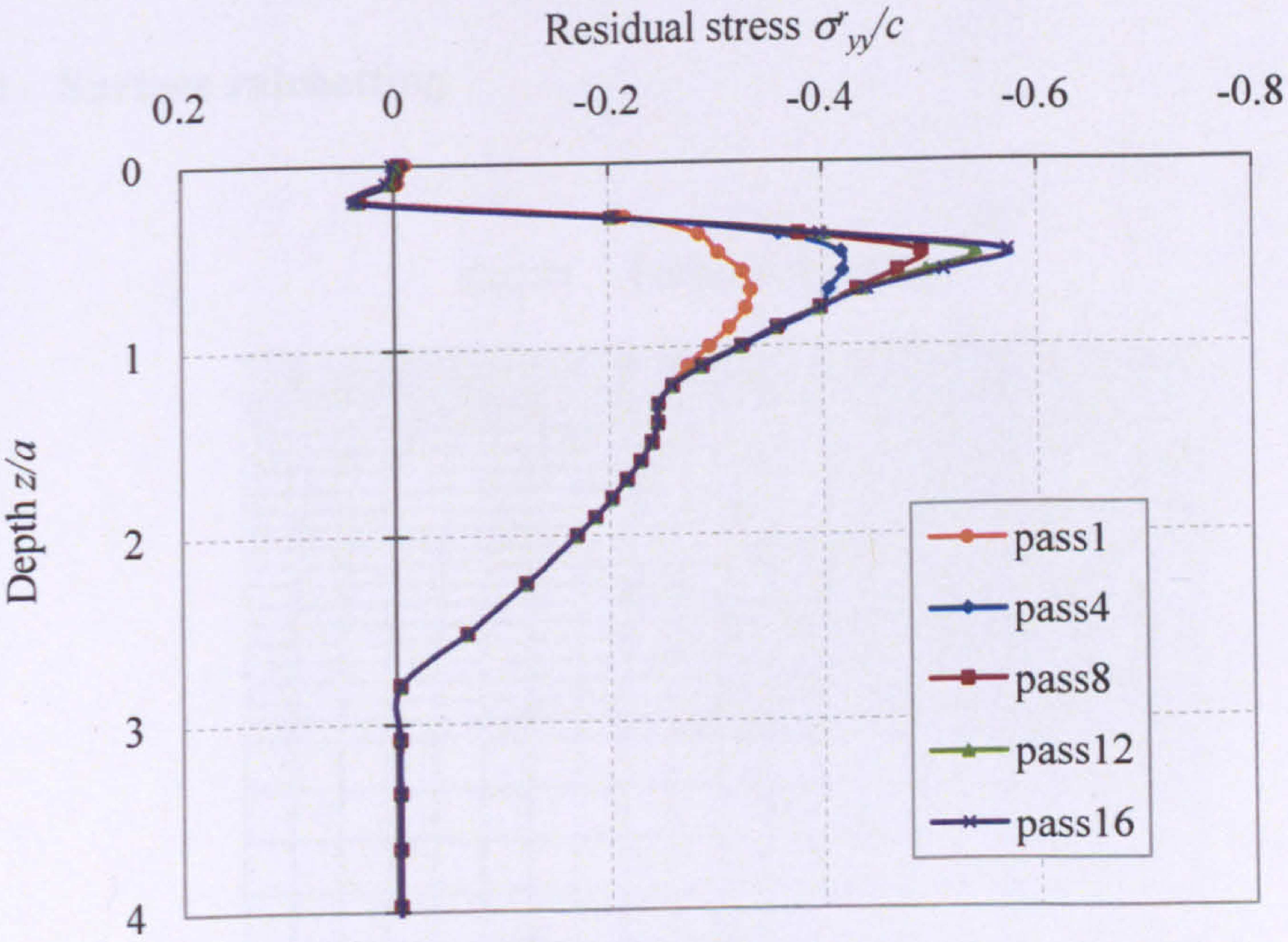

(d)

Figure 3.20. Distributions of plastic strains and residual stresses when $\phi = \psi = 20°$ and $p_0 = 7.6c$

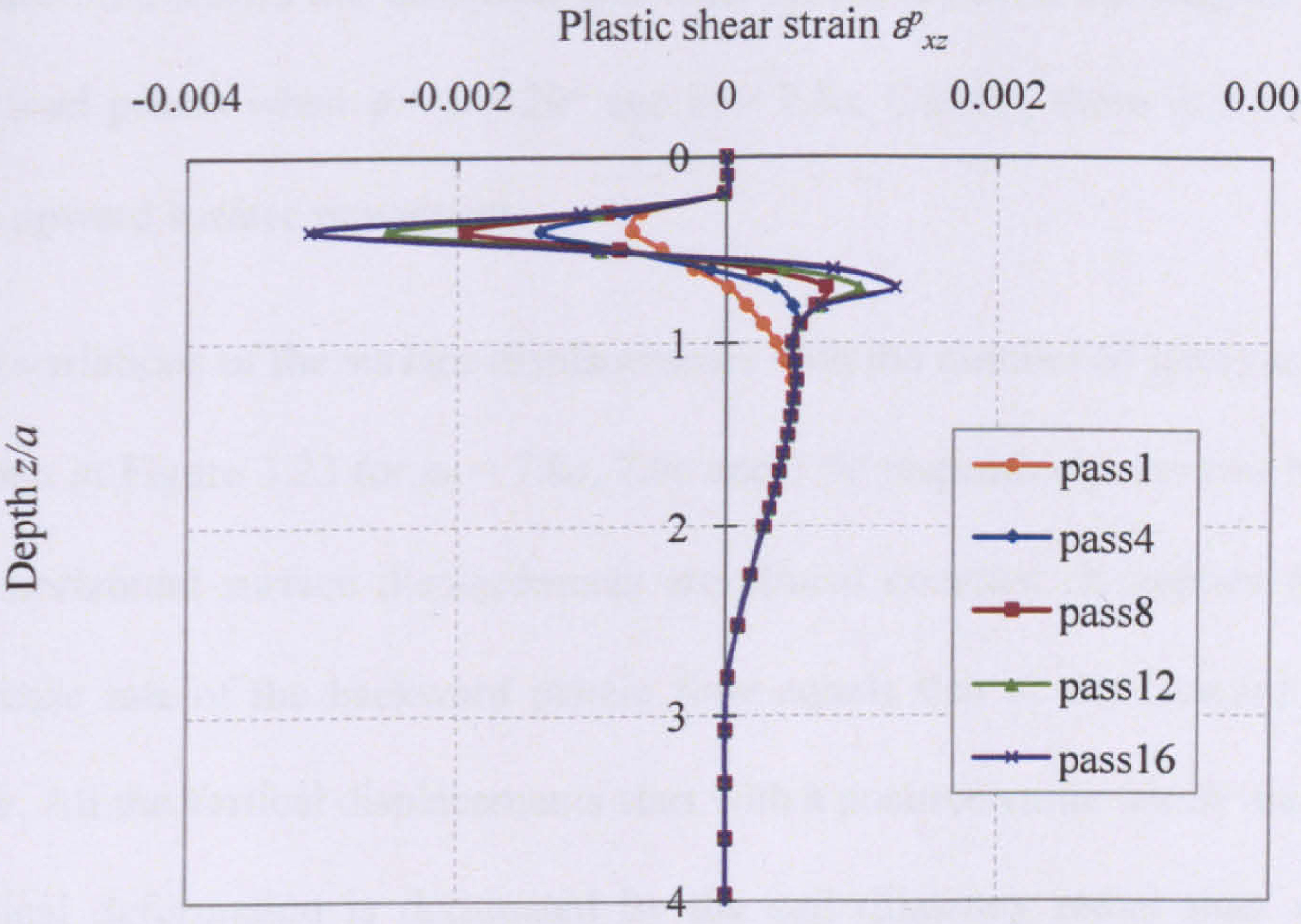

Figure 3.21. Plastic shear strain distributions when $\phi = \psi = 20°$ and $p_0 = 7.8c$

3.4.2 Surface ratchetting

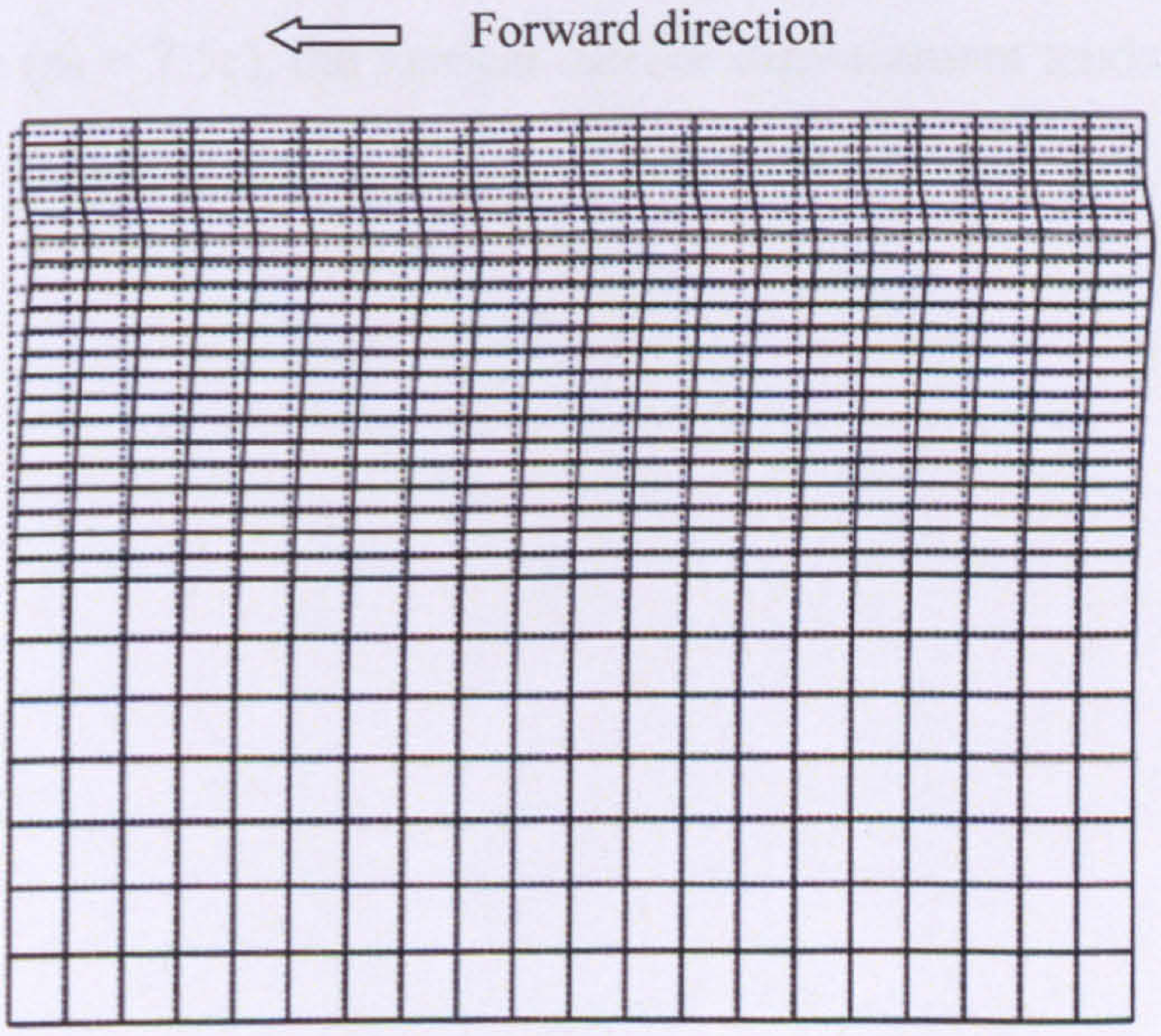

Figure 3.22. Deformed mesh in the Region A after ten passes when $\phi = 20°$ and $p_0 = 7.8c$ (scale factor: 100)

Figure 3.22 shows the deformed and undeformed mesh in the Region A after ten load passes when $\phi = \psi = 20°$ and $p_0 = 7.8c$. Clearly, there is a backward and upward surface movement.

The variations of the surface displacements with the number of load passes are shown in Figure 3.23 for $p_0 = 7.8c$, $7.6c$ and $7.5c$ respectively. As can be seen, the horizontal surface displacements are almost constant. It implies that the increase rate of the backward plastic flow equals that of the forward plastic flow. All the vertical displacements start with a positive value which means the vertical deformation is dominated by the soil dilatancy rather than vertical compression. When the load is above the theoretical shakedown limit, the vertical surface displacement after the first few load passes increases proportionally with the number of load passes. The averaged increments per load pass $G\Delta U_2/p_0a$ (ΔU_2 is increment of the vertical surface displacement) are 0.016 for $p_0 = 7.8c$ and 0.002 for $p_0 = 7.6c$. When the load is below the shakedown limit ($p_0 = 7.5c$), the vertical surface displacement tends to become stabilised.

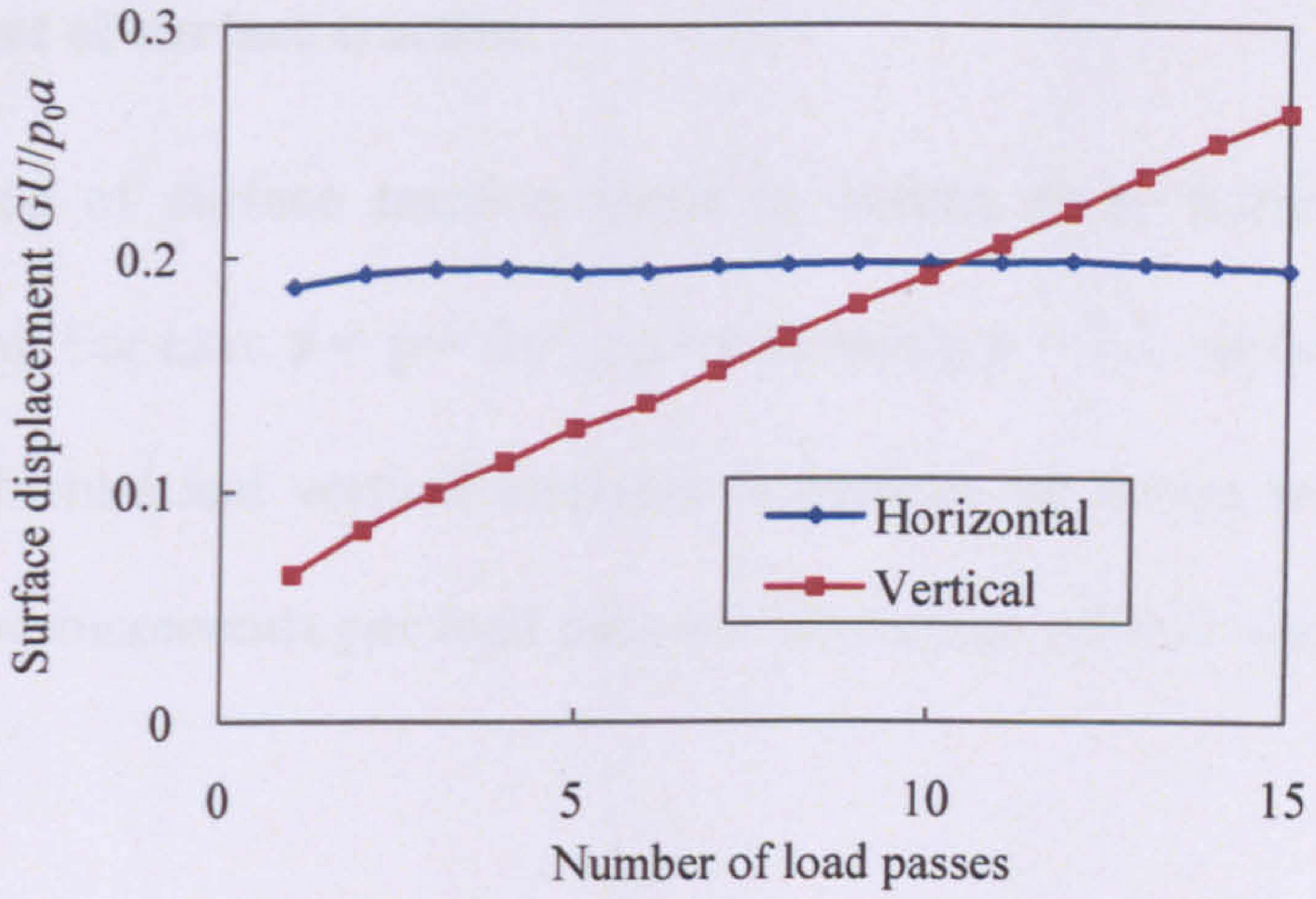

(a) $p_0 = 7.8c$

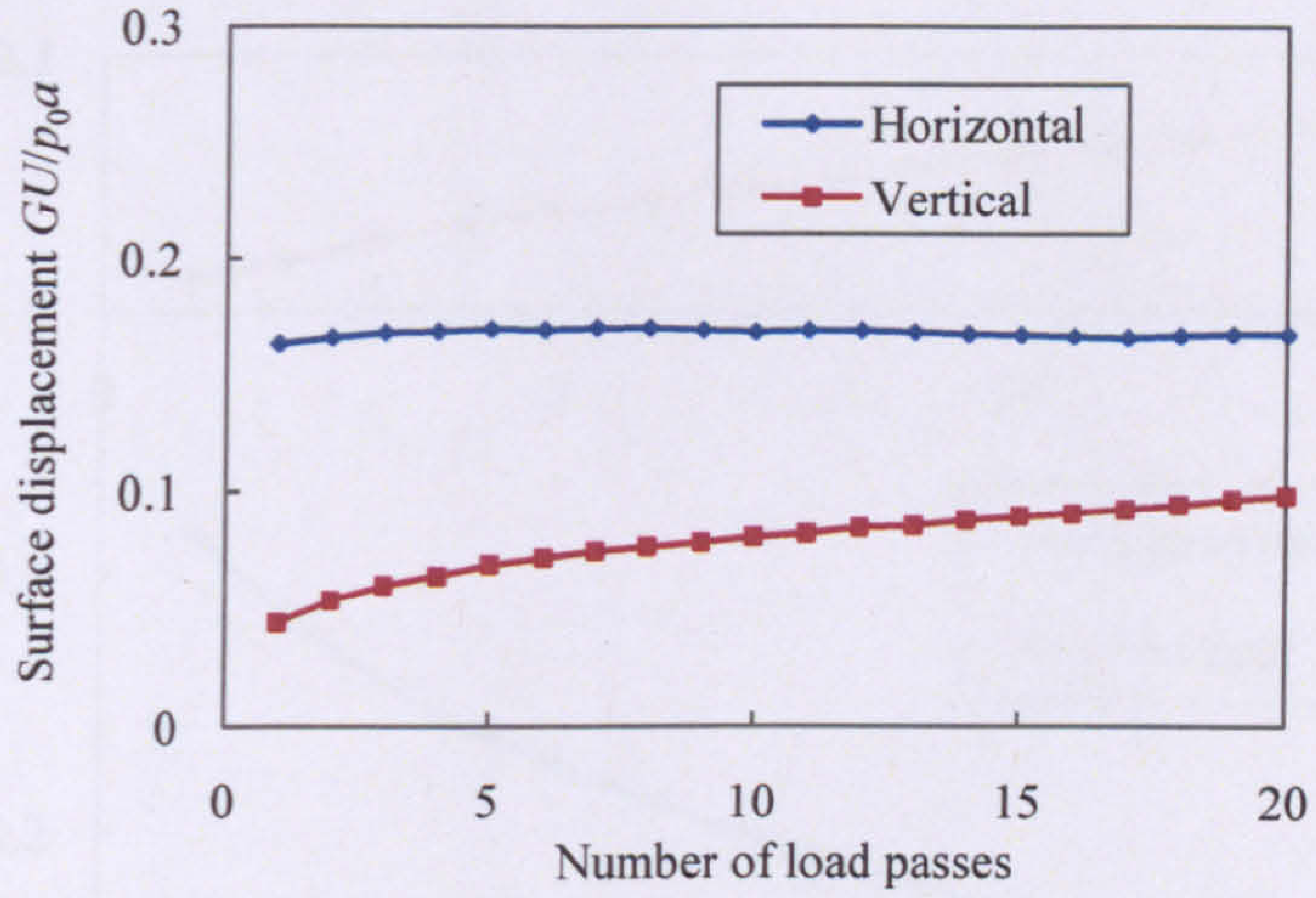

(b) $p_0 = 7.6c$

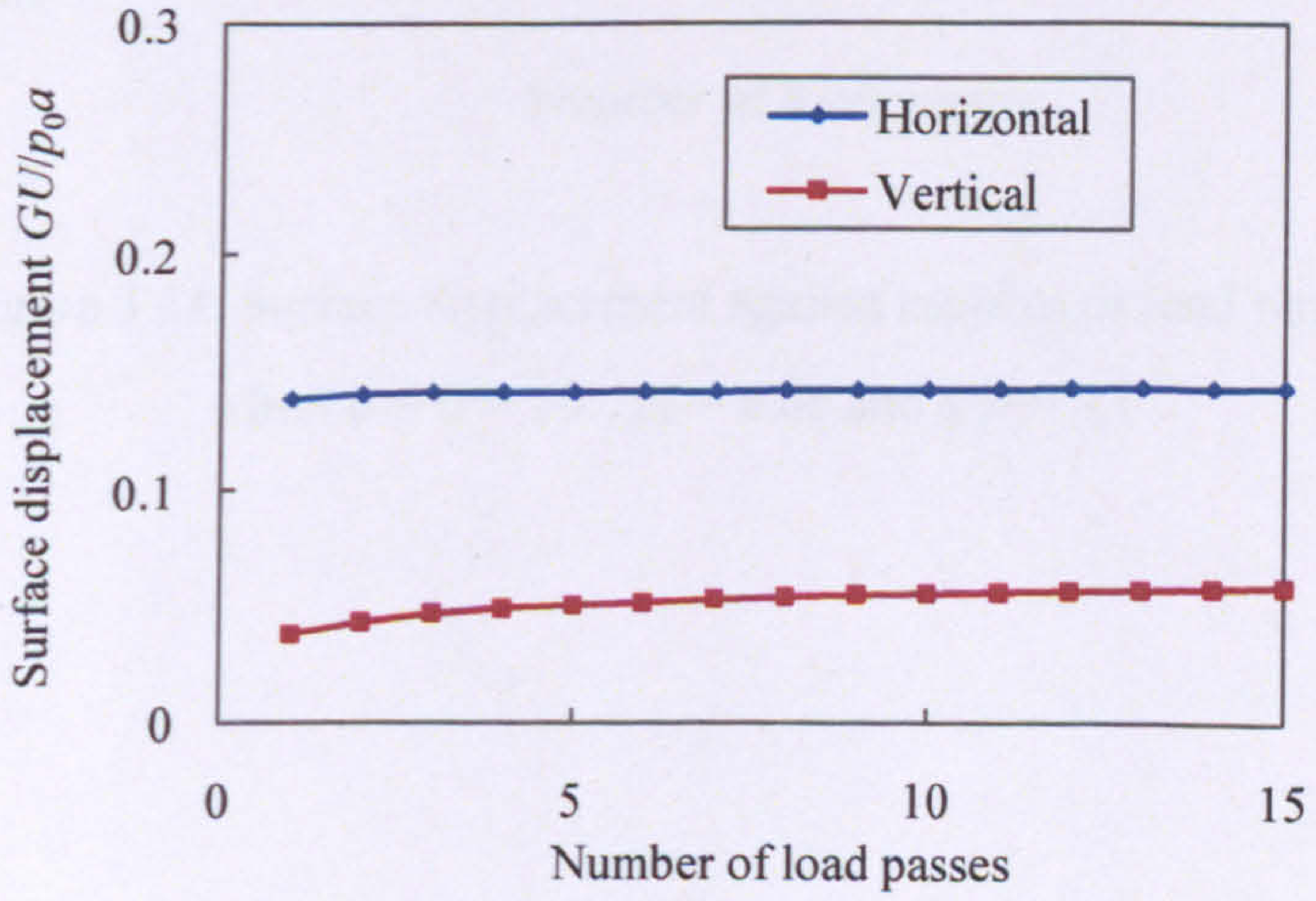

(c) $p_0 = 7.5c$

Figure 3.23. Surface displacement against number of load passes when $\phi = \psi = 20°$

3.4.3 Effect of surface traction

The presence of surface traction tends to induce more horizontal surface displacement. For case $\phi = \psi = 20°$, $p_0 = 6.6c$ and $q/p = 0.1$, surface ratchetting in both horizontal and vertical direction is present, as shown in Figure 3.24. The averaged increments per load pass are $G\Delta U_1/p_0a = 0.011$ and $G\Delta U_2/p_0a = 0.004$.

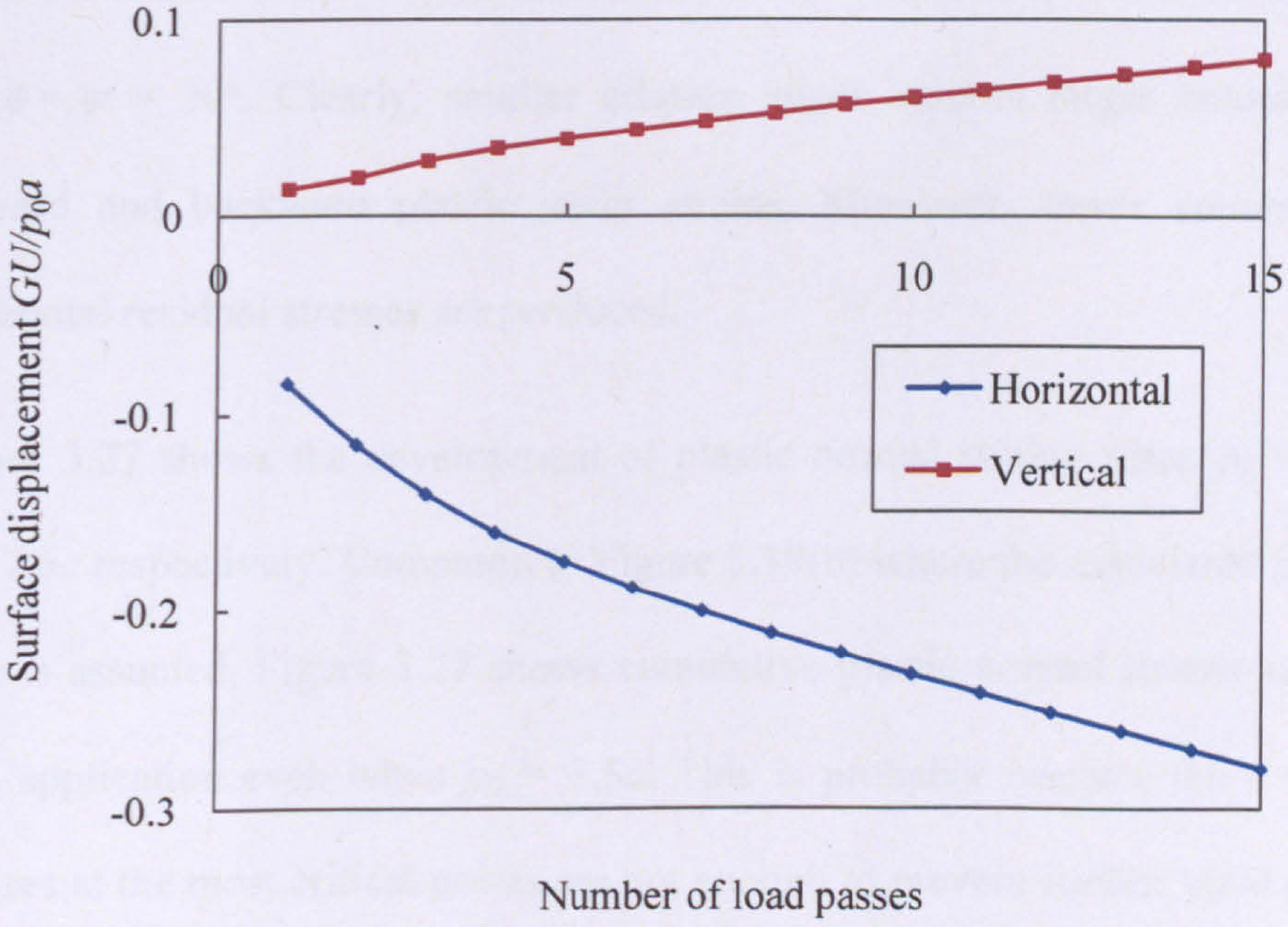

Figure 3.24. Surface displacement against number of load passes when $\phi = \psi = 20°$, $p_0 = 6.6c$ and $q/p = 0.1$

3.4.4 Effect of non-associated plastic flow

The above cases were all studied based on the assumption that the soil material follows associated plastic flow rule (i.e. $\phi = \psi$). In reality, the soil dilation angle is usually smaller than the friction angle. FE analyses were undertaken using friction angle $\phi = 20°$ and dilation angle $\psi = 12°$ so that the effect of non-associated plastic flow can be revealed.

Figure 3.25 and Figure 3.26 compare the fully-developed plastic shear strain and horizontal residual stress distributions for $\phi = 20°$ and $\psi = 12°$ with those for $\phi = \psi = 20°$. Clearly, smaller dilation angle induces larger amounts of forward and backward plastic shear strains. Moreover, fewer amounts of horizontal residual stresses are produced.

Figure 3.27 shows the development of plastic normal strains when $p_0 = 7.5c$ and $7.6c$ respectively. Compared to Figure 3.19(b) where the associated plastic flow is assumed, Figure 3.27 shows cumulative plastic normal strains at each load application even when $p_0 = 7.5c$. This is probably because the residual stresses at the most critical points are not enough to prevent further yield in the half-space. Therefore, the half-space with non-associated plastic flow has less shakedown capacity than that with associated plastic flow.

Figure 3.28 shows the variations of surface displacements with the number of load passes for $p_0 = 7.5c$ and $7.6c$. The horizontal displacements are larger than those in Figure 3.23 and barely change with the increase of load passes. The vertical displacements start from about zero due to less dilation angle, and they accumulate continuously even when $p_0 = 7.5c$.

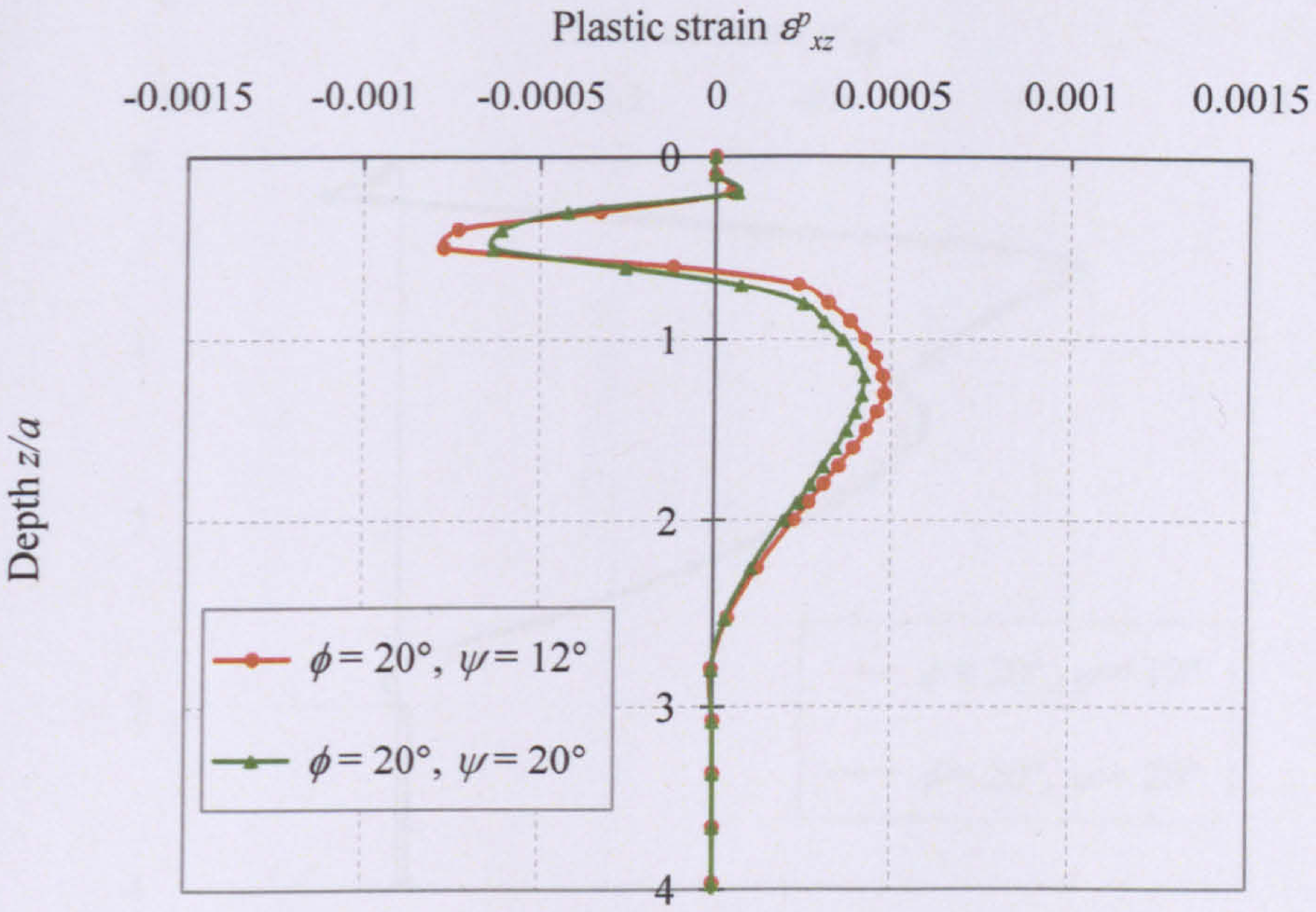

(a) $p_0 = 7.5c$

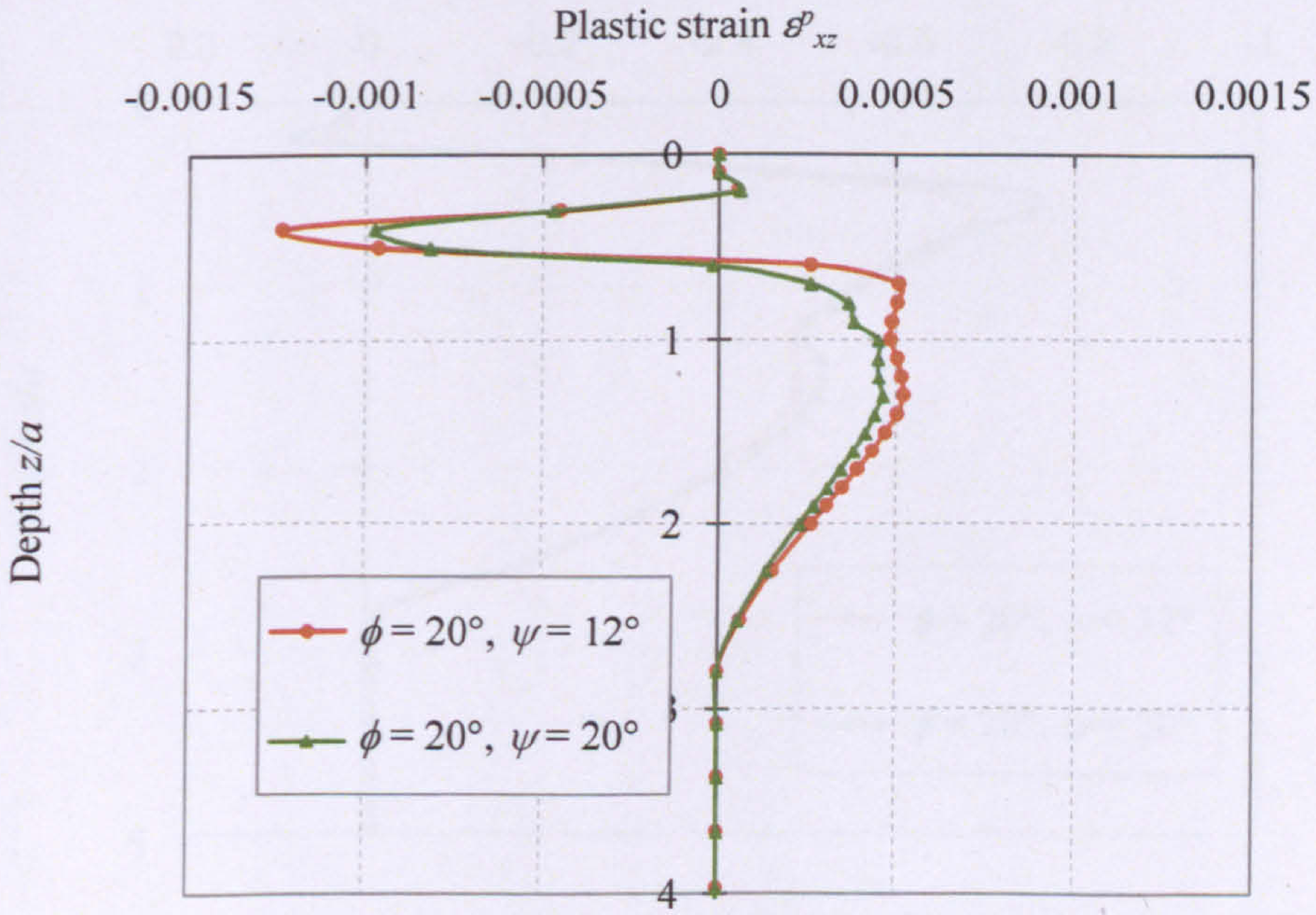

(b) $p_0 = 7.6c$

Figure 3.25. Influences of dilation angle on plastic shear strain distributions

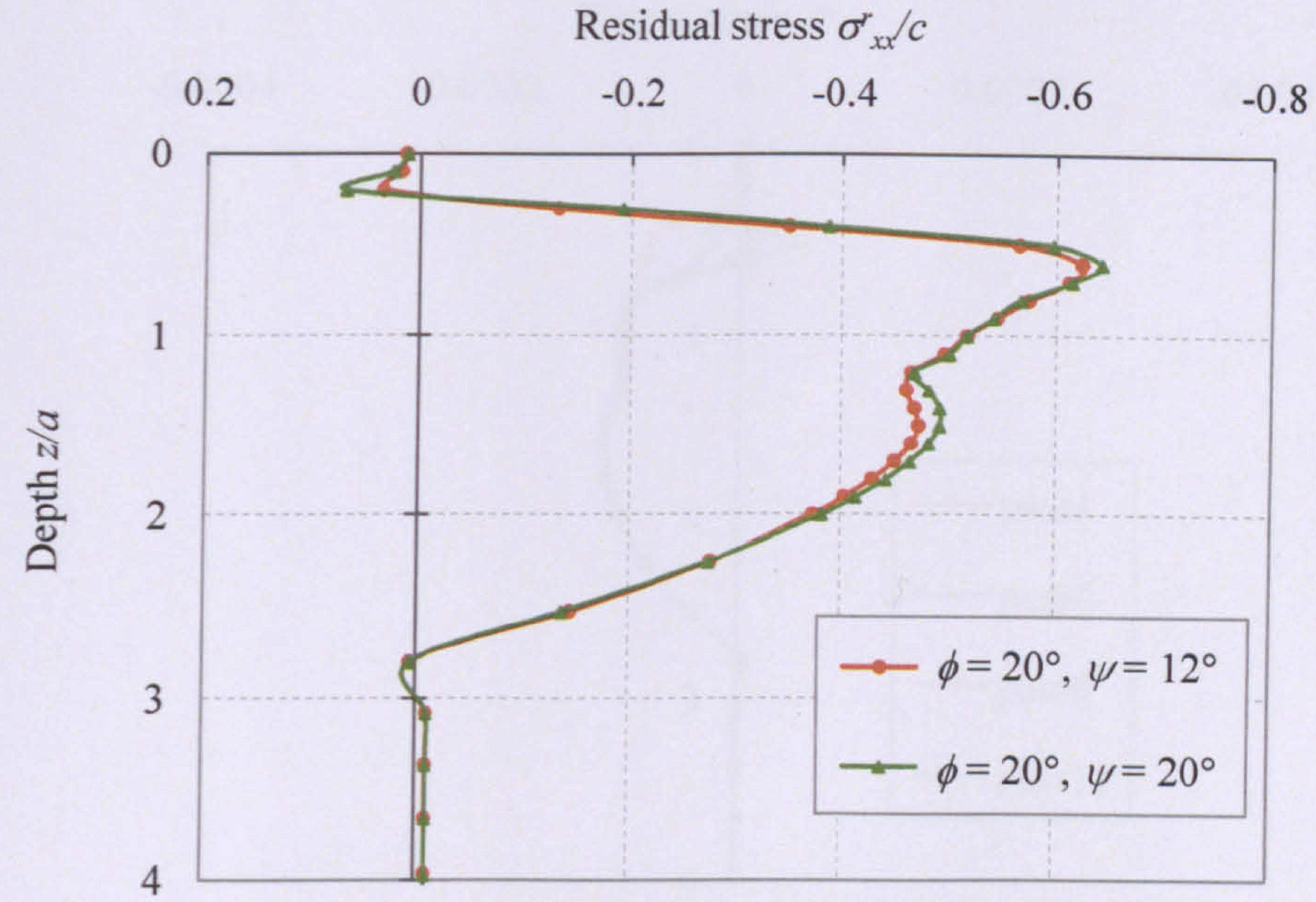

(a) $p_0 = 7.5c$

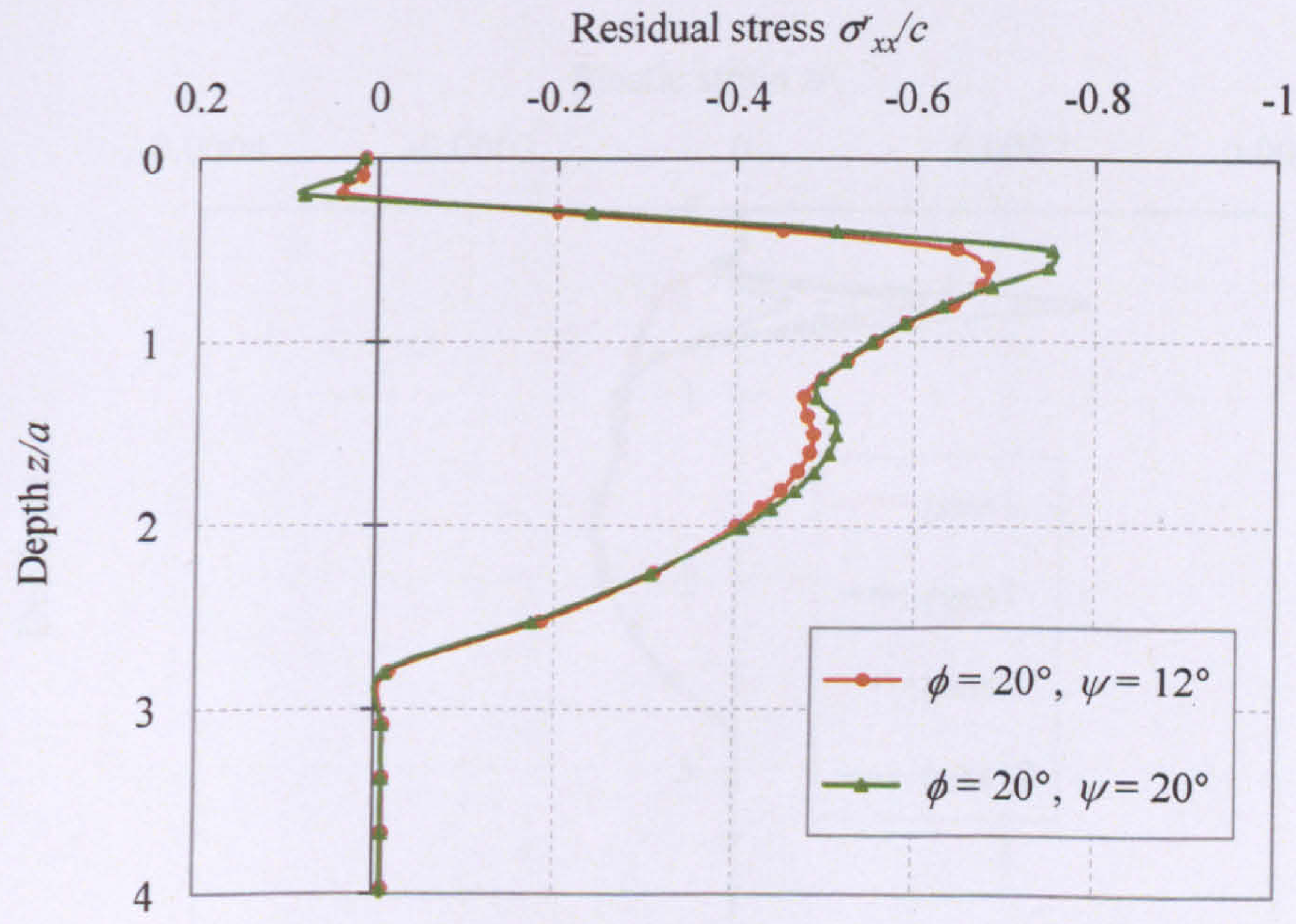

(b) $p_0 = 7.6c$

Figure 3.26. Influences of dilation angle on hotizontal residual stress distributions

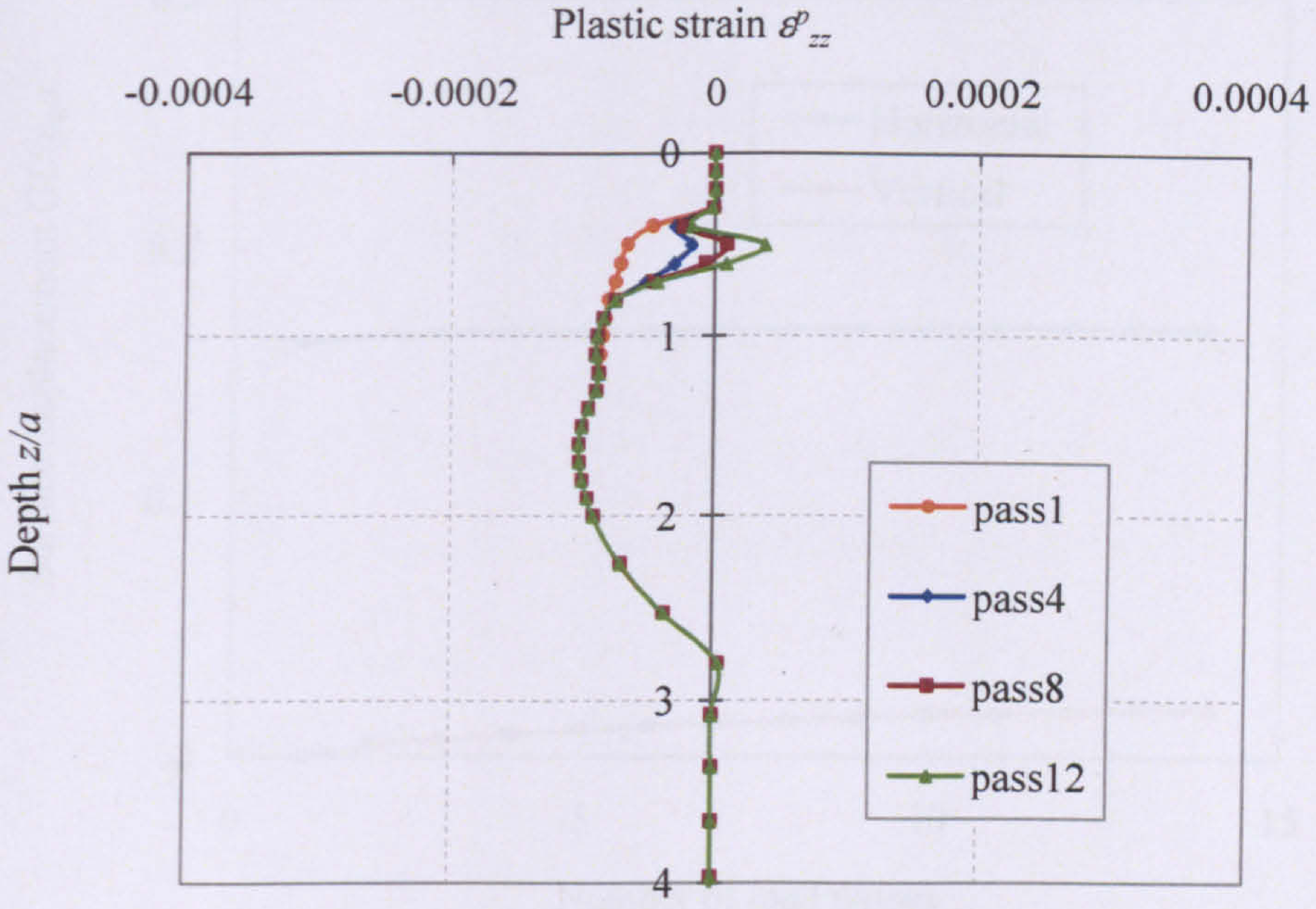

(a) $p_0 = 7.5c$

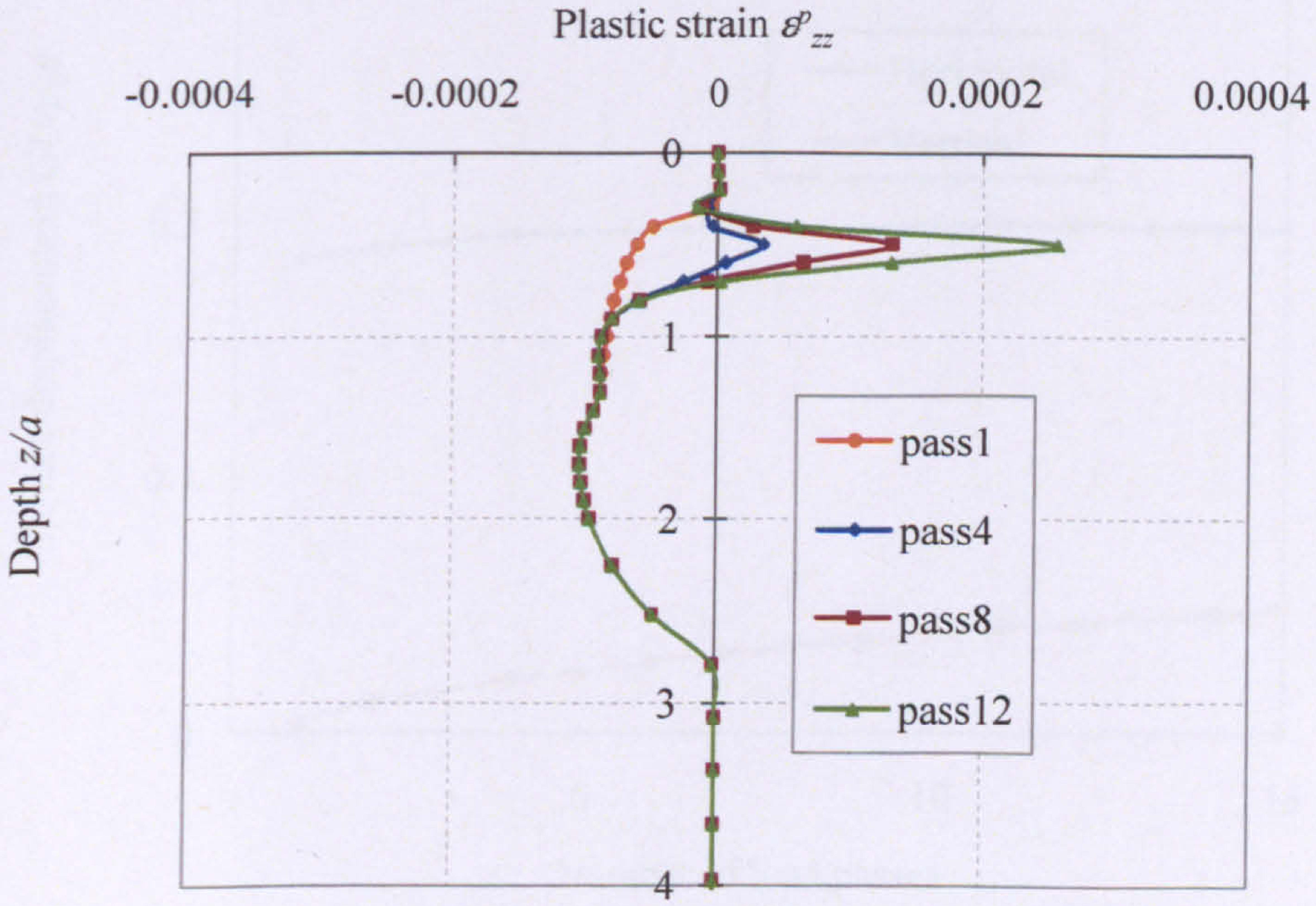

(b) $p_0 = 7.6c$

Figure 3.27. Plastic normal strain distributions when $\phi = 20°$ and $\psi = 12°$

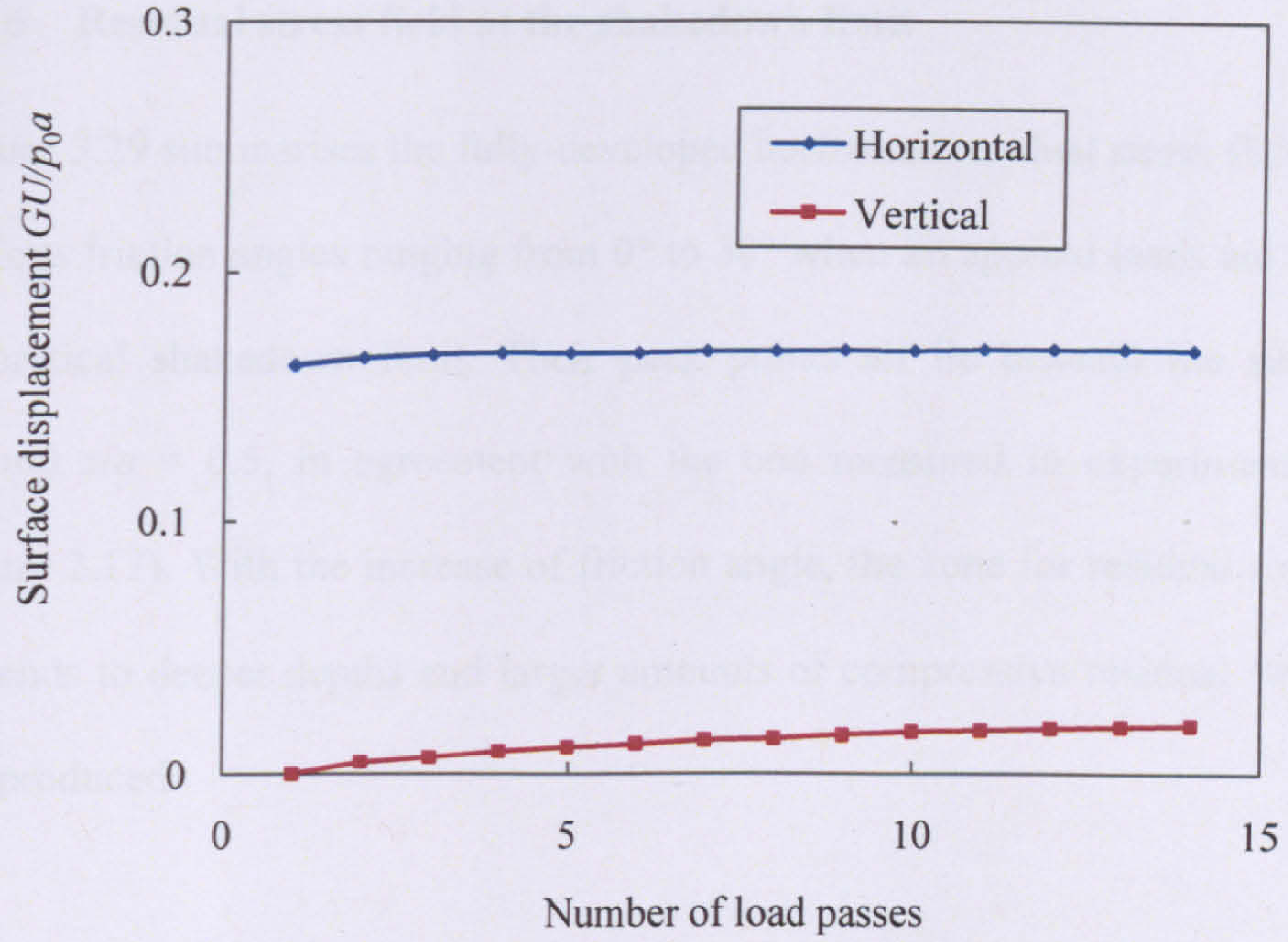

(a) $p_0 = 7.5c$

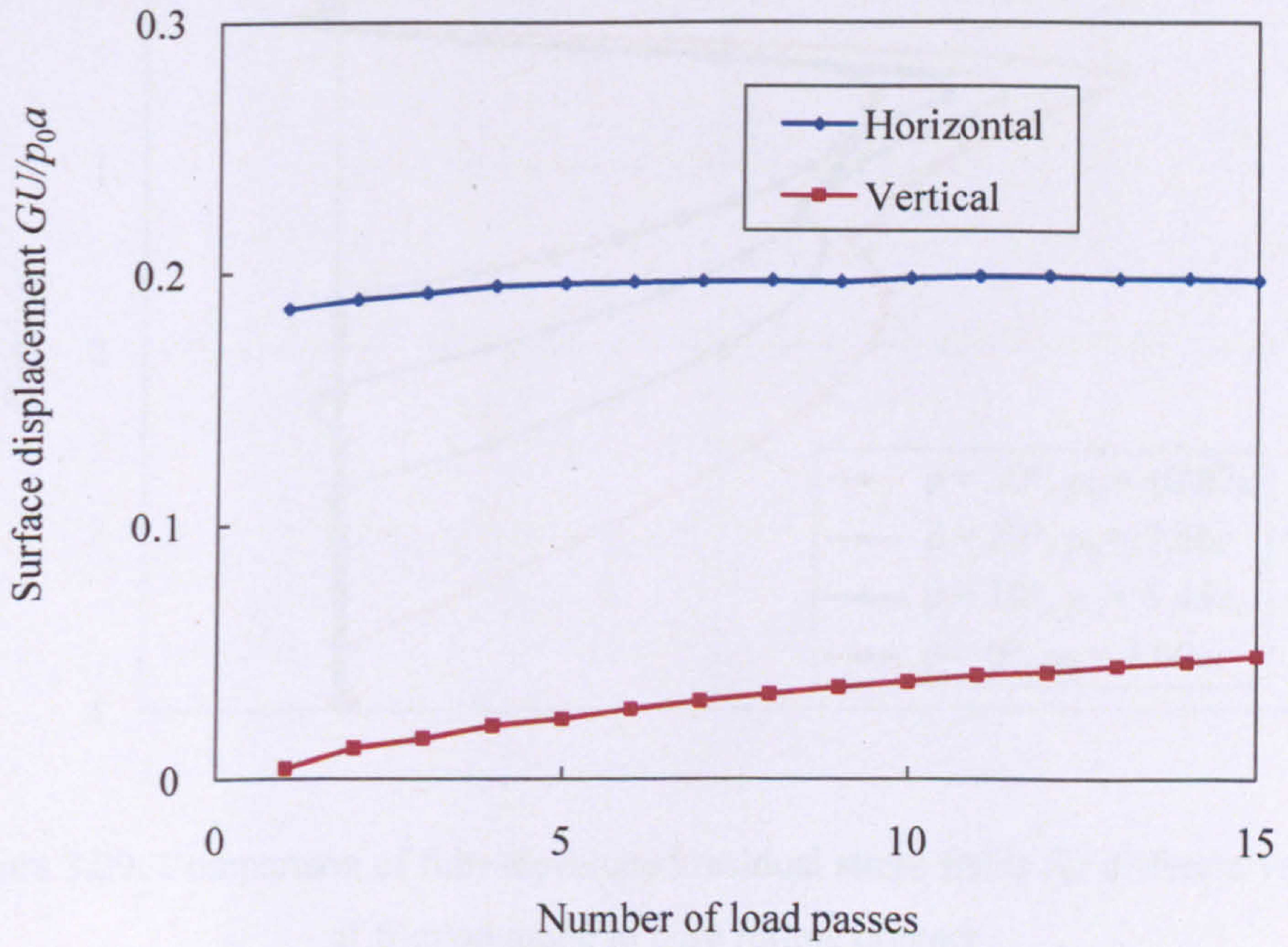

(b) $p_0 = 7.6c$

Figure 3.28. Surface displacement against number of load passes when $\phi = 20°$ and $\psi = 12°$

3.4.5 Residual stress field at the shakedown limit

Figure 3.29 summarises the fully-developed horizontal residual stress fields for various friction angles ranging from 0° to 30° when all applied loads are at the theoretical shakedown limit. Their peak points all lie beneath the surface, around $z/a = 0.5$, in agreement with the one measured in experiment (see Figure 2.17). With the increase of friction angle, the zone for residual stresses expands to deeper depths and larger amounts of compressive residual stresses are produced.

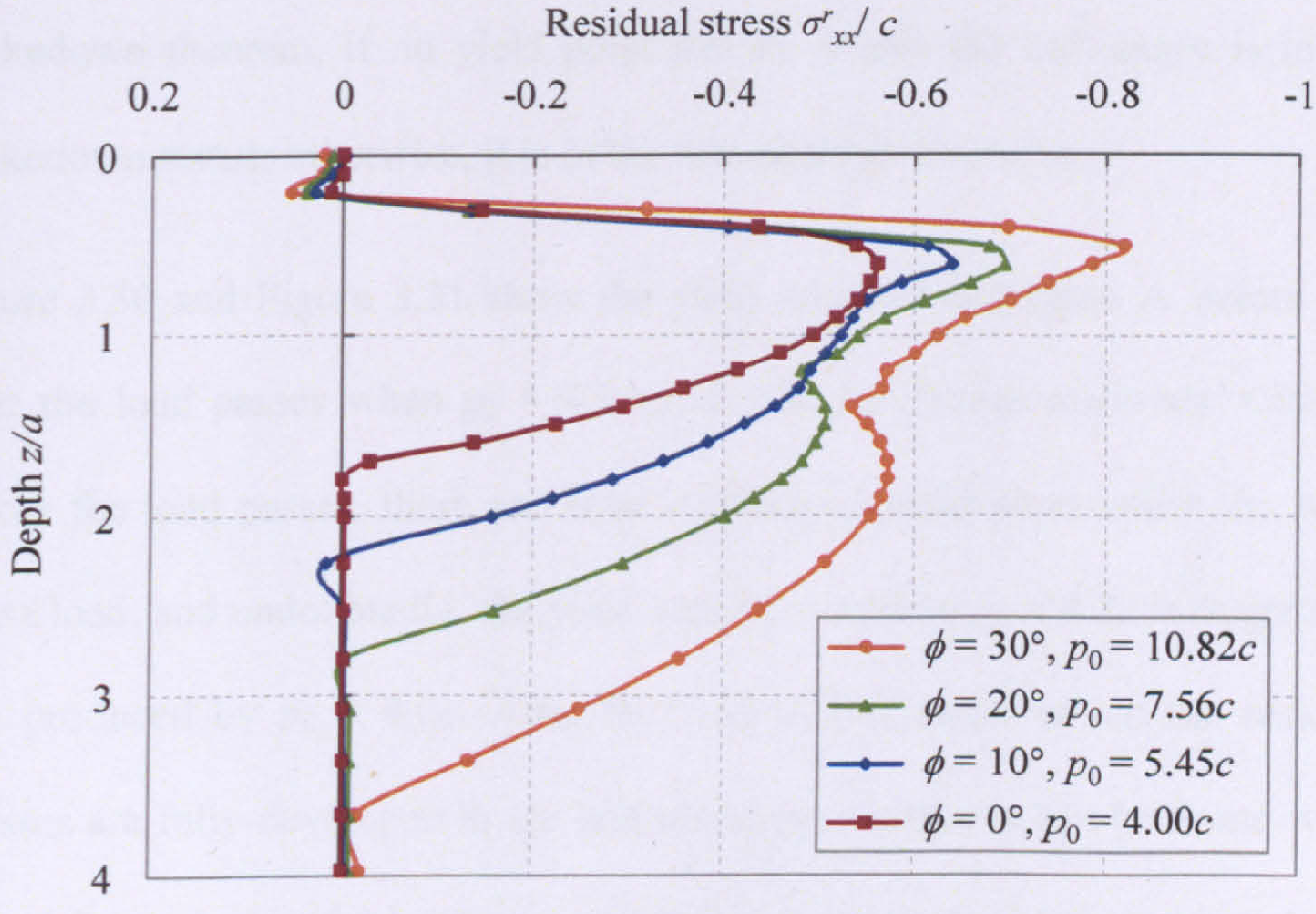

Figure 3.29. Comparison of fully-developed residual stress fields for different values of friction angle in pure rolling contact

3.5 Correlation of Melan's static shakedown theorem with elastic-plastic FE analysis

3.5.1 Shakedown and non-shakedown

In the previous FE simulations, the residual stresses, as a key component in the static shakedown theorem, are fully-developed after a limited number of load passes, and their distributions in the Region A have been suggested of being representative for the line contact problem. By further applying a static load distribution on the Region A, stresses in the half-space can be calculated and the yield points can also be visualised in the ABAQUS. According to Melan's shakedown theorem, if no yield point can be found, the half-space is in the shakedown status; otherwise, it is in the non-shakedown status.

Figure 3.30 and Figure 3.31 show the yield area in the Region A before and after the load passes when p_0 = 4.0*c* and 4.2*c* for Tresca materials. Clearly, before the load passes, there are large continuous yield areas under the static Hertz load, and undoubtedly, the yield area produced by p_0 = 4.2*c* is larger than that produced by p_0 = 4.0*c*. After the load passes under which the residual stresses are fully-developed in the half-space, no yield area can be found when p_0 = 4.0*c*, and two yield areas are observed beneath the loading edges when p_0 = 4.2*c*. This means p_0 = 4.0*c* leads to the shakedown status whereas p_0 = 4.2*c* results in the non-shakedown status. As a result, the shakedown limit should be between 4.0c and 4.2c. A few applications have been undertaken using different load conditions and material properties as summarised in Table

3.2 together with the theoretical shakedown limits. As can be seen, the theoretical shakedown limits generally agree with the numerical observations.

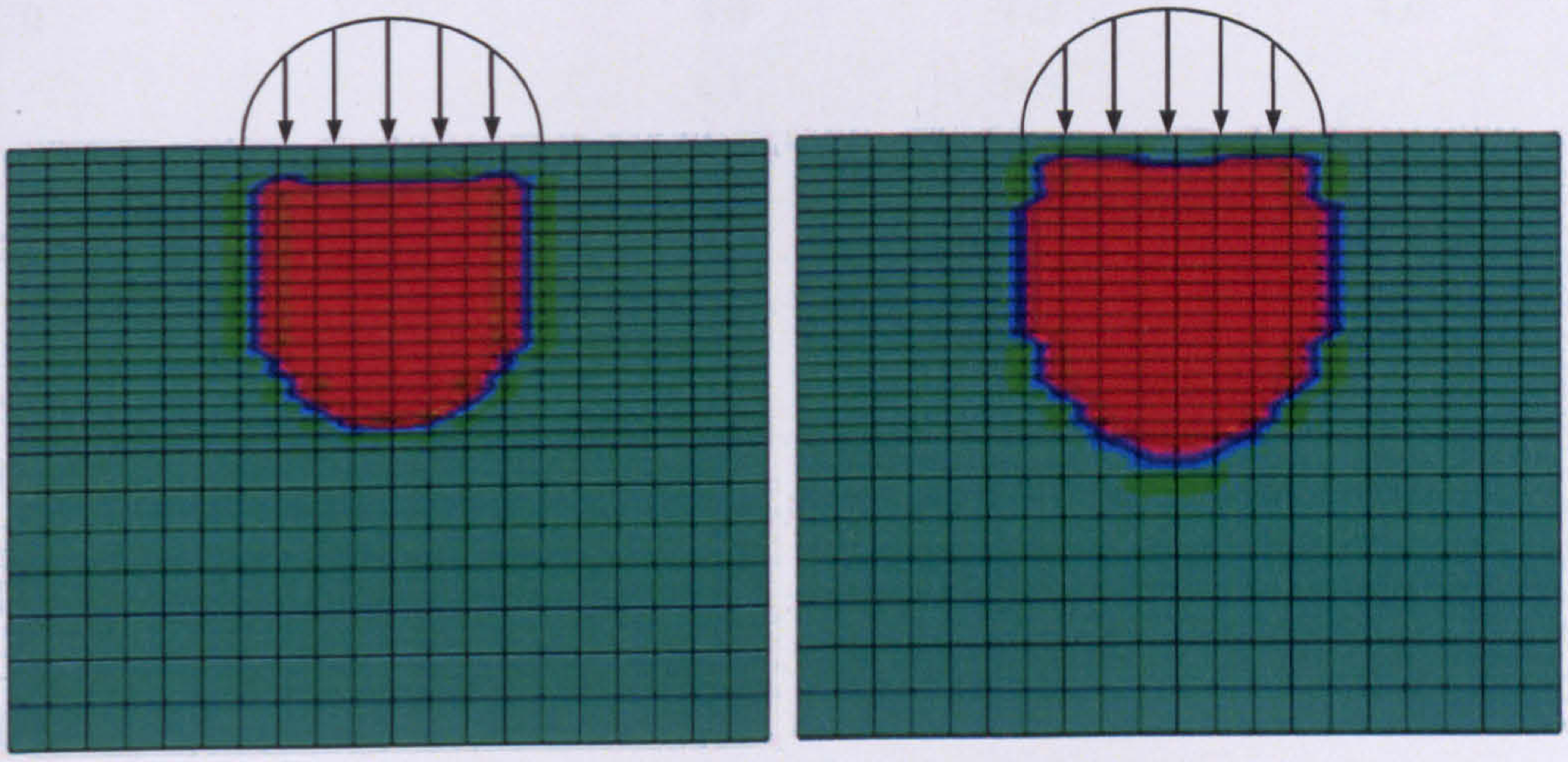

(a) $p_0 = 4.0c$ (b) $p_0 = 4.2c$

Figure 3.30. Indication of yield areas in the Region A before the load passes

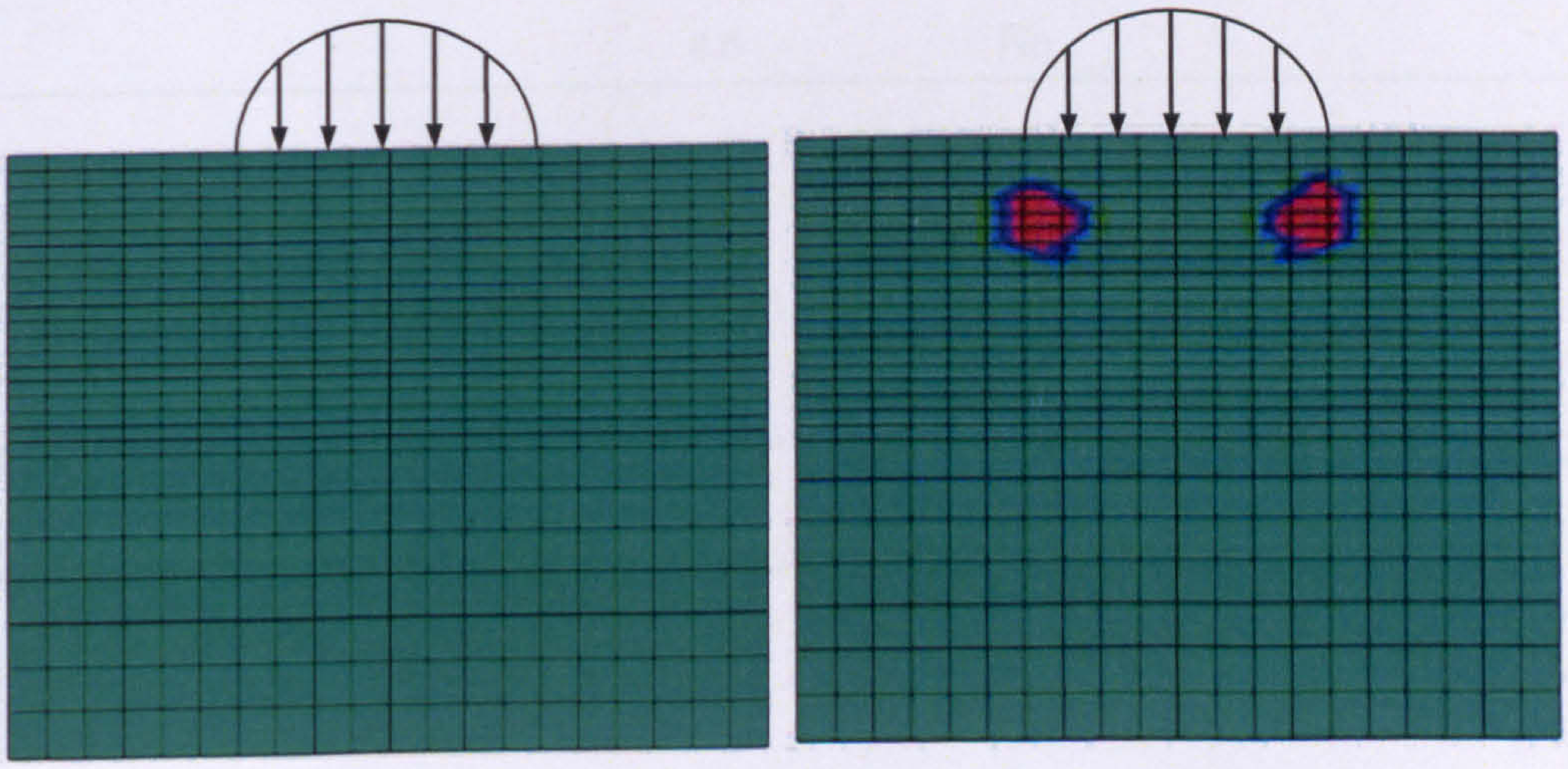

(a) $p_0 = 4.0c$ (b) $p_0 = 4.2c$

Figure 3.31. Indication of yield areas in the Region A after the load passes

Table 3.2. Comparison between the numerical observations and the theoretical shakedown limits

q/p	Friction angle ϕ (°)	p_0/c	Shakedown?	Theoretical shakedown limit
0	0	4.0	Yes	4.0
		4.1	No	
		4.2	No	
0.2	0	3.1	Yes	3.2
		3.2	No	
		3.3	No	
-0.2	0	3.1	Yes	3.2
		3.2	No	
		3.3	No	
0	20	7.5	Yes	7.56
		7.56	No	
		7.6	No	
		7.8	No	
0.1	20	6.3	Yes	6.46
		6.4	No	
		6.46	No	
		6.6	No	

3.5.2 Influence of load history

In the case of Tresca material and $p_0 = 4.2c$, the half-space will never satisfy the static shakedown condition without the change of residual stress field or load magnitude.

With the existing residual stress fields produced by $p_0 = 4.2$, the static Hertz loads were applied using two smaller load magnitudes $p_0 = 4.0c$ and $p_0 = 3.8c$ respectively. Their yield areas are presented in Figure 3.32. It is interesting to notice that the half-space does not yield when $p_0 = 3.8c$, but yields when $p_0 = 4.0c$, though the yield areas are smaller than those in Figure 3.31(b).

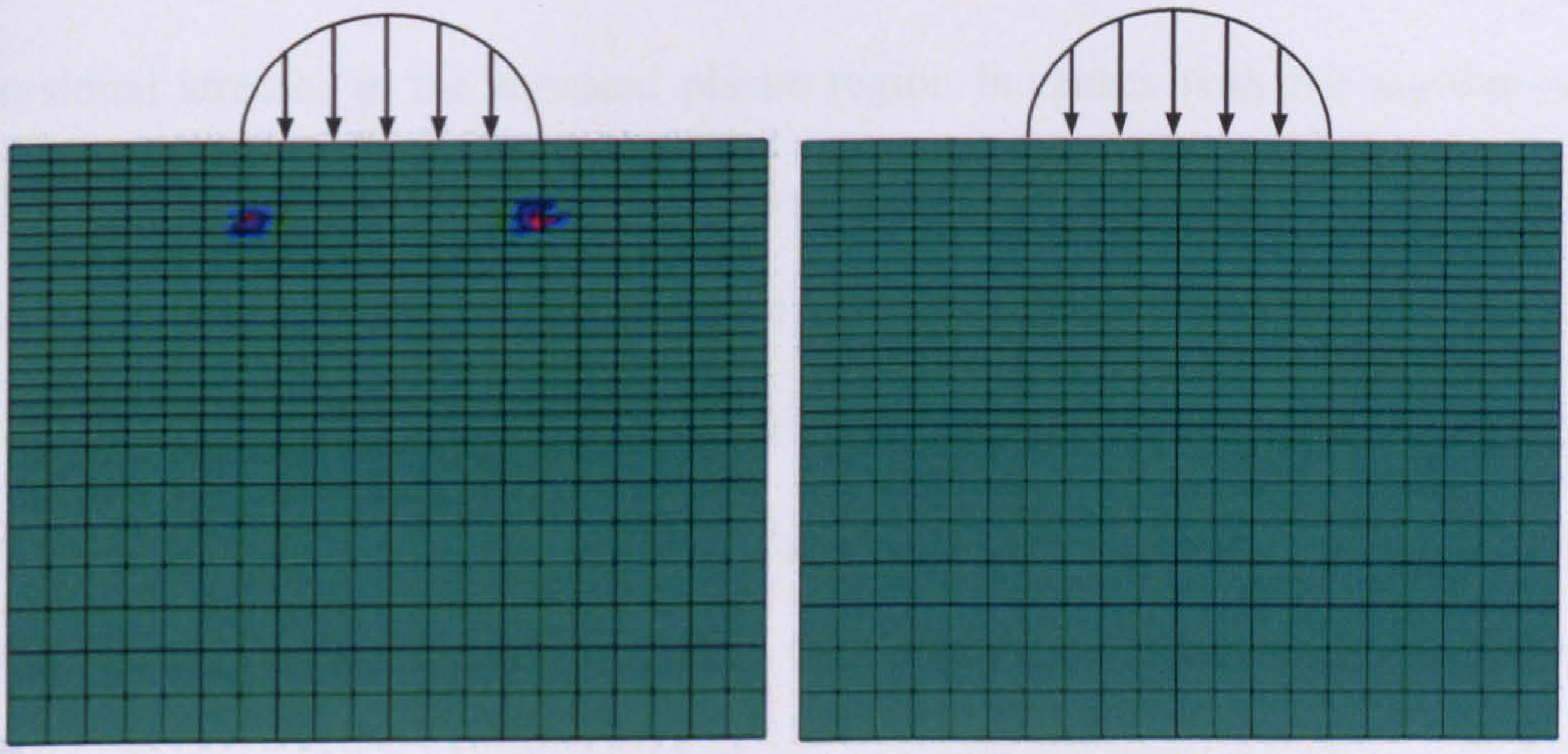

(a) $p_0 = 4.2c \rightarrow p_0 = 4.0c$ (b) $p_0 = 4.2c \rightarrow p_0 = 3.8c$

Figure 3.32. Indication of yield areas in the Region A when different static load magnitudes are applied

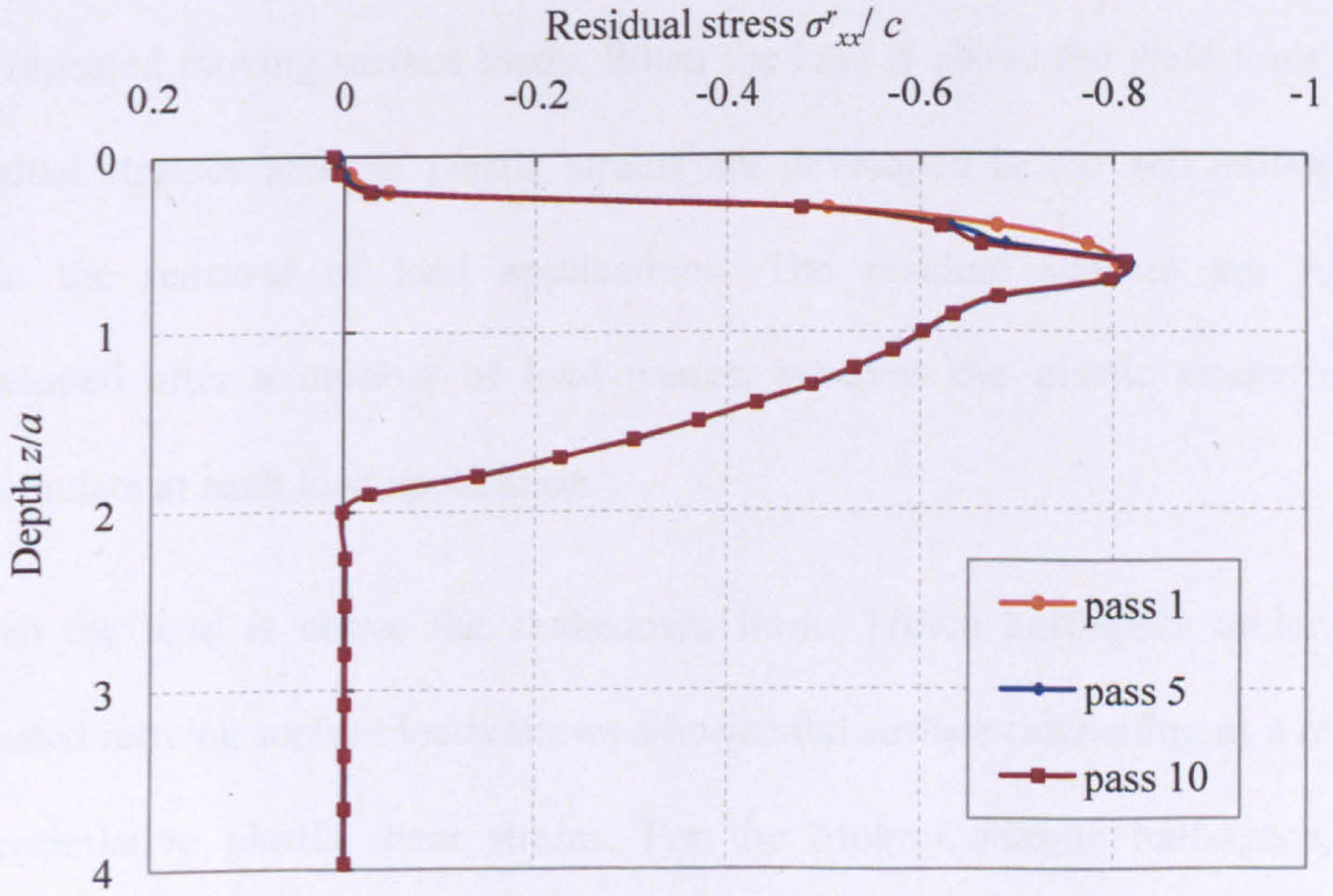

Figure 3.33. The change of residual stress distributions

Efforts were then made by applying repeated load passes with a smaller load magnitude $p_0 = 4.0c$ on the existing residual stress fields (produced by five passes of $p_0 = 4.2c$). Unlike Figure 3.10(c) in which the amount of horizontal residual stresses in the repeated plastic region increases with the number of load passes when $p_0 = 4.2c$, the present analysis shows a reduction of this amount within a very narrow band around the critical depth $h/a = 0.5$ (see Figure 3.33). After ten load passes, only one yield point can be found when a static Hertz load with $p_0 = 4.0c$ is applied on the half-space. This finding implies that once the applied load is within the shakedown limit, no matter what the load history is, the residual stresses will develop in such a way that help the half-space to resist further yield.

3.6 Conclusions

The present FE model is able to simulate the behaviour of soil half-space under the repeated moving surface loads. When the load is above the yield limit, the residual stresses and the plastic strains are developed in the soil half-space upon the removal of load applications. The residual stresses are fully-developed after a number of load passes, whereas the plastic strains may accumulate at each load application.

When the load is above the shakedown limit, Tresca half-space under the repeated moving surface loads shows a horizontal surface ratchetting as a result of cumulative plastic shear strains. For the Mohr Coulomb half-space, an upward surface ratchetting is predicted due to the increasing plastic normal strains caused by the soil dilatancy. The presence of surface traction induces surface horizontal displacement and its direction also has some effect on the distributions of plastic strains and residual stresses. The non-associated plastic flow rule gives less resistance to continuous plasticity than the associated plastic flow rule.

It should be noted the real pavements show the development of rutting (i.e. a downward surface displacement) rather than the upward surface ratchetting. This is because the real pavement problem is actually a three-dimensional problem rather than a two-dimensional plane strain problem considered in the present study. The lateral movement of the soil beneath the load path also contributes to the pavement rutting (Huang, 1993; Juspi, 2007).

Nevertheless, FE analyses in the present study are able to capture the shakedown and non-shakedown phenomena around the theoretical shakedown limit for the two-dimensional pavement model. Residual stresses play an important part in the prevention of further yield. The fully-developed residual stress fields in the FE analyses can also be used to check critical residual stress fields developed in the next chapter.

CHAPTER 4

SOLUTIONS TO STATIC SHAKEDOWN ANALYSIS OF SINGLE-LAYERED ROAD PAVEMENTS

4.1 Introduction

Rutting of a flexible pavement is substantially influenced by the plasticity of the pavement material. However, in the current analytical approaches to pavement design, only the elastic strain at the top of the subgrade is used as a design parameter in prevention of excessive rutting. Shakedown analysis using the shakedown theorem takes into account the material plasticity and allows a direct calculation of shakedown load limit. It can be used to develop an elastic-plastic theoretical framework for pavement design.

This chapter develops direct solutions to shakedown analysis of single-layered pavement under repeated moving surface loads. Melan's lower-bound shakedown theorem has been adopted as the theoretical basis for deriving the shakedown limits. Both two-dimensional (2D) and three-dimensional (3D)

Hertz load distributions are considered. The elastic stress fields have been found and expressed in closed form solutions.

The present 2D and 3D shakedown solutions are compared with other authors' solutions. The critical residual stress fields at the shakedown limit are also compared with the residual stress fields from previous FE calculations. The effects of the soil friction angle, Poisson's ratio and surface frictional coefficient, are studied in detail. The 3D shakedown solutions are also extended to pavements with elliptical contact area.

4.2 Problem definition

Here, the single-layered flexible road pavement is considered as a cohesive-frictional half-space of which the material is homogenous, isotropic and modelled by the Mohr Coulomb criterion. The half-space surface is assumed to remain flat after a number of load applications, and therefore the shape of the contact area and the elastic stress distributions are not influenced by previous plastic flow. Both 2D and 3D pavement models are examined for deriving shakedown limits.

4.2.1 2D pavement model

The 2D plane strain pavement model is established under the simplifying assumption that the load is applied by an infinitely long roller, as shown in Figure 4.1, where $2a$ is the contact width, P is the total normal loads per unit length applied in the vertical direction due to wheel rolling and Q is the total shear loads per unit length applied in the travel direction due to sliding. The normal and shear load distribution p and q on the contact area between the wheel and the pavement surface are described as Equation (4.1).

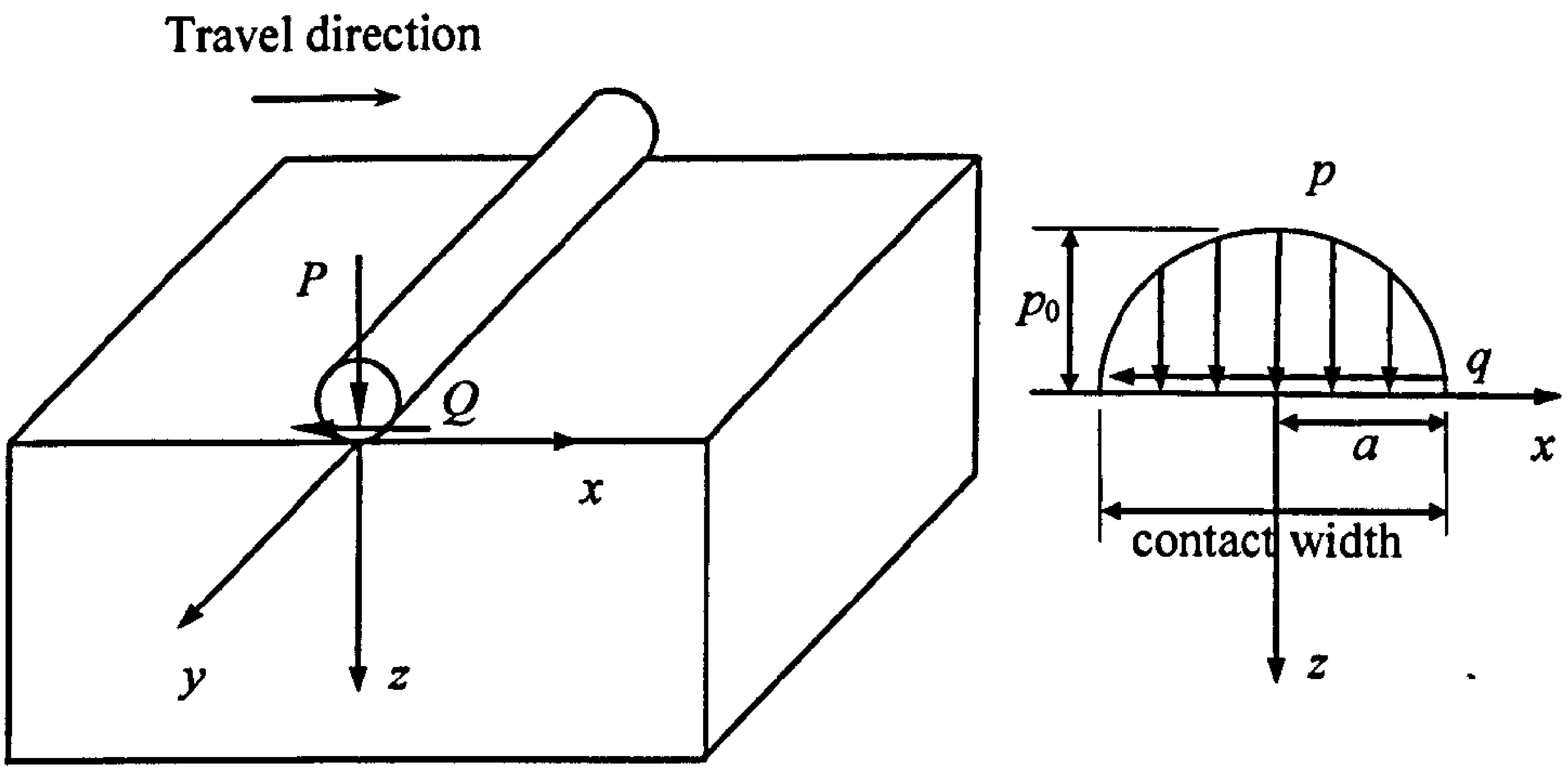

Figure 4.1. A pavement under a 2D moving Hertz load

$$
\begin{gathered}
p=\frac{2P}{\pi a^2}\left(a^2-x^2\right)^{1/2}, \\
q=\frac{2Q}{\pi a^2}\left(a^2-x^2\right)^{1/2}. \\
(-a\le x\le a)
\end{gathered}
\tag{4.1}
$$

This load distribution is normally regarded as the 2D Hertz load distribution (Johnson, 1985; Yu, 2006) and its maximum compressive pressure is $p_0 = 2P/\pi a$ occurring at the load centre ($x = z = 0$). Due to the relation of rolling and sliding, the normal and shear loads are correlated by the frictional coefficient μ as:

$$
Q=\mu P. \tag{4.2}
$$

This frictional coefficient is determined by the materials and the physical conditions of the interface.

4.2.2 3D pavement model

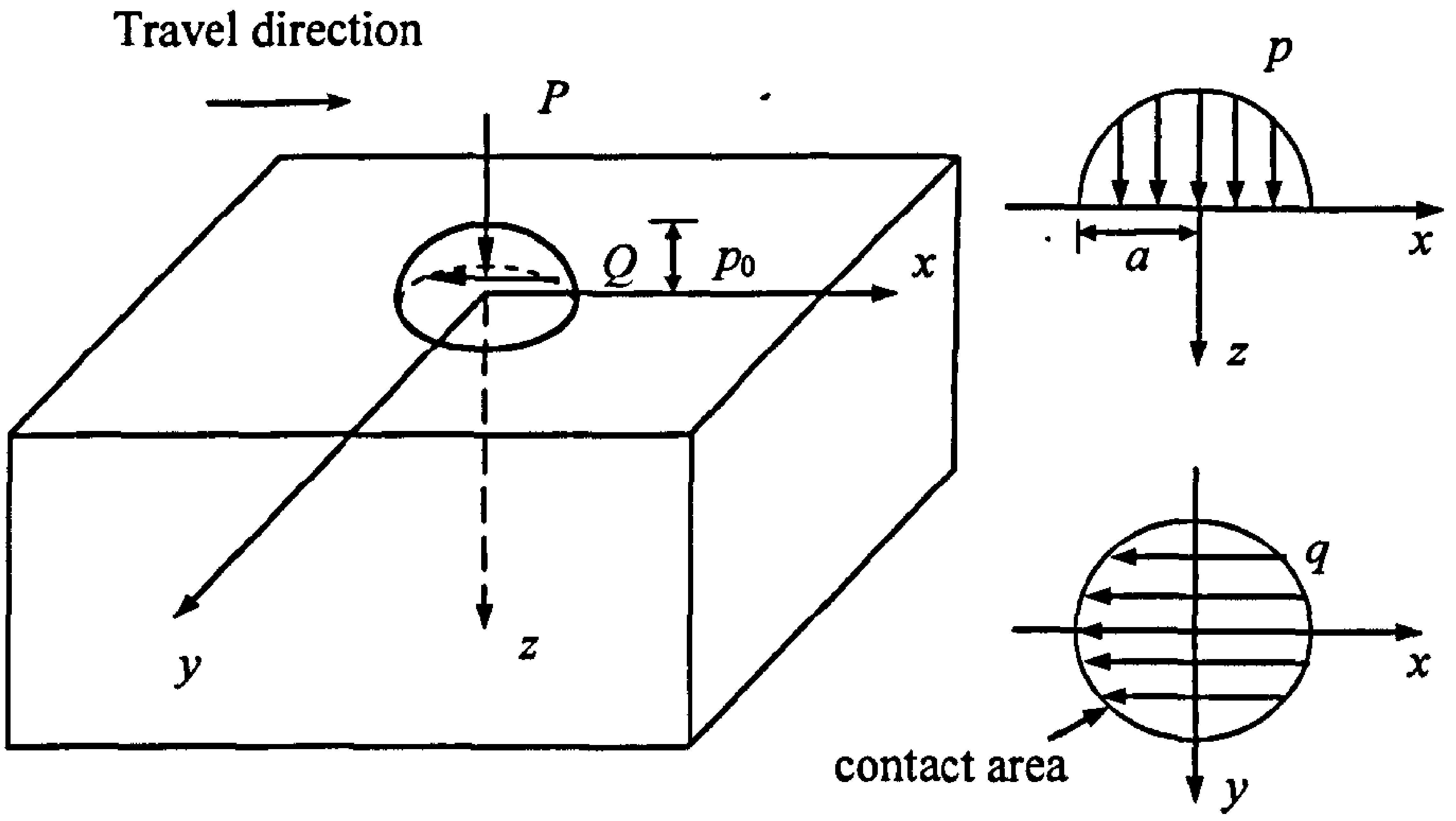

Figure 4.2. A pavement under a 3D moving Hertz load

In the 3D pavement model, it is first considered that the half-space is subject to a surface contact loading limited to a circle of radius, a (see Figure 4.2). The normal and shear load distributions on the surface are given as follows:

$$\begin{gathered} p=\frac{3P}{2\pi a^3}\left(a^2-x^2-y^2\right)^{1/2}, \\ q=\frac{3Q}{2\pi a^3}\left(a^2-x^2-y^2\right)^{1/2}. \\ \left(x^2+y^2\leq a^2\right) \end{gathered} \tag{4.3}$$

This load distribution is often referred to as the 3D Hertz load distribution (Johnson, 1985; Collins and Cliffe, 1987) and it has a maximum compressive pressure $p_0 = 3P/2\pi a^2$ at the centre of the contact area ($x = y = z = 0$). The same proportional relationship between Q and P is assumed as Equation (4.2).

Most of current works (Ponter et al., 1985; Radovsky and Murashina, 1996; Boulbibane and Collins, 2000; Yu, 2005; Boulbibane and Ponter, 2006; Krabbenhøft et al., 2007) adopted the Hertz load distribution for shakedown analysis of pavements. If the load moves along the x-direction, the core task of shakedown analysis of pavements is to find the critical value P (for a given μ and material) below which the structures are under safe and stable condition.

4.3 Elastic stress fields

In order to implement shakedown analysis, the elastic stress fields are required to be solved.

4.3.1 2D Hertz elastic stress fields

The elastic stress fields of a half-space under a 2D Hertz load can be found in literatures and listed below (Johnson, 1985; Yu, 2006).

The stresses due to the normal load

If the compressive stresses are treated as negative, the elastic stresses due to the normal load P are given as follows:

$$
\begin{aligned}
\left(\sigma^e_{xx}\right)_p &= -\frac{2P}{\pi a^2}\left\{m\left(1+\frac{z^2+n^2}{m^2+n^2}\right)-2z\right\}, \\
\left(\sigma^e_{zz}\right)_p &= -\frac{2P}{\pi a^2}m\left(1-\frac{z^2+n^2}{m^2+n^2}\right), \\
\left(\sigma^e_{xz}\right)_p &= \frac{2P}{\pi a^2}n\frac{m^2-z^2}{m^2+n^2}.
\end{aligned}
\qquad (4.4)
$$

The stresses due to the shear load

The elastic stresses due to the tangential shear force Q are given below:

$$\begin{aligned}
&\left(\sigma_{xx}^{e}\right)_{q}=\frac{2Q}{\pi a^{2}}\left\{n\left(2-\frac{z^{2}-m^{2}}{m^{2}+n^{2}}\right)-2x\right\},\\
&\frac{\left(\sigma_{zz}^{e}\right)_{q}}{Q}=\frac{\left(\sigma_{xz}^{e}\right)_{p}}{P},\\
&\frac{\left(\sigma_{xz}^{e}\right)_{q}}{Q}=\frac{\left(\sigma_{xx}^{e}\right)_{p}}{P},
\end{aligned}\tag{4.5}$$

with

$$m^{2}=\frac{1}{2}\left\{\sqrt{\left(a^{2}-x^{2}+z^{2}\right)^{2}+4x^{2}z^{2}}+\left(a^{2}-x^{2}+z^{2}\right)\right\},$$

$$n^{2}=\frac{1}{2}\left\{\sqrt{\left(a^{2}-x^{2}+z^{2}\right)^{2}+4x^{2}z^{2}}-\left(a^{2}-x^{2}+z^{2}\right)\right\},$$

in which the signs of m and n are the same as the signs of z and x respectively.

Total stresses due to the combination of normal and shear loads

It is normally assumed (Johnson, 1985) that the interaction effect between the normal pressure and surface traction can be neglected and therefore the stresses due to the normal pressure and the surface traction are independent to each other. Then, the total elastic stresses at any point (x, z) in the half-space are the sum of the solutions of normal loads and shear loads:

$$\sigma_{ij}^{e}=(\sigma_{ij}^{e})_{p}+(\sigma_{ij}^{e})_{q}.\tag{4.6}$$

4.3.2 3D Hertz elastic stress field

The analytical solutions for elastic stresses at any point (*x*, *y*, *z*) in the half-space, under the 3D Hertz load, defined in Equation (4.3), was given by Hamilton (1983).

The stresses due to the normal load

The elastic stresses due to the normal load *P* are given as follows:

$$\begin{aligned}
\left(\sigma^e_{xx}\right)_p &= \frac{3P}{2\pi a^3}\Bigg[(1+\upsilon)z\varphi+\frac{1}{r^2}\Bigg\{-N\left(x^2+2\upsilon y^2\right)-\frac{Mx^2za}{S} \\
&\quad +\frac{y^2-x^2}{r^2}\bigg[(1-\upsilon)Nz^2-\frac{1-2\upsilon}{3}\left(NS+2AN+a^3\right)-\upsilon Mza\bigg]\Bigg\}\Bigg], \\
\left(\sigma^e_{zz}\right)_p &= \frac{3P}{2\pi a^3}\left[-N+\frac{azM}{S}\right], \\
\left(\sigma^e_{xz}\right)_p &= \frac{3P}{2\pi a^3}\left[-z\left(\frac{xN}{S}-\frac{xzM}{G^2+H^2}\right)\right].
\end{aligned} \tag{4.7}$$

The stresses due to the shear load

The elastic stresses due to the tangential shear force *Q* are given below:

$$\begin{aligned}
(\sigma^e_{xx})_q &= \frac{3Q}{2\pi a^3}\Bigg[\frac{axM}{r^4}\Bigg\{\left(\frac{3}{2}-\frac{2x^2}{r^2}\right)\left(S\upsilon-2A\upsilon+z^2\right)+\frac{x^2z^2}{S}+\frac{7\upsilon r^2}{4}-2\upsilon x^2+r^2\Bigg\} \\
&\quad +\frac{xzN}{r^4}\Bigg\{\left(\frac{3}{2}-\frac{2x^2}{r^2}\right)\left[-\frac{S}{6}(1-2\upsilon)-\frac{A}{3}(1-2\upsilon)-\frac{1}{2}\left(z^2+3a^2\right)\right] \\
&\quad +\frac{a^2x^2}{S}-\frac{\upsilon r^2}{4}-\frac{7r^2}{4}\Bigg\}-x\left(\frac{\upsilon}{4}+1\right)\varphi+\frac{4a^3xz}{3r^4}\left(\frac{3}{2}-\frac{2x^2}{r^2}\right)(1-2\upsilon)\Bigg], \\
(\sigma^e_{zz})_q &= \frac{3Q}{2\pi a^3}\left[\frac{xzN}{2r^2}\left(1-\frac{r^2+z^2+a^2}{S}\right)\right], \\
(\sigma^e_{xz})_q &= \frac{3Q}{2\pi a^3}\Bigg[\frac{3z\varphi}{2}+\frac{azM}{r^2}\left\{1+\frac{x^2}{r^2}-\frac{x^2}{S}\right\} \\
&\quad +\frac{N}{r^2}\left\{-\frac{3}{4}(S+2A)+z^2-\frac{3}{4}a^2-\frac{1}{4}r^2+\frac{z^2}{2}\left(\frac{1}{2}-\frac{2x^2}{r^2}\right)\right\}\Bigg],
\end{aligned} \tag{4.8}$$

where

υ is Poisson's ratio,

$A = r^2 + z^2 - a^2$,

$S = \left(A^2 + 4a^2z^2\right)^{1/2}$,

$r^2 = x^2 + y^2$,

$M = \left(\frac{S+A}{2}\right)^{1/2}$,

$N = \left(\frac{S-A}{2}\right)^{1/2}$,

$\varphi = \tan^{-1}\left(\frac{a}{M}\right)$,

$G = M^2 - N^2 + zM - aN$,

$H = 2MN + aM + zN$.

Similarly, the total elastic stresses at any point (x, y, z) in the 3D half-space has the same expression of Equation (4.6).

4.4 Static shakedown solutions

According to Melan's lower-bound shakedown theorem, the self-equilibrated residual stresses, when combined with the elastic stresses produced by the applied loads, have to lie within the yield criterion. Hence, the establishment of residual stress field is essential for the determination of shakedown limit.

4.4.1 Residual stress fields

Residual stress is such that can remain in the half-space after the load applications as a result of plastic deformation.

2D pavement model

For the problem considered here that the plane strain half-space retains a flat surface after a number of load passes, every cross-section perpendicular to the travel direction experienced the same load history and therefore the residual stress fields are only dependent on the depth z. When the equilibrium and boundary conditions are applied, it is not difficult to find that the normal residual stress σ_{zz}^r and the shear residual stress σ_{xz}^r cannot exist. As a result, the existing residual stresses in the 2D half-space are only σ_{xx}^r and σ_{yy}^r, as functions of depth z. This has also been numerically verified by the FE analyses described in the last chapter.

3D pavement model

The residual stresses in a 3D pavement model are much more complicated than those in the plane strain pavement model, because all the six components of the residual stresses may exist at a general point. For the problem considered here that the material is assumed to be isotropic and homogenous, the residual stress fields must be independent of the travel (x) direction (Johnson, 1985; Kapoor and Johnson, 1992; Boulbibane and Collins, 2000). However, as mentioned by

Boulbibane and Collins (2000), the optimisation problem of the 3D pavement model is still extremely large.

Yu (2005) assumed that the most critical plane for a half-space under a 3D moving Hertz load is one of the *x*-*z* planes (*y* = const). On these planes, the self-equilibrium and boundary conditions eliminate the possibility of σ^r_{zz}, and σ^r_{xz}. It follows that the only non-zero residual stress on these planes that may affect the shakedown limit is the normal residual stress in the travel direction σ^r_{xx}, as a function of *y* and *z*. In the *y*-direction, the residual stress σ^r_{yy} may well exist, as a function of *z*. These residual stress fields have been proved valid by the numerical studies of Shiau (2001), in which the FE meshed and mathematical programming approach were used to search for the optimum residual stress fields.

4.4.2 An analytical shakedown solution

The total stresses for a general point in the half-space can be defined as the sum of the elastic stresses and residual stresses. If the total applied load is denoted by λp_0 (λ is a dimensionless scale parameter, p_0 is conveniently set as unit pressure), then all the induced elastic stresses are also proportional to λ. On the *x*-*z* plane in the 2D pavement model and any *y* = const plane in the 3D pavement model, the total stresses can be expressed as follows:

$$\begin{aligned} \sigma_{xx} &= \lambda\sigma^e_{xx} + \sigma^r_{xx} \\ \sigma_{zz} &= \lambda\sigma^e_{zz} \\ \sigma_{xz} &= \lambda\sigma^e_{xz} \end{aligned} \tag{4.9}$$

Assuming the soil material obeys the Mohr Coulomb yield criterion, Melan's lower-bound shakedown theorem then requires that the total stress state of any point in the half-space has to lie within the Mohr Coulomb failure surface. Since σ_{yy}^r can be chosen such that σ_{yy} is an intermediate principle stress, the above requirement leads to the following expression:

$$f=\left[\left(\lambda\sigma_{xx}^e+\sigma_{xx}^r-\lambda\sigma_{zz}^e\right)^2+4\left(\lambda\sigma_{xz}^e\right)^2\right]^{1/2}+\left(\lambda\sigma_{xx}^e+\sigma_{xx}^r+\lambda\sigma_{zz}^e\right)\sin\phi-2c\cos\phi\leq 0, \quad (4.10)$$

where c is the soil cohesion and ϕ is the friction angle.

The above expression can be rewritten as:

$$f=\left(\sigma_{xx}^r+\mathrm{M}\right)^2+\mathrm{N}\leq 0, \quad (4.11)$$

with

$$\mathrm{M}=\lambda\sigma_{xx}^e-\lambda\sigma_{zz}^e+2\tan\phi\left(c-\lambda\sigma_{zz}^e\tan\phi\right),$$

$$\mathrm{N}=4\left(1+\tan^2\phi\right)\left[\left(\lambda\sigma_{xz}^e\right)^2-\left(c-\lambda\sigma_{zz}^e\tan\phi\right)^2\right].$$

In order to satisfy this requirement, one condition must be met:

$$\mathrm{N}\leq 0\Rightarrow\lambda\leq\frac{c}{\left|\sigma_{xz}^e\right|+\sigma_{zz}^e\tan\phi}. \quad (4.12)$$

By searching for the maximum value of $\left|\sigma_{xz}^e\right|+\sigma_{zz}^e\tan\phi$ through the whole half-space, the condition (4.12) can provide an analytical shakedown limit λ_{sd}. Yu (2005) derived an alternative form of expression (4.11) and obtained the same shakedown condition (4.12). For the 3D pavement problem, because the elastic stresses are symmetric along the central plane ($y = 0$), Yu (2005) searched for the most critical plane under $y \geq 0$ and it was found that the most critical plane was always the central plane $y = 0$. As a result, in the following investigations for the 3D pavement problems, the most critical plane $y = 0$ is focused on.

4.4.3 Critical residual stress fields

The shakedown condition (4.12) is based on the assumption that the first term of Equation (4.11) is zero, and therefore it gives a maximum boundary to the exact lower-bound shakedown limit. Moreover, the residual stress field calculated from λ_{sd} may not fulfil the equilibrium condition. It is instructive to find a possible residual stress field that satisfies both Equation (4.11) and the condition of equilibrium.

According to Equation (4.11), the residual stress σ_{xx}^r at any point i in the half-space must be between two roots of $f = 0$: $-\mathrm{M}_i - \sqrt{-\mathrm{N}_i}$ (smaller root) and $-\mathrm{M}_i + \sqrt{-\mathrm{N}_i}$ (larger root) in which N_i is always negative once the necessary shakedown condition (4.12) is satisfied. For the system to be independent of the travel direction x, the possible residual stress σ_{xx}^r at any depth z is unique and has to lie between two critical residual stresses: $\max\limits_{x}\left(-\mathrm{M}_i - \sqrt{-\mathrm{N}_i}\right)$ (referred to as 'maximum smaller root') and $\min\limits_{x}\left(-\mathrm{M}_i + \sqrt{-\mathrm{N}_i}\right)$ (referred to as 'minimum larger root'), as shown in Equation (4.13) and Figure 4.3. Both critical residual stresses are dependent on the elastic stresses, material properties and load parameter λ. It should be noted that if the maximum smaller root is larger than the minimum larger root, it will be impossible to find a common residual stress that makes $f \leq 0$ at all points at the same depth. In this case, the half-space is in a non-shakedown status; hence smaller load parameter λ is required.

$$\max_x\left(-M_i - \sqrt{-N_i}\right) \leq \sigma^r_{xx} \leq \min_x\left(-M_i + \sqrt{-N_i}\right). \tag{4.13}$$

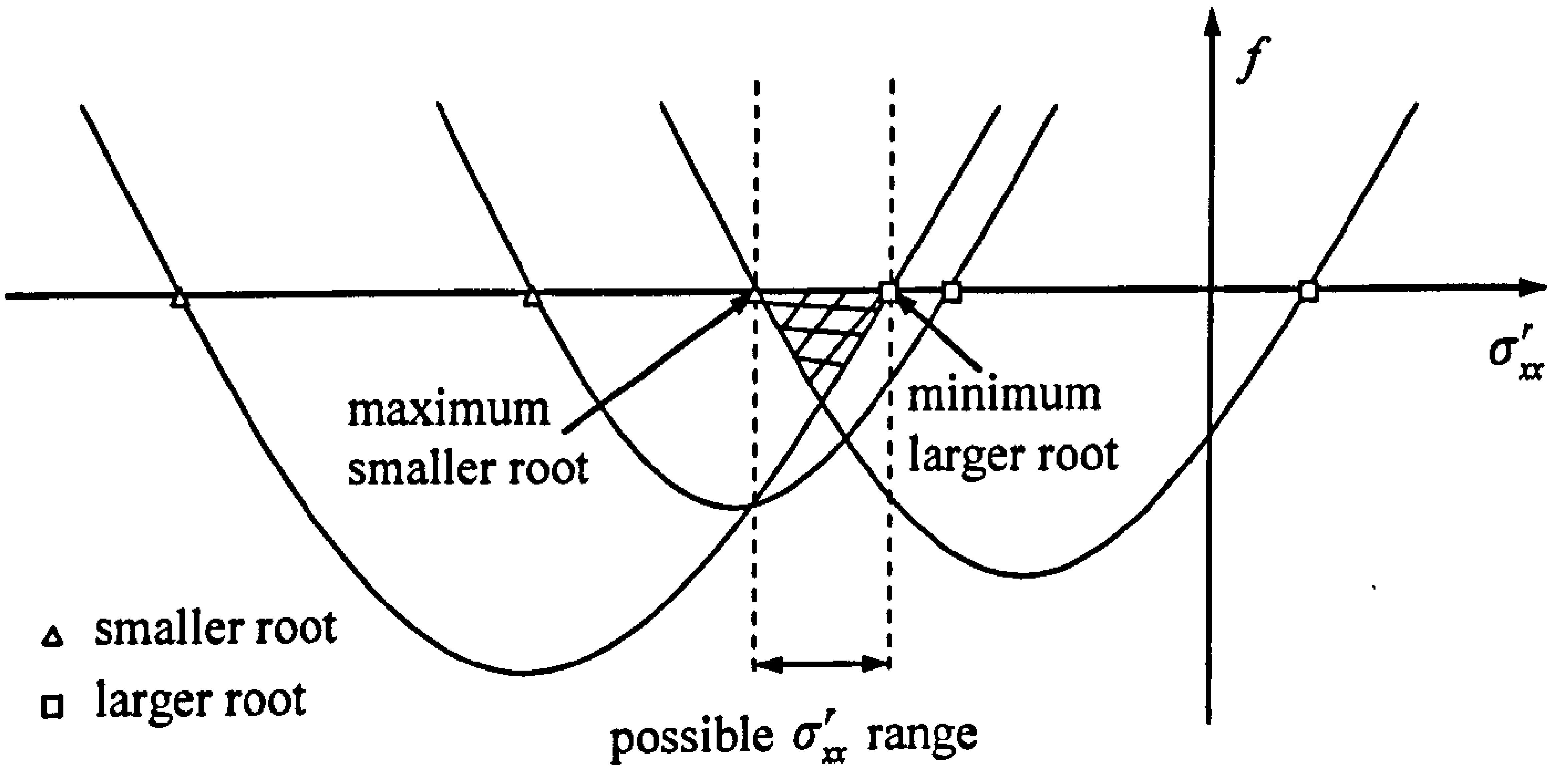

Figure 4.3. Possible residual stress range

At a given load parameter, two critical residual stress fields can be obtained by calculating the maximum smaller root and the minimum larger root at each depth independently. For the load parameter at or within the shakedown limit, these critical residual stress fields actually constitute a region which contains the real residual stress field. For the load parameter in excess of the shakedown limit, there will always be some points providing $f > 0$ at the critical residual stresses.

4.4.4 A rigorous lower-bound shakedown solution

Based on the condition of the critical residual stresses, a procedure of searching for the best lower-bound shakedown limit of pavements under repeated moving surface loads is developed as outlined in Figure 4.4.

First, using the load parameter λ_{sd} obtained from the necessary shakedown condition (4.12), possible residual stresses $-\mathrm{M}_i + \sqrt{-\mathrm{N}_i}$ and $-\mathrm{M}_i - \sqrt{-\mathrm{N}_i}$ are calculated for every point in the whole half-space. Then, a critical residual stress field is obtained by calculating either the minimum larger root or the maximum smaller root at each depth. This step reduces the residual stress field as function of depth z. Shakedown condition under this load parameter can be checked by substituting λ_{sd} and the critical residual stress field into Equation (4.11). If the maximum value of f among all points is found to be very close to 0 (said 1e-3 here), the present lower-bound shakedown solution $\lambda_{sd}^{'}$ coincides with the analytical shakedown solution λ_{sd}. Otherwise, if $\max(f)$ is larger than 1e-3, a smaller load parameter is required. In the latter case, the problem becomes how to determine the maximum permissible load parameter $\lambda_{sd}^{'}$ at which the sum of corresponding elastic stresses and critical residual stresses fulfils the Mohr Coulomb yield condition at every location in the half-space.

Noticing that the load parameters have to lie between λ_{sd} and 0, a method of bisection is utilised to find the optimum shakedown limit efficiently. The method of bisection takes a load parameter $\lambda_3 = (\lambda_1 + \lambda_2)/2$ in which the initialised λ_1 is 0 and the initialised λ_2 is λ_{sd}, then recalculates the critical residual stress field, followed by the search for the maximum value of *f*. Here, a condition $1e-4 \le \max(f) \le 1e-3$ is checked in consideration of a total stress state that just violates the yield condition. If $\max(f)$ is larger than 1e-3, the current load parameter is too large, λ_2 is updated by λ_3; else if $\max(f)$ is smaller than 1e-4, λ_1 is updated by λ_3. The above procedure is repeated until the condition $1e-4 \le \max(f) \le 1e-3$ is satisfied. The final load parameter λ_3 is the exact lower-bound shakedown limit $\lambda_{sd}^{'}$, and the point providing the maximum value of f is the critical point.

In addition, it is expected that the residual stress itself satisfies the yield condition inherently (i.e. $f(\sigma_{xx}^{r}) \le 0$) once the chosen boundary is large enough. This can be checked by using Equation (4.14) which is obtained by substituting the horizontal residual stress only into the Equation (4.11). As it can be seen, the obtained critical residual stresses have to lie between two residual stress limits which are only dependent on the soil cohesion c and angle of friction ϕ.

$$\frac{2c\cos\phi}{\sin\phi-1} \le \sigma_{xx}^{r} \le \frac{2c\cos\phi}{\sin\phi+1}. \tag{4.14}$$

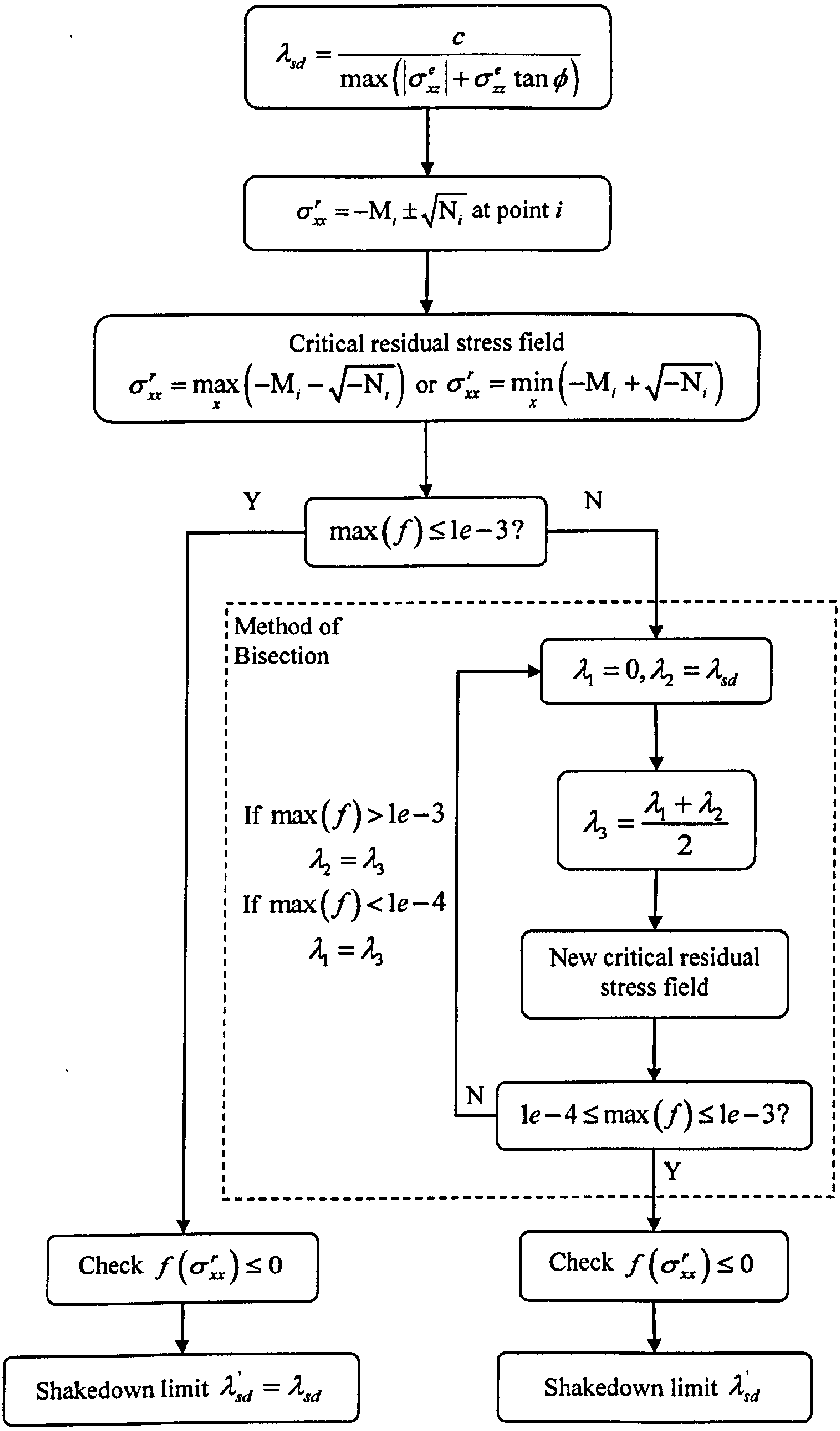

Figure 4.4. Flow chart of the lower-bound shakedown solution

The above procedure as well as the elastic stress solutions for the Hertz load was programmed in FORTRAN. The minimum larger root and the maximum smaller root were utilised independently, and the same shakedown limits were obtained. It was found in the numerical applications that a very small change of the load parameter λ_3 (said 1e-3) around the lower-bound shakedown limit $\lambda_{sd}^{'}$ results in a significant change of $\max(f)$, from 1e-7 to 1e-3 and therefore the above condition $1e-4 \le \max(f) \le 1e-3$ can provide an accurate shakedown limit.

The method of bisection was also checked by using an alternative method that reduces the load parameter gradually from the analytical shakedown limit λ_{sd} until a condition $\max(f) \le 1e-7$ is satisfied. Both methods gave the same shakedown limits and the latter one was much more time-consuming if the decrease increment was very small.

4.5 Shakedown limits of pavements

The shakedown load limits of pavements may be represented by normalised shakedown limits: $k_{\max} = \lambda_{sd} p_0 / c$ for the analytical shakedown limit and $k_{\max}^{'} = \lambda_{sd}^{'} p_0 / c$ for the rigorous lower-bound shakedown limit (p_0 is the maximum compressive pressure). The normalised shakedown limits are dependent on the soil friction angle ϕ and surface frictional coefficient μ. In Subsections 4.5.1 and 4.5.2, Poisson's ratio is taken as 0.3. The effect of Poisson's ratio on the shakedown limit will be investigated in Subsection 4.5.3.

4.5.1 Effect of frictional coefficient and soil friction angle

2D shakedown limits

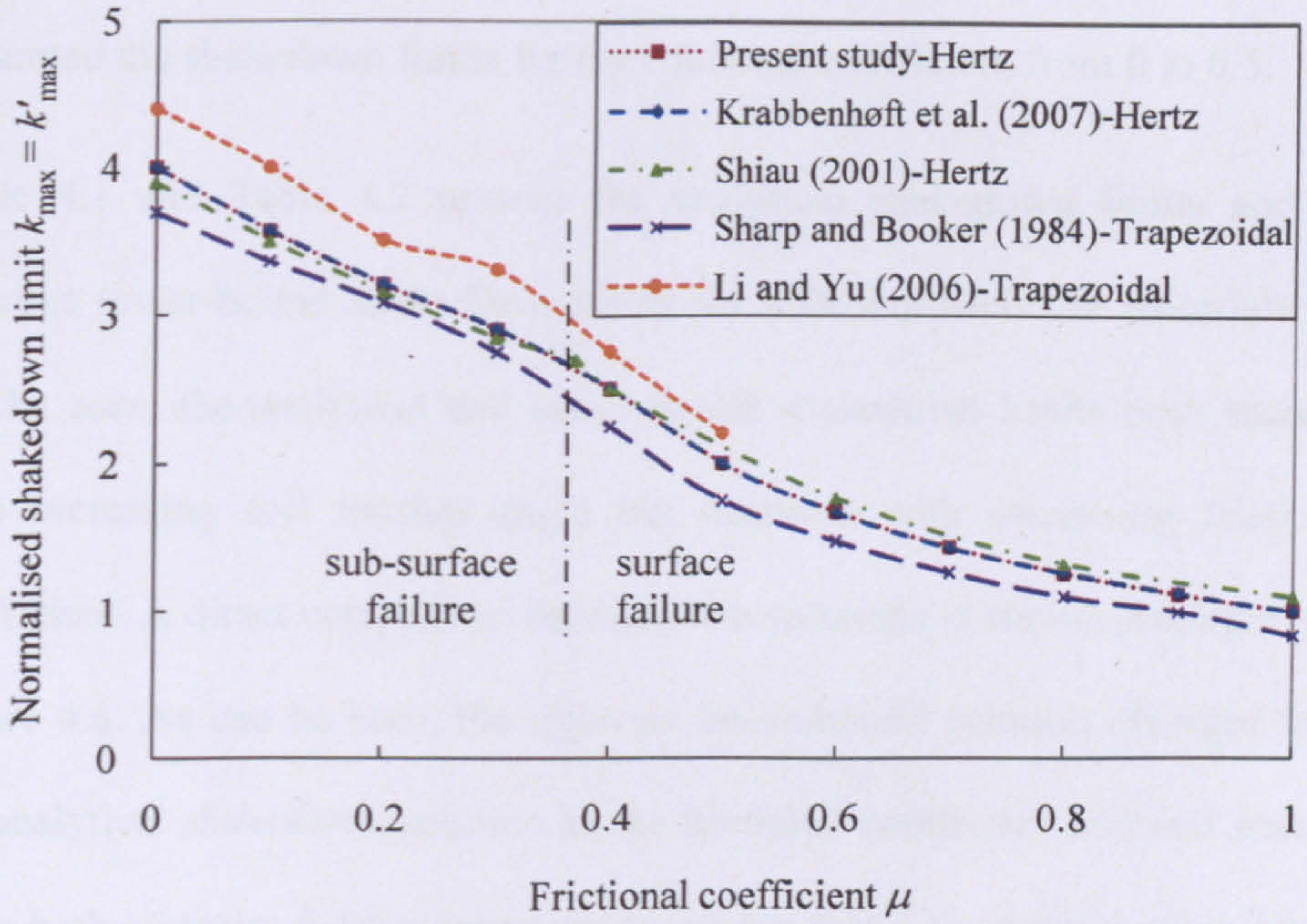

Figure 4.5. 2D shakedown limits versus frictional coefficients for cohesive materials

Figure 4.5 demonstrates the variation of 2D shakedown limit with the frictional coefficients μ for cohesive materials. Here, the analytical shakedown limits are the same as the rigorous lower-bound shakedown limits. The normalised shakedown limit decreases markedly with increasing frictional coefficient. Further investigation shows that the critical point moves towards the surface with the rise of frictional coefficient. When $0.3 < \mu < 0.4$, the failure mode changes from subsurface failure (i.e. critical point lies below the surface) to surface failure (i.e. critical point lies on the surface). The present 2D shakedown solutions are in agreement with the static shakedown solutions of Shiau (2001) and Krabbenhøft et al. (2007) in which the Hertz load distributions were adopted. Moreover, the present results are between Sharp and Booker (1984)'s lower-bounds and Li and Yu (2006)'s upper-bounds in which the trapezoidal load distributions were applied. Li and Yu (2006) only presented the shakedown limits for the frictional coefficient from 0 to 0.5.

Table 4.1 and Table 4.2 present the analytical shakedown limits and the rigorous lower-bound shakedown limits for cohesive-frictional materials. As can be seen, the analytical and lower-bound shakedown limits both increase with increasing soil friction angle but decrease with increasing frictional coefficient. A direct comparison between two solutions is shown graphically in Figure 4.6. As can be seen, the rigorous lower-bound solution diverges from the analytical shakedown solution as the frictional coefficient and soil friction angle both increase. Further investigation shows that if the critical point lies on the surface of the pavement, the lower-bound shakedown limit is lower than the analytical shakedown limit; otherwise, both solutions are identical. In addition, the present lower-bound shakedown limits agree well with those in Krabbenhøft et al. (2007), and the present analytical shakedown solution are identical to the upper-bound solution obtained by Collins and Cliffe (1987) which considered a sliding mechanism with 'V' cross section.

When the normalised lower-bound shakedown limit $k'_{\max} = \lambda'_{sd} p_0 / c$ is multiplied by the corresponding frictional coefficient, shakedown limit in terms of surface traction $\lambda'_{sd} q_0 / c$ is obtained, as shown in Figure 4.7. It is interesting to notice that $\lambda'_{sd} q_0 / c$ barely changes with increasing frictional coefficient once the critical point lies on the surface of the pavement. This implies the 2D lower-bound shakedown limit is not affected by the normal pressure when surface failure occurs.

Table 4.1. 2D analytical shakedown limit $k_{\max} = \lambda_{sd} p_0 / c$

(Note: Underlined shakedown limits correspond to surface failure.)

μ	ϕ= 0°	5°	10°	15°	20°	25°	30°	35°	40°	45°
0.0	4.00	4.66	5.45	6.40	7.56	9.00	10.82	13.16	16.25	20.39
0.1	3.56	4.11	4.76	5.53	6.46	7.59	8.98	10.72	12.95	15.86
0.2	3.20	3.67	4.21	4.85	5.61	6.52	7.63	9.00	10.70	12.88
0.3	2.90	3.30	3.77	4.31	4.95	5.70	6.61	7.71	9.08	10.80
0.4	2.50	3.00	3.40	3.87	4.41	5.06	5.82	6.74	7.87	9.28
0.5	2.00	2.42	3.09	3.51	3.98	4.54	5.19	5.98	6.94	8.13
0.6	1.67	1.95	2.36	3.01	3.62	4.11	4.68	5.37	6.20	7.23
0.7	1.43	1.63	1.91	2.31	2.98	3.75	4.26	4.87	5.60	6.50
0.8	1.25	1.40	1.60	1.88	2.29	3.00	3.91	4.45	5.11	5.41
0.9	1.11	1.23	1.38	1.58	1.87	2.31	3.10	4.10	4.69	5.90
1.0	1.00	1.10	1.21	1.37	1.57	1.87	2.37	3.34	4.34	4.99

Table 4.2. 2D rigorous lower-bound shakedown limit $k'_{\max} = \lambda'_{sd} p_0 / c$

(Note: Underlined shakedown limits correspond to surface failure.)

μ	ϕ= 0°	5°	10°	15°	20°	25°	30°	35°	40°	45°
0.0	4.00	4.66	5.45	6.40	7.56	9.00	10.82	13.16	16.25	20.39
0.1	3.56	4.11	4.76	5.53	6.46	7.59	8.98	10.72	12.95	14.24
0.2	3.20	3.67	4.21	4.85	5.34	5.54	5.79	6.13	6.55	7.09
0.3	2.90	3.30	3.38	3.46	3.56	3.69	3.86	4.08	4.37	4.73
0.4	2.50	2.51	2.54	2.59	2.67	2.76	2.89	3.05	3.27	3.54
0.5	2.00	2.01	2.03	2.07	2.13	2.21	2.31	2.44	2.62	2.83
0.6	1.67	1.67	1.69	1.73	1.77	1.84	1.93	2.03	2.18	2.36
0.7	1.43	1.43	1.45	1.48	1.52	1.58	1.65	1.74	1.87	2.02
0.8	1.25	1.25	1.27	1.30	1.33	1.38	1.44	1.53	1.63	1.77
0.9	1.11	1.12	1.13	1.15	1.18	1.23	1.28	1.36	1.45	1.57
1.0	1.00	1.00	1.02	1.04	1.06	1.10	1.16	1.22	1.31	1.42

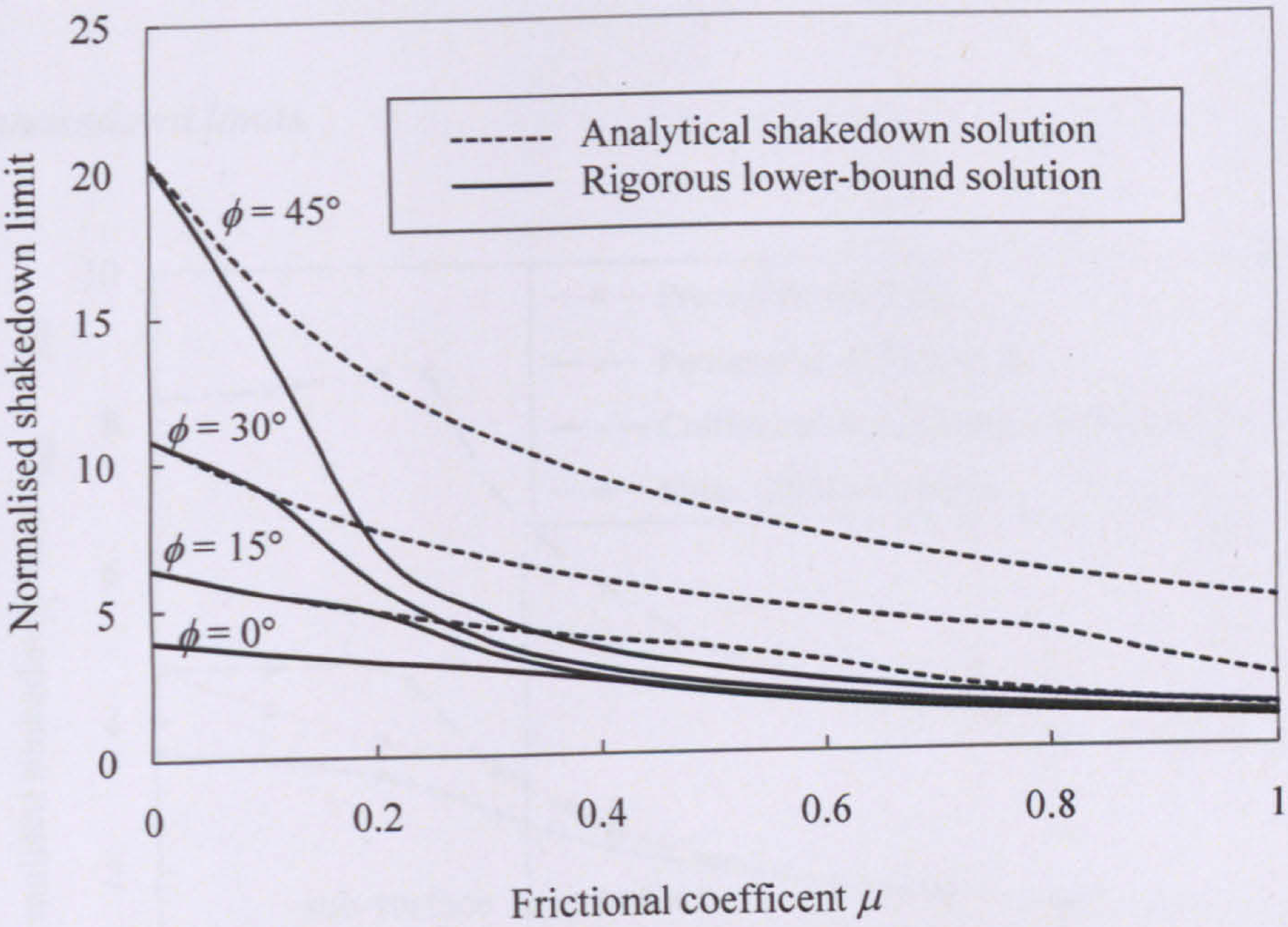

Figure 4.6. 2D shakedown limits versus frictional coefficients for various friction angles for cohesive-frictional materials

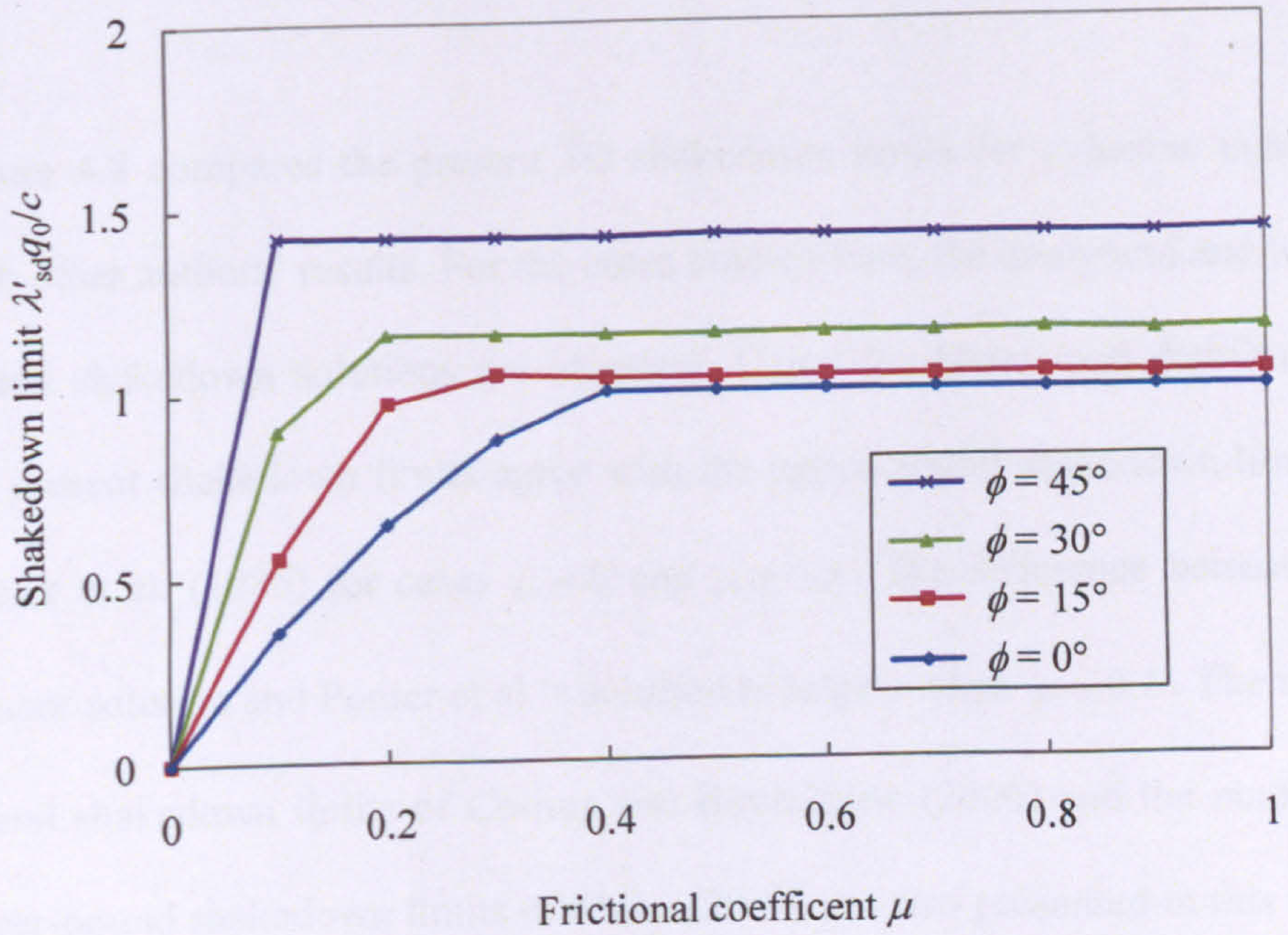

Figure 4.7. Effect of surface traction on the 2D lower-bound shakedown limit

3D shakedown limits

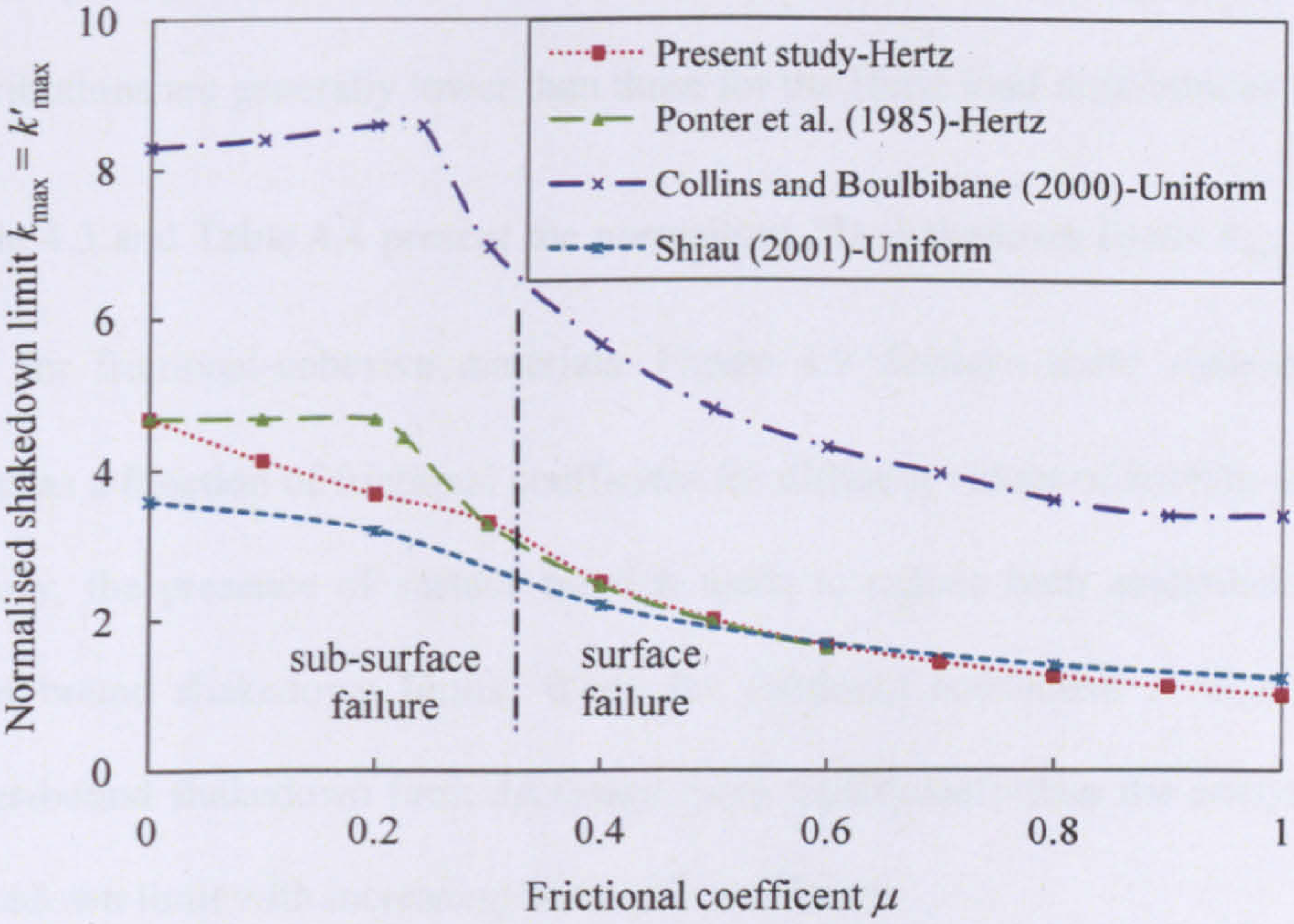

Figure 4.8. 3D shakedown limits versus frictional coefficients for cohesive materials

Figure 4.8 compares the present 3D shakedown limits for cohesive materials with other authors' results. For the cases studied here, the analytical and lower-bound shakedown solutions are identical. Using the Hertz load distributions, the present shakedown limits agree with the upper-bound shakedown limits of Ponter et al. (1985) for cases $\mu = 0$ and $\mu \geq 0.3$. The difference between the present solution and Ponter et al.'s solution is largest when $\mu = 0.2$. The upper-bound shakedown limits of Collins and Boulbibane (2000) and the numerical lower-bound shakedown limits of Shiau (2001) are also presented in this figure using the uniform load distributions. As can be seen, Collins and Boulbibane's upper-bounds are much higher than other solutions. This is because plane strain condition was assumed in the cross-section perpendicular to the travel direction and the deformations are not fully three-dimensional. The numerical results of Shiau (2001) indicate that the shakedown limits for the uniform load distributions are generally lower than those for the Hertz load distributions.

Table 4.3 and Table 4.4 present the normalised 3D shakedown limits $k_{\max}$ and $k'_{\max}$ for frictional-cohesive materials. Figure 4.9 displays these shakedown limits as a function of frictional coefficient for different values of friction angle. Clearly, the presence of surface traction tends to reduce both analytical and lower-bound shakedown limits. When the frictional coefficient is high, the lower-bound shakedown limit decreases more significantly than the analytical shakedown limit with increasing frictional coefficient.

Compared to the 2D pavement model, the 3D pavement model always provides higher shakedown limits. The difference between them is of the most significant in the case of normal load only and decreases with increasing frictional coefficient. In the case of normal loading only, the 3D pavement model has a critical point (0.86*a*, 0, 0.36*a*) providing a shakedown limit $k_{\max} = k'_{\max} = 4.68c$, while the 2D pavement model has a critical point (0.87*a*, 0.5*a*) and gives a shakedown limit $k_{\max} = k'_{\max} = 4.00c$.

Figure 4.10 shows the lower-bound shakedown limits in terms of the surface traction. At a specific value of friction angle, the value of $\lambda_{sd} q_0 / c$ ceases to increase when a limit is reached. It implies that the 3D lower-bound shakedown limit is independent of the normal pressure when surface failure occurs.

Table 4.3. 3D analytical shakedown limit $k_{\max} = \lambda_{sd} p_0 / c$

(Note: Underlined shakedown limits correspond to surface failure.)

μ	ϕ=0°	5°	10°	15°	20°	25°	30°	35°	40°	45°
0.0	4.68	5.52	6.53	7.75	9.25	11.12	13.48	16.51	20.50	25.89
0.1	4.13	4.83	5.65	6.63	7.80	9.23	11.01	13.21	16.04	19.70
0.2	3.68	4.27	4.96	5.77	6.73	7.87	9.24	10.96	13.09	15.79
0.3	3.32	3.83	4.41	5.09	5.89	6.83	7.96	9.34	11.02	13.14
0.4	2.50	3.21	3.96	4.55	5.23	6.03	6.97	8.12	9.51	11.23
0.5	2.00	2.43	3.10	4.11	4.70	5.39	6.20	7.17	8.36	9.81
0.6	1.67	1.96	2.37	3.03	4.26	4.87	5.58	6.42	7.44	8.69
0.7	1.43	1.64	1.92	2.33	2.99	4.31	5.06	5.81	6.71	7.80
0.8	1.25	1.41	1.61	1.89	2.30	3.01	4.53	5.30	6.10	7.07
0.9	1.11	1.23	1.38	1.59	1.87	2.32	3.14	4.88	5.60	6.47
1.0	1.00	1.10	1.22	1.37	1.58	1.88	2.39	3.36	5.17	5.97

Table 4.4. 3D rigorous lower-bound shakedown limit $k'_{\max} = \lambda'_{sd} p_0 / c$

(Note: Underlined shakedown limits correspond to surface failure.)

μ	ϕ=0°	5°	10°	15°	20°	25°	30°	35°	40°	45°
0.0	4.68	5.52	6.53	7.75	9.25	11.12	13.48	16.51	20.50	25.89
0.1	4.13	4.83	5.65	6.63	7.80	9.23	11.01	13.21	16.04	18.71
0.2	3.68	4.27	4.96	5.77	6.73	7.07	7.42	7.88	8.48	9.27
0.3	3.32	3.83	4.21	4.35	4.52	4.70	4.93	5.23	5.62	6.13
0.4	2.50	3.06	3.15	3.24	3.38	3.52	3.69	3.91	4.20	4.58
0.5	2.00	2.40	2.52	2.58	2.69	2.81	2.95	3.13	3.36	3.65
0.6	1.67	1.95	2.10	2.16	2.23	2.33	2.46	2.60	2.79	3.04
0.7	1.43	1.64	1.80	1.84	1.91	1.99	2.10	2.23	2.39	2.60
0.8	1.25	1.41	1.57	1.60	1.67	1.74	1.83	1.94	2.09	2.27
0.9	1.11	1.23	1.37	1.43	1.48	1.54	1.62	1.72	1.85	2.01
1.0	1.00	1.10	1.21	1.29	1.33	1.38	1.45	1.54	1.66	1.80

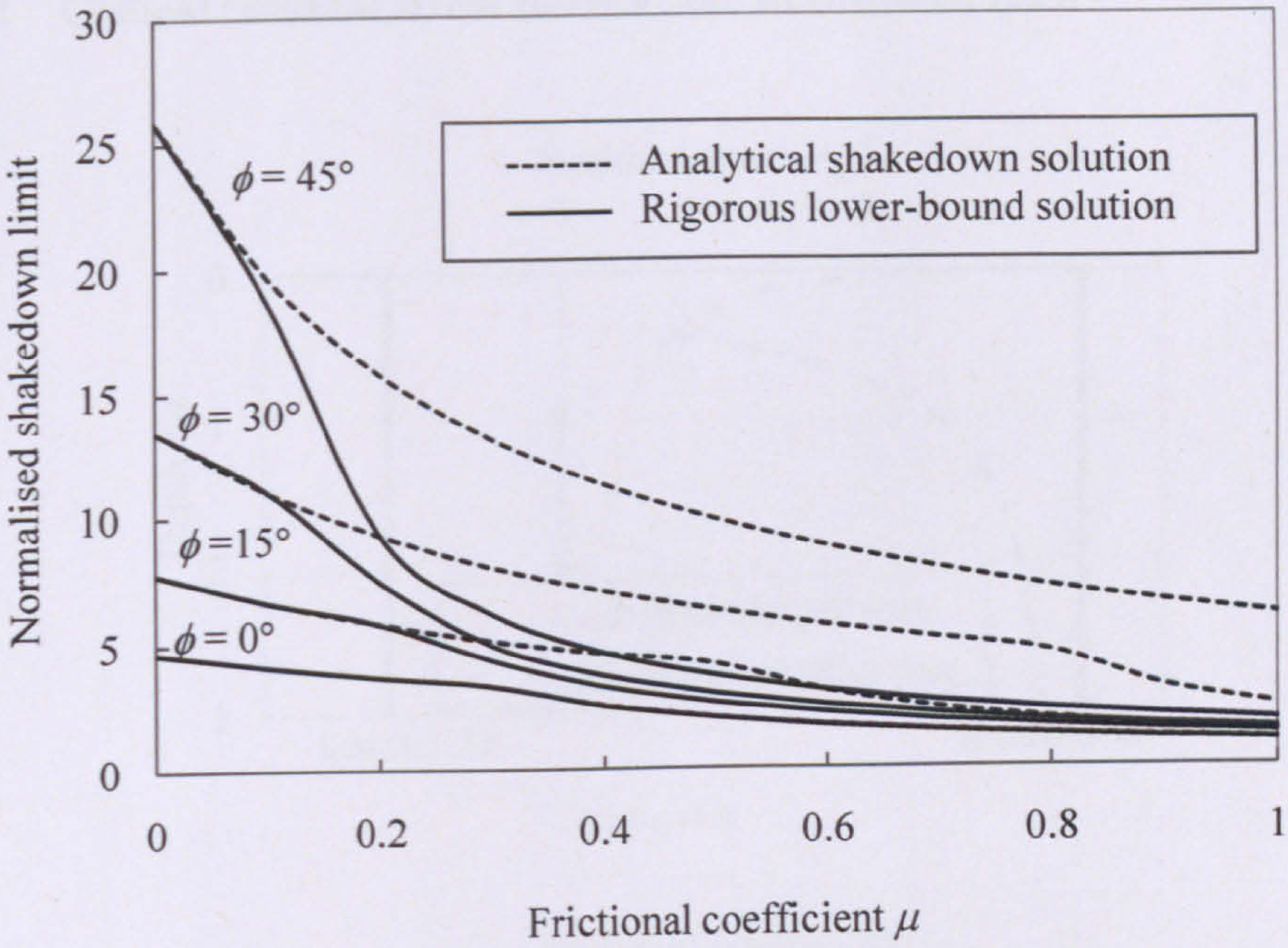

Figure 4.9. 3D shakedown limits versus frictional coefficients for various friction angles for cohesive-frictional materials

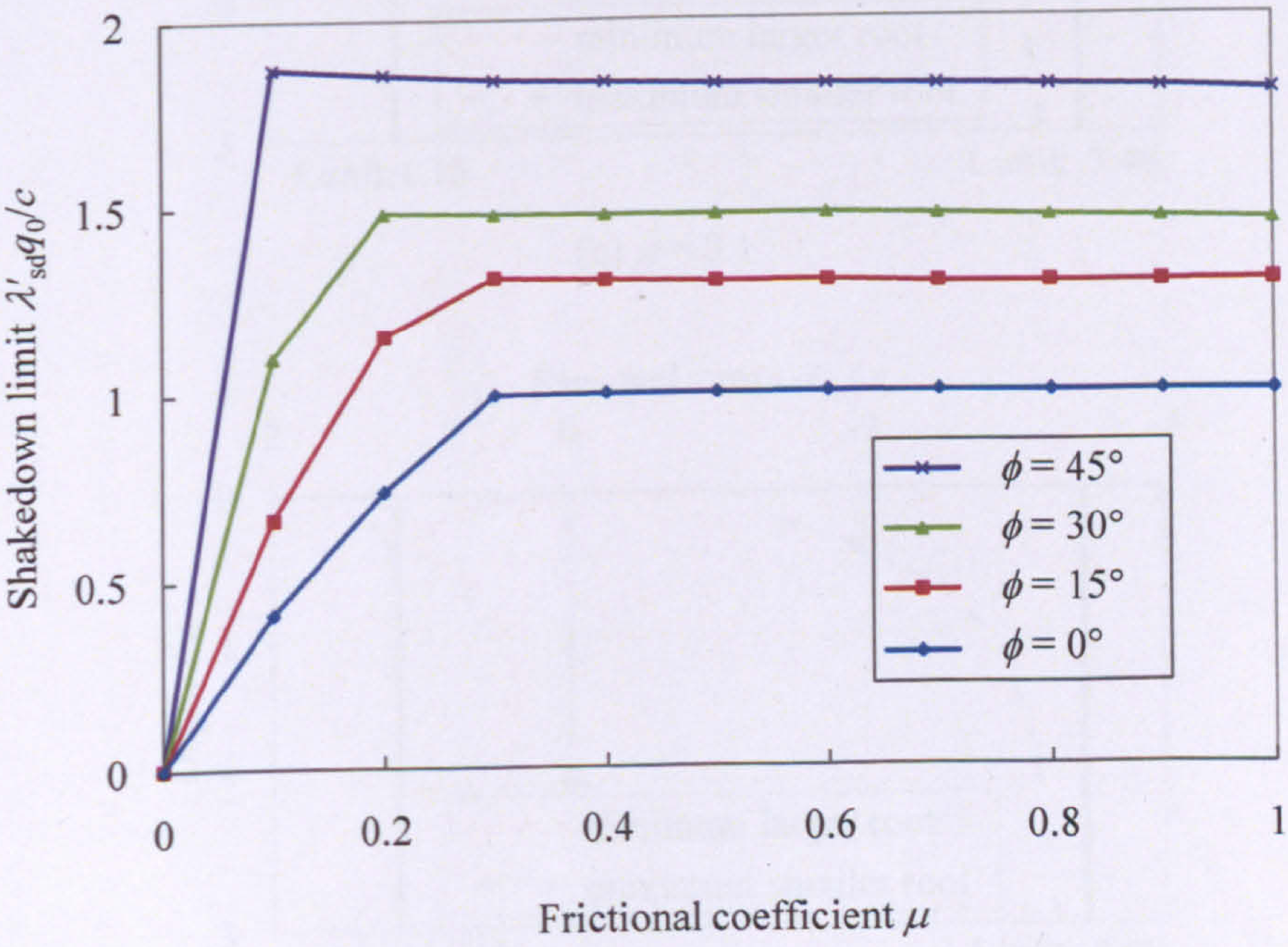

Figure 4.10. Effect of surface traction on the 3D lower-bound shakedown limit

4.5.2 Critical residual stress fields at the shakedown limit

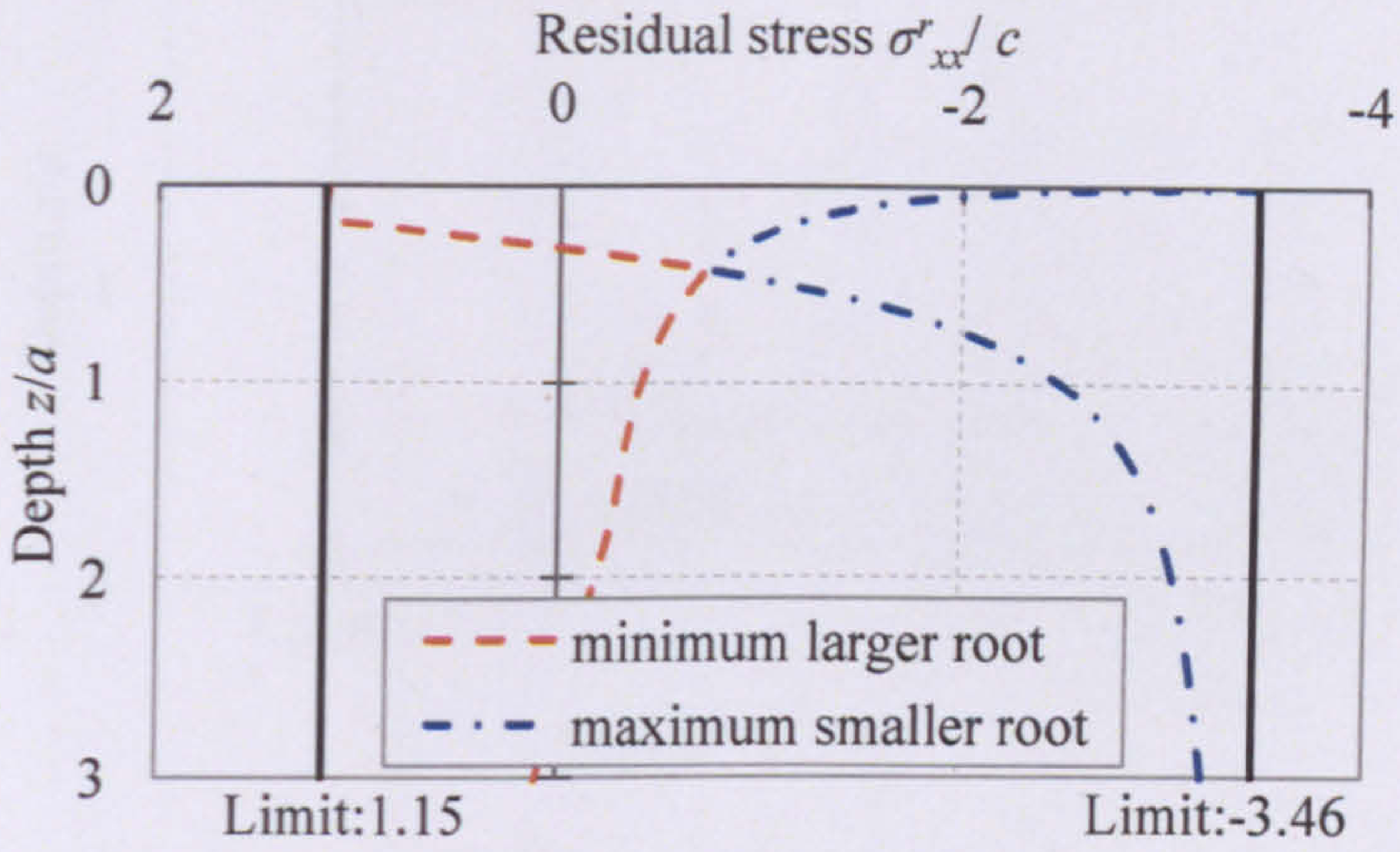

(a) $\mu = 0$

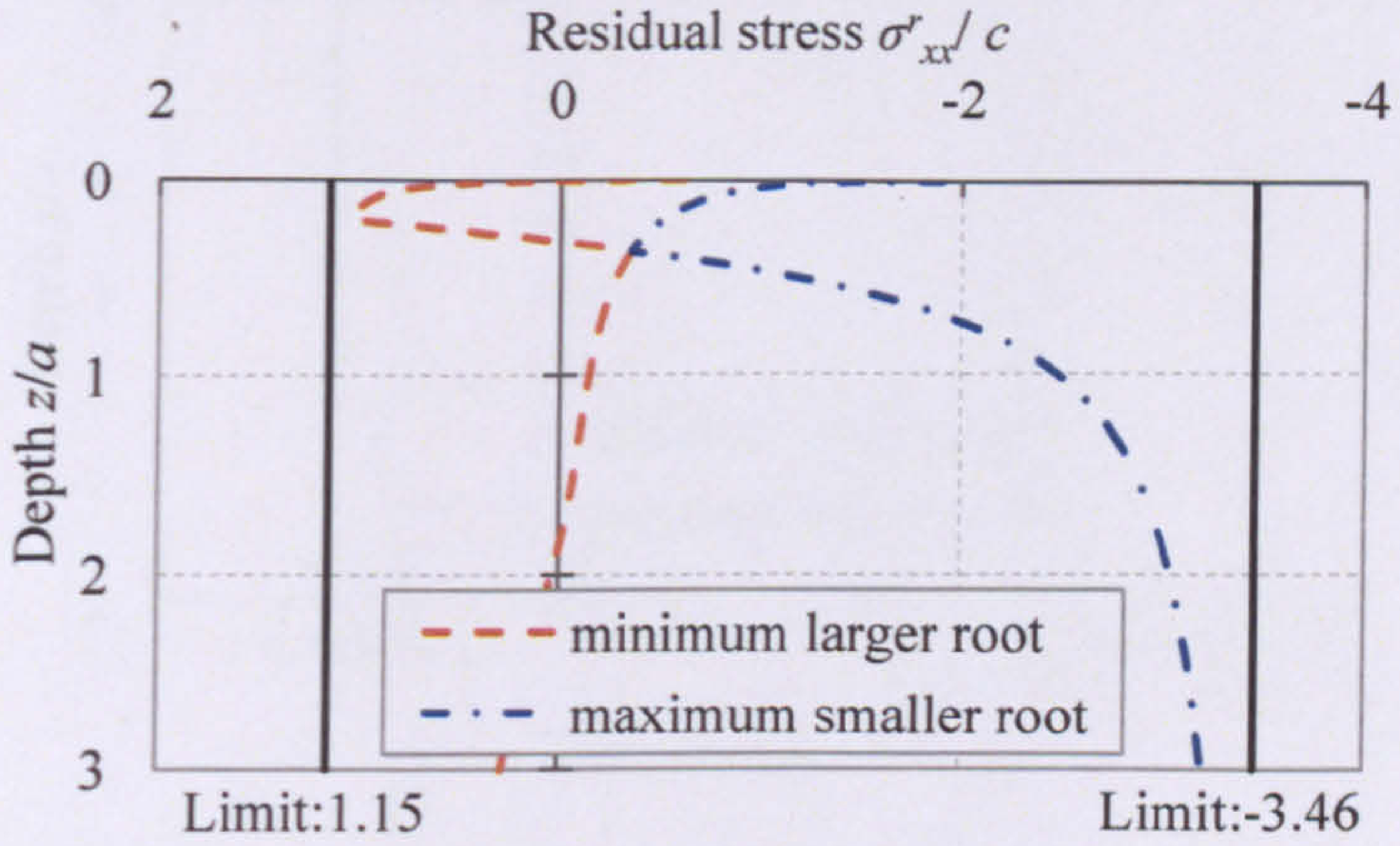

(b) $\mu = 0.1$

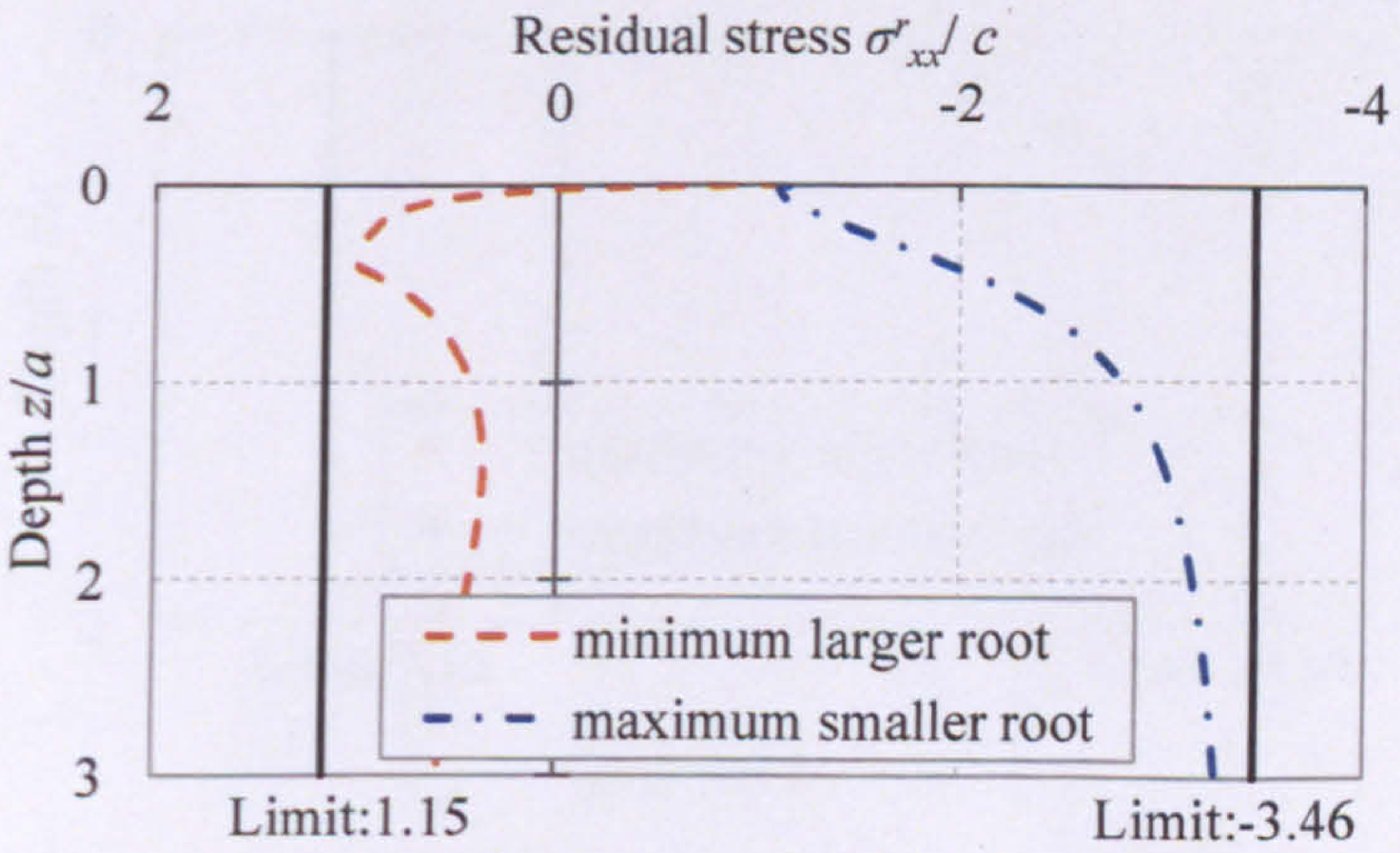

(c) $\mu = 0.2$

Figure 4.11. Critical residual stress fields in 2D pavement models when $\phi = 30°$

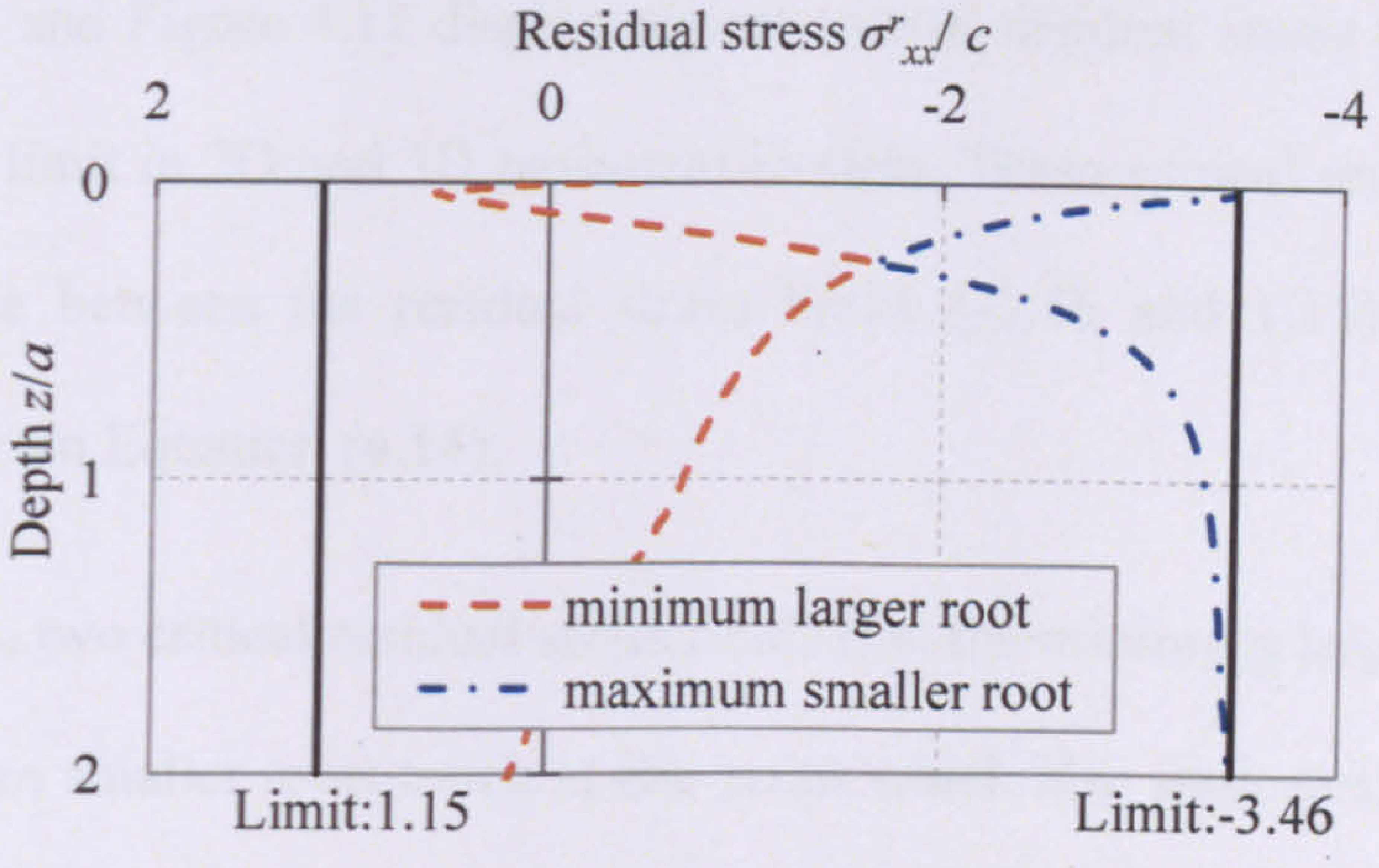

(a) $\mu = 0$

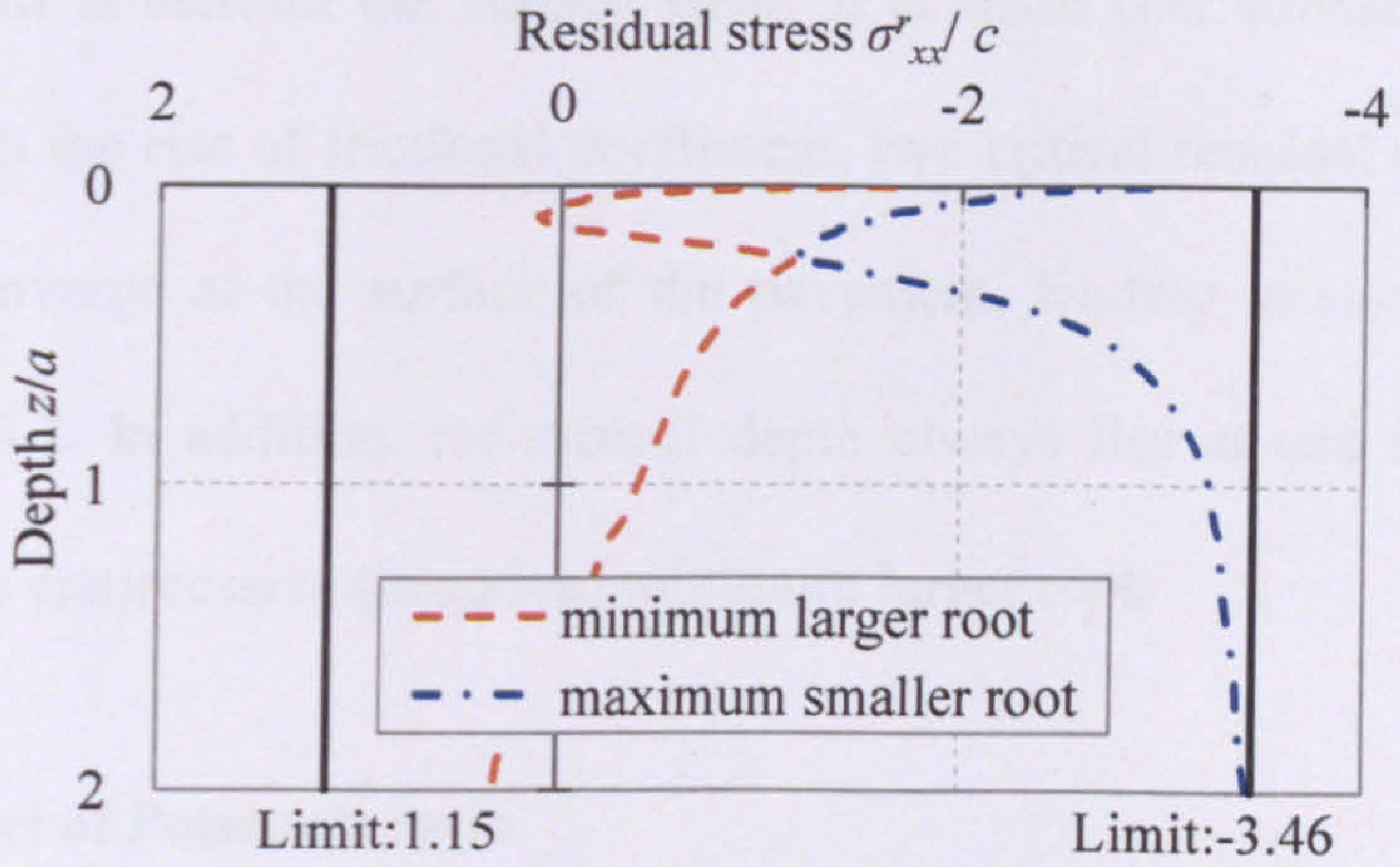

(b) $\mu = 0.1$

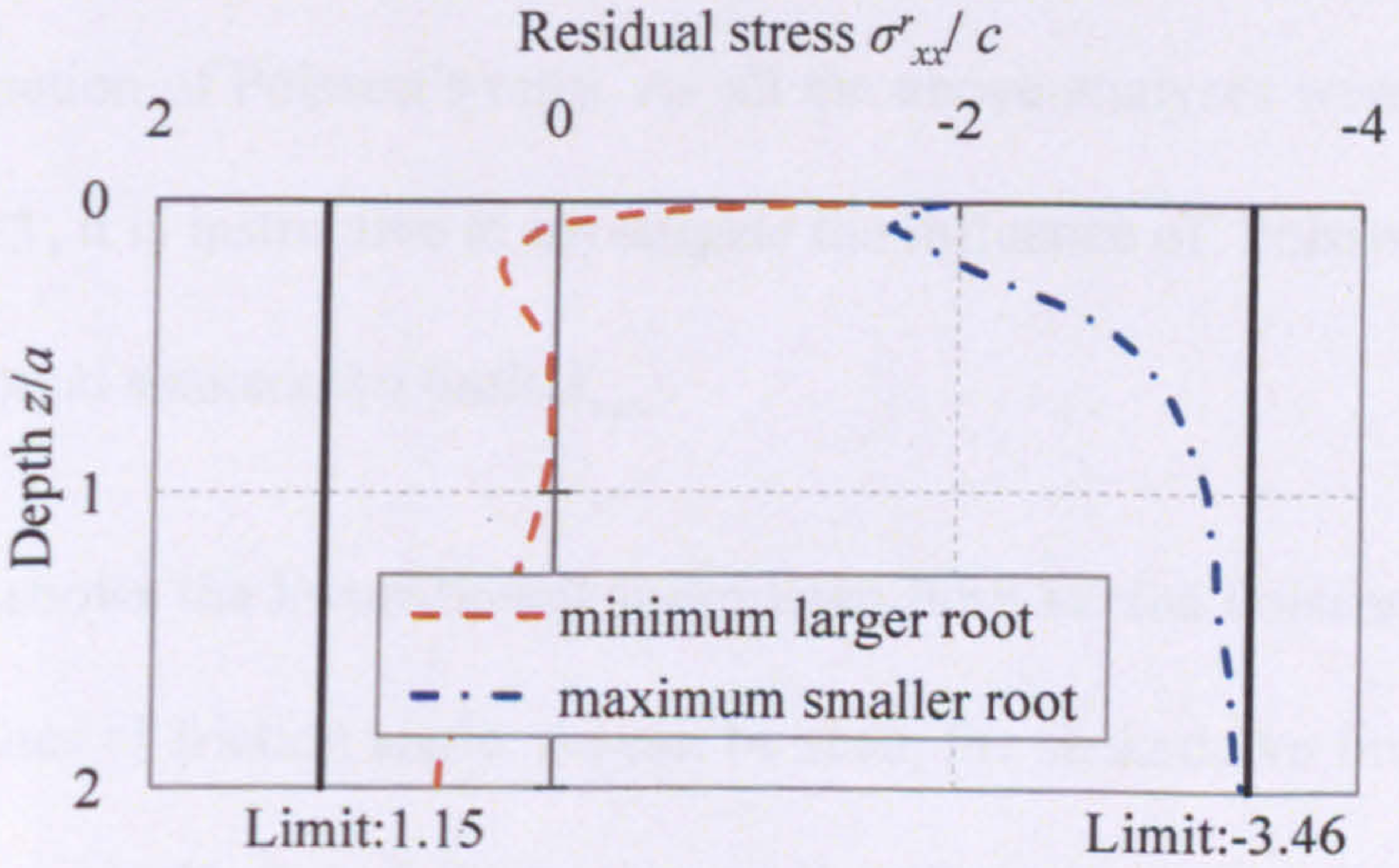

(c) $\mu = 0.2$

Figure 4.12. Critical residual stress fields in 3D pavement models when $\phi = 30°$

Figure 4.11 and Figure 4.12 display typical critical residual stress fields at the shakedown limit in 2D and 3D pavement models. These critical residual stress fields all lie between the residual stress limits (-3.46 and 1.15) which are calculated from Equation (4.14).

In each case, two critical residual stress fields (i.e. the minimum larger root and the maximum smaller root) touch at one point which also indicates the critical depth of the pavement (i.e. depth of the critical point). As can be seen, the critical depth is beneath the surface when μ is small (i.e. subsurface failure mode). With the rise of frictional coefficient, two critical residual stress fields tends to converge at the surface of the pavement, leading to surface failure when μ = 0.2. In addition, the critical depth always lies at one of the peak points of the compressive (negative) minimum larger root.

4.5.3 Effect of Poisson's ratio

Equations (4.7) - (4.8) show that the elastic stress field σ_{xx}^{e} due to the 3D Hertz load is a function of Poisson's ratio. As all the above analyses were conducted when $\upsilon = 0.3$, it is instructive to investigate the influence of Poisson's ratio on the lower-bound shakedown limit $k_{\max}^{'}$.

Figure 4.13 shows the lower-bound shakedown limit versus Poisson's ratio for different values of friction angle. As can be seen, the shakedown limit does not change when ϕ = 0°, but decreases proportionally with increasing Poisson's ratio when ϕ > 0°. It should be noted that when subsurface failure occurs, the lower-bound shakedown limit is not affected by Poisson's ratio ($k_{\max}^{'} = k_{\max}$).

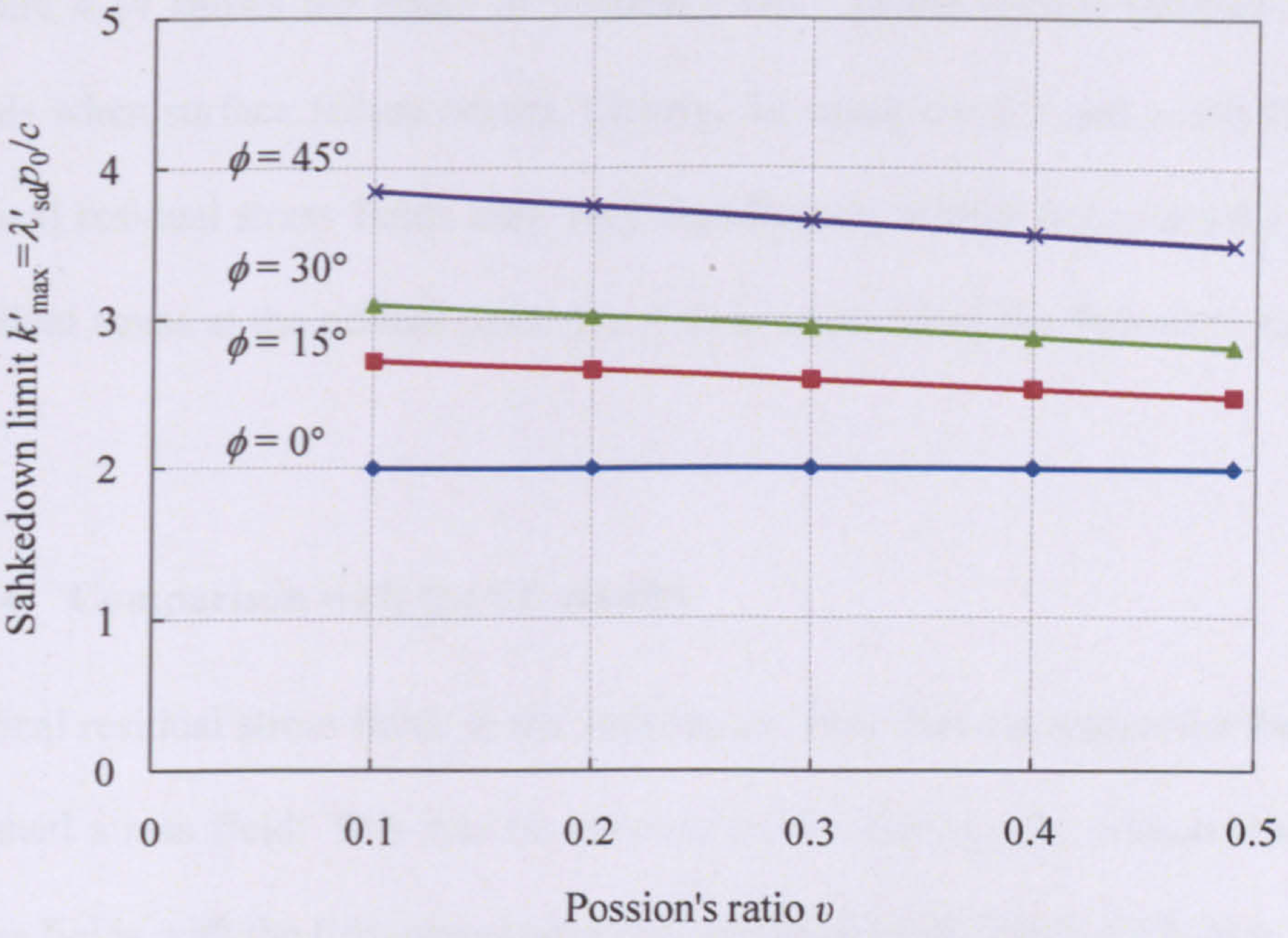

Figure 4.13. 3D shakedown limits $k^{'}_{\max}$ versus Poisson's ratio for various friction angles when $\mu = 0.5$

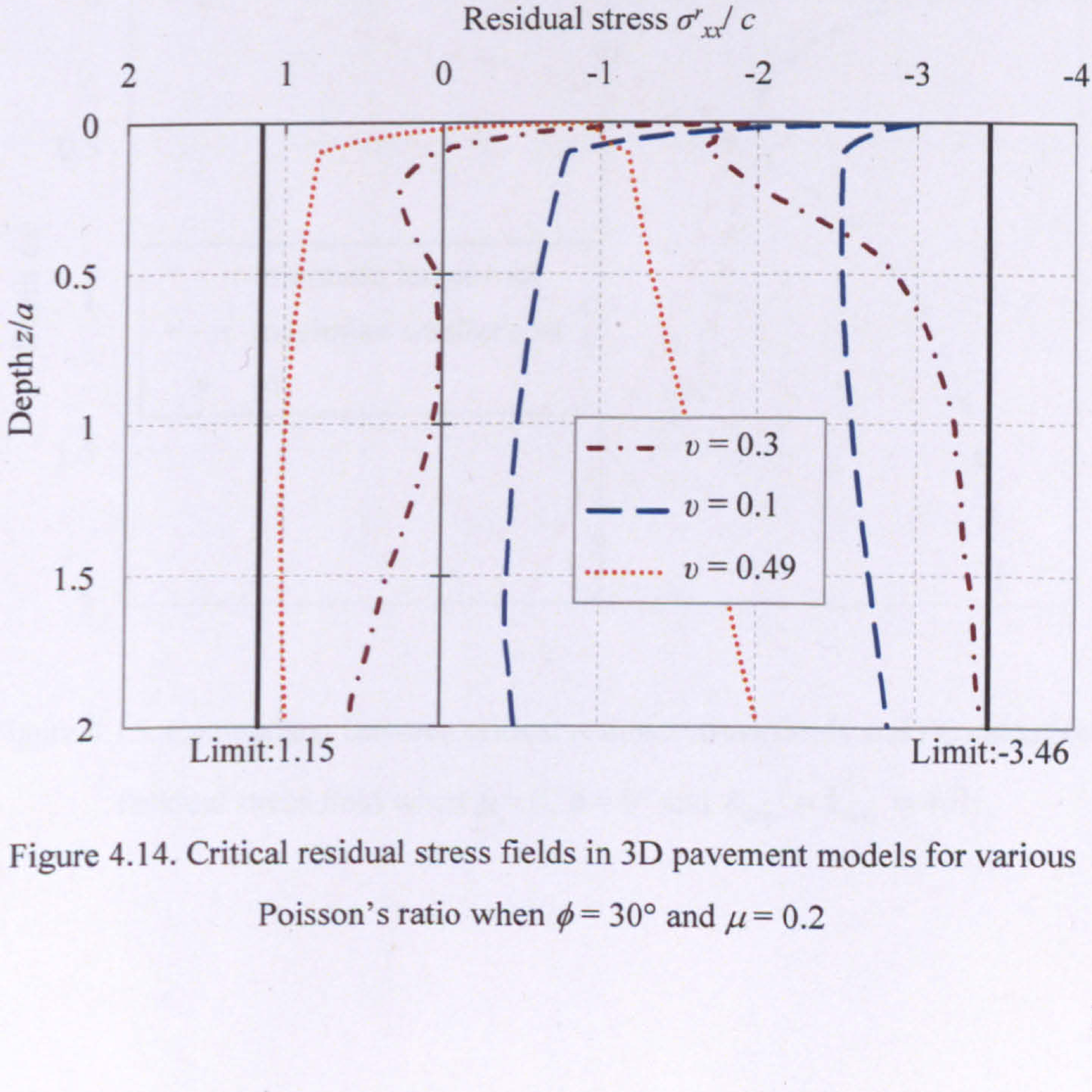

Figure 4.14. Critical residual stress fields in 3D pavement models for various Poisson's ratio when $\phi = 30°$ and $\mu = 0.2$

Figure 4.14 shows the effect of Poisson's ratio on the critical residual stress fields when surface failure occurs. Clearly, for cases $\upsilon = 0.1$ and $\upsilon = 0.49$, the critical residual stress fields only vary significantly within $0 \le z/a \le 0.1$. The residual stress at the critical point ($z/a = 0$) is small when the Poisson's ratio is low.

4.5.4 Comparison with the FE results

Critical residual stress fields at the shakedown limit forms a region for the real residual stress field. This can be checked by comparing the critical residual stress fields with the fully-developed residual stresses obtained in Chapter 3.

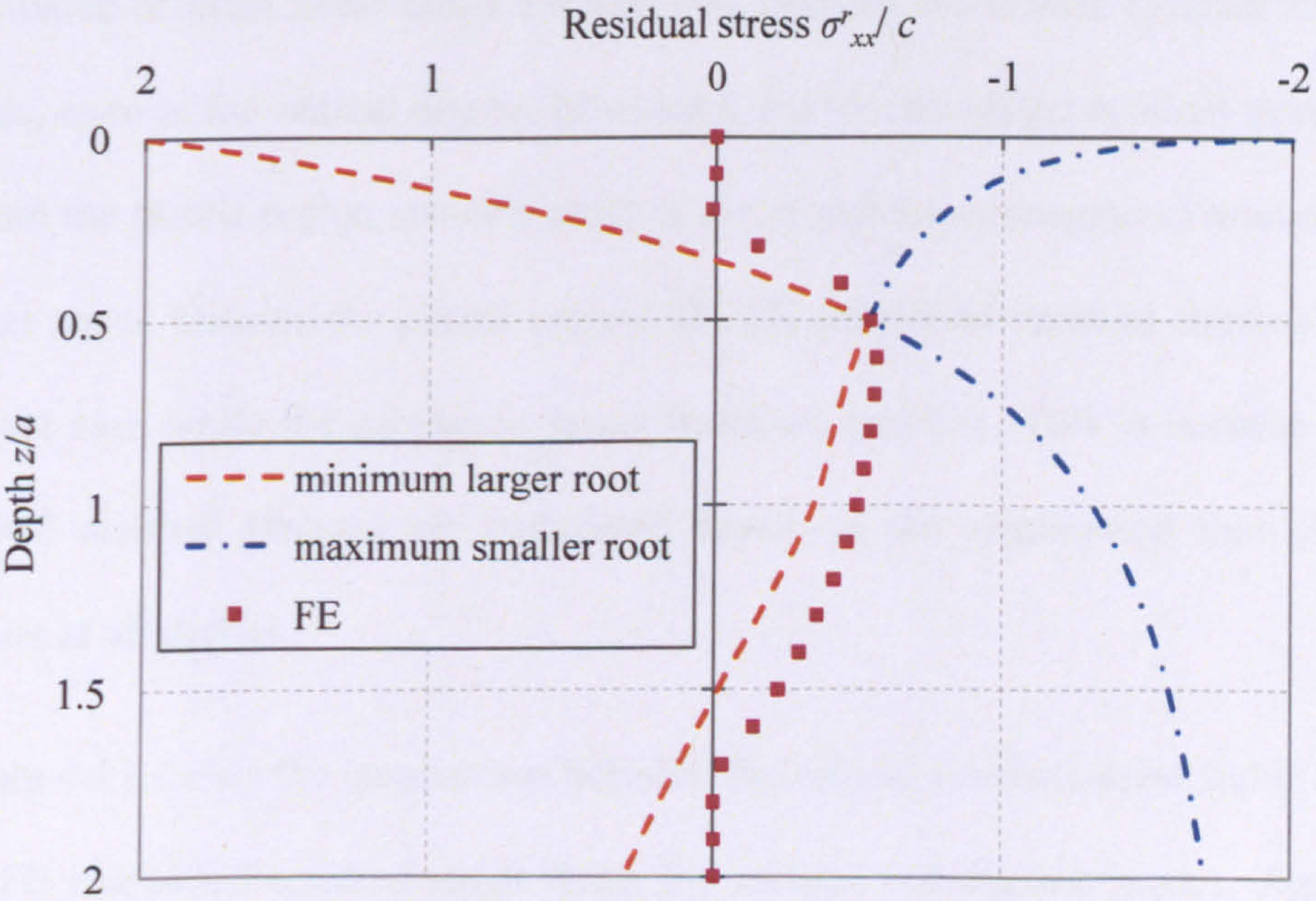

Figure 4.15. Comparison between critical residual stress fields and FE calculated residual stress field when $\mu = 0$, $\phi = 0°$ and $k_{\max} = k'_{\max} = 4.0$

For case $\mu = 0$, $\phi = 0°$ and $k_{\max} = k'_{\max} = 4.0$, the FE calculated residual stress field lies between the minimum larger root and the maximum smaller root (two critical residual stress fields), as shown in Figure 4.15. Moreover, the FE result agrees with the critical residual stresses at the critical depth ($z/a = 0.5$), giving $\sigma^r_{xx}/c = 0.53$. This is also identical to the residual stress given by Johnson (1962) for Tresca materials.

Figure 4.16 compares the critical residual stress fields with the FE results for a range of frictional coefficients, from -0.4 to 0.4. It should be noted that the sign of frictional coefficient does not affect the critical residual stress fields in the lower-bound solution. However, it may cause slightly different residual stress fields in the FE calculations as mentioned in Chapter 3. Clearly, the FE calculated residual stress fields are well contained by the critical residual stress fields, even at the critical depths. Moreover, the FE calculated residual stresses within the plastic region are very close to the compressive (negative) minimum larger roots. Outside the plastic region, the FE calculated residual stresses are almost zero while the minimum larger roots are positive. This is because the critical residual stresses are calculated based on the assumption that yield occurs at all depths.

Figure 4.17 shows the comparison between the critical residual stress fields and the FE calculated residual stress fields for various soil friction angles. Again, the critical residual stress fields are verified as they provide boundaries to the FE results. The compressive minimum larger roots are also close to the FE calculated residual stresses, particularly for those near the critical depth.

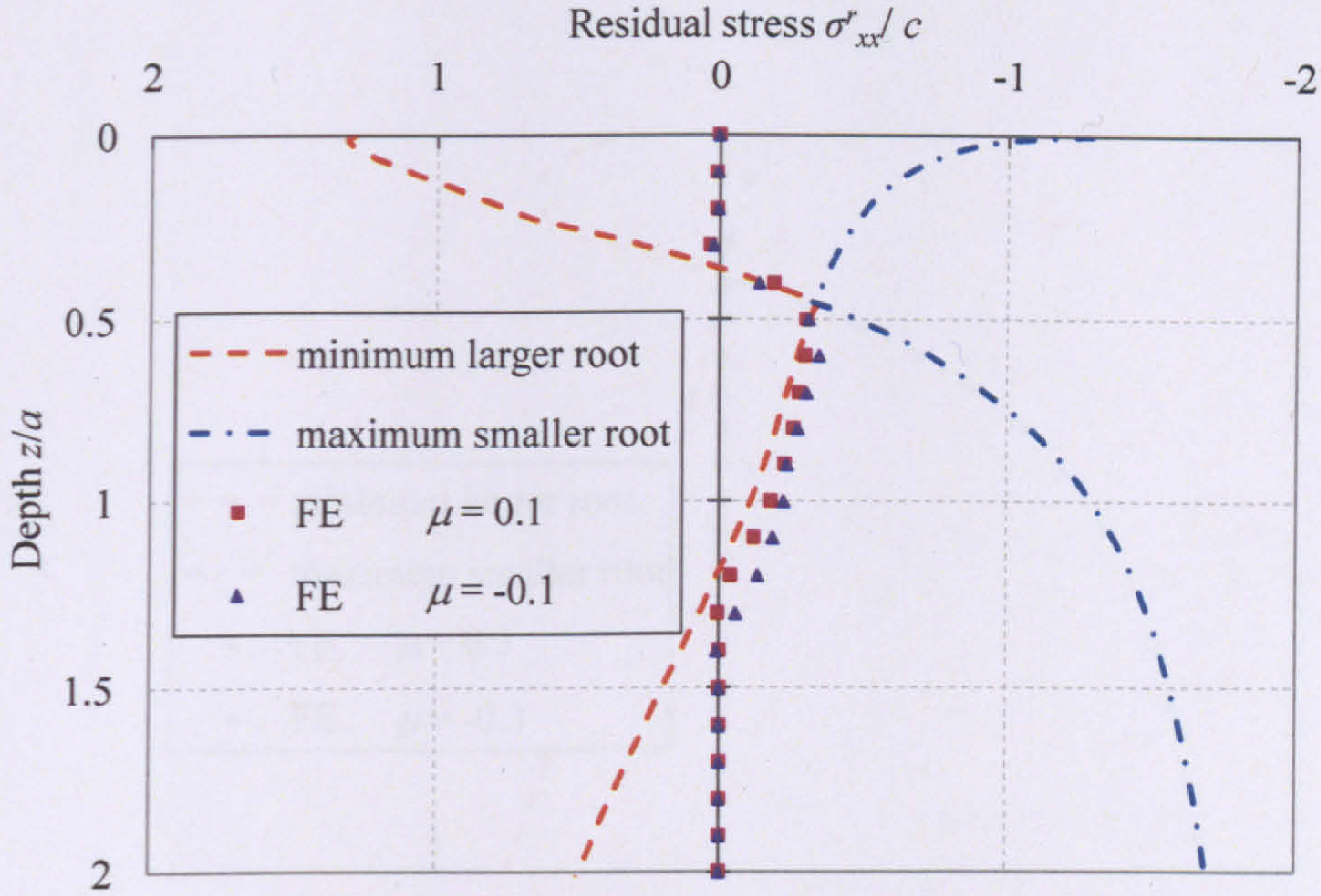

(a) $\mu = \pm0.1$

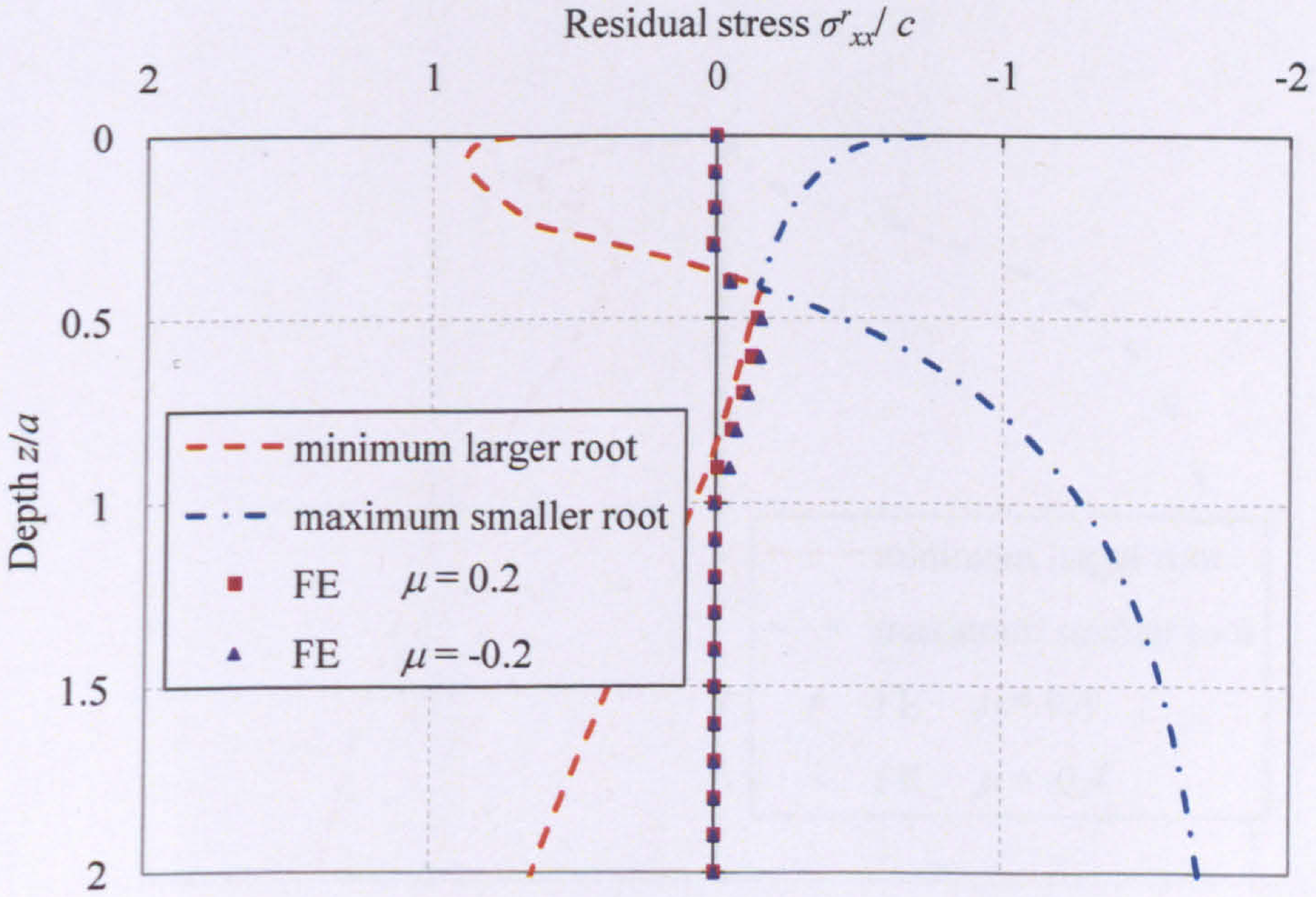

(b) $\mu = \pm0.2$

Figure 4.16 continued on following page

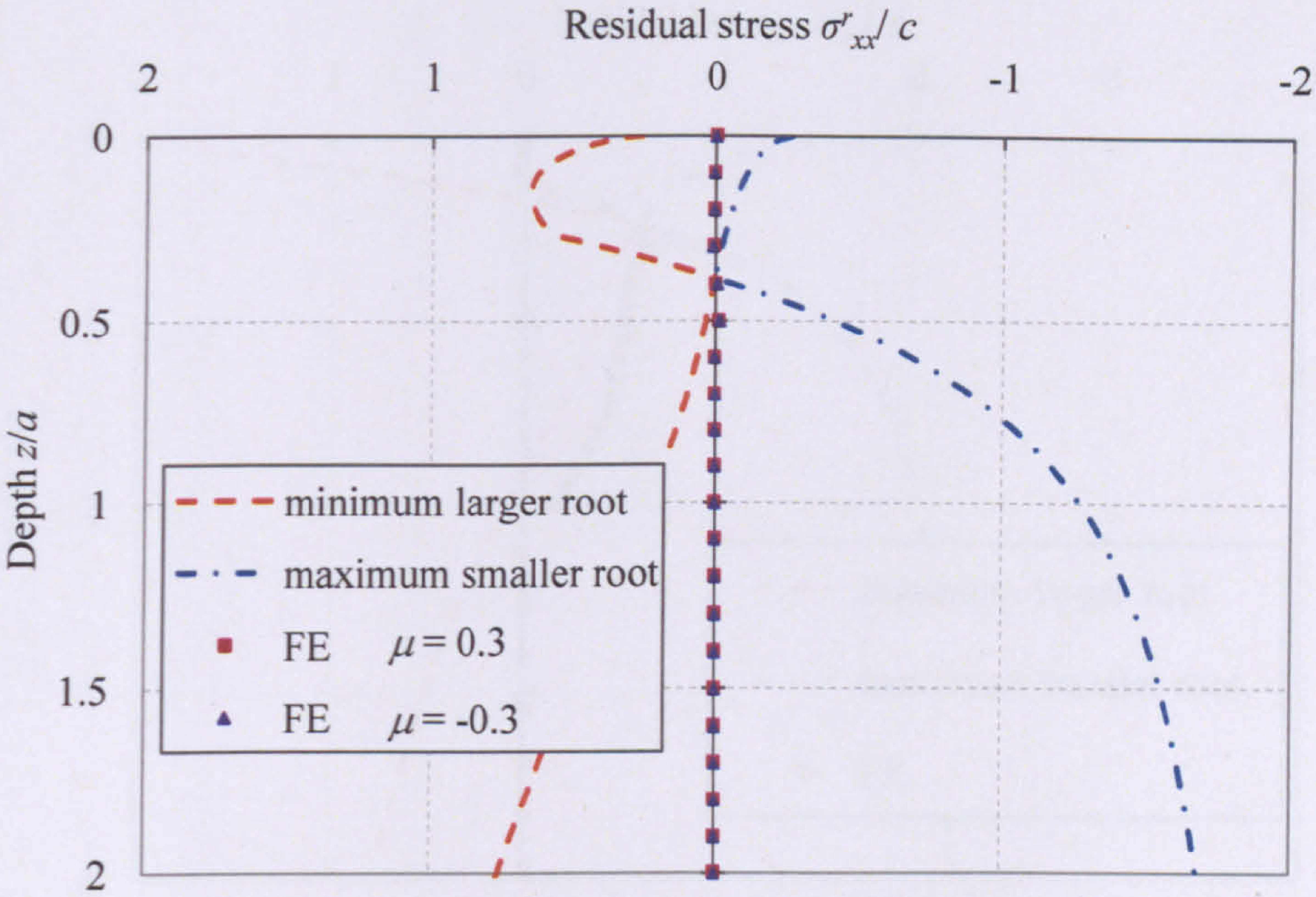

(c) $\mu = \pm 0.3$

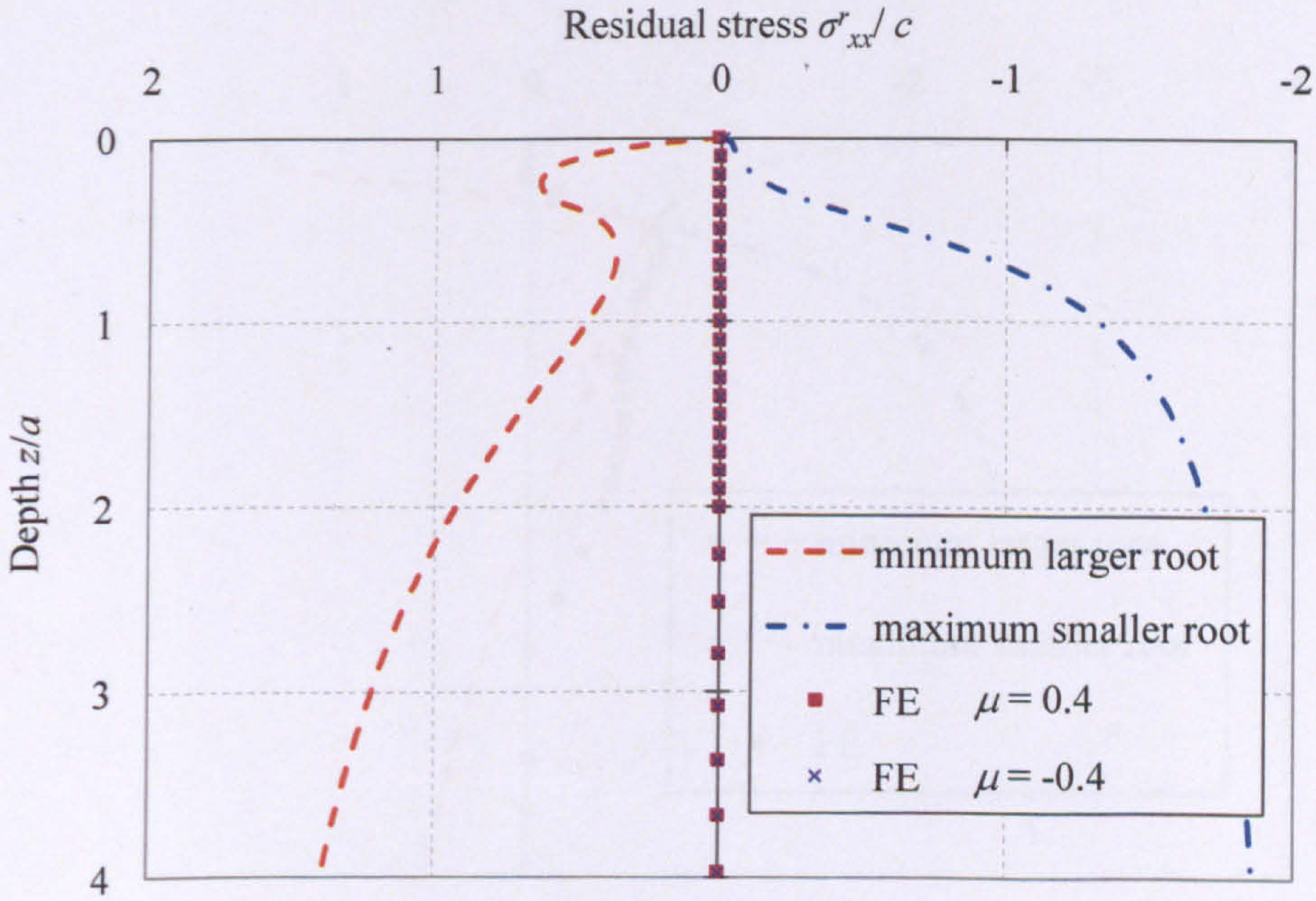

(d) $\mu = \pm 0.4$

Figure 4.16. Comparison between critical residual stress fields and FE calculated residual stress fields for various frictional coefficients when $\phi = 0°$

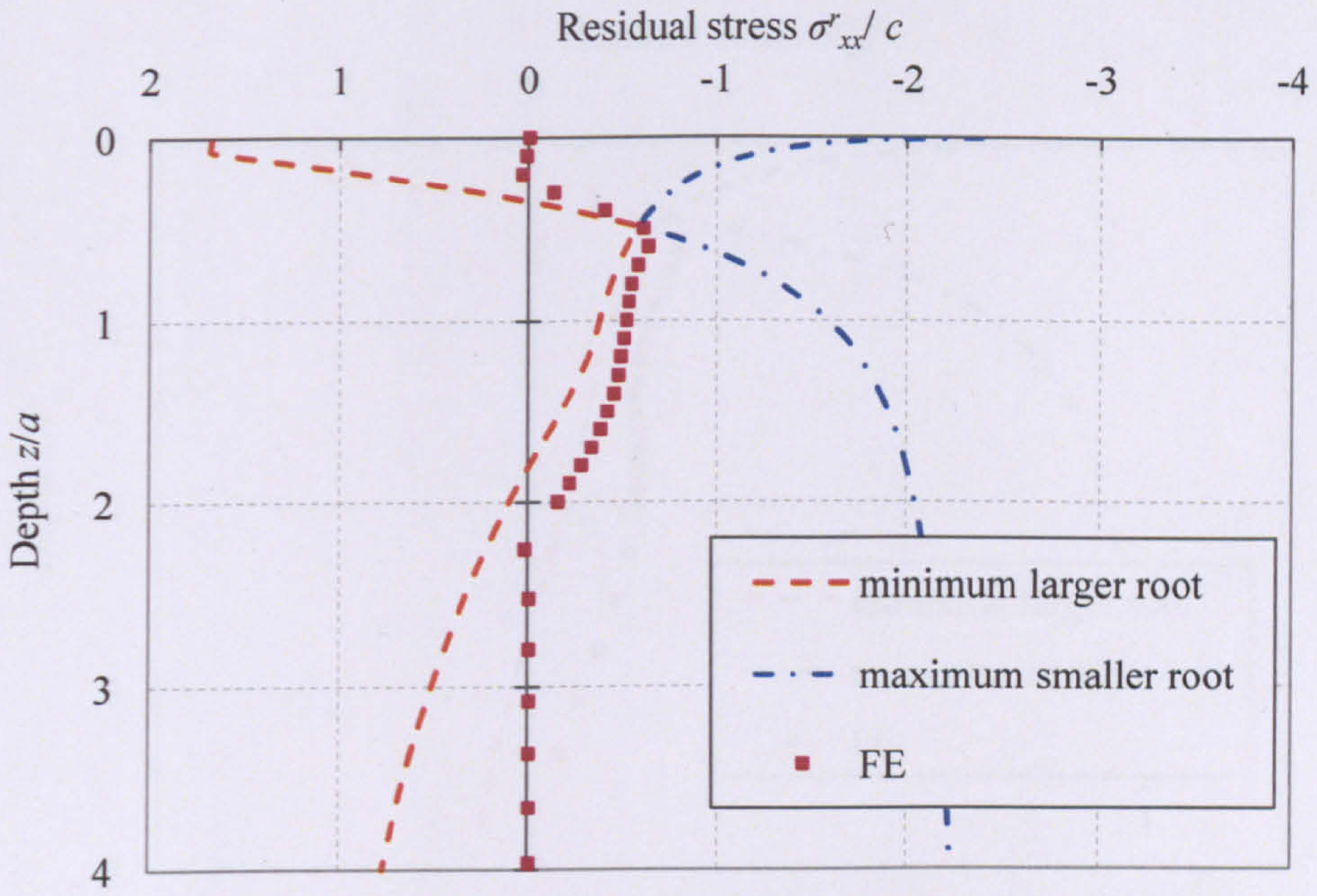

(a) $\phi = 10°$

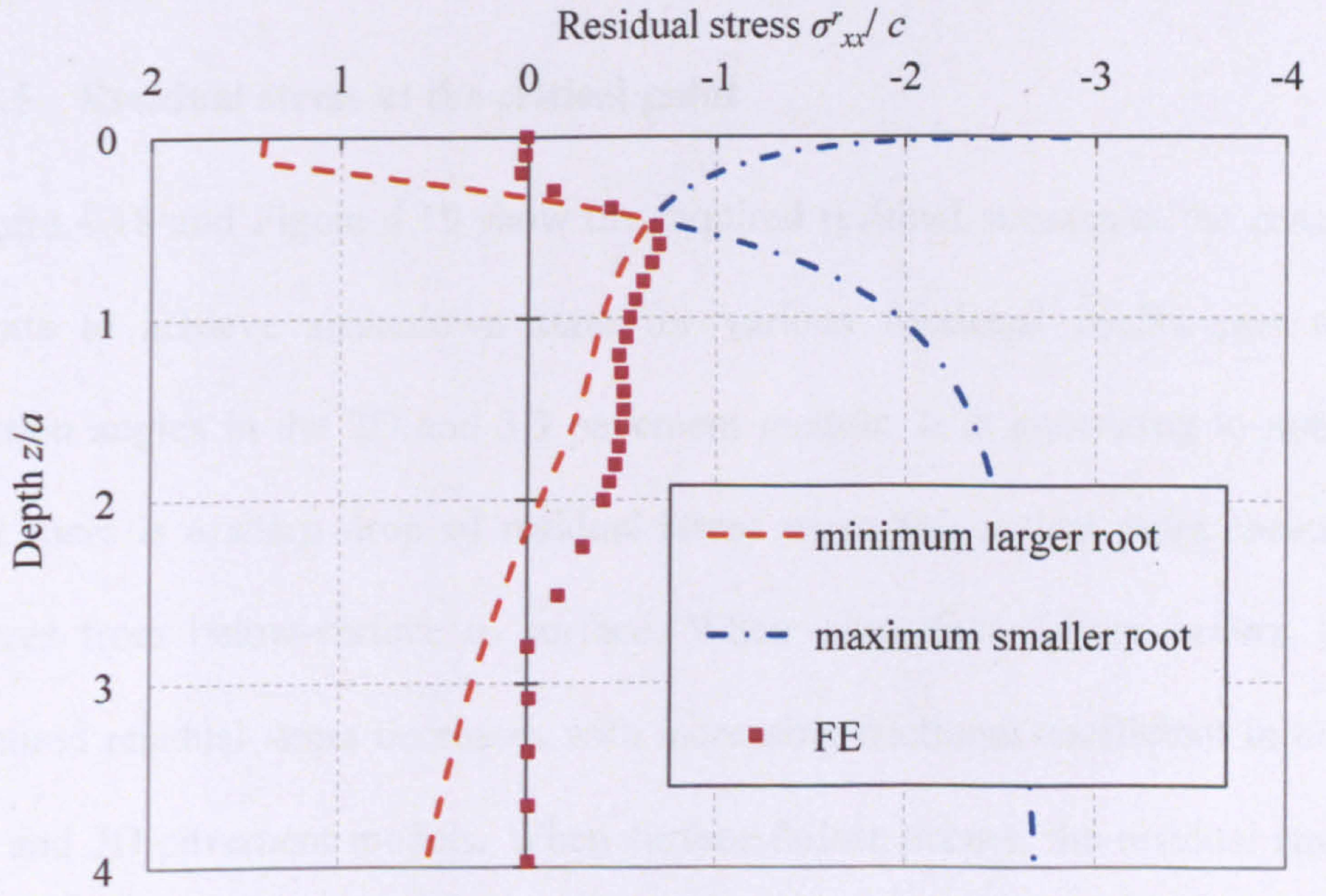

(b) $\phi = 20°$

Figure 4.17 continued on following page

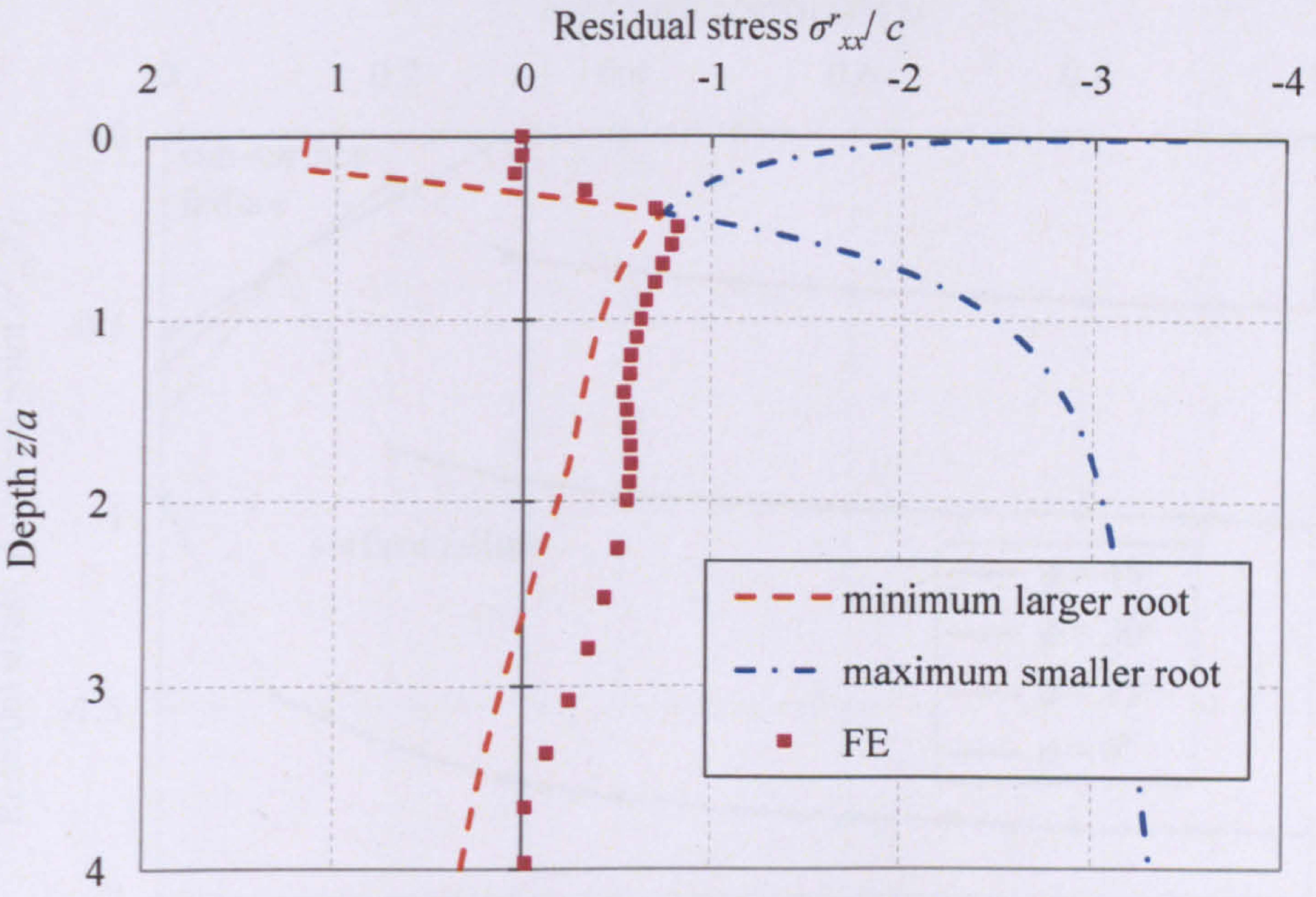

(c) $\phi = 30°$

Figure 4.17. Comparison between critical residual stress fields and FE calculated residual stress fields for various friction angles when $\mu = 0$

4.5.5 Residual stress at the critical point

Figure 4.18 and Figure 4.19 show the required residual stresses at the critical points to achieve shakedown state for various frictional coefficients and friction angles in the 2D and 3D pavement models. It is interesting to notice that there is a sharp drop of residual stress when the critical point location moves from below-surface to surface. When subsurface failure occurs, the required residual stress decreases with increasing frictional coefficient in both 2D and 3D pavement models. When surface failure occurs, the residual stress decreases in the 2D model (except when ϕ=0°) but increases in the 3D model with the rise of frictional coefficient. In addition, the residual stress in the 3D pavement model is always smaller than that in the 2D pavement model.

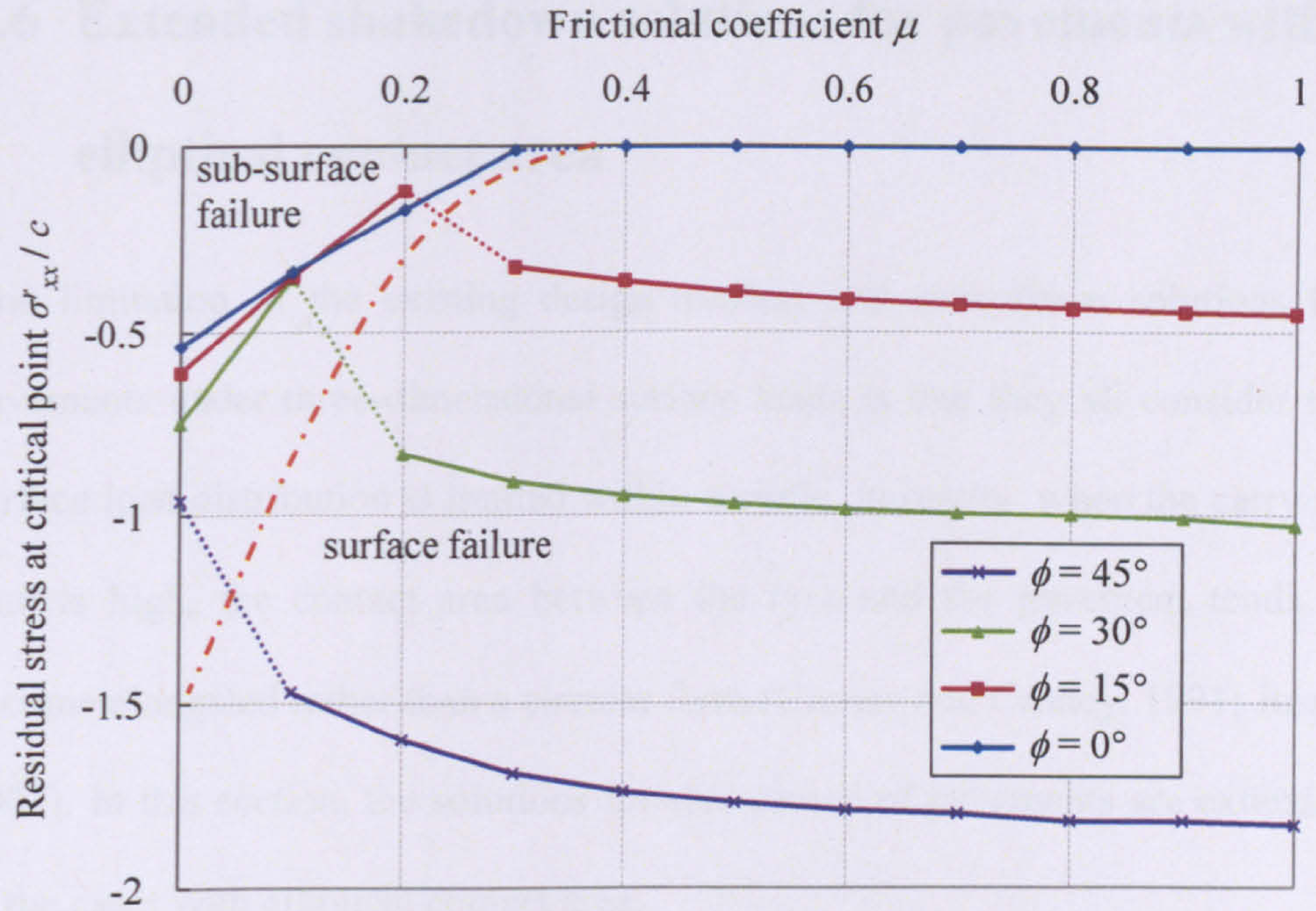

Figure 4.18. Residual stress at critical point versus frictional coefficient for various friction angles in 2D pavement models

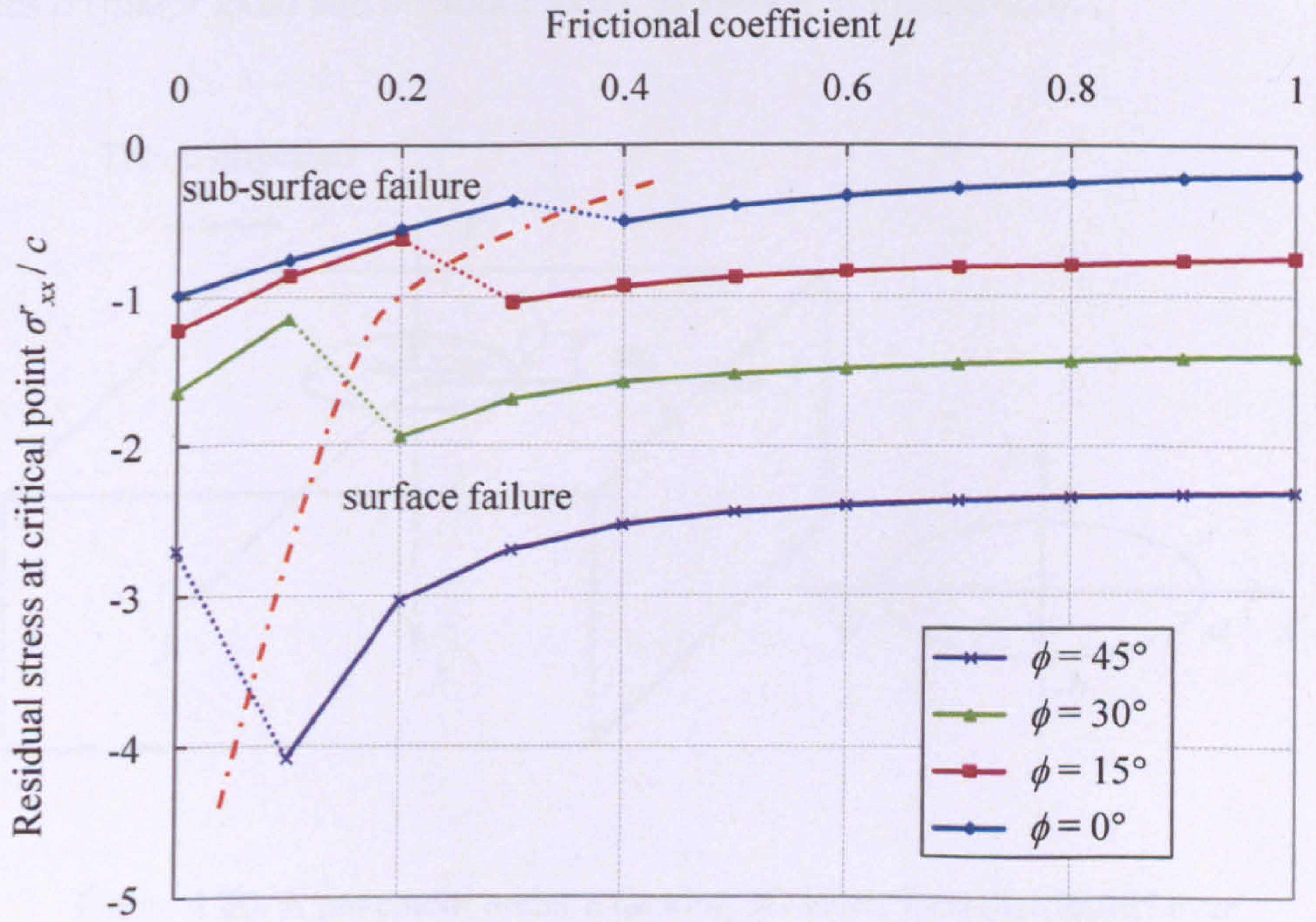

Figure 4.19. Residual stress at critical point versus frictional coefficient for various friction angles in 3D pavement models

4.6 Extended shakedown solutions for pavements with elliptical contact area

One limitation of the existing design method and shakedown solutions for pavements under three-dimensional surface loads is that they all consider the surface load distribution is limited within a circle. In reality, when the carrying load is high, the contact area between the tyre and the pavement tends to become elongated rather than a circular form (Croney and Croney, 1991; Juspi, 2007). In this section, the solutions for shakedown of pavements are extended to the cases with elliptical contact area.

4.6.1 Load distributions

The surface contact loading is limited to an elliptical contact area with semi-axes *a* (major axis) and *b* (minor axis), as shown in Figure 4.20.

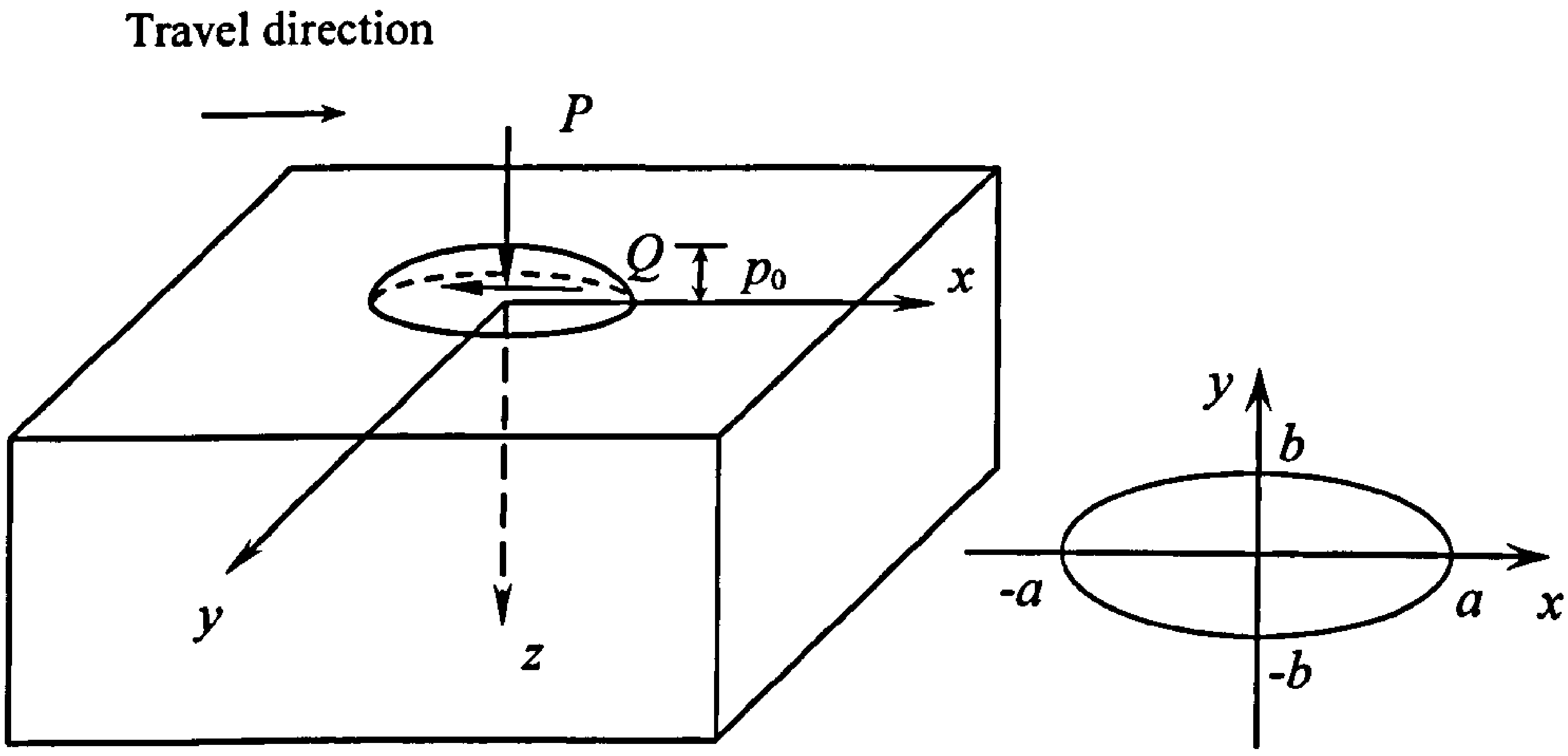

Figure 4.20. A pavement under a moving 3D Hertz load distributed over an elliptical contact area

The total normal and shear force P and Q are distributed over the elliptical contact area and formulated as:

$$
\begin{gathered}
p=\frac{3P}{2\pi ab}\left(1-\frac{x^2}{a^2}-\frac{y^2}{b^2}\right)^{1/2}, \\
q=\frac{3Q}{2\pi ab}\left(1-\frac{x^2}{a^2}-\frac{y^2}{b^2}\right)^{1/2}. \\
\left(\frac{x^2}{a^2}+\frac{y^2}{b^2}\leq 1\right)
\end{gathered}
\tag{4.15}
$$

where the normal and shear force have the correlation $\mu = Q/P$ and μ is the frictional coefficient. This load distribution, also referred to as the 3D Hertz load distribution (Johnson, 1985; Ponter et al., 1985), has a maximum compressive pressure $p_0 = 3P/2\pi ab$ at the centre of the loading area ($x = y = z = 0$).

4.6.2 Elastic stress fields

The analytical solutions for elastic stresses at any point (x, y, z) in the half-space, due to the 3D Hertz load distribution, defined in Equation (4.15), were derived by Bryant and Keer (1982) and Sackfield and Hills (1983a, 1983b). The stress expressions that are relevant to the present study are given below.

There are some typos in Sackfield and Hills (1983b). The corrected stress expressions of σ_{zz} and σ_{xz} due to the normal and shear loads are given as follows:

$$\left(\sigma_{zz}^{e}\right)_{p}=\frac{3P}{2\pi ab}\left[-\frac{bz^{3}}{a^{4}s^{5}HG}\right],$$
$$\left(\sigma_{xz}^{e}\right)_{p}=\frac{3P}{2\pi ab}\left[-\frac{bxz^{2}}{a^{4}s^{3}\left(s^{2}+1\right)HG}\right],\tag{4.16}$$

$$\left(\sigma_{zz}^{e}\right)_{q}=\frac{3Q}{2\pi ab}\left[-\frac{bxz^{2}}{a^{4}s^{3}\left(s^{2}+1\right)HG}\right],$$
$$\left(\sigma_{xz}^{e}\right)_{q}=\frac{3Q}{2\pi ab}\left[-\frac{bx^{2}z}{a^{4}s\left(s^{2}+1\right)^{2}HG}+\frac{bz\left(I_{1}-I_{3}\right)}{a^{2}}\right],\tag{4.17}$$

where

a,b are the lengths of the major and minor axes of the contact ellipse,

s is the largest root of $\frac{x^{2}}{a^{2}\left(s^{2}+1\right)}+\frac{y^{2}}{a^{2}\left(s^{2}+\left(b/a\right)^{2}\right)}+\frac{z^{2}}{a^{2}s^{2}}=1$,

$$H=\frac{x^{2}}{a^{2}\left(s^{2}+1\right)^{2}}+\frac{y^{2}}{a^{2}\left(s^{2}+\left(b/a\right)^{2}\right)^{2}}+\frac{z^{2}}{a^{2}\left(s^{2}\right)^{2}},$$

$$G=\left[\left(s^{2}+1\right)\left(s^{2}+\left(b/a\right)^{2}\right)\right]^{1/2},$$

$$I_{1}=\int_{s}^{\infty}\frac{dw}{\left(1+w^{2}\right)^{3/2}\left(\left(b/a\right)^{2}+w^{2}\right)^{1/2}},$$

$$I_{3}=\int_{s}^{\infty}\frac{dw}{w^{2}\left(1+w^{2}\right)^{1/2}\left(\left(b/a\right)^{2}+w^{2}\right)^{1/2}}.$$

The stress expressions of σ_{xx} used in this section is taken from Bryant and Keer (1982), as shown below:

$$\left(\sigma_{xx}^{e}\right)_{p}=\frac{3P}{2\pi ab}\left(1-e^{2}\right)^{1/2}\times\left[\left(1-2\upsilon\right)\left(\frac{x^{2}}{a^{2}}I_{8}-I_{11}\right)\right. \\ \left.-2\upsilon\Psi\left(\rho,x,y,z\right)+2\left(1-\upsilon\right)\frac{z}{a}\Psi_{1}\left(\rho\right)-\frac{x^{2}z}{a^{3}}\frac{\Delta\left(\rho\right)}{\rho^{3}\Theta\left(\rho,\zeta,\nu\right)}\right], \tag{4.18}$$

$$\left(\sigma_{xx}\right)_{q}=\frac{3Q}{2\pi ab}\left(1-e^{2}\right)^{1/2}\frac{x}{a}\times\left[\left(1-2\upsilon\right)\left(3\frac{z}{a}I_{8}+\frac{x^{2}}{a^{2}}I_{10}\right)\right. \\ \left.-2\left(1+\upsilon\right)\Psi_{1}\left(\rho\right)+6\upsilon I_{9}-\frac{x^{2}}{a^{2}}\frac{\left(\rho^{2}-1\right)\Delta\left(\rho\right)}{\rho^{5}\Theta\left(\rho,\zeta,\nu\right)}\right], \tag{4.19}$$

where

υ is Poisson's ratio,

$e^{2}=1-\left(b/a\right)^{2}\ \left(0<e<1\right)$,

ρ,ζ,ν are roots of $\frac{x^{2}}{a^{2}s^{2}}+\frac{y^{2}}{a^{2}\left(s^{2}-e^{2}\right)}+\frac{z^{2}}{a^{2}\left(s^{2}-1\right)}=1\ \left(\rho^{2}\geq\zeta^{2}\geq\nu^{2}\right)$,

$\Psi_{1}\left(\rho\right)=\frac{1}{e^{2}}\left[\Gamma\left(\phi,e\right)-\mathrm{E}\left(\phi,e\right)\right]$,

$\Psi\left(\rho,x,y,z\right)=\frac{-z\mathrm{E}\left(\phi,e\right)}{a\left(1-e^{2}\right)}+\frac{1}{\left(1-e^{2}\right)}\frac{\mathrm{Z}\left(\zeta,\nu;e\right)\sqrt{\rho^{2}-e^{2}}}{\rho}$,

$I_{8}=\frac{1}{2\beta}\left\{\phi_{2}\left(\rho,x,y;e\right)-\frac{\alpha}{2}\varsigma_{0}\left(\rho,x,y\right)\right\}$,

$I_{9}=\frac{1}{3e^{2}}\left[\left(e^{2}-2\right)\Psi_{1}\left(\rho\right)-\frac{\Delta\left(\rho\right)}{\rho^{3}}+\Gamma\left(\phi,e\right)\right]$,

$$I_{10} = I_7 - e^2 J_{110},$$

$$I_{11} = \frac{1}{2e}\left\{-\delta(\rho,x,y;e)\frac{C}{e^2} - \left(\frac{\beta}{e^2}+\frac{\alpha}{2}\right)\varsigma_0(\rho,x,y) - \phi_2(\rho,x,y;e)\right\},$$

$$I_7 = \frac{z}{a}\left[\frac{1}{\beta\omega^2}\left\{\alpha - \frac{\alpha\rho^2 - 2\beta + \alpha^2}{\chi_0(\rho,x,y;e)}\right\} + \frac{\varsigma_0(\rho,x,y)}{2\beta}\right],$$

$$J_{110} = \frac{z}{2a\beta^2}\left[\frac{\beta}{\rho^2\chi_0(\rho,x,y;e)} - \frac{3\alpha^2 - 8\beta}{\omega^2}\right.$$
$$\left. + \frac{\left(3\alpha^2 - 8\beta\right)\rho^2 + \left(3\alpha^2 - 10\beta\right)\alpha}{\omega^2\chi_0(\rho,x,y;e)} - \frac{3}{2}\alpha\varsigma_0(\rho,x,y)\right],$$

$$\vartheta = \arcsin(1/\rho),$$

$$\Gamma(\vartheta,e) = \int_0^{\vartheta}\frac{d\xi}{\left(1 - e^2\sin^2\xi\right)^{1/2}},$$

$$\mathrm{E}(\vartheta,e) = \int_0^{\vartheta}\left(1 - e^2\sin^2\xi\right)^{1/2} d\xi,$$

$$\Theta(\rho,\zeta,\nu) = \left(\rho^2 - \zeta^2\right)\left(\rho^2 - \nu^2\right),$$

$$\Delta(\rho) = \sqrt{\left(\rho^2 - 1\right)\left(\rho^2 - e^2\right)},$$

$$\mathrm{Z}(\zeta,\nu;e) = \sqrt{\frac{\left(1 - \zeta^2\right)\left(1 - \nu^2\right)}{1 - e^2}},$$

$$\alpha = -\left[e^2 + \frac{x^2}{a^2} + \frac{y^2}{a^2}\right],$$

$$\beta = e^2 \frac{x^2}{a^2},$$

$$B = e^2 - \frac{x^2}{a^2} - \frac{y^2}{a^2},$$

$$C = -e^2 \frac{y^2}{a^2},$$

$$K = \sqrt{B^2 - 4C},$$

$$\omega = \sqrt{\alpha^2 - 4\beta},$$

$$\delta(\rho, x, y; e) = \frac{1}{\sqrt{-C}} \left\{ \arcsin \frac{B(\rho^2 - e^2) + 2C}{(\rho^2 - e^2)K} - \arcsin \frac{B}{K} \right\},$$

$$\phi_2(\rho, x, y; e) = \frac{\chi_0(\rho, x, y; e)}{\rho^2} - 1,$$

$$\chi_0(\rho, x, y; e) = \sqrt{\rho^4 + \alpha\rho^2 + \beta},$$

$$\varsigma_0(\rho, x, y) = \frac{1}{\sqrt{\beta}} \log \frac{2\sqrt{\beta}\chi_0(\rho, x, y) + 2\beta + \rho^2\alpha}{\rho^2(2\sqrt{\beta} + \alpha)}.$$

The above elastic stress expressions have been programmed in FORTRAN and verified through comparing with the FE results.

4.6.3 Effect of frictional coefficient and soil friction angle

Based on the elastic stress fields defined by Equations (4.16) - (4.19), shakedown solutions for pavements with elliptical contact area are obtained. Some typical results are presented in this subsection to investigate the effect of frictional coefficient and soil friction angle. Poisson's ratio is taken as 0.3.

Figure 4.21 presents the results demonstrating the dependence of the normalised analytical shakedown limit $k_{\max} = \lambda_{sd} p_0 / c$ on both the friction angle ϕ and surface frictional coefficient μ when b/a = 0.5. The curves are similar to the ones in Figure 4.9 for a special case b/a = 1 (circular contact shape). Moreover, the numerical search for the most critical point throughout the half-space shows that the critical point always lies on the central plane $y = 0$.

Figure 4.22 shows the normalised lower-bound shakedown limits $k'_{\max} = \lambda'_{sd} p_0 / c$ against the frictional coefficients μ for various values of friction angle when b/a = 0.5. The data again show similar trend to those observed in Figure 4.9. Compared to the analytical shakedown solution, the lower-bound shakedown solution gives smaller shakedown limits when the critical point is located at the surface of the pavement.

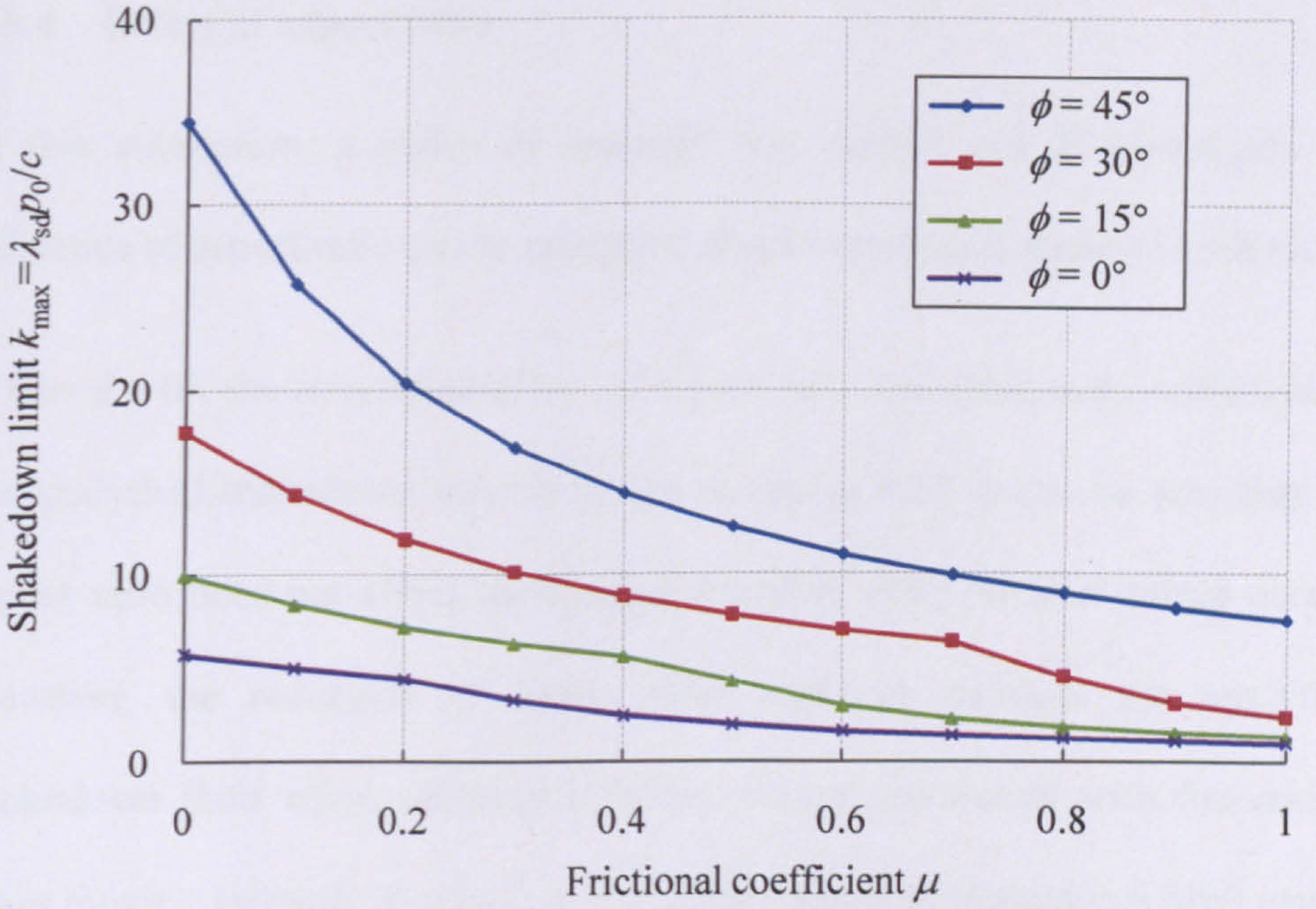

Figure 4.21. 3D shakedown limits $k_{\max}$ versus frictional coefficients for various values of friction angle when b/a=0.5

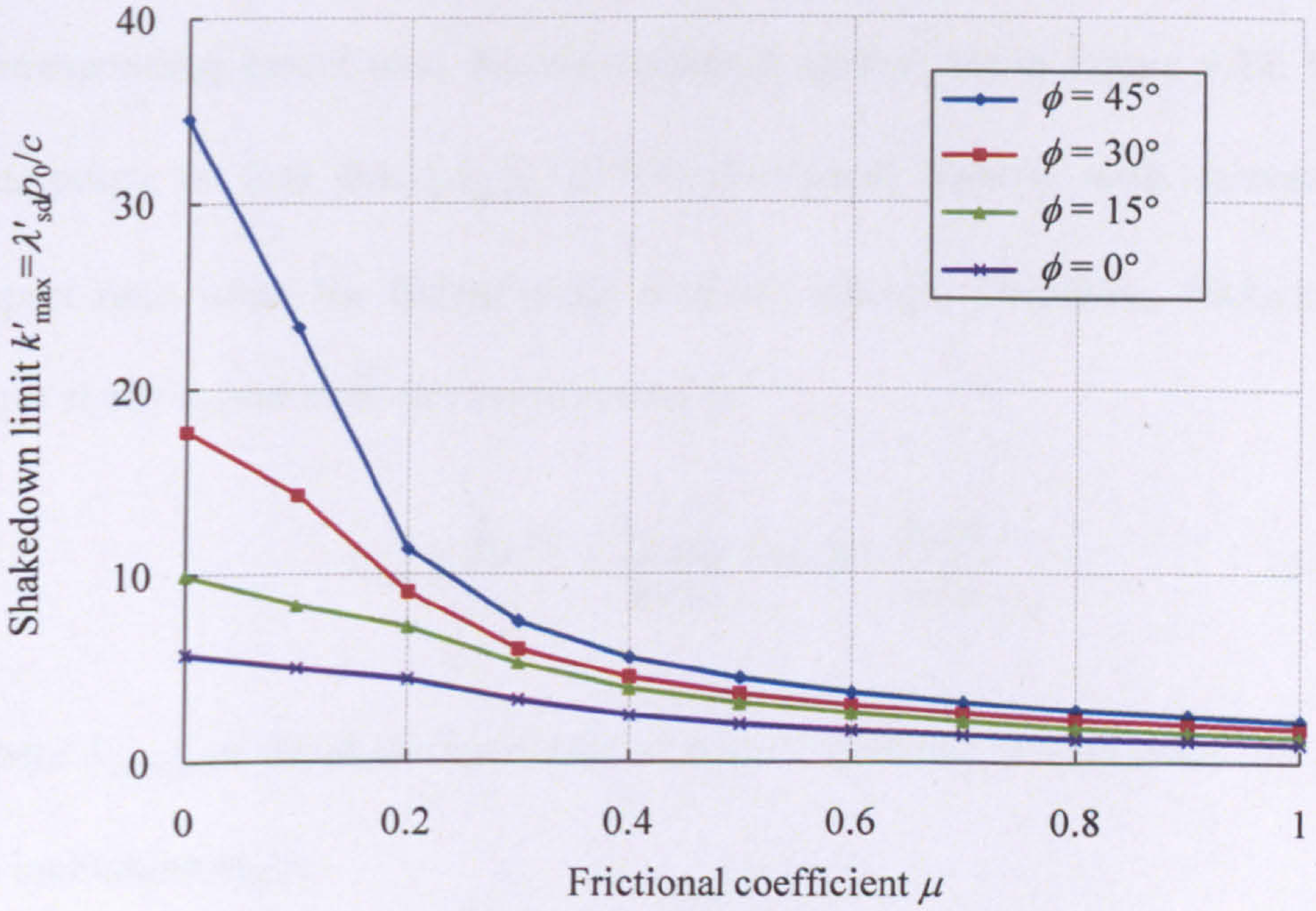

Figure 4.22. 3D shakedown limits $k'_{\max}$ versus frictional coefficients for various values of friction angle when b/a=0.5

4.6.4 Effect of aspect ratio

In this subsection, a series of analyses was carried out to investigate the influence of aspect ratio on the analytical and lower-bound shakedown limits.

When $\phi = 0°$, the interactive effect of aspect ratio and frictional coefficient on the analytical shakedown limit is shown in Figure 4.23. It can be seen that the aspect ratio does not affect the shakedown limit when surface failure occurs. However, the reduction of aspect ratio tends to increase the analytical shakedown limit when subsurface failure occurs, associated with the critical point moving upwards. For case $\mu = 0.2$, the analytical shakedown limit ceases to increase at $b/a = 0.36$, because the critical point moves to the surface of the pavement.

The above shakedown limits $k_{\max} = \lambda_{sd} p_0 / c$ when multiplied by the corresponding aspect ratio b/a are presented against b/a in Figure 4.24. It is interesting to find that $(\lambda_{sd} p_0 / c)*(b/a)$ reduces linearly with decreasing aspect ratio when the failure mode does not change. Therefore, shakedown limit at any aspect ratio can be expressed as:

$$k_{\max} = \frac{\lambda_{sd} p_0}{c} = \frac{k_{circular}}{b/a} + \tan\theta - \frac{\tan\theta}{b/a} \qquad (4.20)$$

where $k_{circular}$ is the shakedown limit at $b/a = 1$ (circular contact area) and θ is an inclination angle.

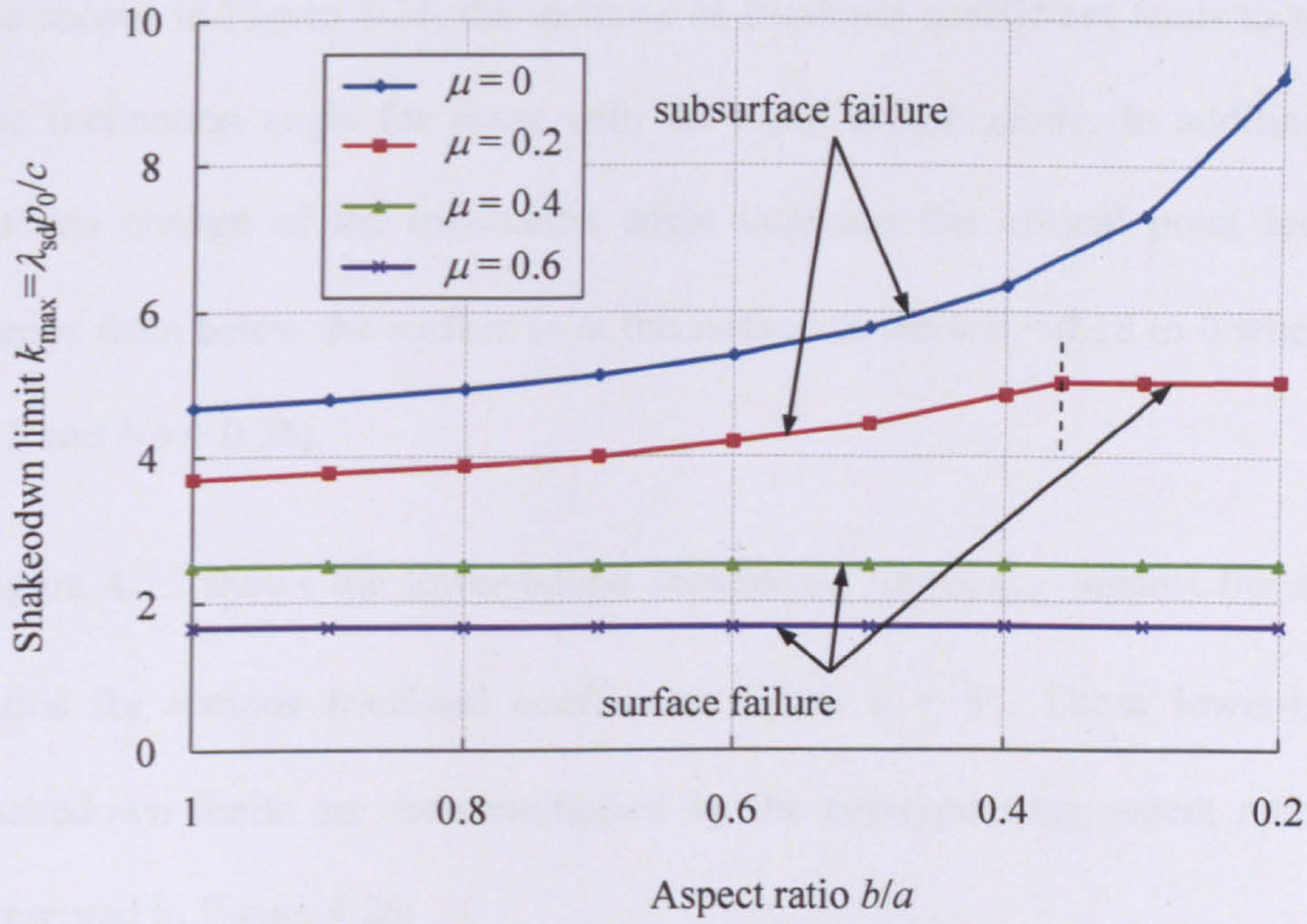

Figure 4.23. 3D shakedown limits k_{max} versus aspect ratios for various values of frictional coefficient when $\phi = 0°$

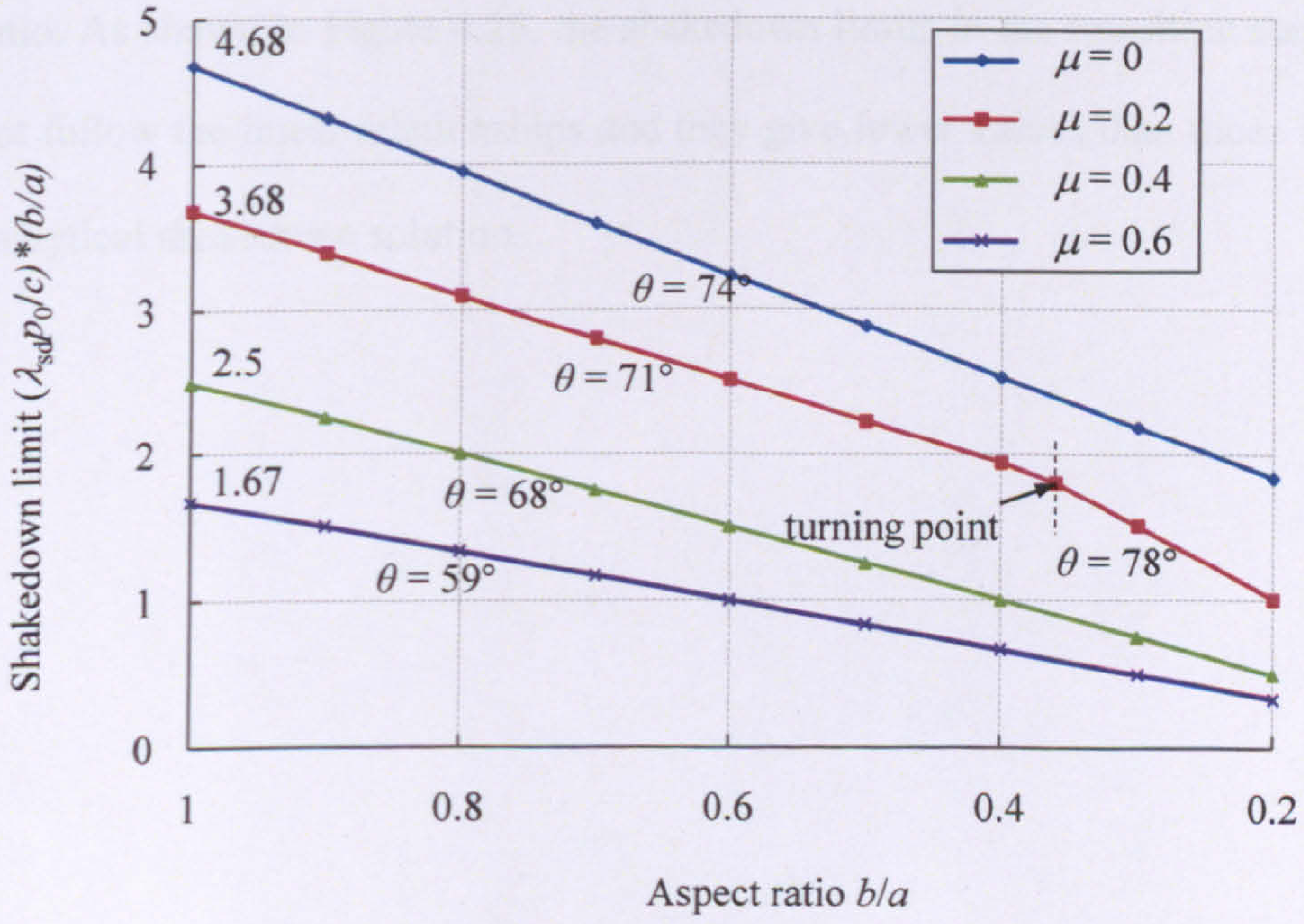

Figure 4.24. 3D shakedown limits $k_{max} * (b/a)$ versus aspect ratios for various values of frictional coefficient when $\phi = 0°$

As shown in Figure 4.24, the increase of frictional coefficient tends to reduce the inclination angle for cases with the same failure mode. In addition, the sudden change of the inclination angle indicates the critical point location jumps from below the surface to at the surface (from $h/a = 0.18$ to 0 when $\mu = 0.2$ and $b/a = 0.36$).

Figure 4.25 shows the lower-bound shakedown limits $k'_{\max}$ against the aspect ratios for various frictional coefficients when $\phi = 0°$. These lower-bound shakedown limits are then multiplied by the corresponding aspect ratio and presented in Figure 4.26.

The lower-bound shakedown solution is the same as the analytical shakedown solution in most cases. However, there exists some transition cases rather than a turning point when the failure mode is about to change with increasing aspect ratio. As shown in Figure 4.26, the shakedown limits in the transition stage do not follow the linear relationships and they give lower values than those in the analytical shakedown solution.

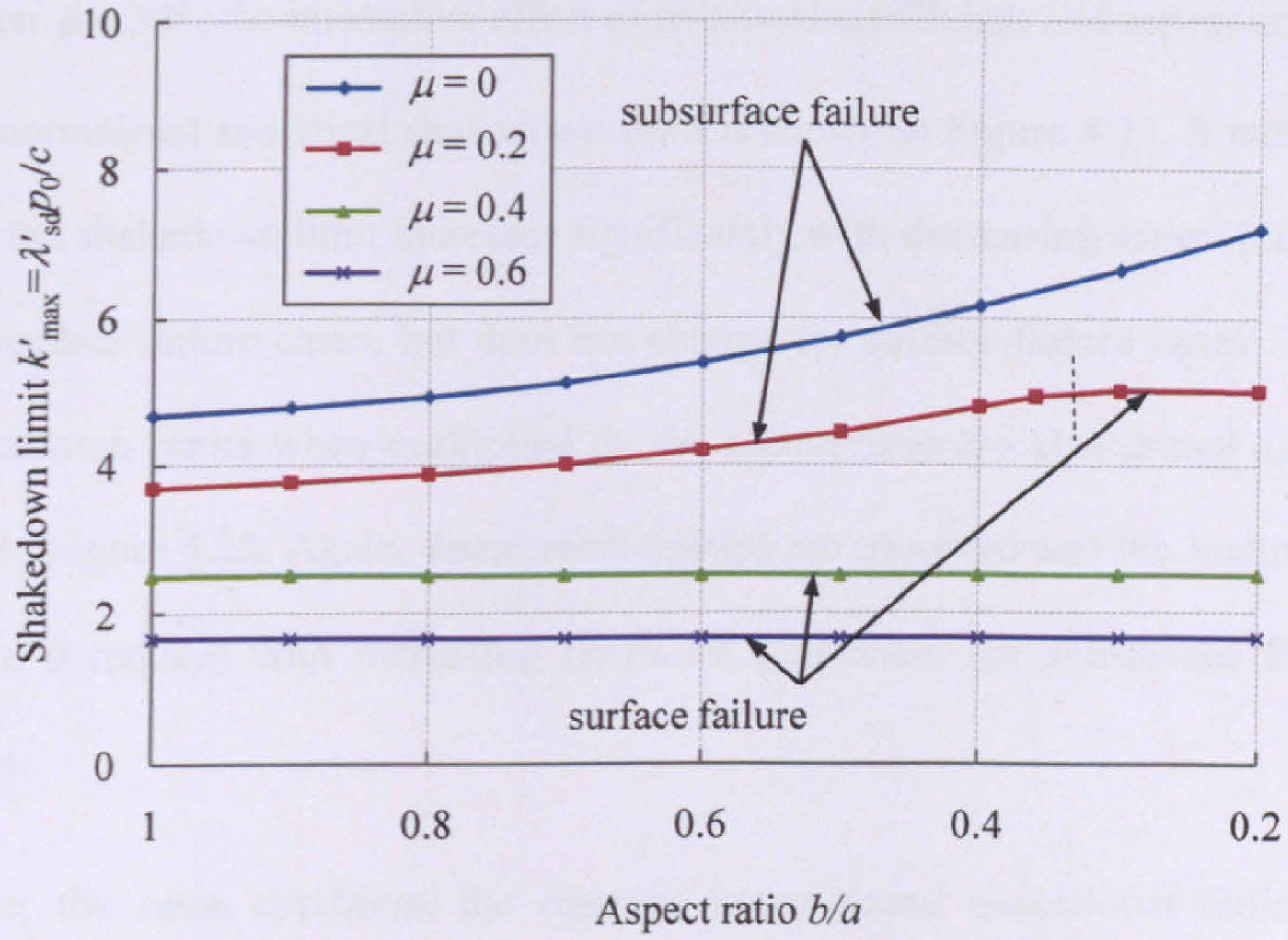

Figure 4.25. 3D shakedown limits $k'_{\max}$ versus aspect ratios for various values of frictional coefficient when $\phi = 0°$

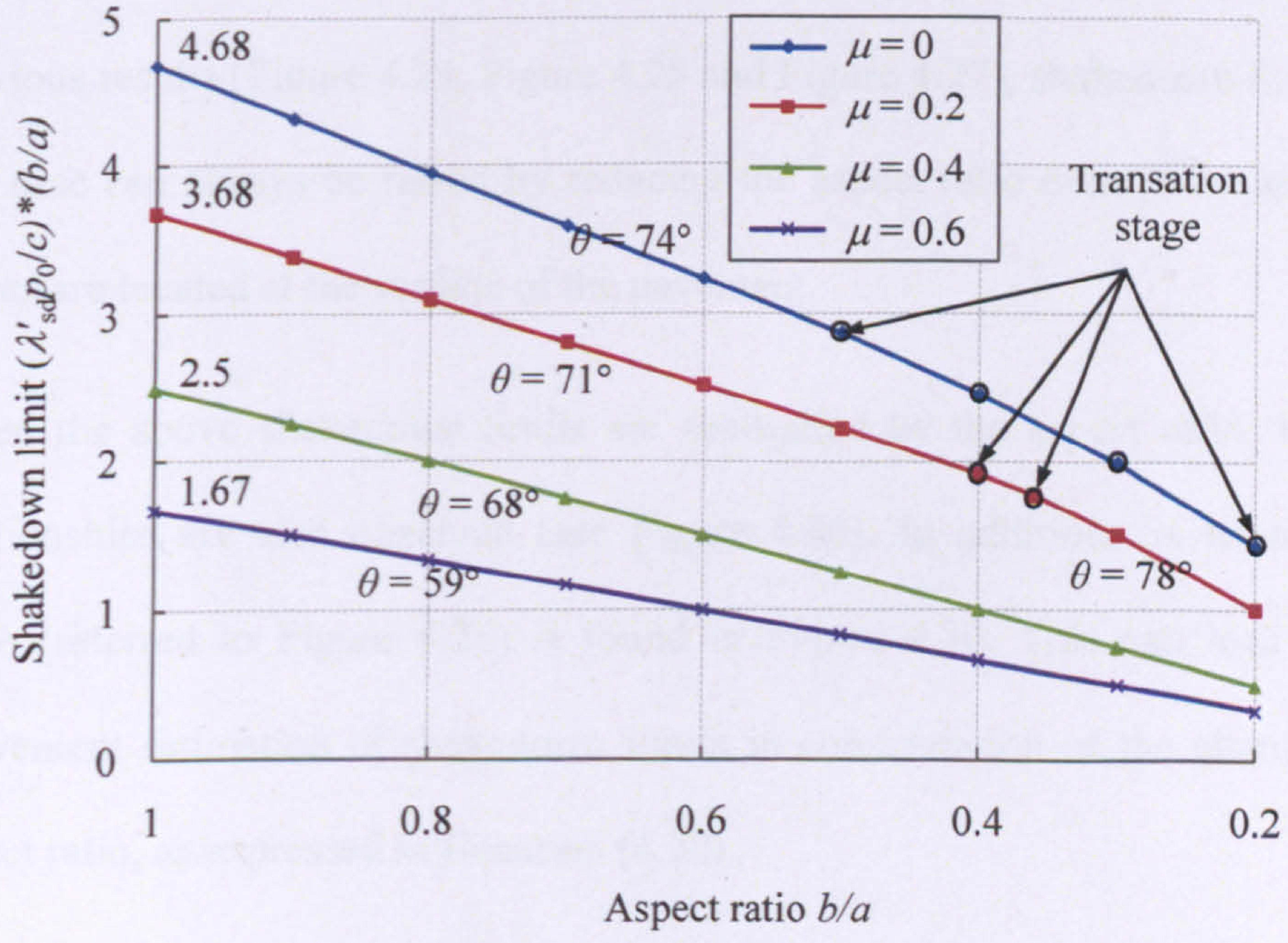

Figure 4.26. 3D shakedown limits $k'_{\max} * (b/a)$ versus aspect ratios for various values of frictional coefficient when $\phi = 0°$

When $\phi = 30°$, the interactive effect of frictional coefficient and aspect ratio on the normalised analytical shakedown limit is shown in Figure 4.27. It indicates that the shakedown limit increases significantly with decreasing aspect ratio for subsurface failure cases, but does not change for surface failure cases. These shakedown limits when multiplied by the aspect ratio are also drawn against b/a in Figure 4.28. Again, linear relationships are observed and the inclination angle θ reduces with increasing frictional coefficient for subsurface failure cases.

Under the same condition, the rigorous lower-bound shakedown limits are shown against the aspect ratios in Figure 4.29. As can be seen, surface failure occurs from $\mu = 0.2$ in Figure 4.29 rather than from $\mu = 0.8$ in Figure 4.27. In addition, the lower-bound shakedown limits with the surface failure mode are always lower than the corresponding cases in Figure 4.27. Different from previous results (Figure 4.23, Figure 4.25 and Figure 4.27), shakedown limit in this case can always be raised by reducing the aspect ratio even if the critical points are located at the surface of the pavement.

When the above shakedown limits are multiplied by the aspect ratio, linear relationships are also observed (see Figure 4.30). In addition, no transition stage (referred to Figure 4.26) is found in Figure 4.30. This can lead to a convenient estimation of shakedown limits in consideration of the change of aspect ratio, as expressed in Equation (4.20).

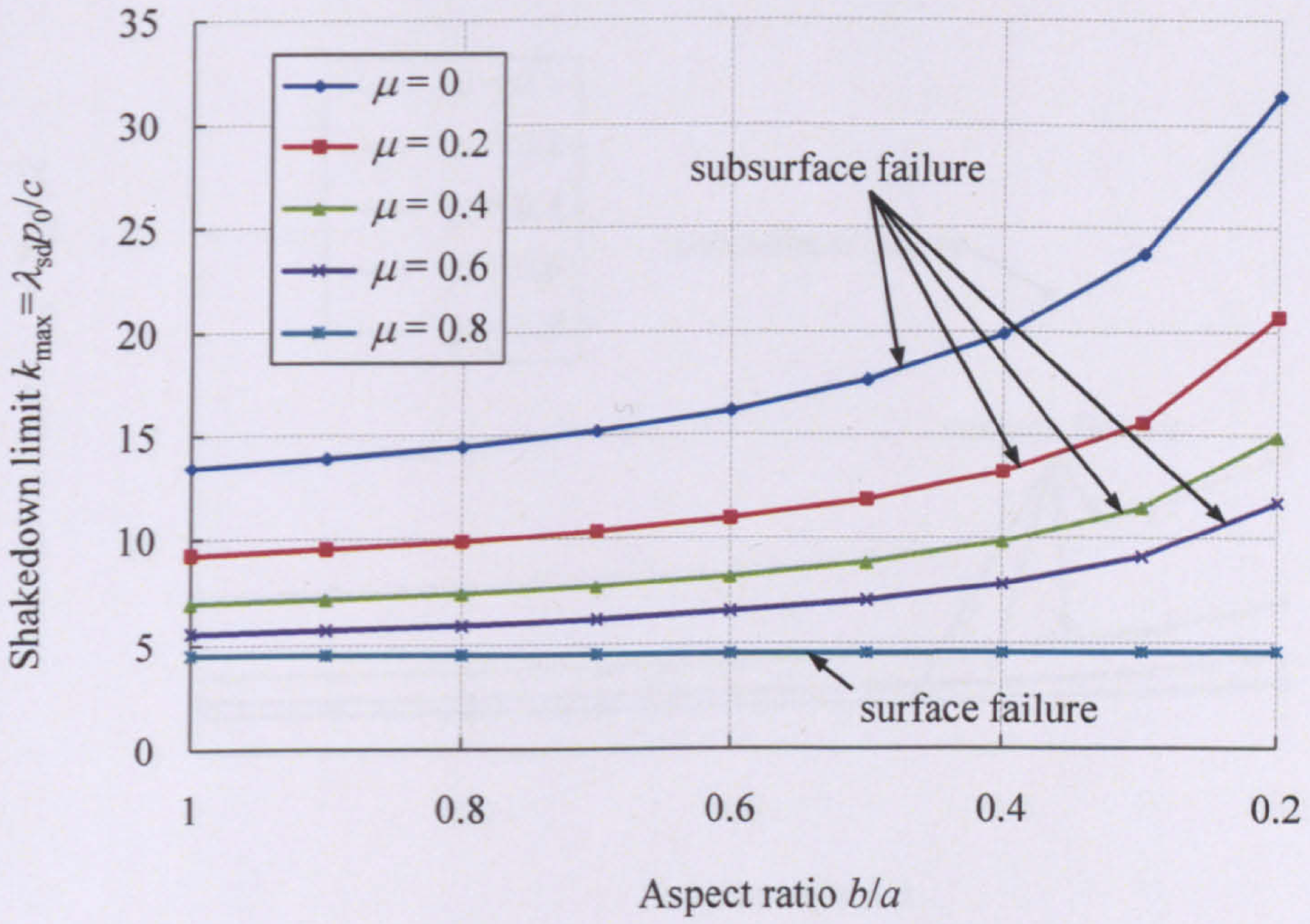

Figure 4.27. 3D shakedown limits $k_{\max}$ versus aspect ratios for various values of frictional coefficient when $\phi = 30°$

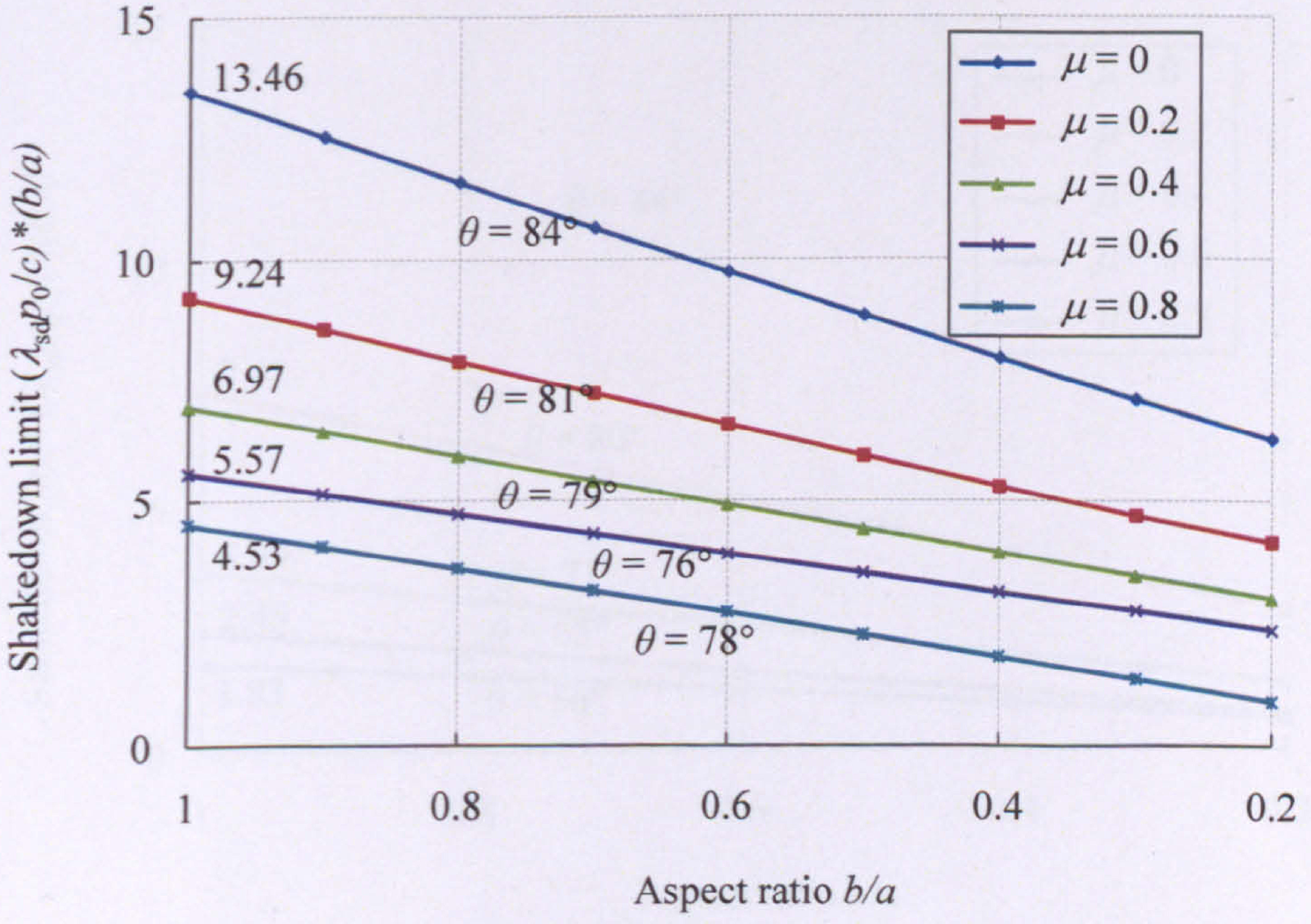

Figure 4.28. 3D shakedown limits $k_{\max} * (b/a)$ versus aspect ratios for various values of frictional coefficient when $\phi = 30°$

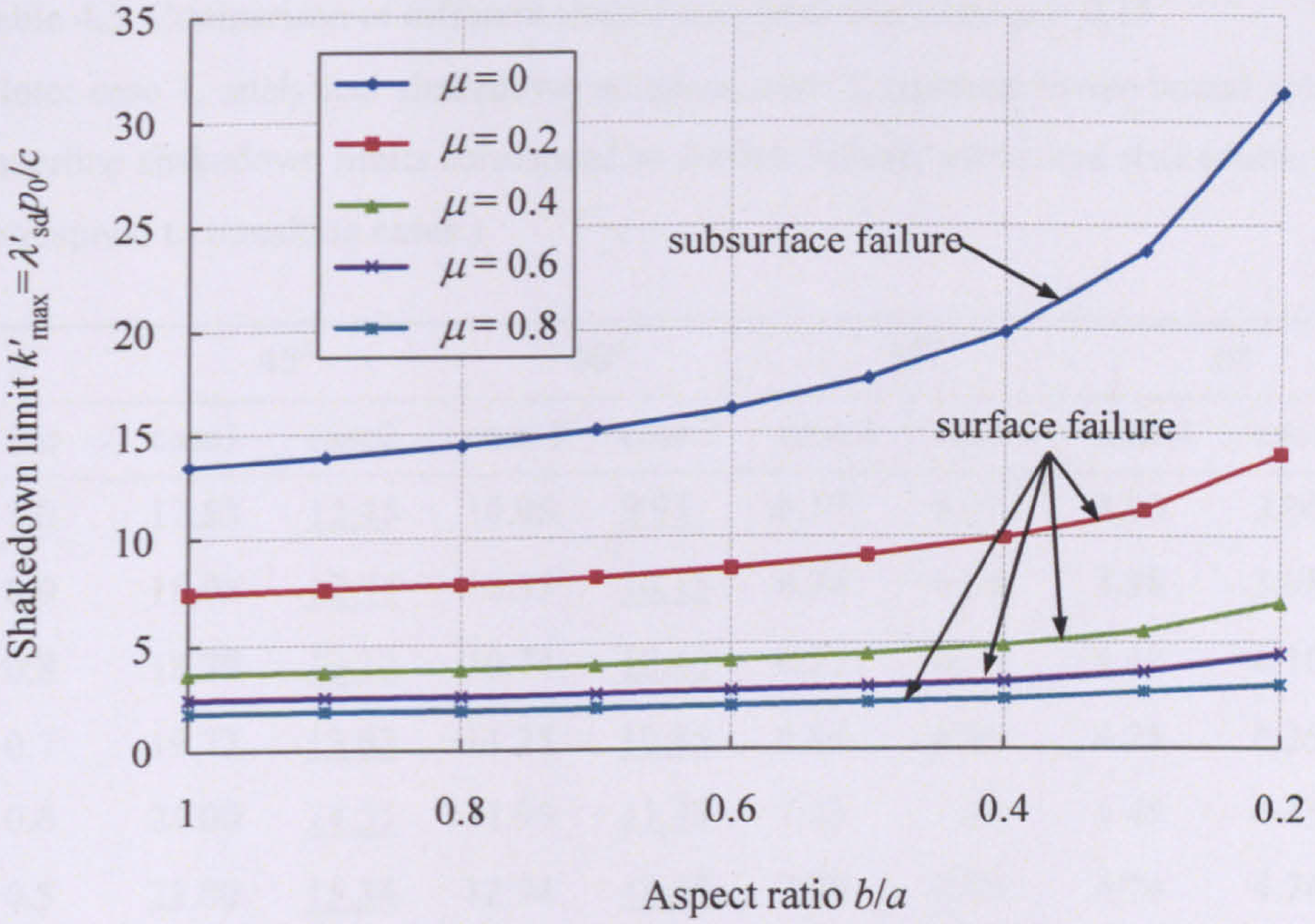

Figure 4.29. 3D shakedown limits $k'_{\max}$ versus aspect ratios for various values of frictional coefficient when $\phi = 30°$

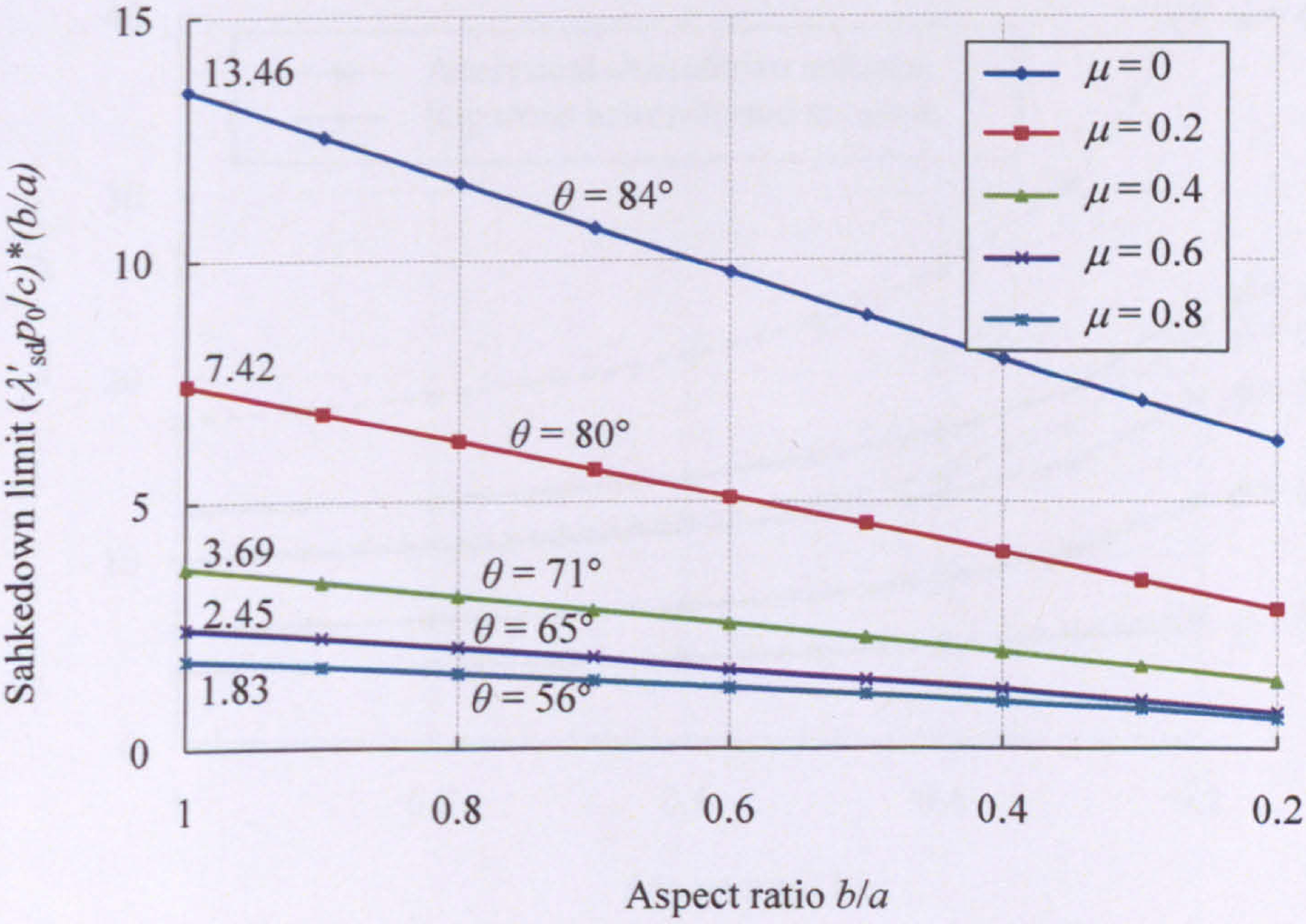

Figure 4.30. 3D shakedown limits $k'_{\max} *(b/a)$ versus aspect ratios for various values of frictional coefficient when $\phi = 30°$

Table 4.5. Comparison of different shakedown solutions when $\mu = 0.15$

(Note: case 1, analytical shakedown solution; case 2, rigorous lower-bound solution; underline shakedown limits correspond to surface failure; asterisked shakedown limits correspond to transition cases.)

ϕ	45°		30°		15°		0°	
b/a	case1	case2	case 1	case 2	case 1	case 2	case 1	case 2
1.0	17.53	12.45	10.05	9.93	6.17	6.17	3.90	3.90
0.9	18.08	12.74	10.35	10.15	6.34	6.34	3.98	3.98
0.8	18.79	13.12	10.74	10.45	6.55	6.55	4.10	4.10
0.7	19.72	13.63	11.25	10.85	6.84	6.84	4.25	4.25
0.6	21.00	14.31	11.95	11.38	7.23	7.23	4.45	4.45
0.5	22.80	15.34	12.94	12.18	7.79	7.79	4.74	4.74
0.4	25.59	16.76	14.48	13.26	8.65	8.65	5.18	5.14*
0.3	30.22	19.12	17.08	15.08	10.10	10.10	5.90	5.57*
0.2	39.73	23.87	22.28	18.72	13.03	13.02*	6.70	6.00*

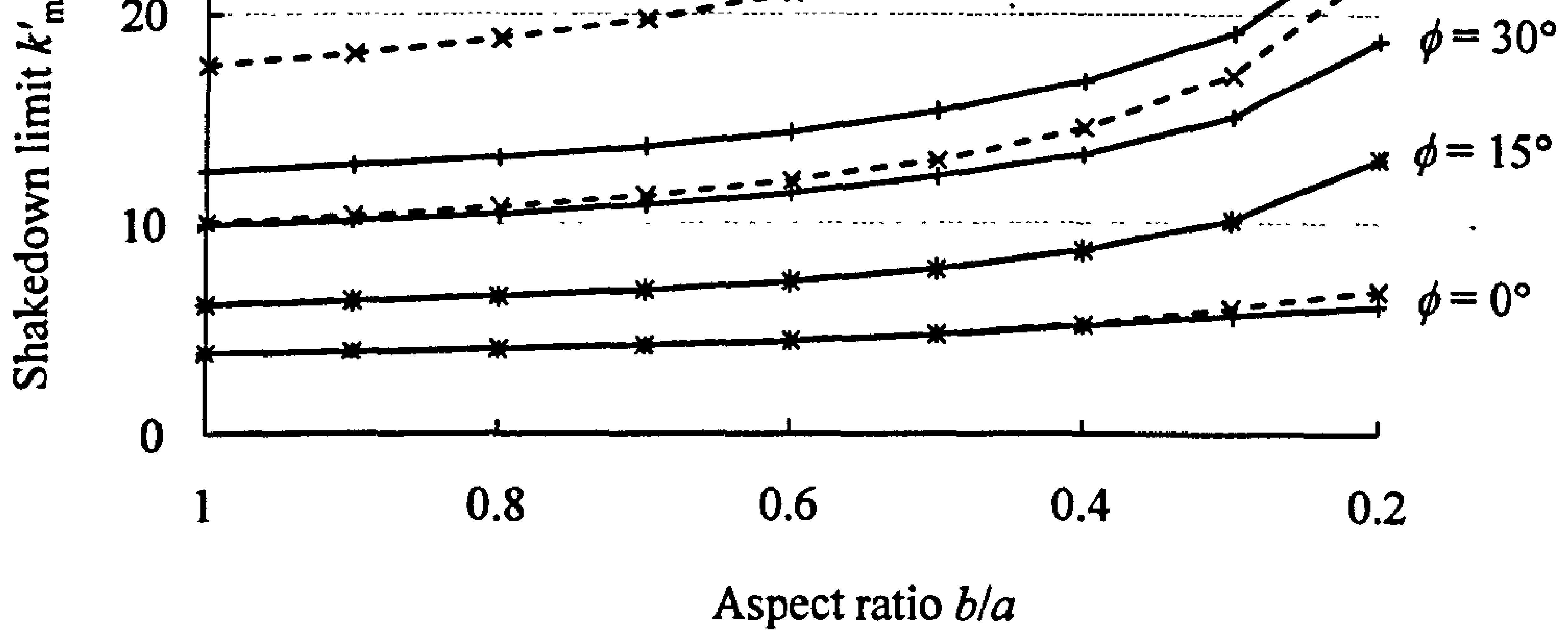

Figure 4.31. Comparison of shakedown limits from analytical shakedown solution and lower-bound solution for various friction angles and b/a when $\mu = 0.15$

Table 4.5 and Figure 4.31 compare the analytical shakedown solution and the rigorous lower-bound solution for various friction angles when the frictional coefficient is 0.15. As can be seen, differences between two solutions mainly appear when the friction angle is relatively high (ϕ = 30°, 45°) and the critical point in the lower-bound solution is initiated at the pavement surface. The difference tends to increase with decreasing aspect ratio. When the friction angle is relatively low (ϕ = 0°, 15°), both solutions are identical in most cases and their critical points mostly lie within the half-space. Transition cases only occur when the aspect ratio b/a and soil friction angle ϕ are both very small and they give rise to a little difference between the lower-bound and the analytical shakedown solutions.

4.6.5 Residual stress distributions

The influence of aspect ratio on the critical residual stress fields at the shakedown limit is shown in Figure 4.32. Clearly, for each case studied here, two critical residual stress fields converge at one critical point beneath the pavement surface. Moreover, with the reduction of aspect ratio b/a, the critical point gradually moves towards the surface. Similar to the results for shakedown of pavements with circular contact area (see Figure 4.12), the critical points for cases b/a = 0.8 and 0.6 occur at the peak points of the compressive (negative) minimum larger root. However, when b/a = 0.4, the critical point lies a little away from the peak point and this probably leads to the transition case in the lower-bound shakedown solution.

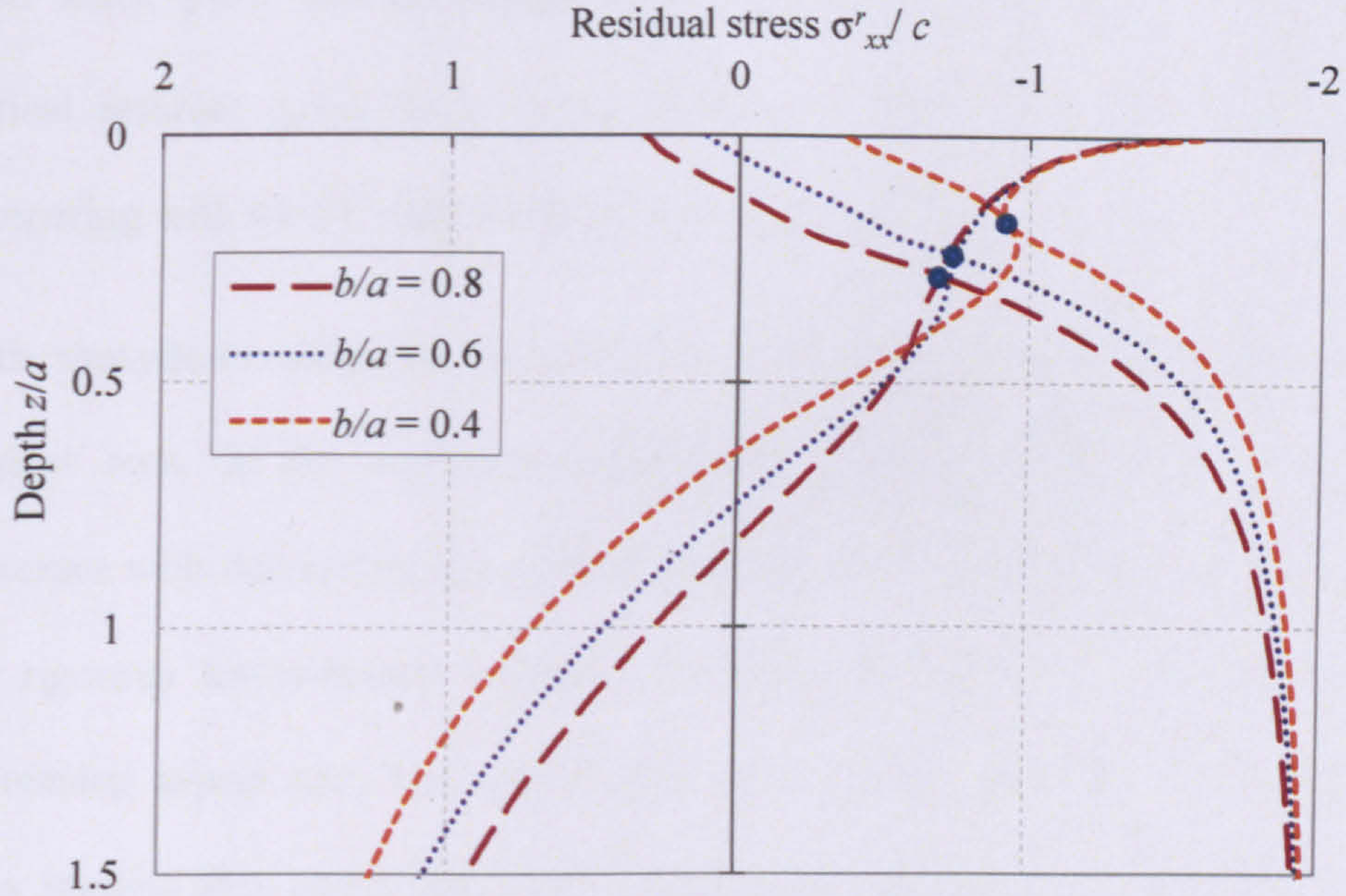

Figure 4.32. Critical residual stress fields for various aspect ratios when $\phi = 0°$ and $\mu = 0.15$

4.7 Conclusions

An analytical shakedown solution and a rigorous lower-bound shakedown solution to the stability problem of pavements subjected to 2D and 3D moving surface loads have been derived. The analytical shakedown solution gives a necessary condition for shakedown, while the rigorous lower-bound solution provides a lower-bound to the shakedown limit by using a self-equilibrated critical residual stress field.

For the single-layered pavements, the shakedown limit is dependent on the surface frictional coefficient and soil friction angle. The rigorous lower-bound shakedown solution for 3D pavements is also slightly affected by the Poisson's ratio when $\phi \neq 0$ and the critical point lies on the pavement surface. The critical residual stress fields at the shakedown limit have been verified by comparing with the FE calculated residual stress fields.

Both shakedown solutions have been extended to pavements with elliptical contact area. In the analytical shakedown solution, the shakedown limit increases with decreasing aspect ratio *b/a* only for subsurface failure cases. In the rigorous lower-bound solution, the shakedown limit can be raised by decreasing aspect ratio for both surface failure and subsurface failure cases. This implies that under the same contact area, the pavement with elliptical contact shape is able to afford more loads than the one with circular contact shape.

Generally speaking, the rigorous lower-bound solution is lower than the analytical shakedown solution for cases when the critical point lies on the surface of the pavement (i.e. rolling with significant sliding). However these solutions are identical for cases when the critical point lies within the pavement (i.e. rolling with limited sliding). For pavements with elliptical contact area, some transition cases may exist in the rigorous lower-bound solution, which give slightly lower shakedown limits than those in the analytical shakedown solution even when subsurface failure occurs. These transition cases only appear when the friction angle and aspect ratio are both very small.

Solutions derived in this chapter can be used to verify and benchmark numerical shakedown results.

CHAPTER 5

SHAKEDOWN ANALYSIS OF MULTI-LAYERED ROAD PAVEMENTS

5.1 Introduction

Shakedown analysis in Chapter 4 is concerned with isotropic, homogenous single-layered road pavements. In reality, the road pavements consist of several layers of different materials. For the purpose of practical pavement design, approaches to shakedown analysis of multi-layered road pavements are developed in the present chapter. These approaches are based on the shakedown solutions in Chapter 4 and take into account the variation of material properties.

The proposed approaches are first validated through comparing with the results in Chapter 4 for single-layered road pavements. Then, they are applied to two-layered road pavements when subjected to 2D or 3D moving surface loads. The influences of material properties and layer thicknesses are examined in detail and the results are compared with other authors' solutions. Shakedown analyses are also carried out in order to compare with experimental results of Juspi (2007). Finally, a simple design procedure using the shakedown theory is developed for layered pavements.

5.2 Approaches to shakedown analysis of layered road pavements

5.2.1 Analytical shakedown solution for layered pavements

For the problem considered here that the material properties vary from one layer to another, Equation (4.12) should be modified to take the layered system into account. The modified equation is given as follows:

$$\begin{aligned} \lambda_{sd} &= \min\left(\lambda_{sd}^{1}, \lambda_{sd}^{2}, \cdots, \lambda_{sd}^{m}\right), \\ \lambda_{sd}^{n} &= \frac{c_n}{\max\left(\left|\sigma_{xz}^{e}\right| + \sigma_{zz}^{e} \tan\phi_n\right)}, \end{aligned} \tag{5.1}$$

where

c_n : soil cohesion at *n*th layer,

ϕ_n : soil friction angle at *n*th layer,

σ_{ij}^{e} : elastic stresses induced by unit pressure,

λ_{sd}^{n} : analytical shakedown limit parameter for *n*th layer,

λ_{sd} : analytical shakedown limit parameter for the layered pavement.

Moreover, elastic stress fields in the layered structure are much more complicated than those in a homogeneous half-space. They are dependent on material elastic parameters at each layer (Young's modulus E_n and Poisson's ratio υ_n) and so far have not yet been given by any closed form expression. Therefore, FE analyses for elastic stress fields are carried out by means of the FE software ABAQUS.

In order to implement shakedown analysis of layered pavements, the function $|\sigma^e_{xz}| + \sigma^e_{zz} \tan\phi_n$ is programmed into the user subroutine UVARM, which defines the function as an output variable for every integration point. As a result, in the ABAQUS output field, the integration point providing the maximum value of $|\sigma^e_{xz}| + \sigma^e_{zz} \tan\phi_n$ at each layer can be found and the shakedown limit parameter for each layer λ^n_{sd} can be calculated. According to Equation (5.1), the minimum one among the obtained λ^n_{sd} is taken as the analytical shakedown limit parameter λ_{sd} for the layered pavement.

5.2.2 Rigorous lower-bound shakedown solution for layered pavements

It is very difficult to obtain the rigorous lower-bound shakedown limit for layered pavements by only using the ABAQUS, since the lower-bound shakedown solution involves an optimisation procedure as outlined in Figure 4.4. Therefore, MATLAB is introduced to implement the lower-bound shakedown analysis.

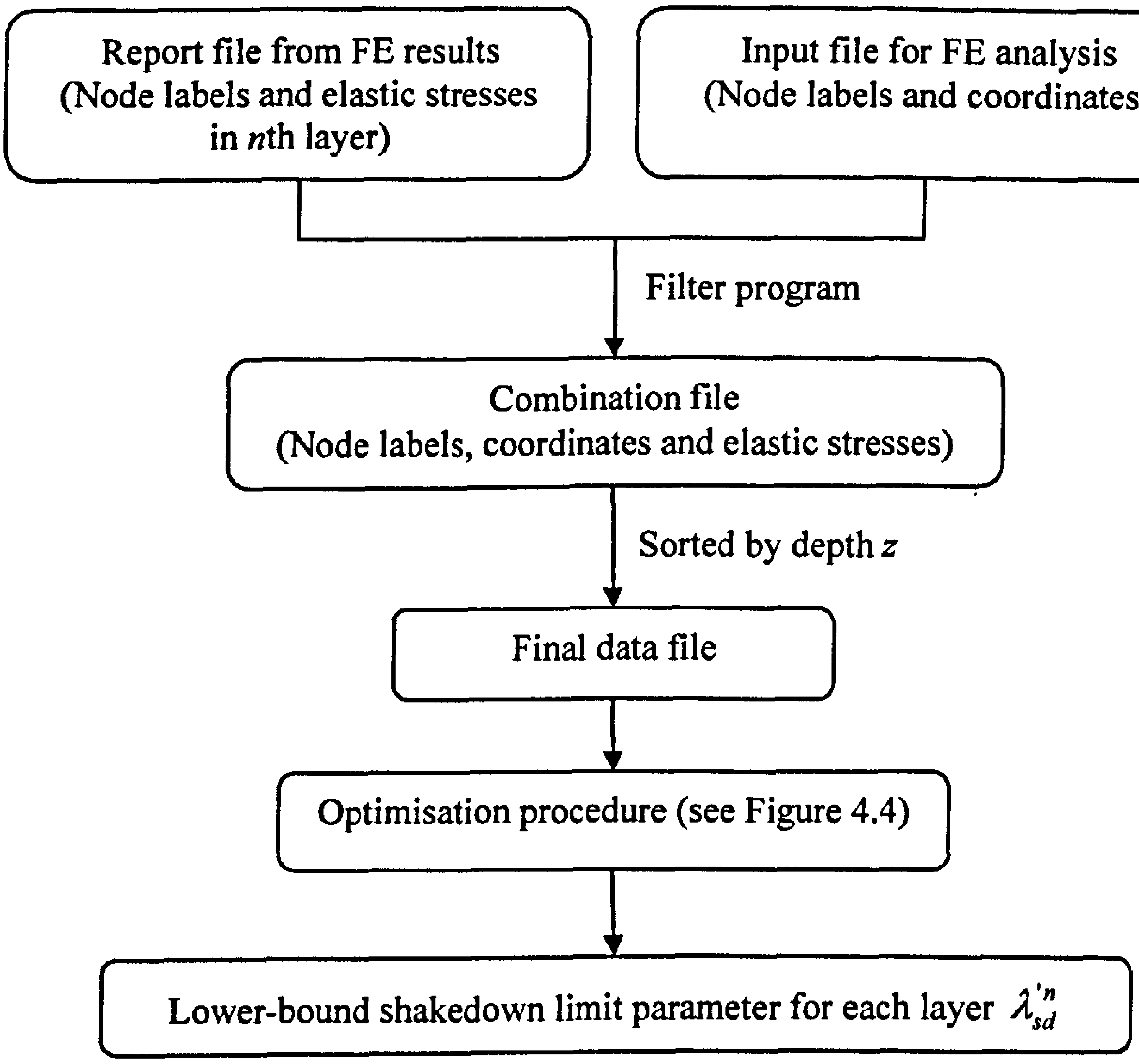

Figure 5.1. Flow chart for data processing in MATLAB

Figure 5.1 shows a program flow chart for the lower-bound shakedown analysis of layered pavements using the MATLAB. As can be seen, the initial data (coordinates and elastic stresses of every node) are taken from the FE analysis. The coordinate information of all nodes is stored in an input file, while the elastic stress information of each layer is recorded in sequence of node label in a report file.

For each layer, a filter program is used to match the coordinate of each node with the corresponding elastic stresses. The combined data are then sorted by depth z in order to determine the critical residual stresses at each depth (referred to Section 4.4). Using the optimisation procedure outlined in Figure 4.4, lower-bound shakedown limit parameter for *n*th layer $\lambda_{sd}^{'n}$ can be obtained, as well as the critical point in each layer. Finally, the lower-bound shakedown limit parameter for the layered pavement $\lambda_{sd}^{'}$ is the minimum one among all $\lambda_{sd}^{'n}$, as shown below:

$$\lambda_{sd}^{'} = \min\left(\lambda_{sd}^{'1}, \lambda_{sd}^{'2}, \cdots, \lambda_{sd}^{'m}\right). \tag{5.2}$$

5.3 FE models

5.3.1 2D model

Figure 5.2 presents a typical 2D plane strain FE model with first layer thickness h_1/D = 1. There are a restraint on horizontal movement at vertical boundaries and a restraint on vertical movement at bottom boundary. On the top surface, normal and shear loads (*P* and *Q*) are distributed as Equation (4.1), linked by a frictional coefficient $\mu = Q/P$. The size of the simulated region is chosen to be large enough so that boundary conditions have negligible effect on the shakedown limit. The half-space is discretised by eight-noded, reduced-integrated, quadrilateral elements (CPE8R). Very fine mesh is applied in the vicinity of loading area, as small as approximately 0.02*D* × 0.02*D*, to capture stresses in a reasonable accuracy. The half-space is assumed to be continuous with different material properties for each layer, and higher mesh density is applied near the interface between two layers.

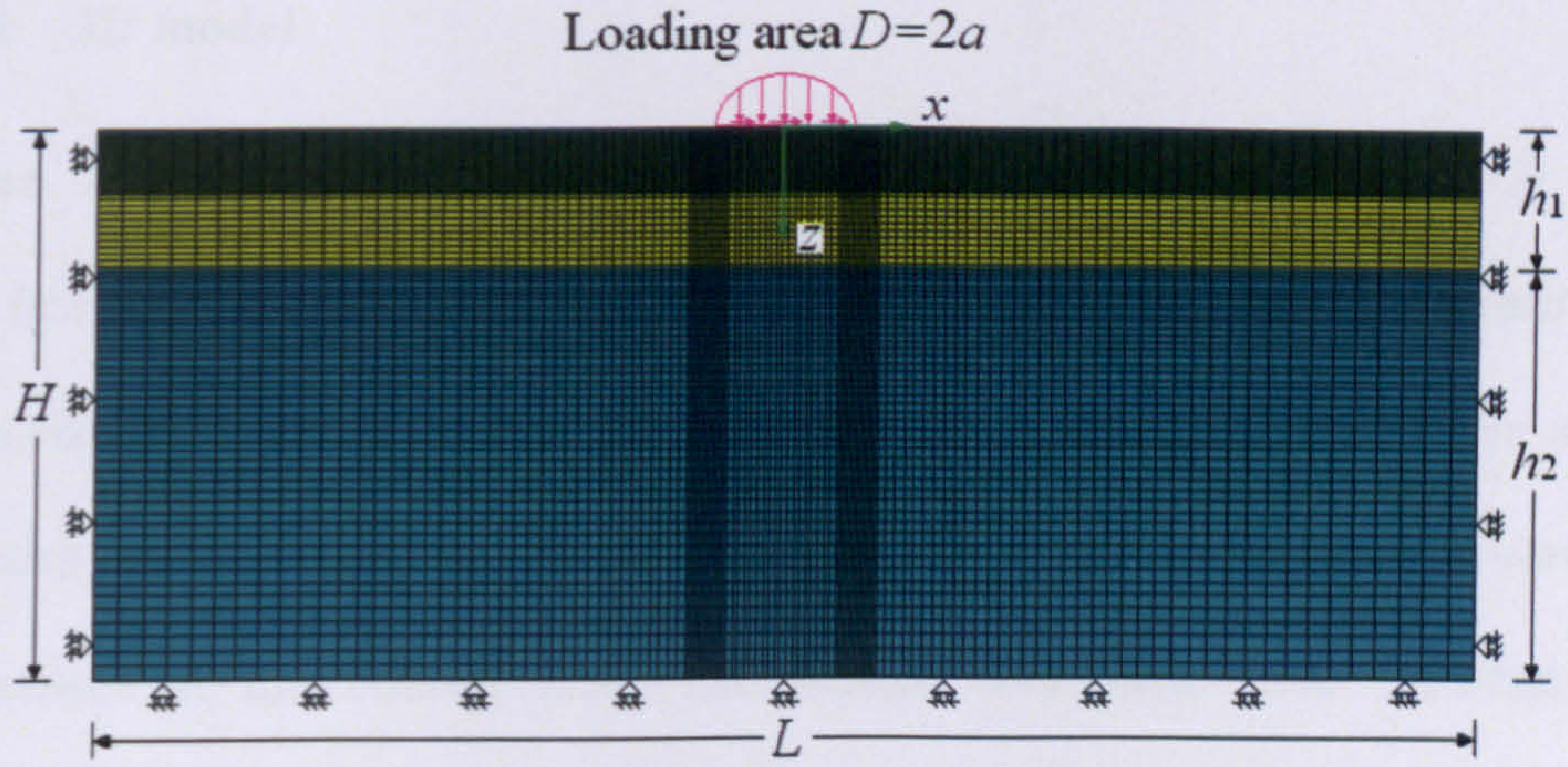

Figure 5.2. A typical 2D FE mesh and boundary conditions

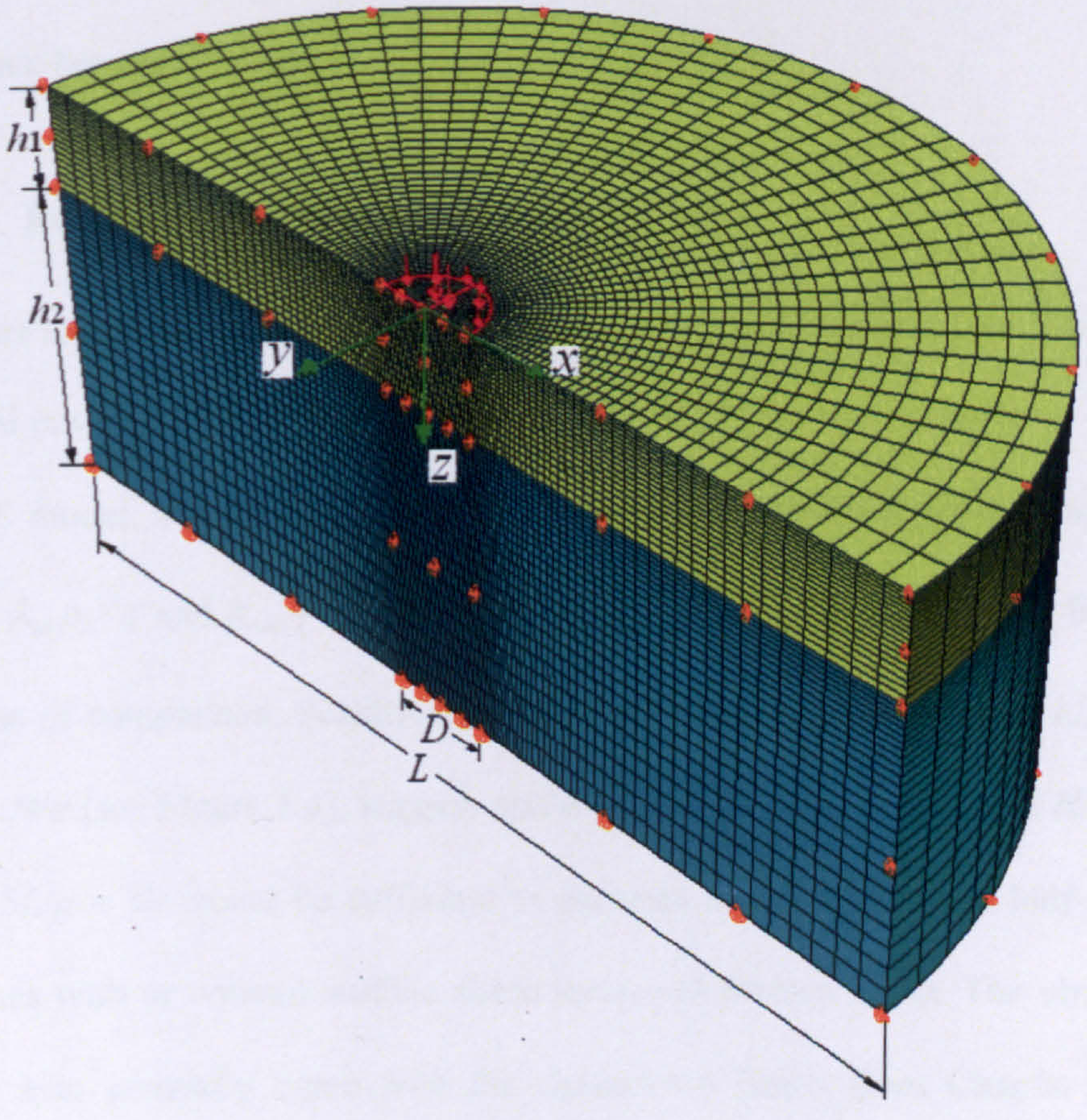

Figure 5.3. A typical 3D FE mesh and boundary conditions

5.3.2 3D model

Figure 5.3 shows a typical 3D FE model with first layer thickness $h_1/D = 1$. The front face $y = 0$ represents a plane of symmetry, and therefore a restraint on horizontal (but not vertical) movement is imposed on this face. There are a restraint on horizontal movement at the back face and a restraint on vertical movement at the bottom face. The normal and shear load distributions formulated as Equation (4.3) are applied on the top surface limited within a half circle due to the symmetric condition. The simulation region is discretised by twenty-noded, reduced-integrated, brick elements (C3D20R), and the mesh density is relatively high in the vicinity of the loading area and near the interface between two layers.

5.3.3 Results verification

In order to validate of the proposed approaches, shakedown analyses of single-layered pavements were first performed. Poisson's ratio was assumed as 0.3 in the FE model. The analytical and lower-bound shakedown limits, defined as $k_{\max} = \lambda_{sd} p_0 / c$ and $k'_{\max} = \lambda'_{sd} p_0 / c$ respectively, are presented in pairs for the purpose of comparison. Sensitive studies on the dimensions of length L/a and height H/a (see Figure 5.4), suggest that a mesh with the dimension of $H/a = 8$ and $0.5L/a = 10$ would be sufficient to accurate model the infinite half-space for cases with or without surface shear force and friction angle. The obtained results also generally agree with the shakedown limits from Chapter 4, as shown in Figure 5.5 for the 2D pavement model and in Figure 5.6 for the 3D pavement model.

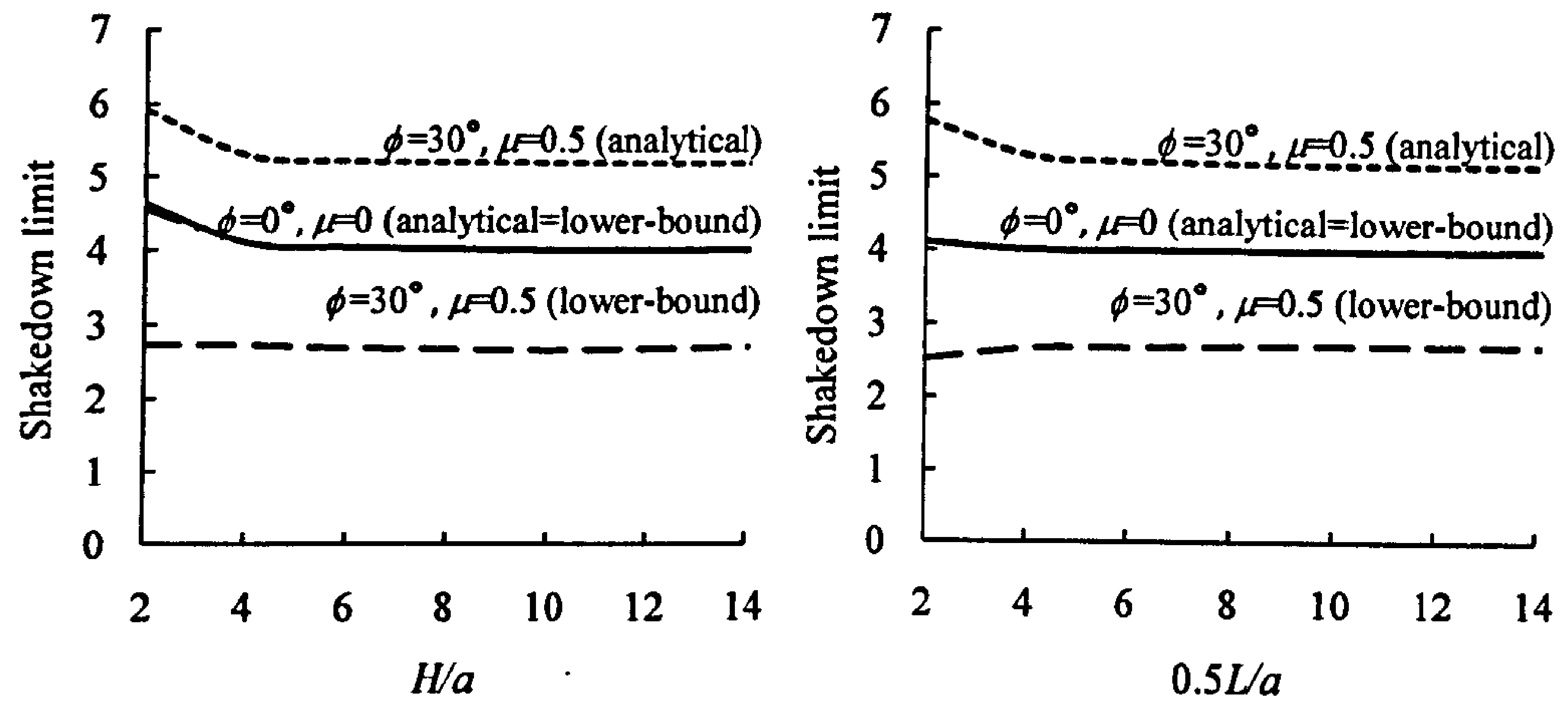

(a) (b)

Figure 5.4. Sensitive studies for shakedown limits of 2D pavement model

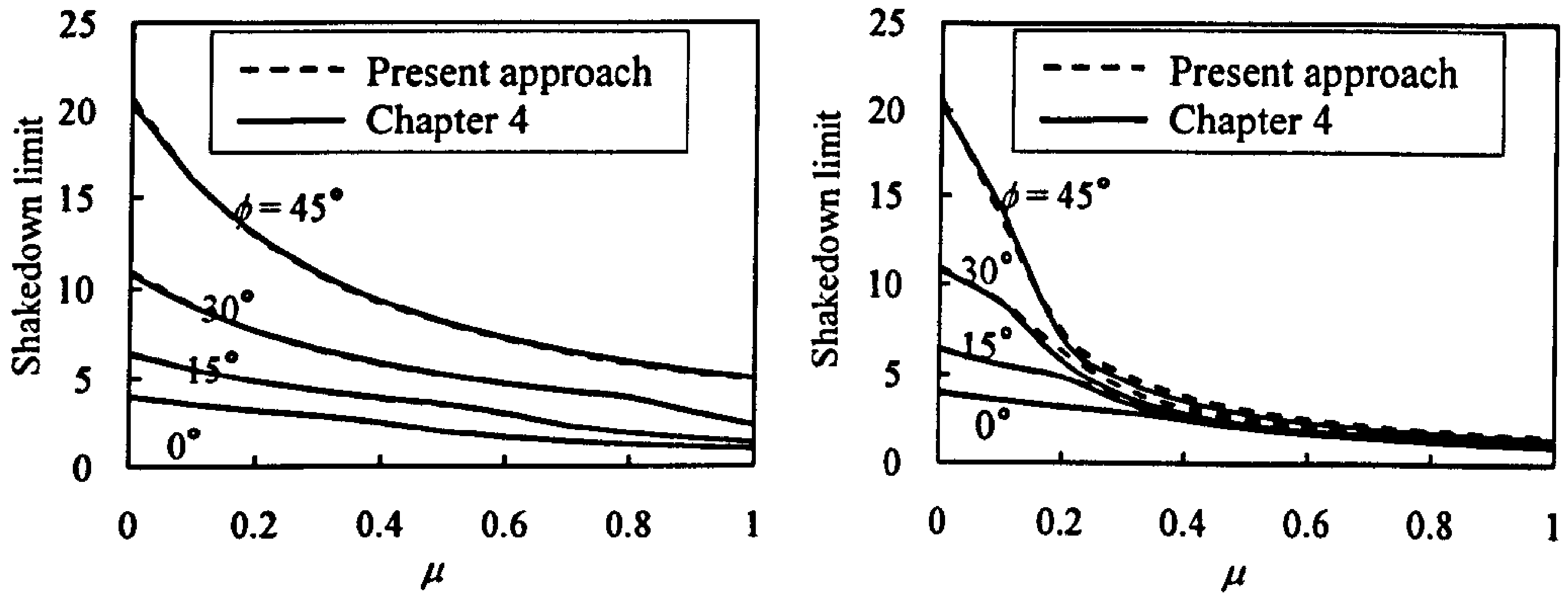

(a) Analytical shakedown limit (b) Rigourous lower-bound limit

Figure 5.5. Comparison of shakedown limits for 2D pavement model

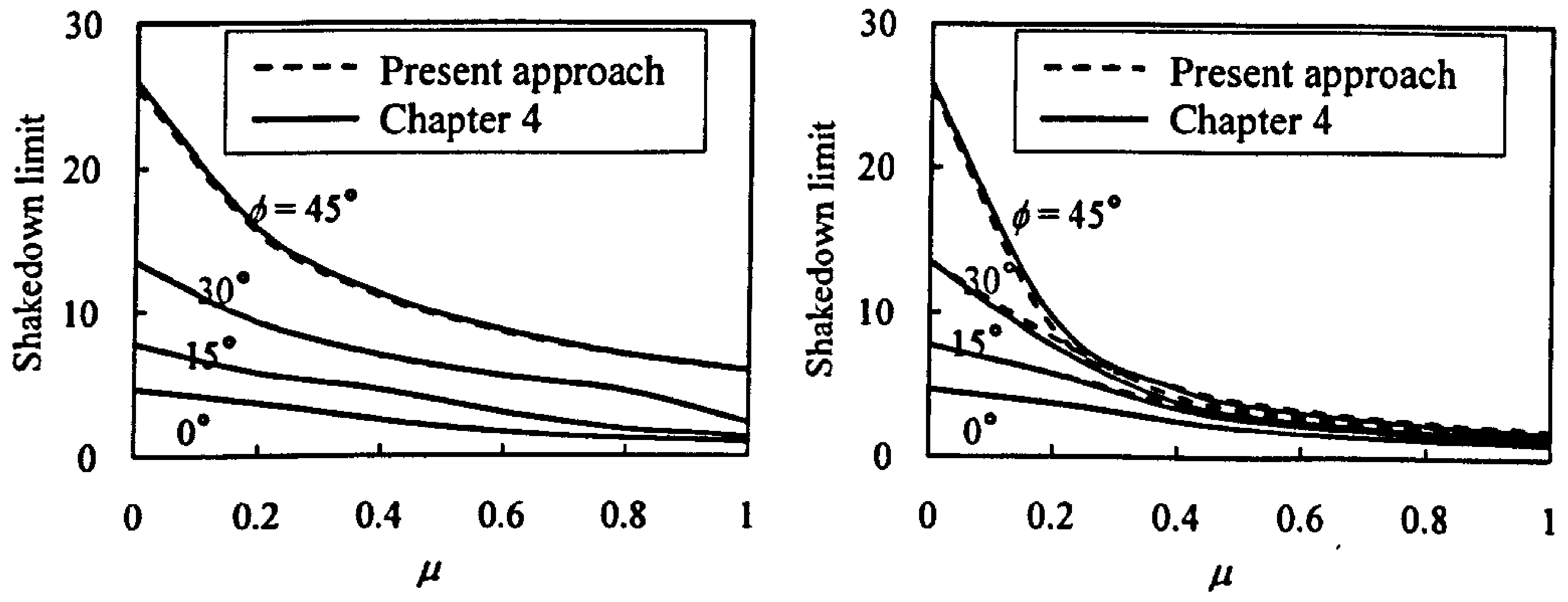

(a) Analytical shakedown limit (b) Rigorous lower-bound limit

Figure 5.6. Comparison of shakedown limits for 3D pavement model

5.3.4 UVARM distributions

ABAQUS is able to output the contour of UVARM, which is defined as function $\left|\sigma_{xz}^{e}\right| + \sigma_{zz}^{e} \tan\phi$. Figure 5.7 and Figure 5.8 show typical UVARM distributions in the 2D and 3D pavement models. When $\phi = 0°$ and $p_0 = 1e4$, the maximum value of UVARM occurs beneath the surface for $\mu = 0$ and at the surface for $\mu = 0.5$. Compared with the Figure 5.7, Figure 5.8 shows similar UVARM contours on the most critical plane $y = 0$. However, the maximum value of UVARM in the 2D model is larger than that in the 3D model. As a result, the 2D shakedown limit is smaller than the 3D shakedown limit.

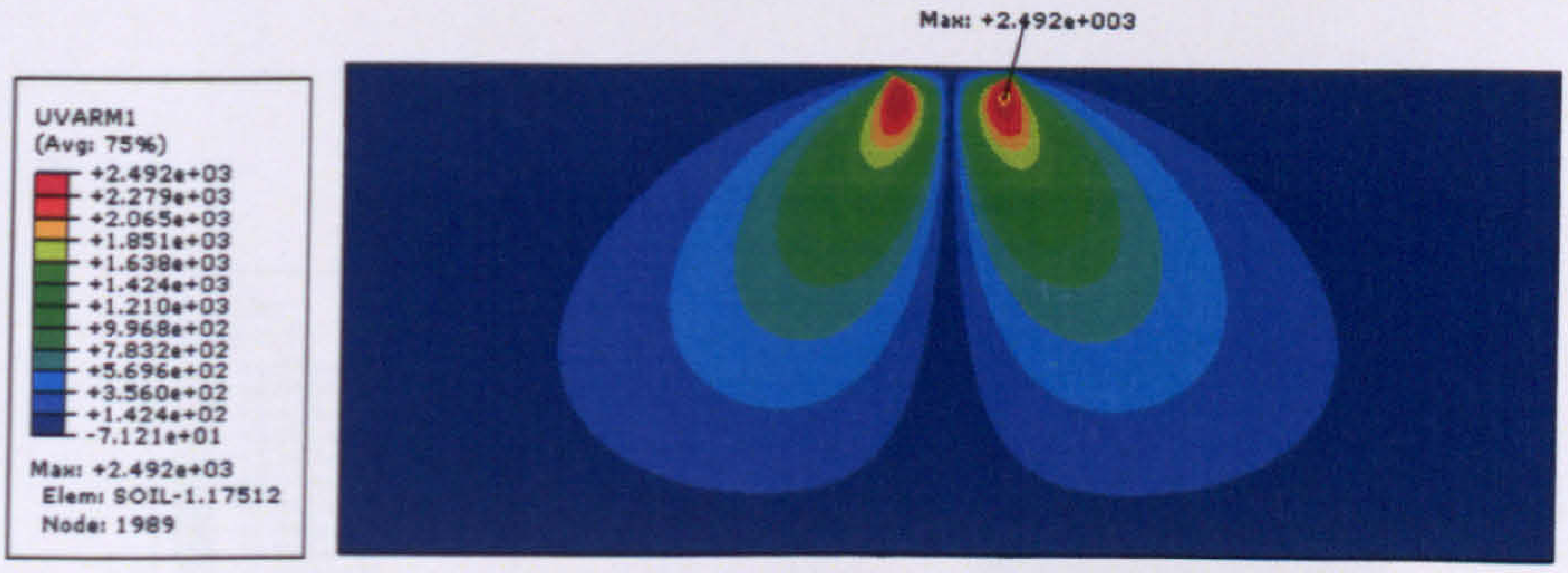

(a) $\mu = 0$

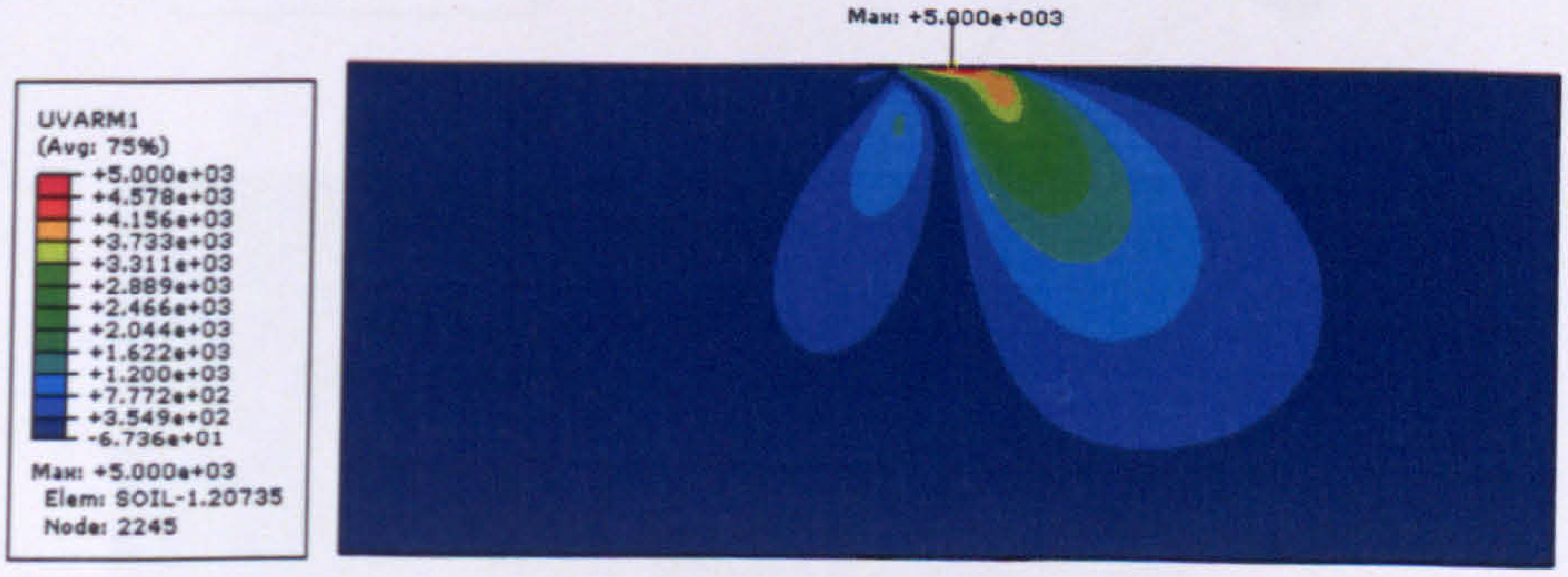

(b) $\mu = 0.5$

Figure 5.7. UVARM distributions in the 2D pavement models when $\phi = 0°$ and $p_0 = 1e4$

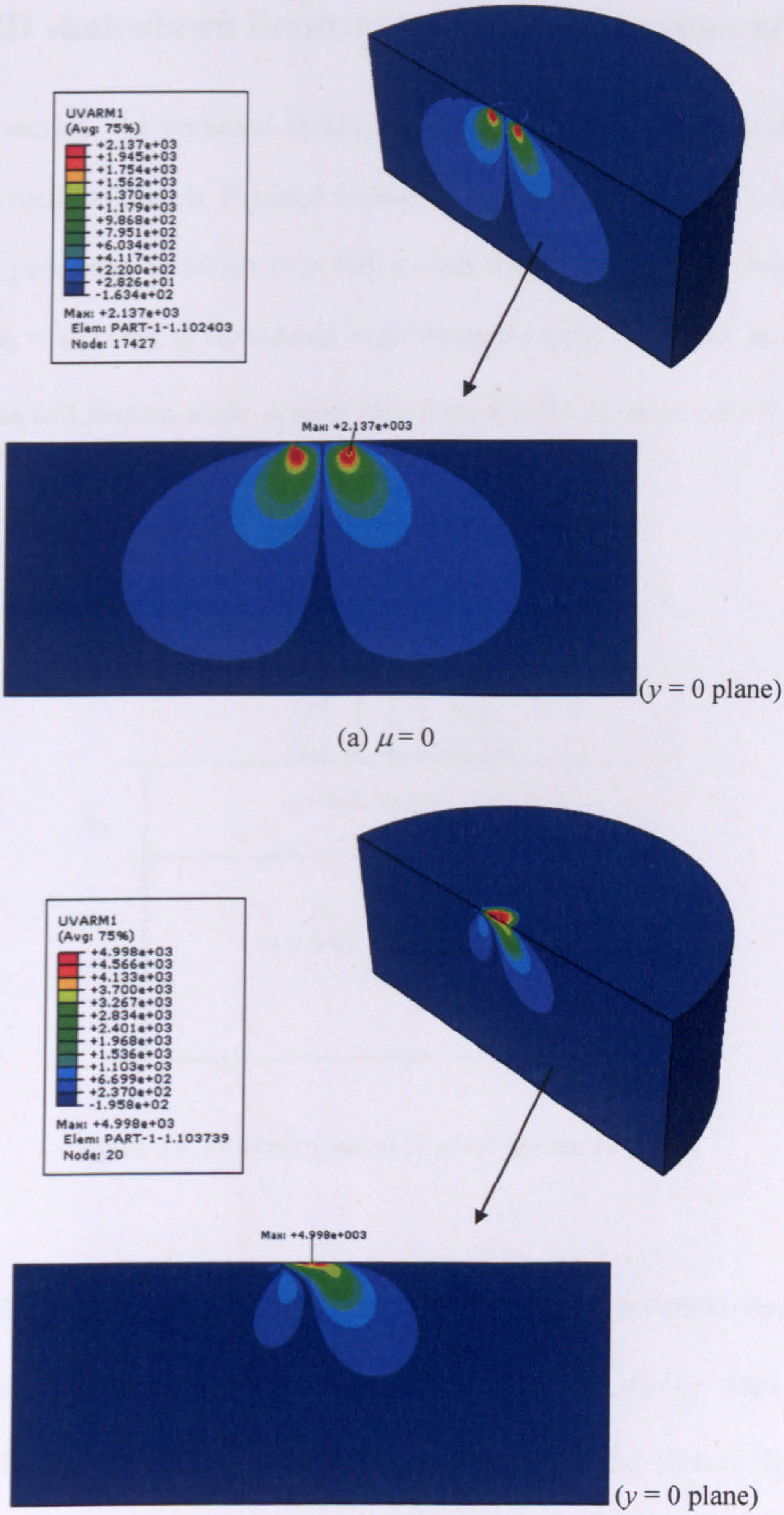

(a) $\mu = 0$

(b) $\mu = 0.5$

Figure 5.8. UVARM distributions in the 3D pavement models when $\phi = 0°$ and $p_0 = 1e4$

5.4 2D shakedown limits of two-layered pavements

In this section, the proposed shakedown approaches are applied to 2D two-layered road pavements. Figure 5.9 shows the problem notation of a 2D two-layered pavement, in which D is full contact width. A pure cohesive second layer ($\phi_2 = \psi_2 = 0°$) is considered, with Poisson's ratio $\upsilon_2 = 0.49$. In the first layer, the soil friction angle ϕ_1 may vary from 0 to 45 degrees, with Poisson's ratio $\upsilon_2 = 0.2$.

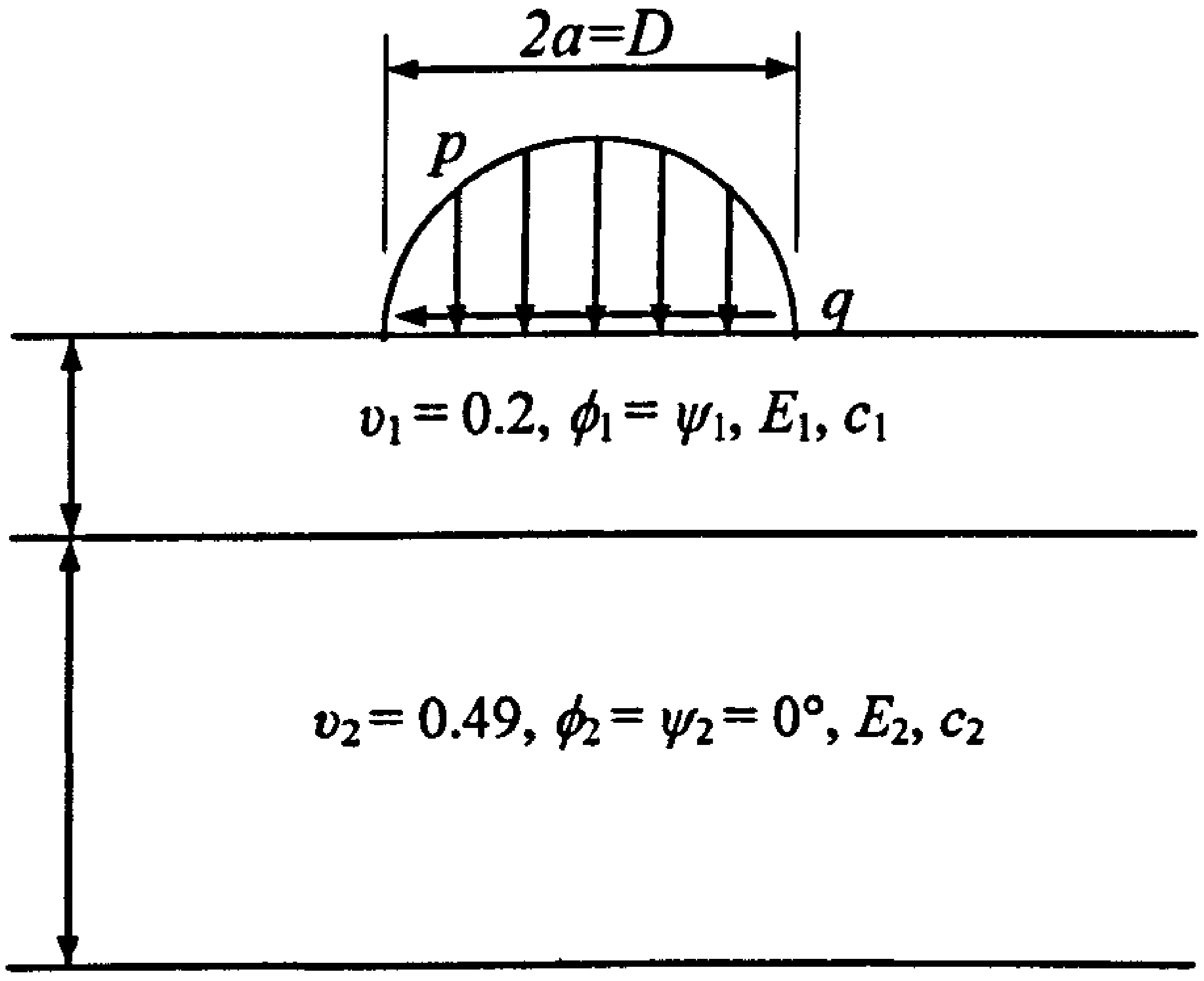

Figure 5.9. Problem notation of a two-layered pavement

In the following studies, the normalised analytical and lower-bound shakedown limits are represented as $k_{\max} = \lambda_{sd} p_0 / c_2$ and $k'_{\max} = \lambda'_{sd} p_0 / c_2$ respectively. These shakedown limits are not only dependent on the surface frictional coefficient and soil friction angle, but also on material stiffness ratio E_1/E_2, strength ratio c_1/c_2 and normalised first layer thickness h_1/D.

5.4.1 Effect of stiffness ratio and frictional coefficient

Figure 5.10 demonstrates the influence of stiffness ratio E_1/E_2 on the 2D analytical shakedown limit for various values of strength ratio c_1/c_2 when $\mu = 0$ and $\mu = 0.5$. Clearly, at a given value of strength ratio, there always exists an optimum stiffness ratio that would provide the maximum resistance to pavement failure (i.e. the shakedown limit is maximised). For cases $c_1/c_2 > 1$, the shakedown limit firstly increases then decreases with the rise of E_1/E_2. The peak point indicates the change of critical point location from the second layer (increasing part) to the first layer (decreasing part). For cases $c_1/c_2 < 1$, failure always occurs in the first layer, and therefore the shakedown limit keeps decreasing with increasing E_1/E_2.

Figure 5.11 shows the effect of stiffness ratio on the 2D lower-bound shakedown limit. Compared with Figure 5.10, the lower-bound shakedown limit after the peak point drops more quickly with increasing E_1/E_2, associated with the optimum stiffness ratio moving left. For case $\mu = 0$, both solutions (Figure 5.10(a) and Figure 5.11(a)) are identical when the critical point is located at the top of the second layer (increasing part) or within the first layer (occurs when c_1/c_2 and E_1/E_2 are both small). However, they are different when the critical point occurs at the base of the first layer. For case $\mu = 0.5$, the lower-bound shakedown limits (Figure 5.10(b)) are smaller than the analytical shakedown limits (Figure 5.11(b)) when the critical point lies on the surface of the first pavement layer (decreasing part).

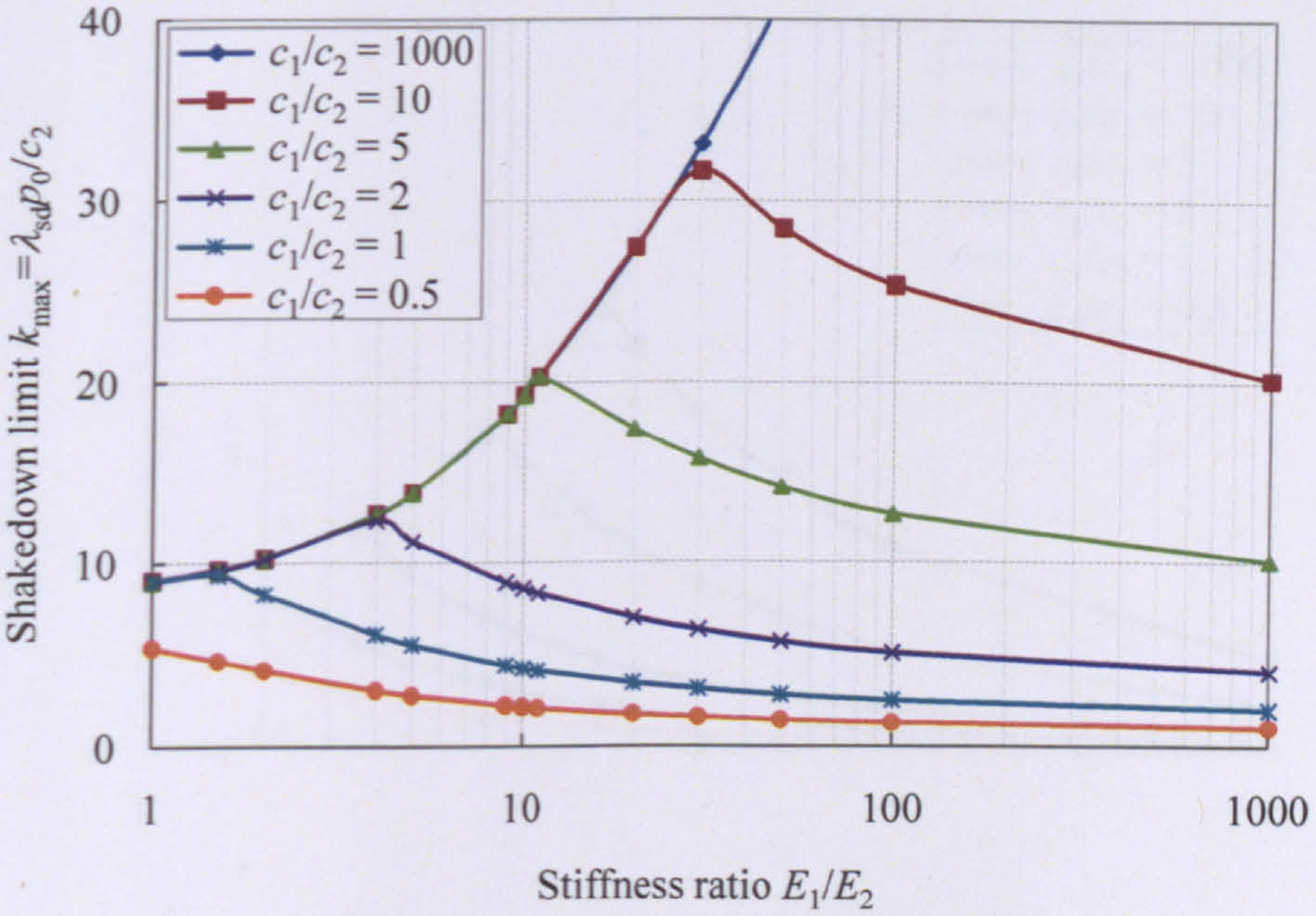

(a) $\mu = 0$

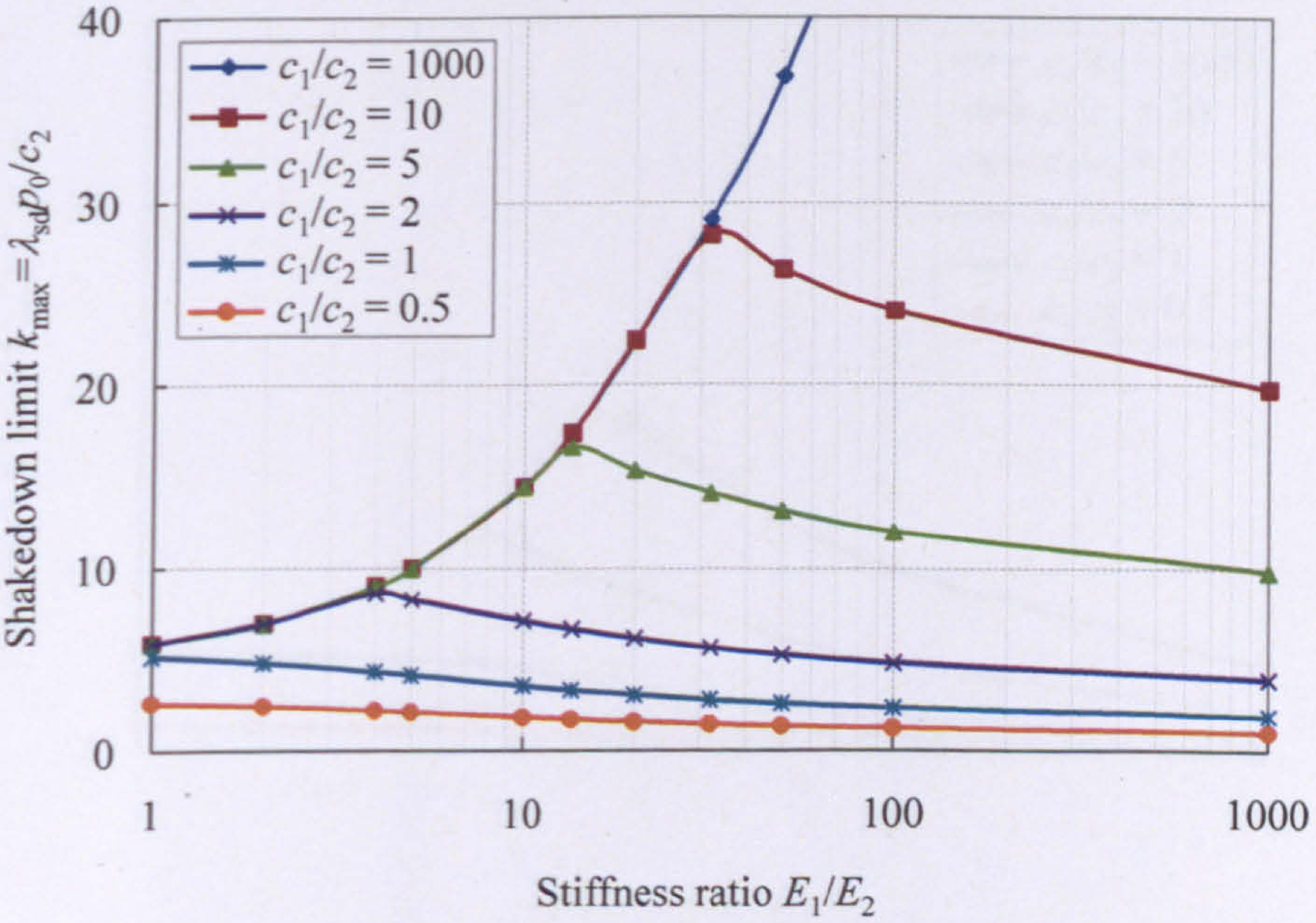

(b) $\mu = 0.5$

Figure 5.10. 2D analytical shakedown limits versus stiffness ratios for various values of strength ratio when $h_1/D = 1$ and $\phi_1 = 30°$

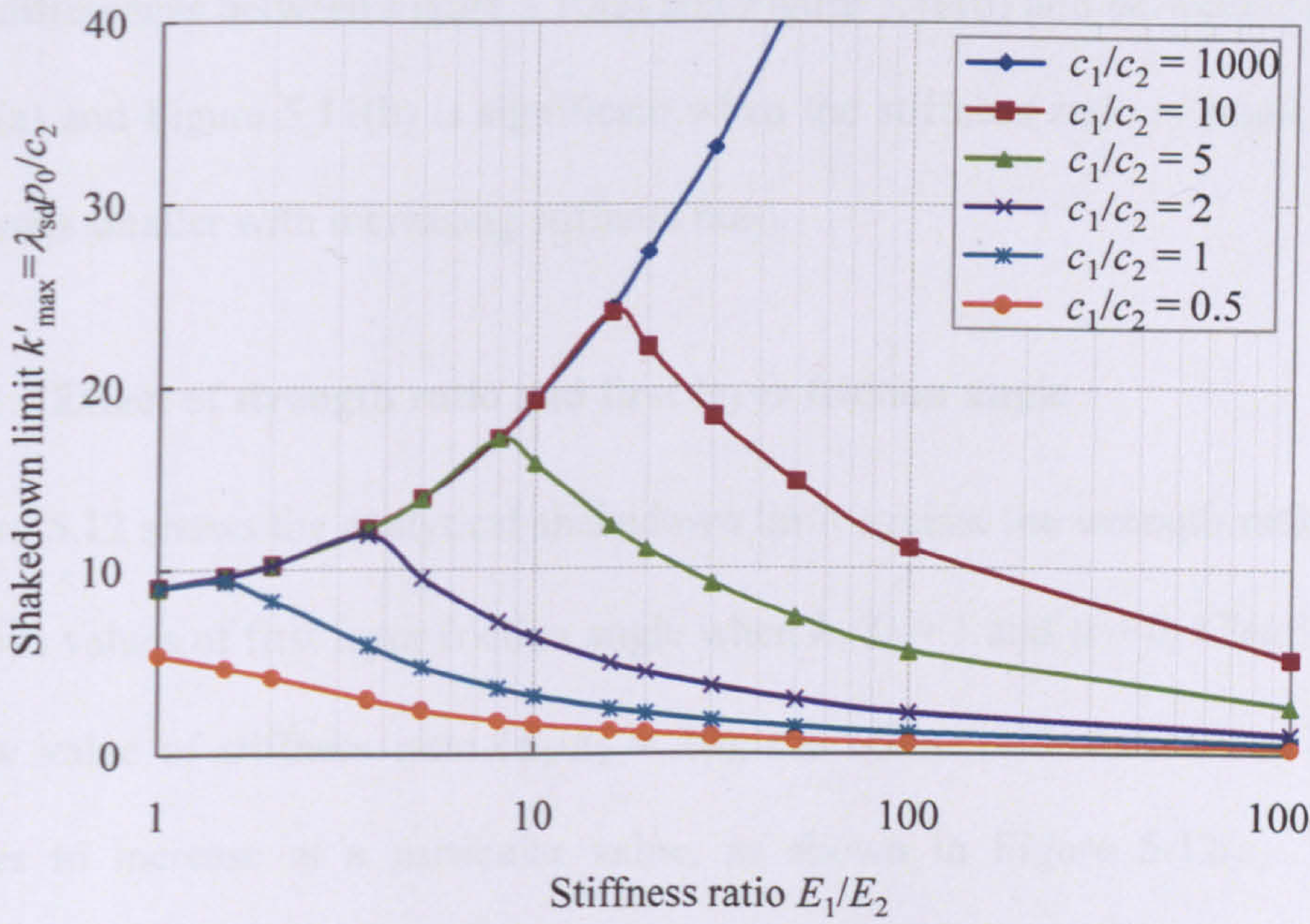

(a) $\mu = 0$

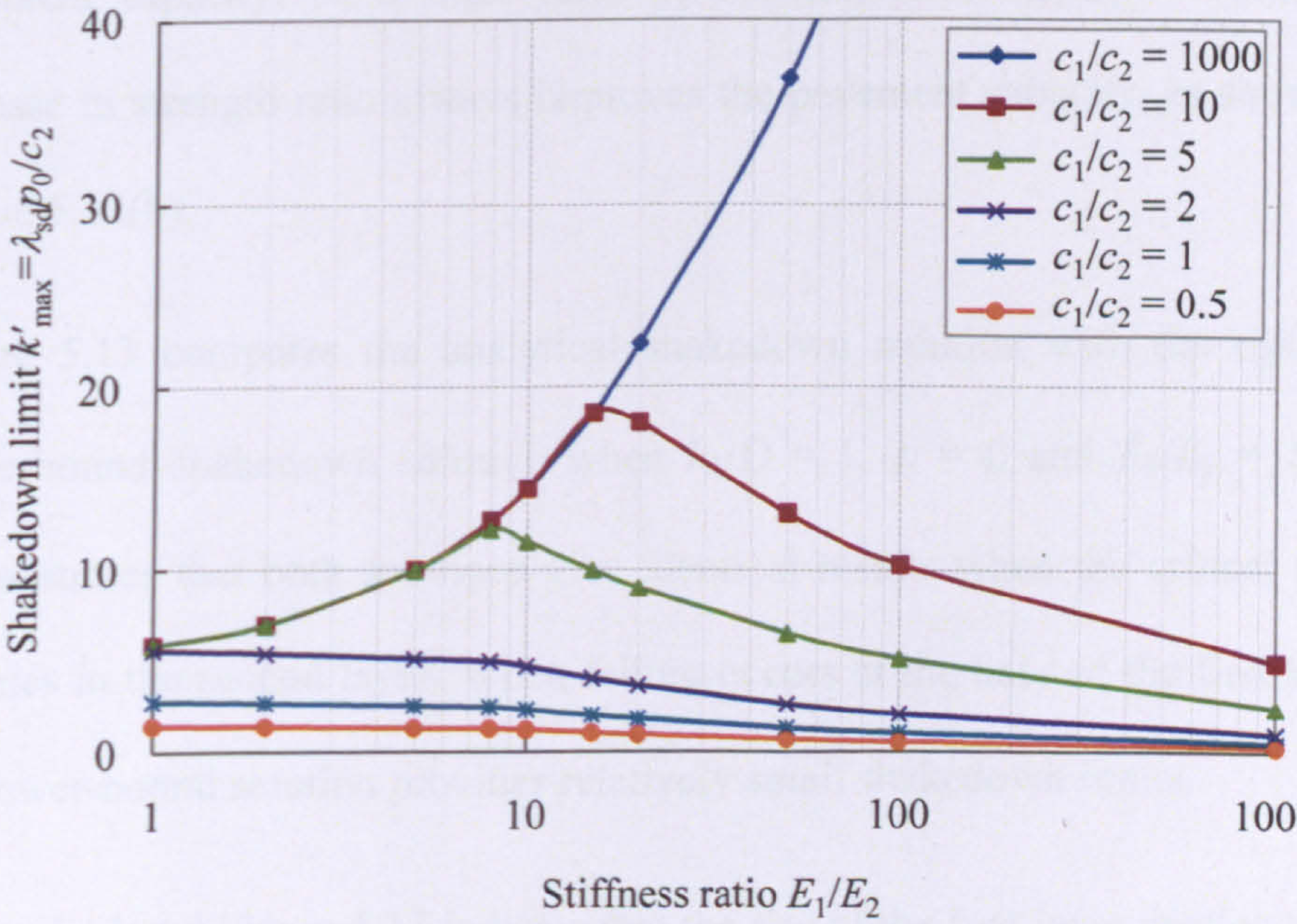

(b) $\mu = 0.5$

Figure 5.11. 2D lower-bound shakedown limits versus stiffness ratios for various values of strength ratio when $h_1/D = 1$ and $\phi_1 = 30°$

The differences between Figure 5.10(a) and Figure 5.10(b) and between Figure 5.11(a) and Figure 5.11(b) is significant when the stiffness ratio is small, and becomes smaller with increasing stiffness ratio.

5.4.2 Effect of strength ratio and first layer friction angle

Figure 5.12 shows the analytical shakedown limit against the strength ratio for various values of first layer friction angle when $h_1/D = 1$ and $\mu = 0$. Clearly, at a low value of stiffness ratio ($E_1/E_2 = 10$), the normalised shakedown limit ceases to increase at a particular value, as shown in Figure 5.12(a). This indicates that the critical point location transfers from the first layer to the second layer. Further increase of the strength ratio will not improve the pavement capacity. At a high value of stiffness ratio ($E_1/E_2 = 1000$), an increase in strength ratio always improves the pavement capacity, as shown in Figure 5.12(b).

Figure 5.13 compares the analytical shakedown solution with the rigorous lower-bound shakedown solution when $h_1/D = 1$, $\mu = 0$ and $E_1/E_2 = 10$. It demonstrates that both solutions give identical results when the critical point initiates in the second layer. When failure occurs at the base of the first layer, the lower-bound solution provides relatively small shakedown limits.

Figure 5.12 and Figure 5.13 indicate that the rise of the first layer friction angle obviously increases the pavement shakedown limit when the critical point lies in the first layer.

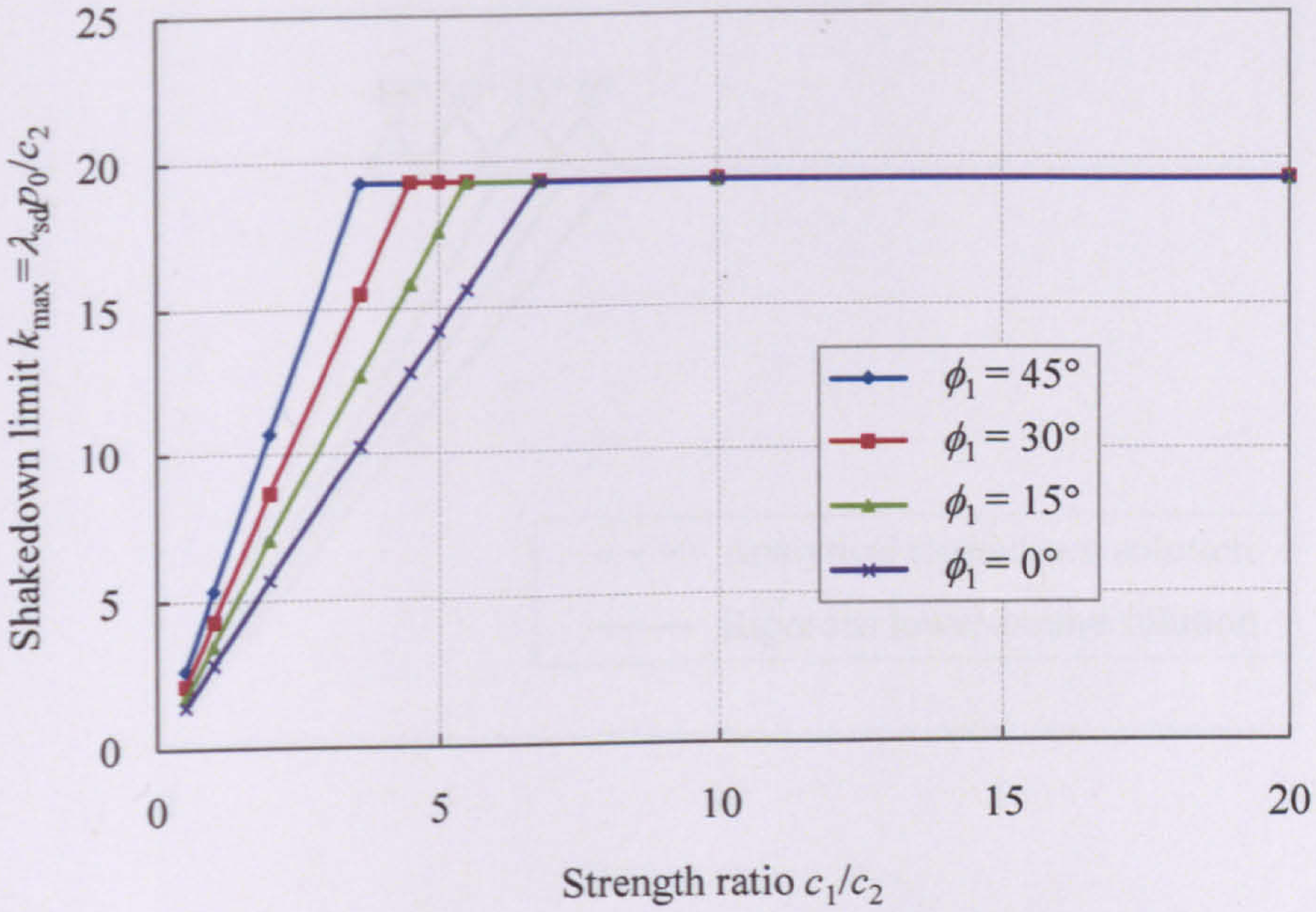

(a) $E_1/E_2 = 10$

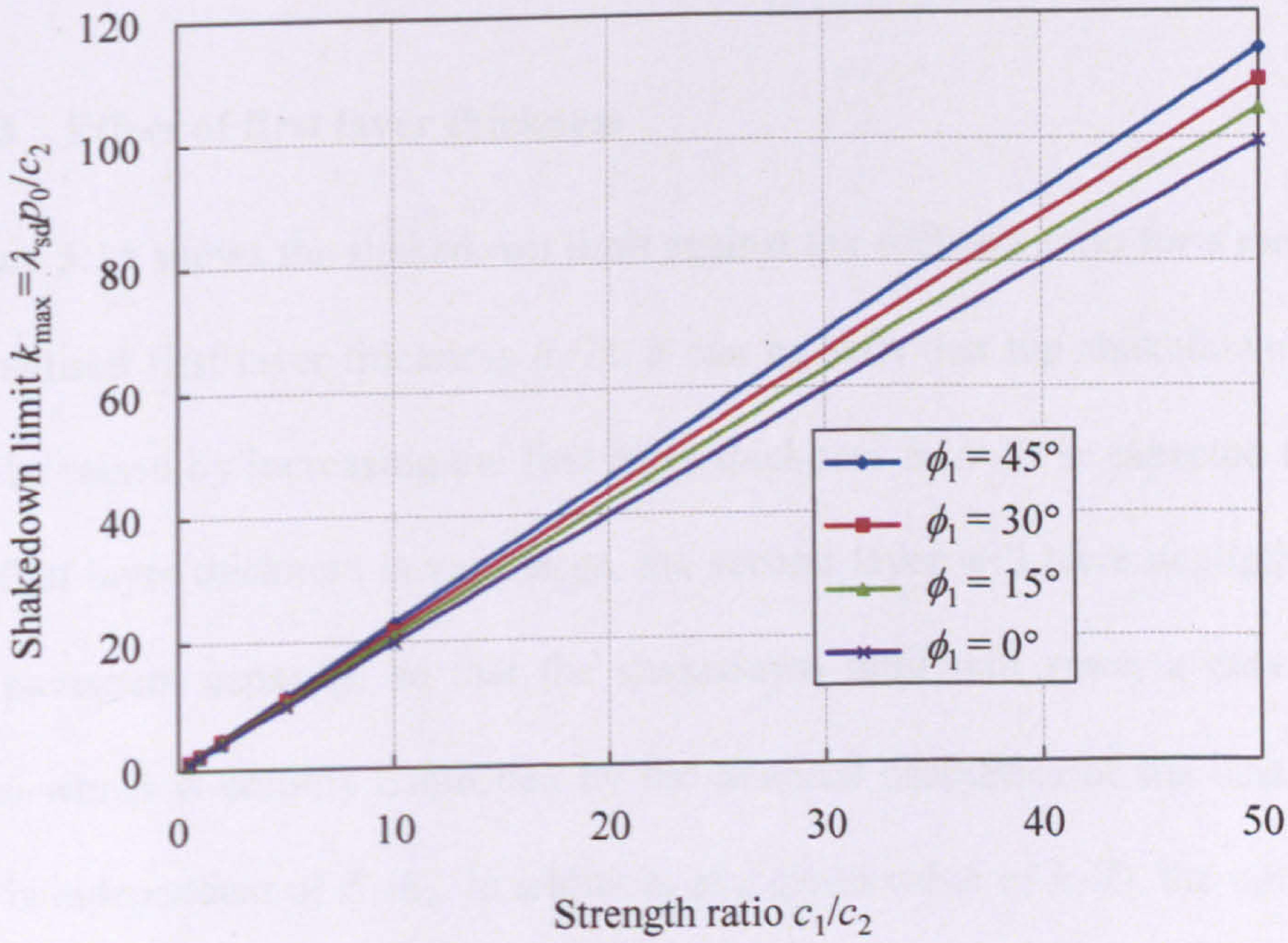

(b) $E_1/E_2 = 1000$

Figure 5.12. 2D shakedown limits versus strength ratios for various values of first layer friction angle when $h_1/D = 1$ and $\mu = 0$

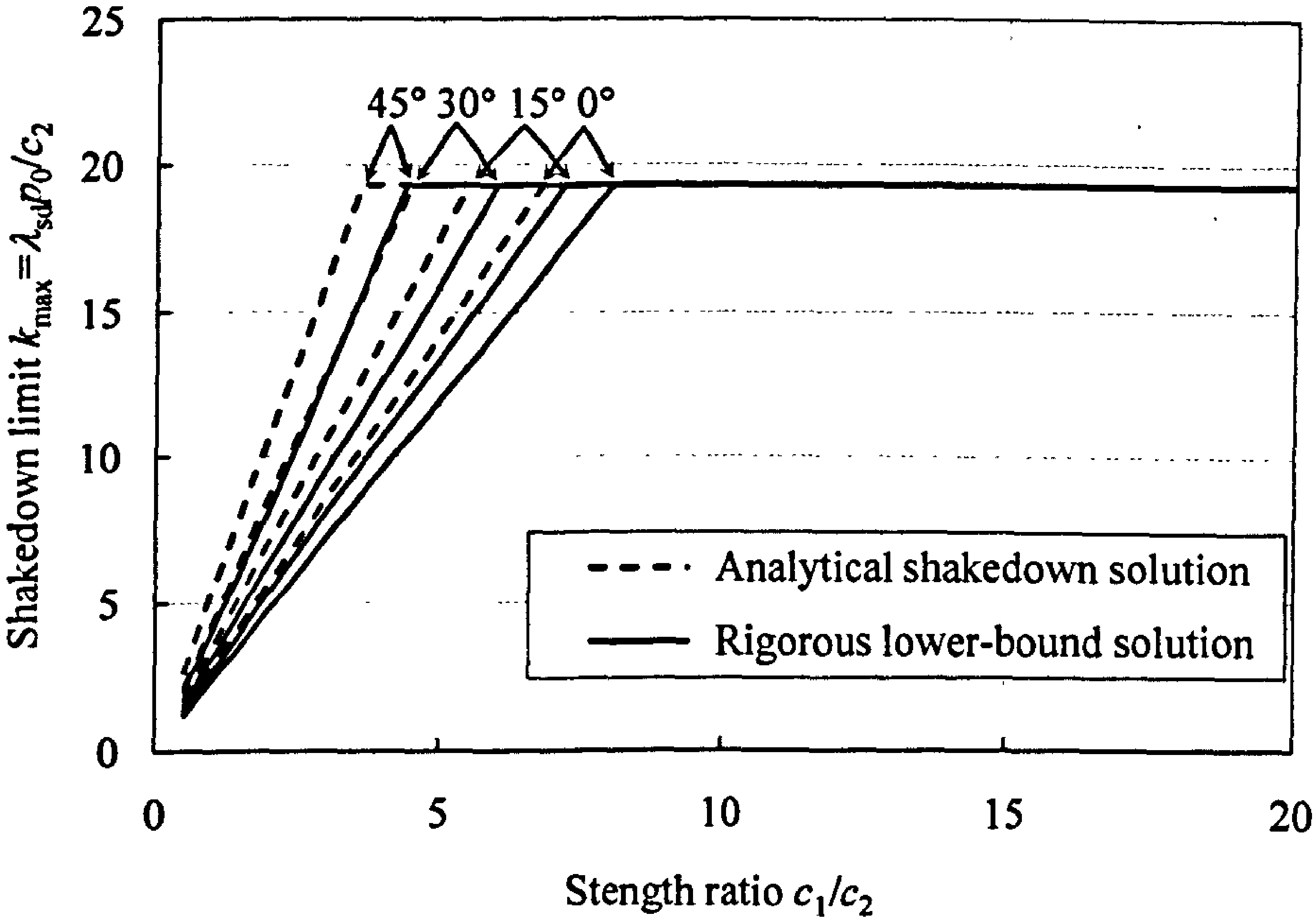

Figure 5.13. Comparison of analytical and lower-bound shakedown limits when $h_1/D = 1$, $\mu = 0$ and $E_1/E_2 = 10$

5.4.3 Effect of first layer thickness

Figure 5.14 shows the shakedown limit against the stiffness ratio for a range of normalised first layer thickness h_1/D. It can be seen that the shakedown limit can be raised by increasing the first layer thickness h_1/D. It is expected that if the first layer thickness is very large, the second layer will have negligible on the pavement capacity, so that the shakedown limit will reach a maximum value which is entirely controlled by the material properties of the first layer and is independent of E_1/E_2. In addition, at a given value of h_1/D, the optimum stiffness ratio in the lower-bound shakedown solution (see Figure 5.14(b)) is smaller than that in the analytical shakedown solution (see Figure 5.14(a)).

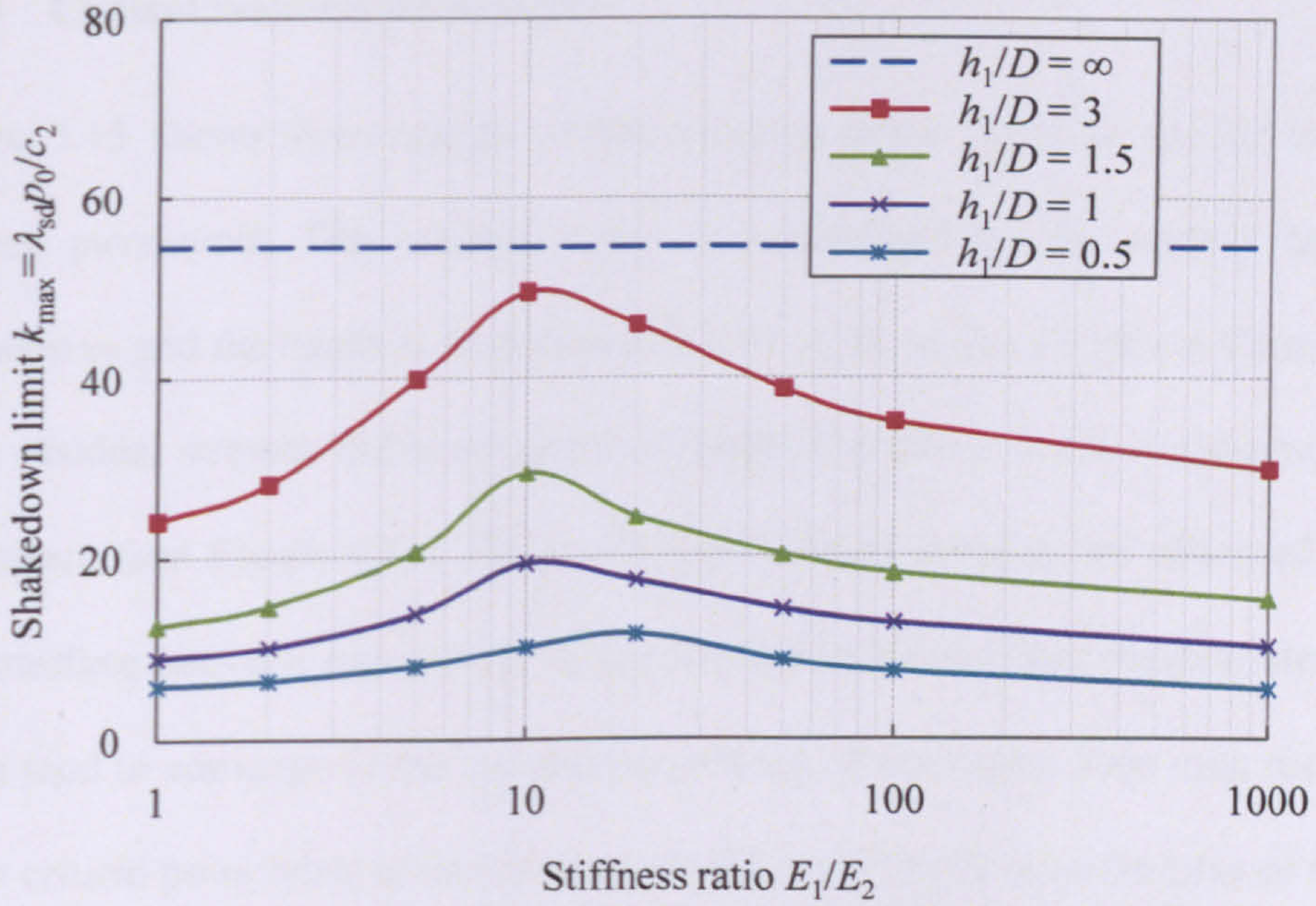

(a) Analytical shakedown solution

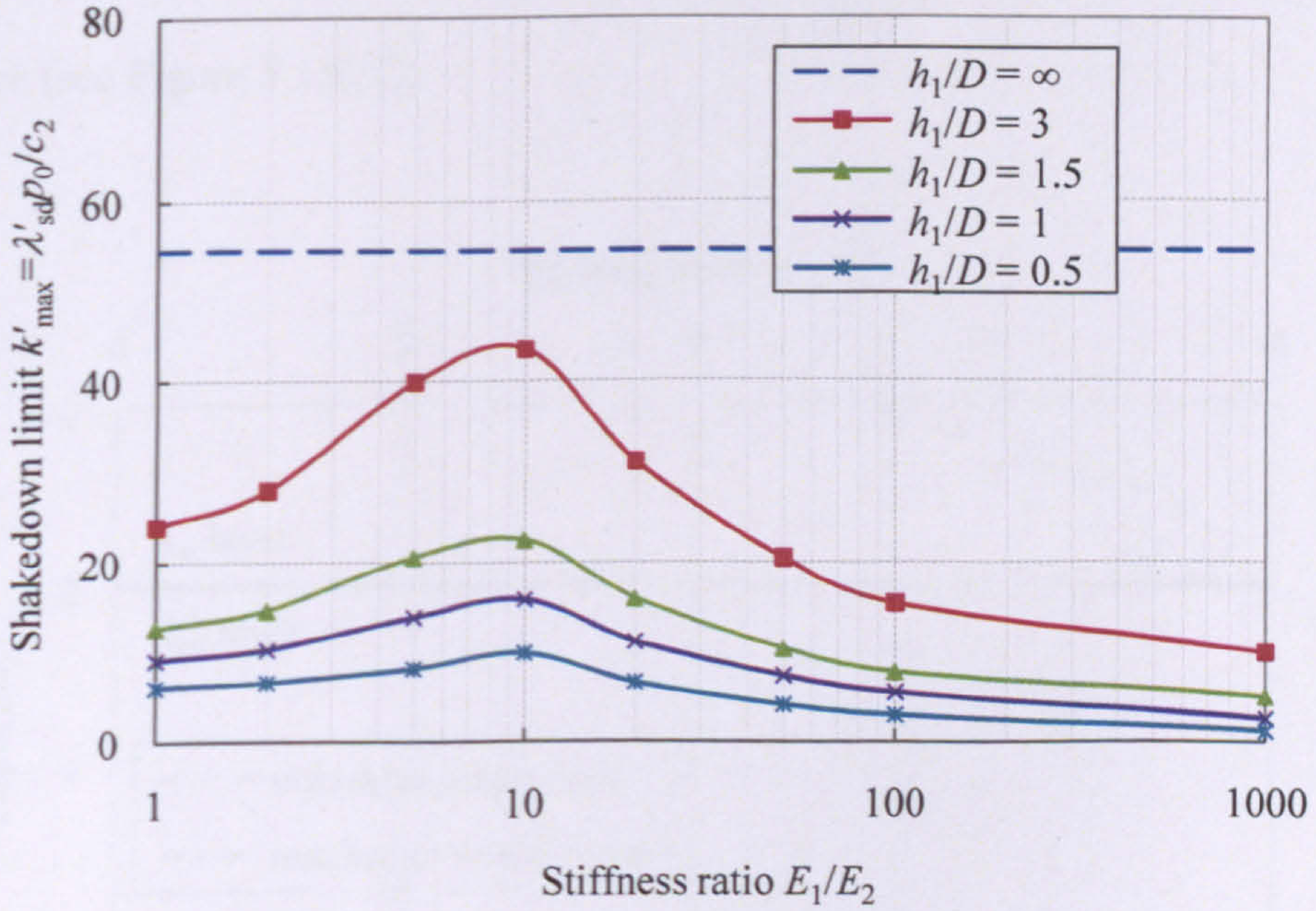

(b) Rigorous lower-bound solution

Figure 5.14. Interactive effect of stiffness ratio and first layer thickness on 2D shakedown limits when $\phi_1 = 30°$, $\mu = 0$ and $c_1/c_2 = 5$

5.4.4 Critical residual stress fields

Figure 5.15 shows three typical critical residual stress fields in the 2D two-layered pavements. The residual stress is normalised by the second layer cohesion c_2 and the depth is normalised by half of the contact width *a*. Clearly, these residual stresses fields are quite different from those in the homogenous half-space (see Figure 4.11). Discontinuous residual stresses are observed at the interface between two layers. In the first layer, two critical residual stress fields tend to converge at the top and the bottom of this layer. This may result in the critical point lying at the surface (see Figure 5.15(c)) or at the base of the first layer (see Figure 5.15(a)). In the second layer, two critical residual stresses fields tend to converge at the top of the second layer, leading to second layer failure (see Figure 5.15(b)).

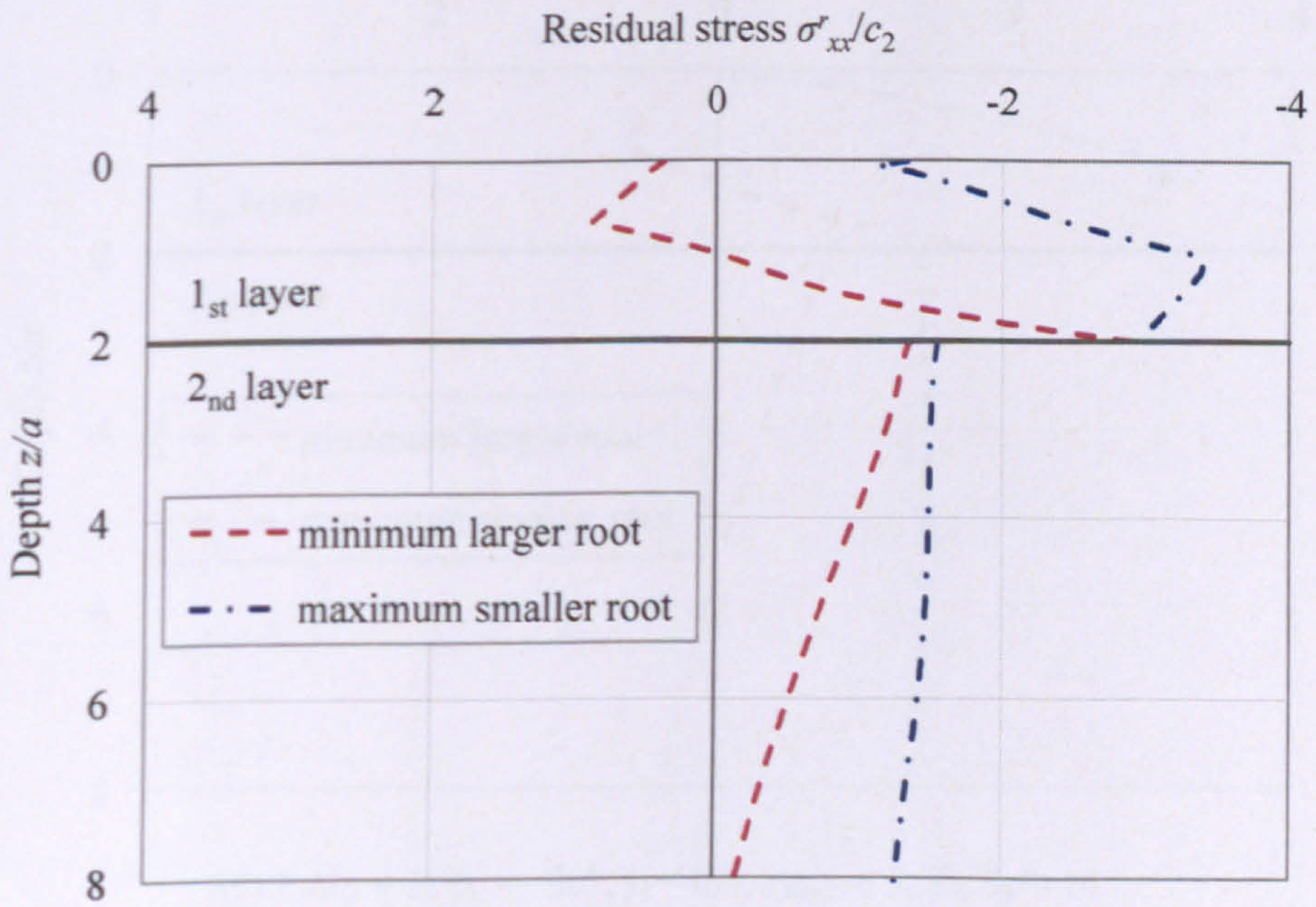

(a) $h_1/2a = 1$, $\phi_1 = 30°$, $\mu = 0$, $c_1/c_2 = 5$, $E_1/E_2 = 10$

Figure 5.15 continued on following page

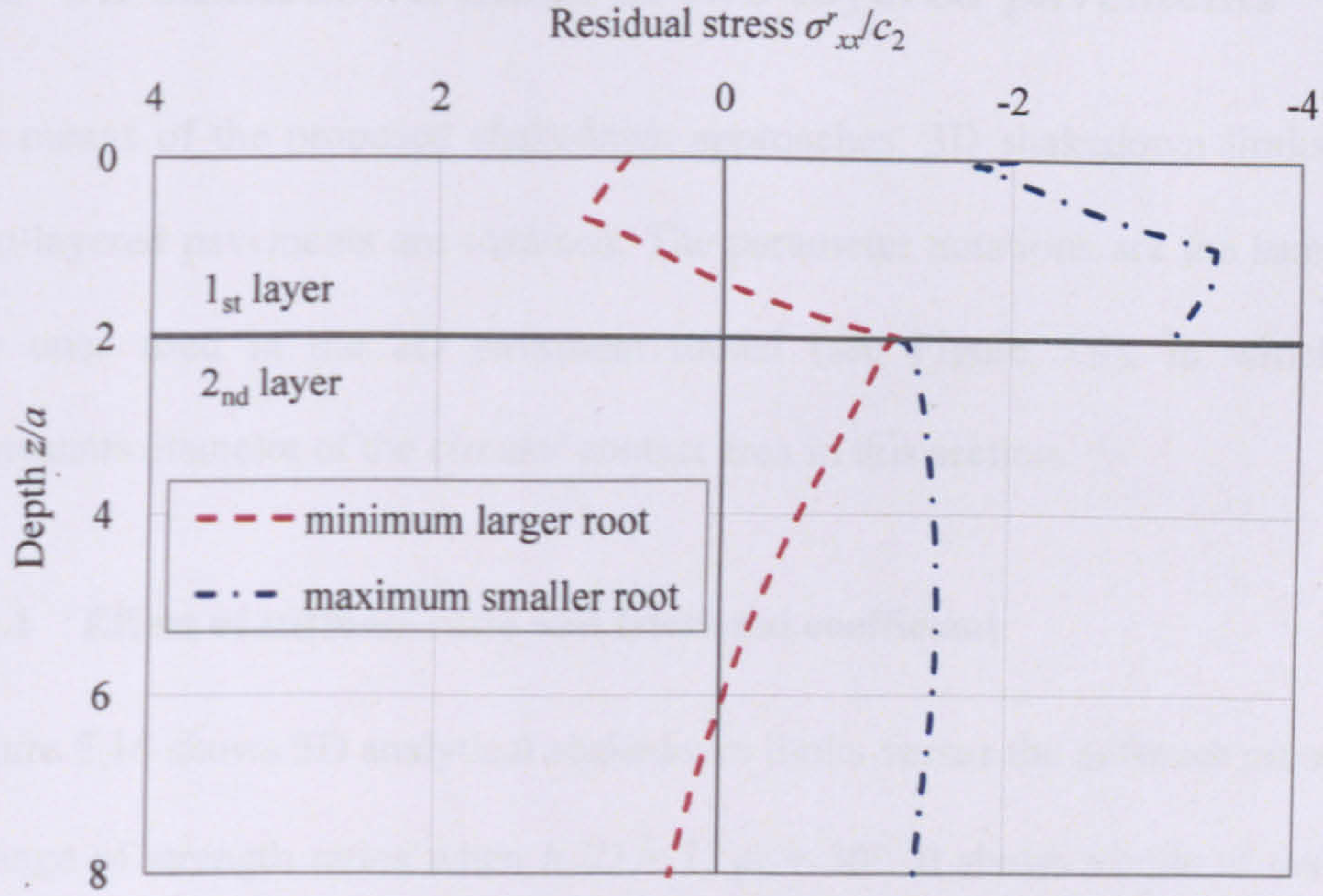

(b) $h_1/2a = 1$, $\phi_1 = 30°$, $\mu = 0$, $c_1/c_2 = 5$, $E_1/E_2 = 5$

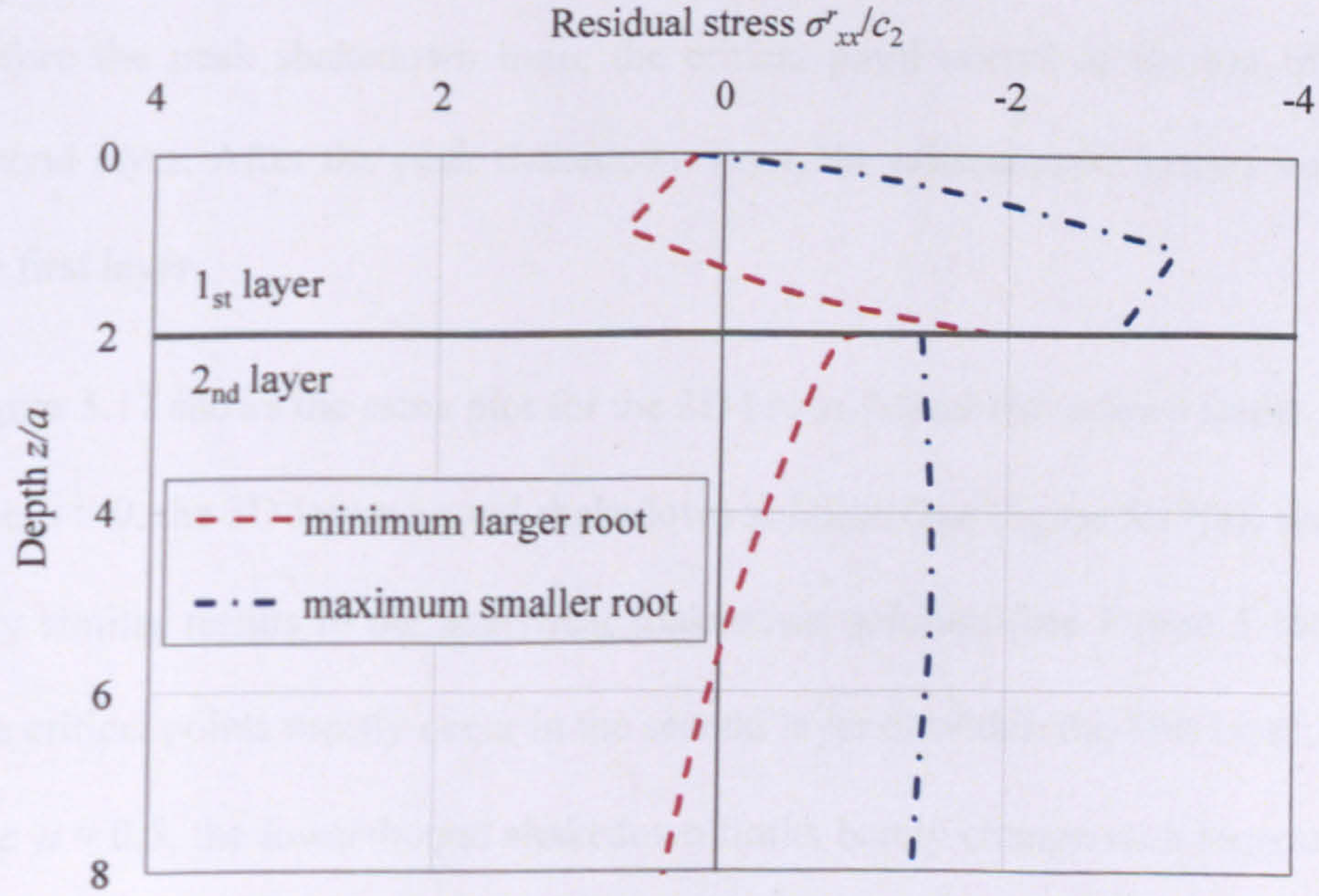

(c) $h_1/2a = 1$, $\phi_1 = 30°$, $\mu = 0.5$, $c_1/c_2 = 5$, $E_1/E_2 = 10$

Figure 5.15. Typical critical residual stress fields in 2D two-layered pavements

5.5 3D shakedown limits of two-layered pavements

By means of the proposed shakedown approaches, 3D shakedown limits for two-layered pavements are obtained. The parameter notations are the same as the ones used in the 2D pavement model (see Figure 5.9), in which D represents diameter of the circular contact area in this section.

5.5.1 Effect of stiffness ratio and frictional coefficient

Figure 5.16 shows 3D analytical shakedown limits versus the stiffness ratio for a range of strength ratios when $h_1/D = 1$, $\phi_1 = 30°$. It shows trends of curves which are similar to Figure 5.10. At a given value of strength ratio, the existence of peak shakedown limit is evident in the case of normal loading only (see Figure 5.16(a)) but is less obvious when $\mu = 0.5$ (see Figure 5.16(b)). Before the peak shakedown limit, the critical point occurs at the top of the second layer. After the peak shakedown limit, the critical point occurs within the first layer.

Figure 5.17 shows the same plot for the 3D lower-bound shakedown limits. For case $\mu = 0$, the 3D lower-bound shakedown solution (see Figure 5.17(a)) shows very similar results to the analytical shakedown solution (see Figure 5.16(a)). The critical points mostly occur in the second layer or within the first layer. For case $\mu = 0.5$, the lower-bound shakedown limits barely change with increasing E_1/E_2 after the peak point (see Figure 5.17(b)). The values are smaller than the analytical shakedown limits (see Figure 5.16(b)) because surface failure occurs.

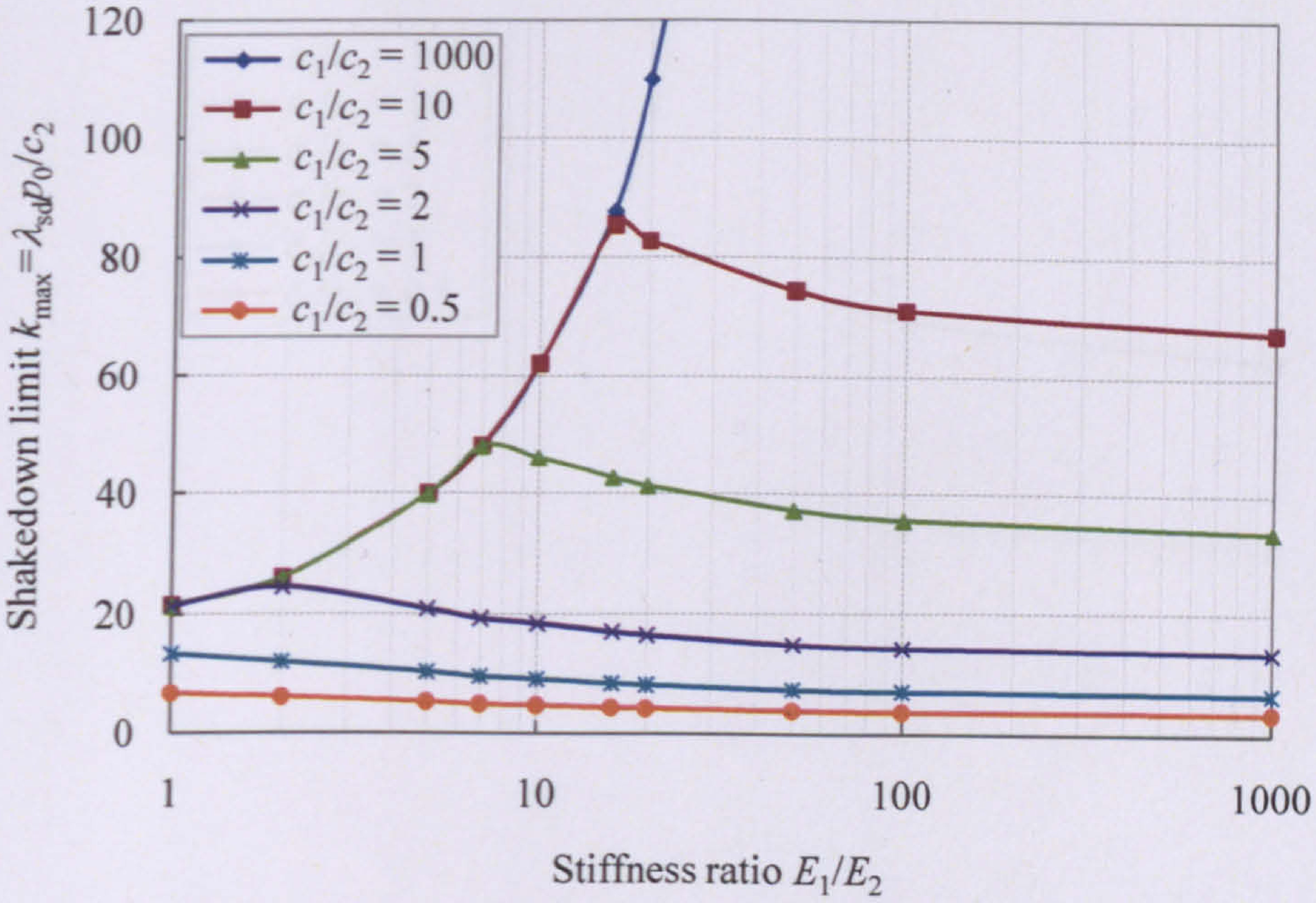

(a) $\mu = 0$

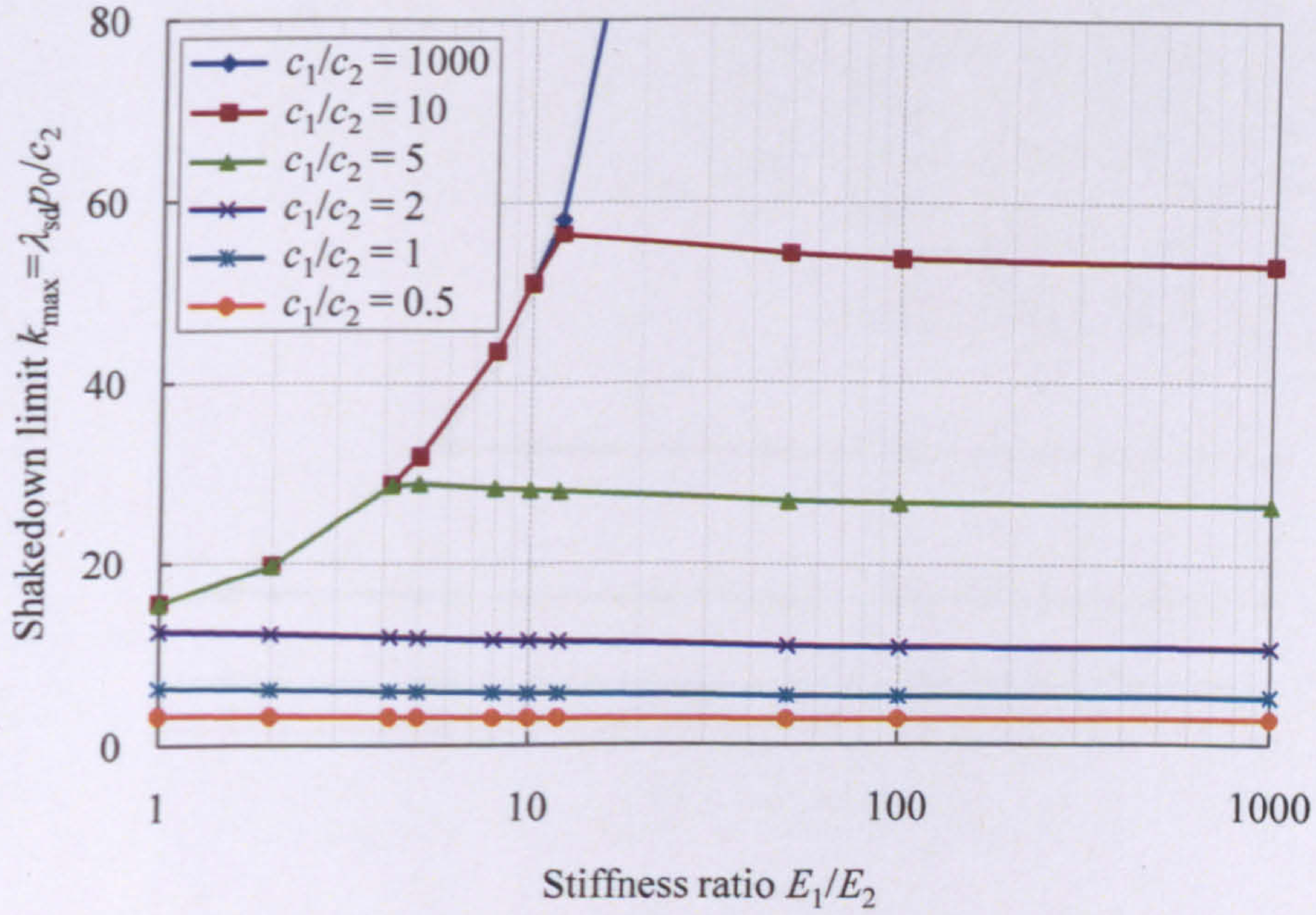

(b) $\mu = 0.5$

Figure 5.16. 3D shakedown limits versus stiffness ratios for various values of strength ratio when $h_1/D = 1$ and $\phi_1 = 30°$

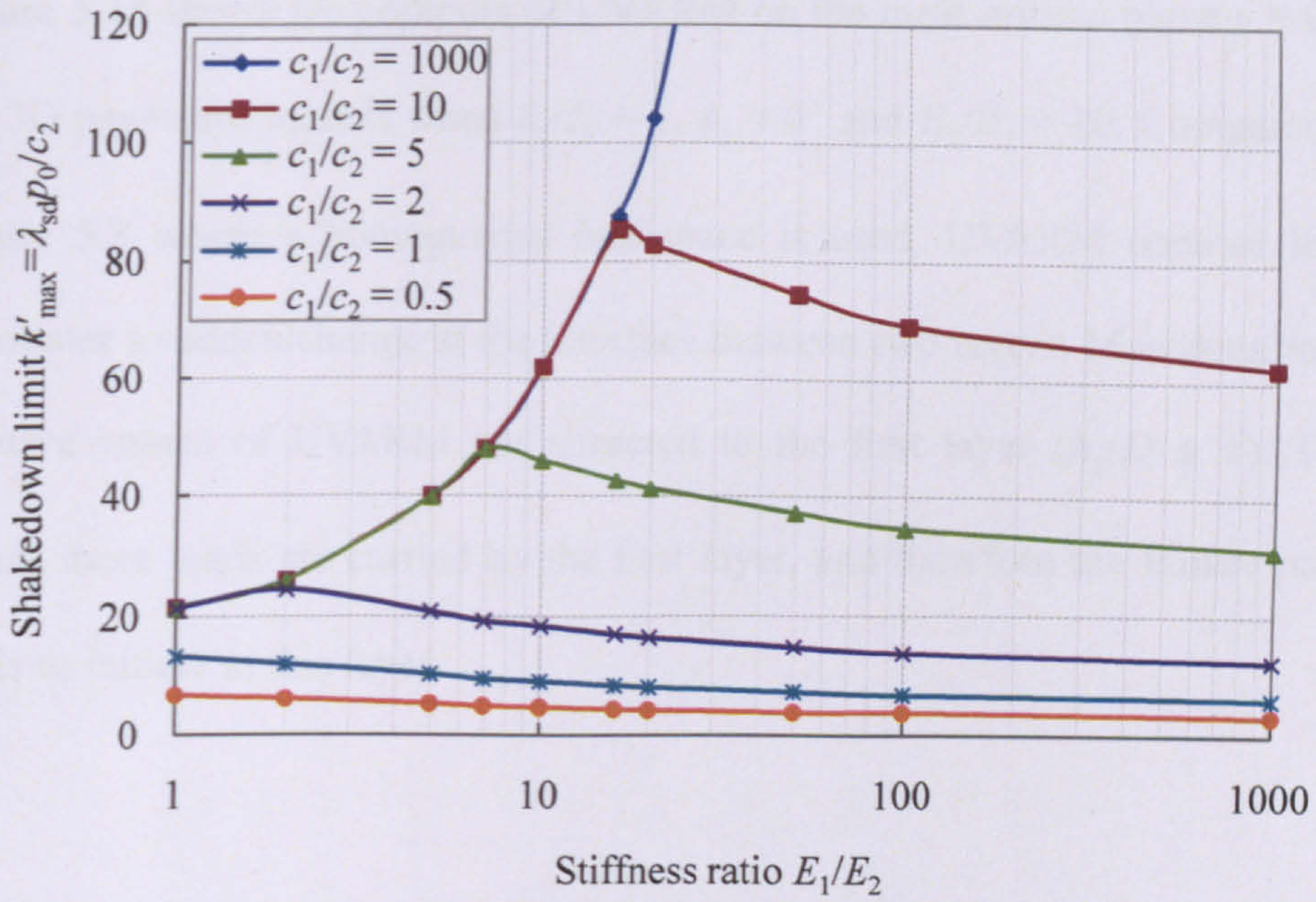

(a) $\mu = 0$

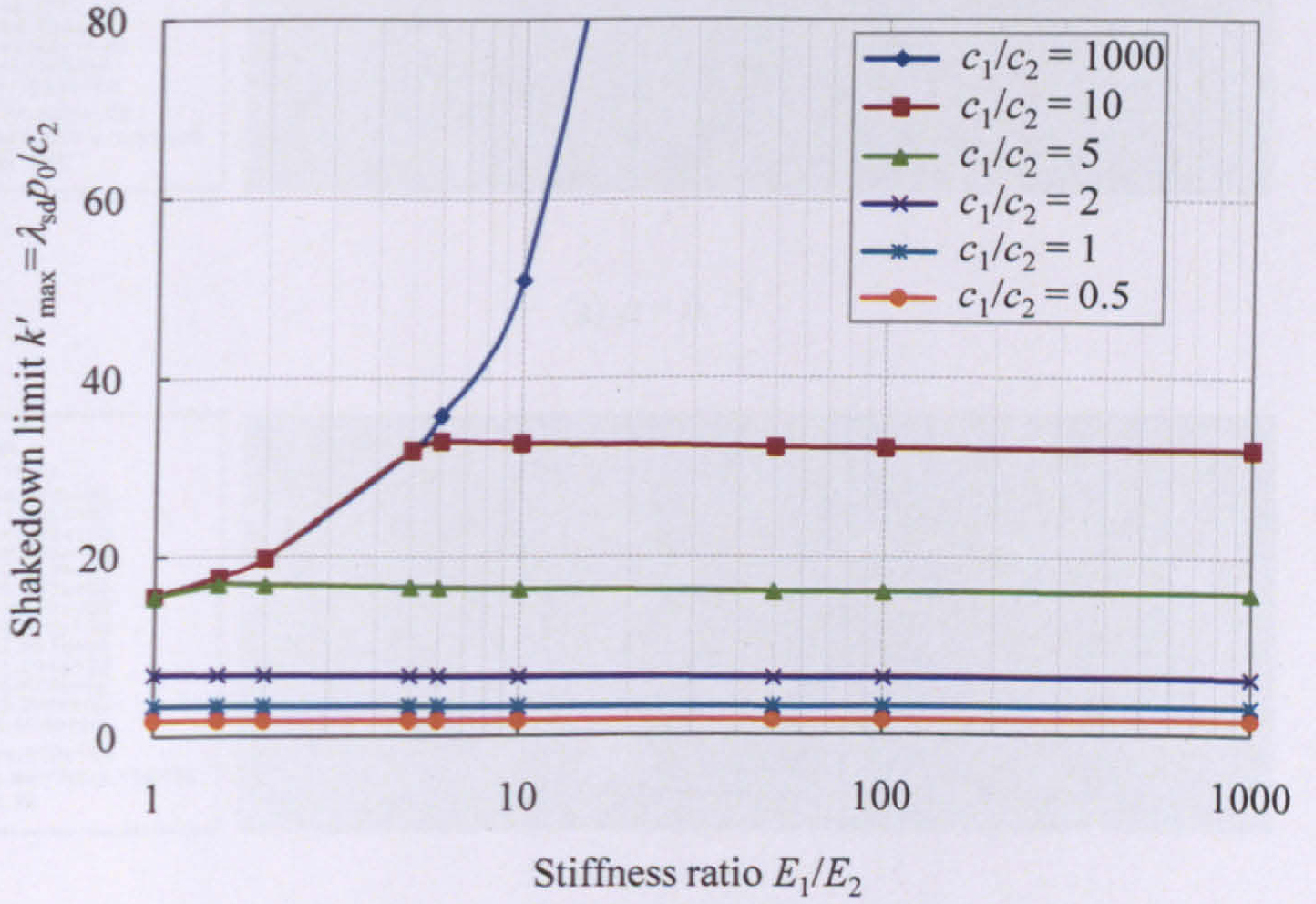

(b) $\mu = 0.5$

Figure 5.17. 3D shakedown limits versus stiffness ratios for various values of strength ratio when $h_1/D = 1$ and $\phi_1 = 30°$

Figure 5.18 shows the contours of UVARM on the most critical plane $y = 0$ in the 3D pavement models when $h_1/D = 1$, $\phi_1 = 0°$ and $E_1/E_2 = 10$. Compared to Figure 5.8 where a homogenous half-space is used, UVARM contour lines encounter a sudden change at the interface between two layers. Moreover, most positive values of UVARM are attracted to the first layer ($h_1/D \leq 1$). This means more loads are carried by the first layer, and therefore the failure point tends to initiate in this layer.

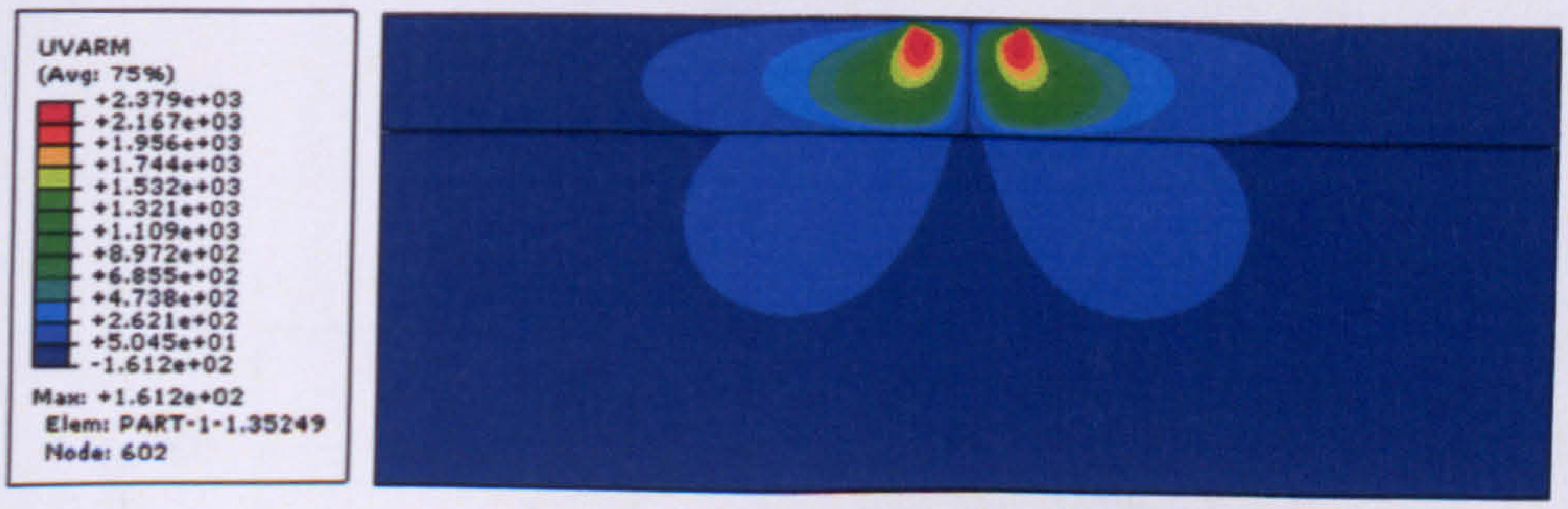

(a) $\mu = 0$

(b) $\mu = 0.5$

Figure 5.18. UVARM distributions on $y = 0$ plane in the 3D pavement models when $h_1/D = 1$, $\phi_1 = 0°$, $E_1/E_2 = 10$ and p_0 =1e4

5.5.2 Effect of strength ratio and first layer friction angle

Figure 5.19 shows the 2D and 3D shakedown limits against strength ratios for various values of first layer friction angle. Clearly, the 3D shakedown limits are about two times higher than the 2D shakedown limits. The 3D shakedown limit also grows faster than the 2D shakedown limit with increasing strength ratio when the critical point lies in the first layer.

In addition, while the lower-bound shakedown solution and the analytical shakedown solution are different in the 2D pavement models (see Figure 5.13), they are identical in the 3D pavement models.

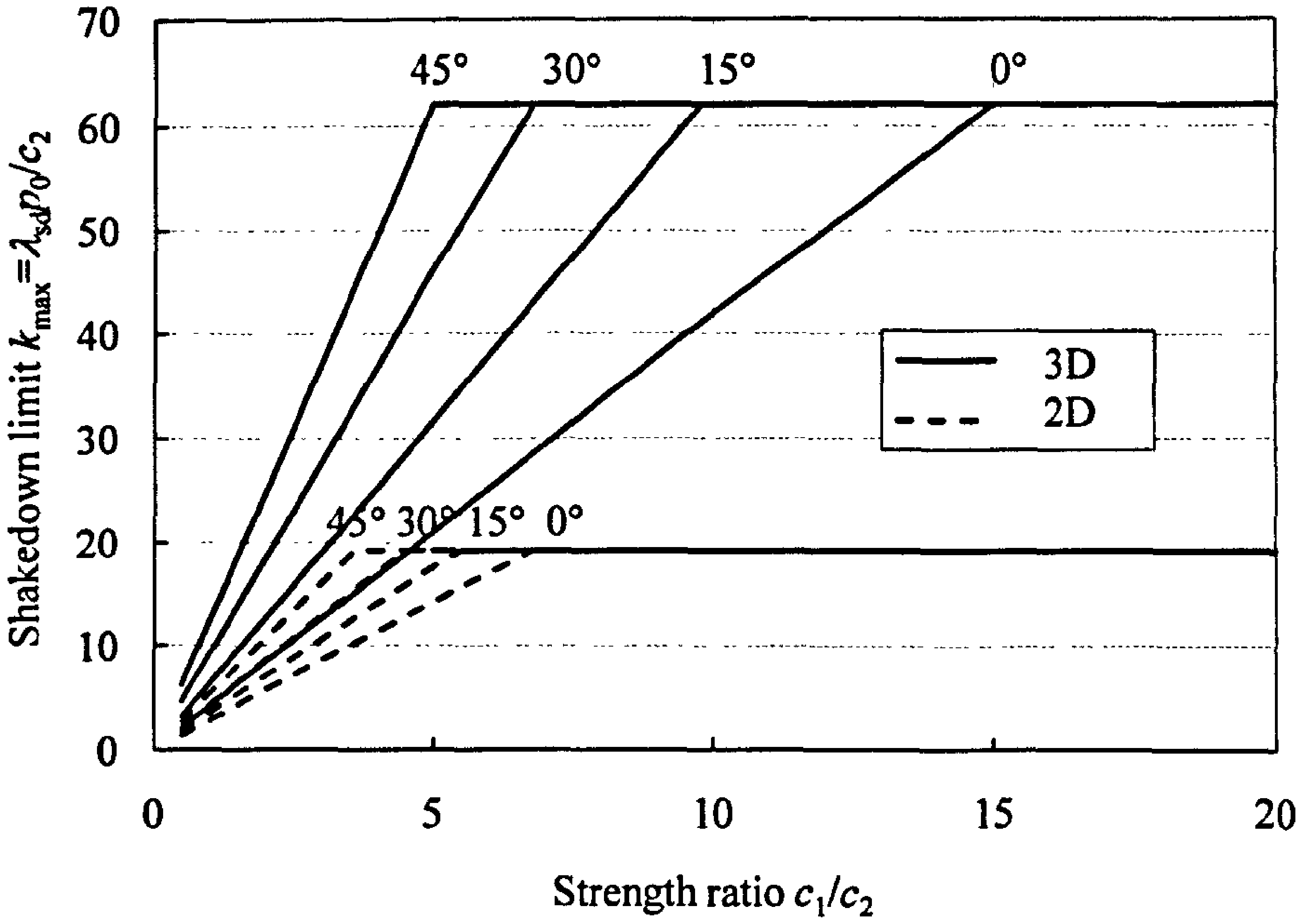

(a) Analytical shakedown solution

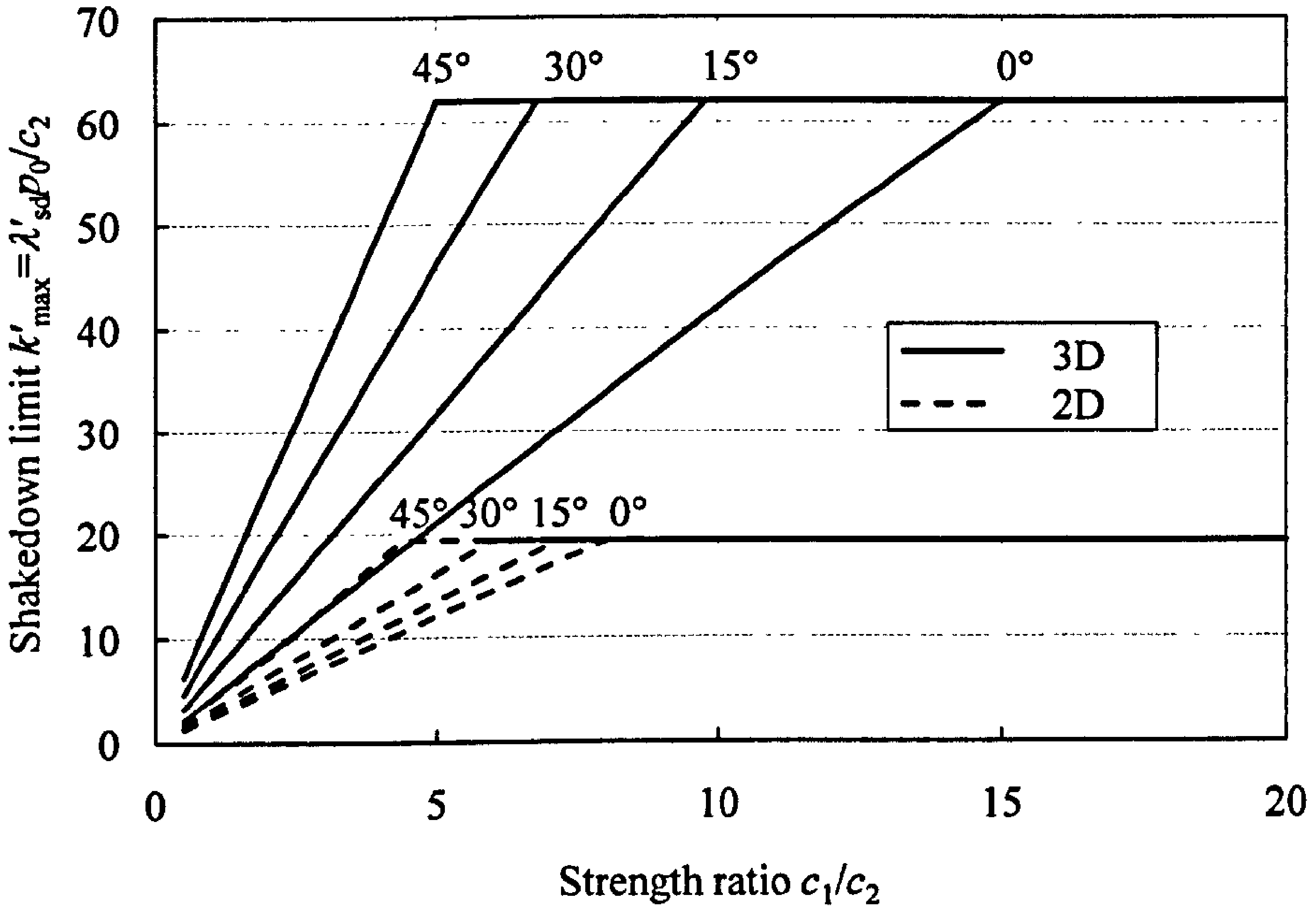

(b) Rigorous lower-bound solution

Figure 5.19. 2D and 3D shakedown limits versus strength ratios for various values of first layer friction angle when $h_1/D = 1$, $\mu = 0$ and $E_1/E_2 = 10$

5.5.3 Effect of first layer thickness

Figure 5.20 shows the influence of the normalised first layer thickness h_1/D on the analytical and lower-bound shakedown limits. Clearly, larger h_1/D gives rise to higher shakedown limit. Two shakedown solutions only have a slight difference when the first layer thickness is small ($h_1/D \leq 1$) and the stiffness ratio is high, because their critical points lie at the base of the first layer. For case $h_1/D = 3$, the shakedown limit barely changes with increasing stiffness ratio and are very close to those obtain for an infinite homogenous half-space. This implies that effective depth of the 3D Hertz load is around 3 in this particular case, definitely smaller than that of the 2D Hertz load (see Figure 5.14).

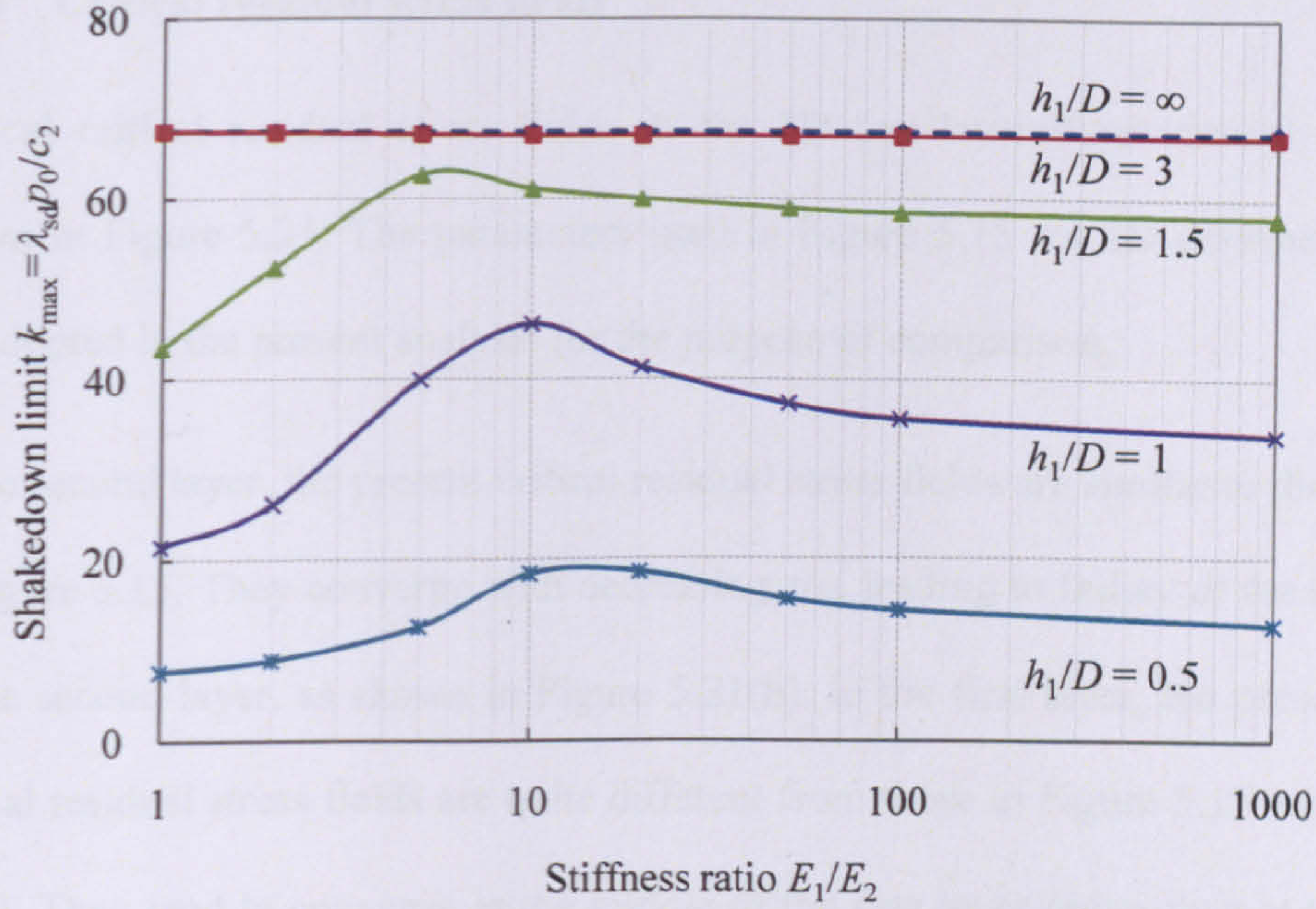

(a) Analytical shakedown solution

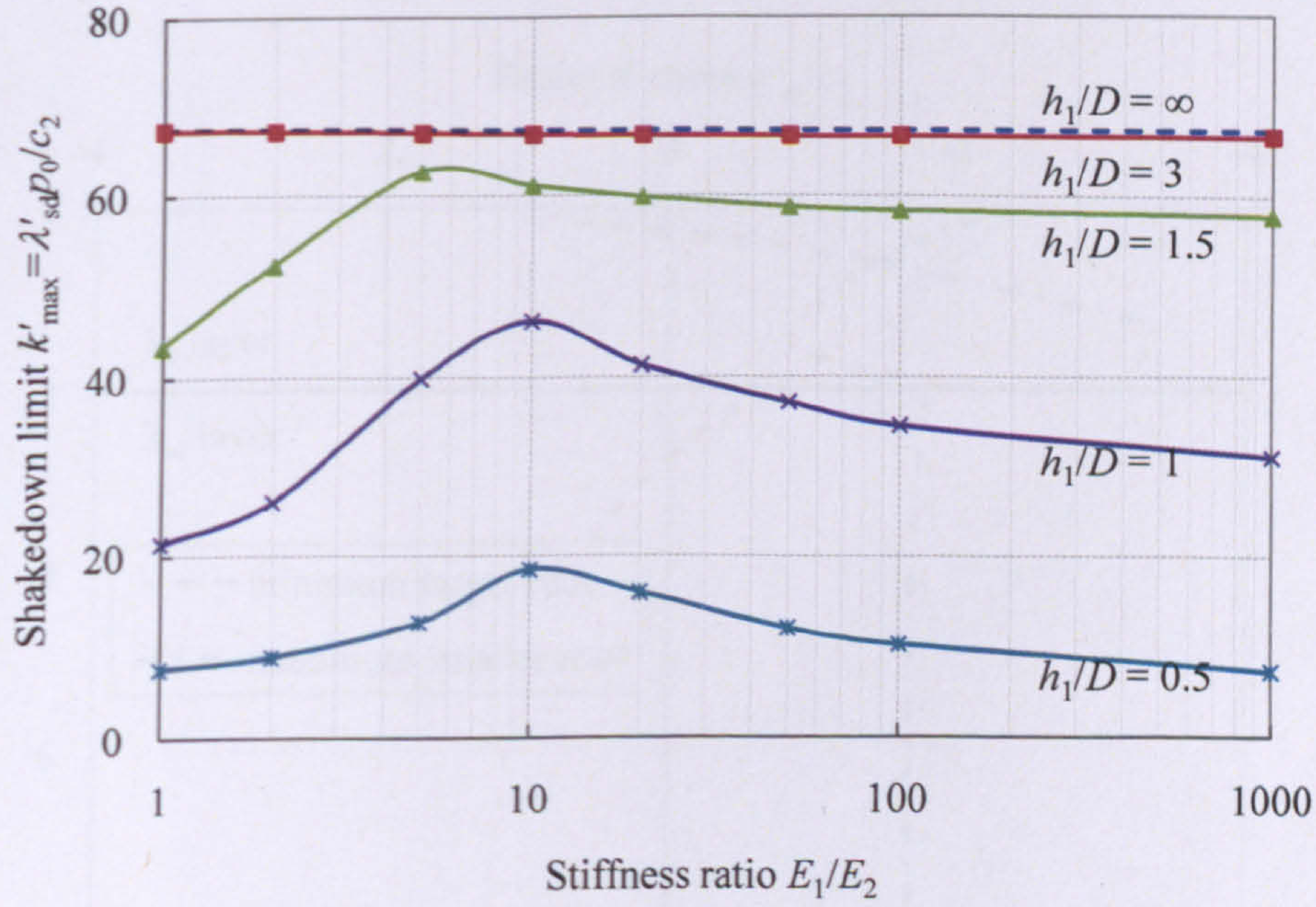

(b) Rigorous lower-bound solution

Figure 5.20. Interactive effect of stiffness ratio and first layer thickness on 3D analytical shakedown limits when $\phi_1 = 30°$, $\mu = 0$ and $c_1/c_2 = 5$

5.5.4 Critical residual stress fields

Typical critical residual stress fields in the 3D two-layered pavements are shown in Figure 5.21. The parameters used in Figure 5.15 for 2D pavements are adopted in the present analysis for the purpose of comparison.

In the second layer, the present critical residual stress fields are similar to those in Figure 5.15. They converge with decreasing z/a, leading to failure at the top of the second layer, as shown in Figure 5.21(b). In the first layer, the present critical residual stress fields are quite different from those in Figure 5.15 when $\mu = 0$. They tend to converge in the middle of the first layer rather than at the top or bottom (see Figure 5.21(a) and Figure 5.21 (b)). Figure 5.21(c) indicates the critical point is located at the surface due to high frictional coefficient.

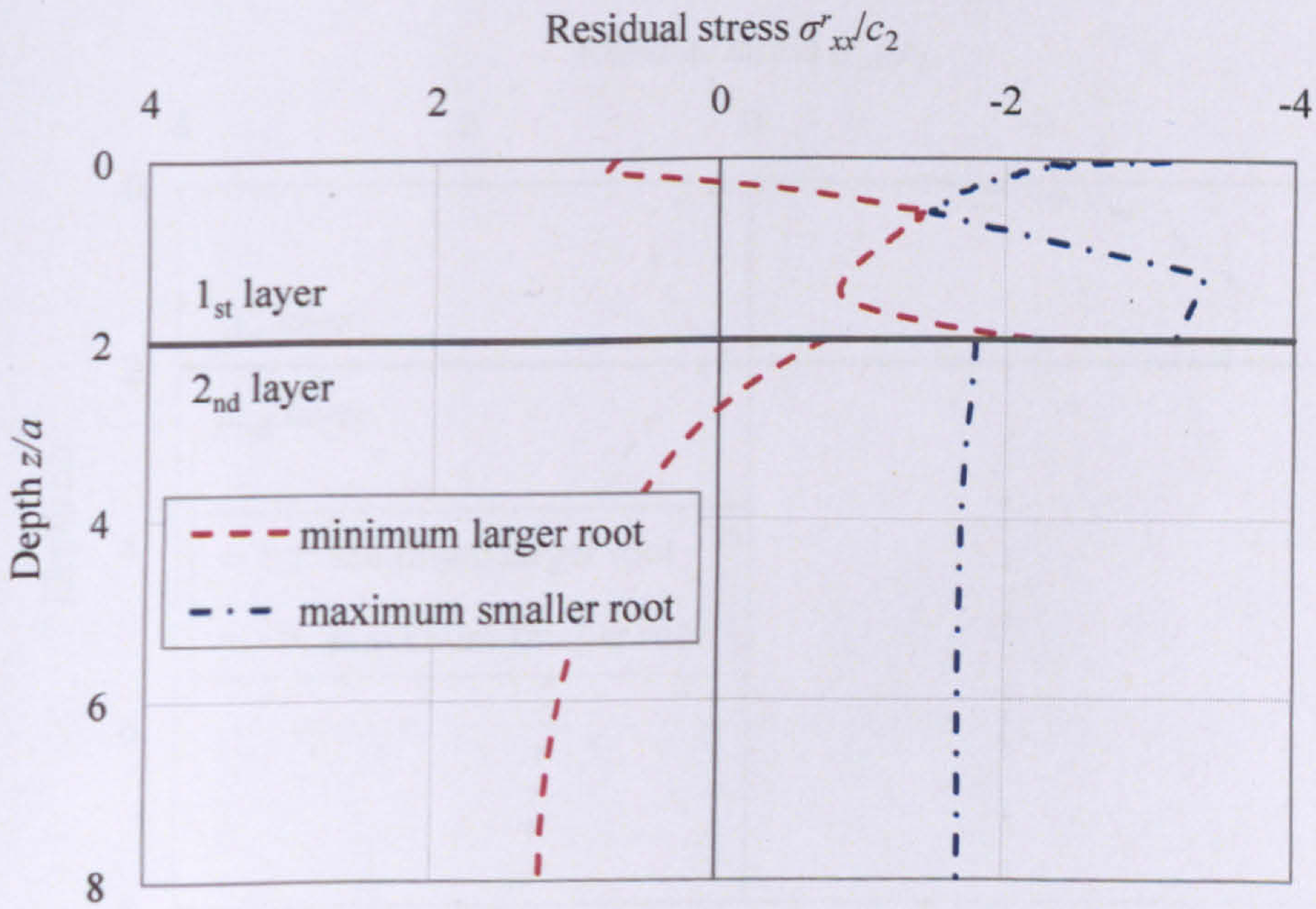

(a) $h_1/2a = 1$, $\phi_1 = 30°$, $\mu = 0$, $c_1/c_2 = 5$, $E_1/E_2 = 10$

Figure 5.21 continued on following page

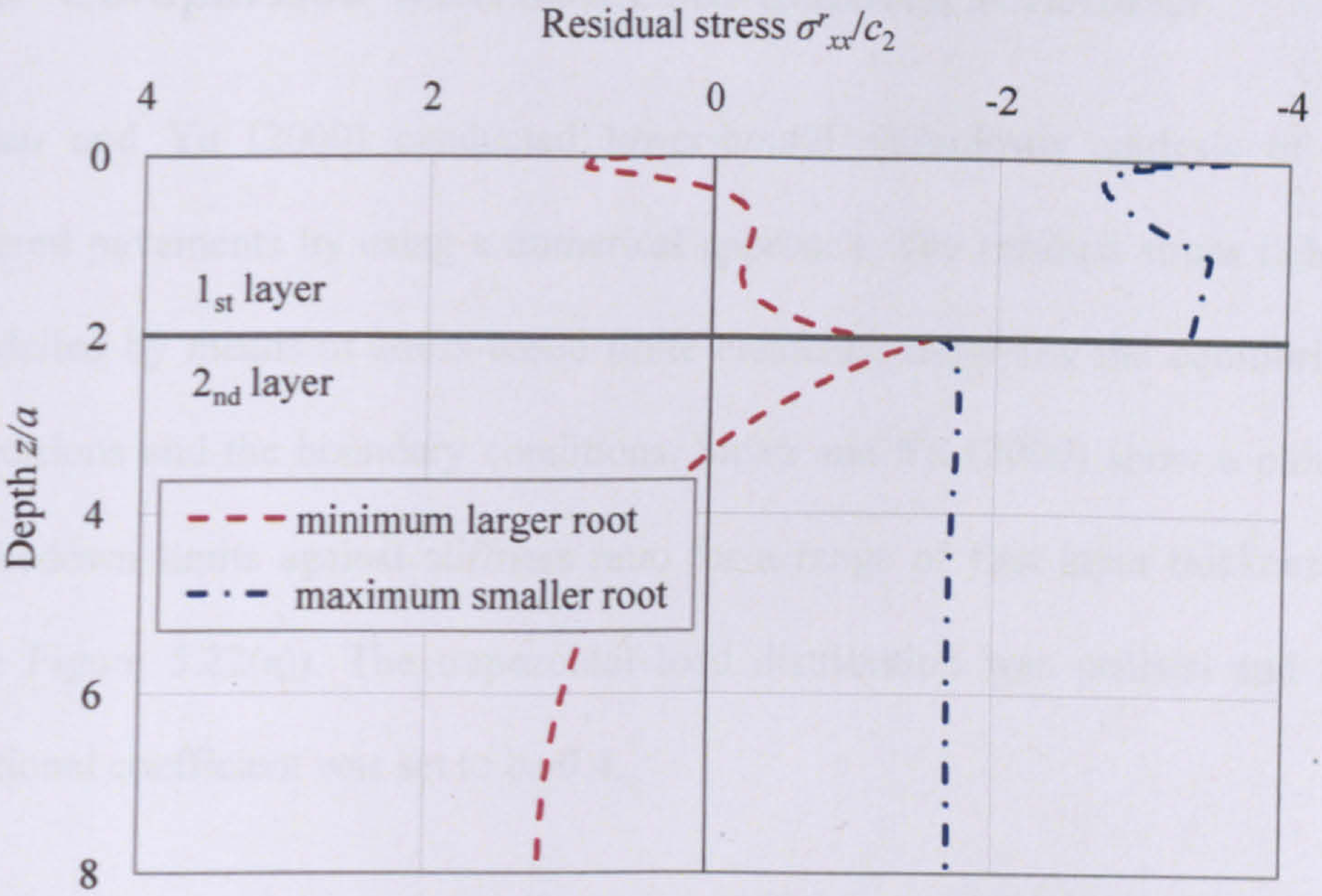

(b) $h_1/2a = 1$, $\phi_1 = 30°$, $\mu = 0$, $c_1/c_2 = 5$, $E_1/E_2 = 5$

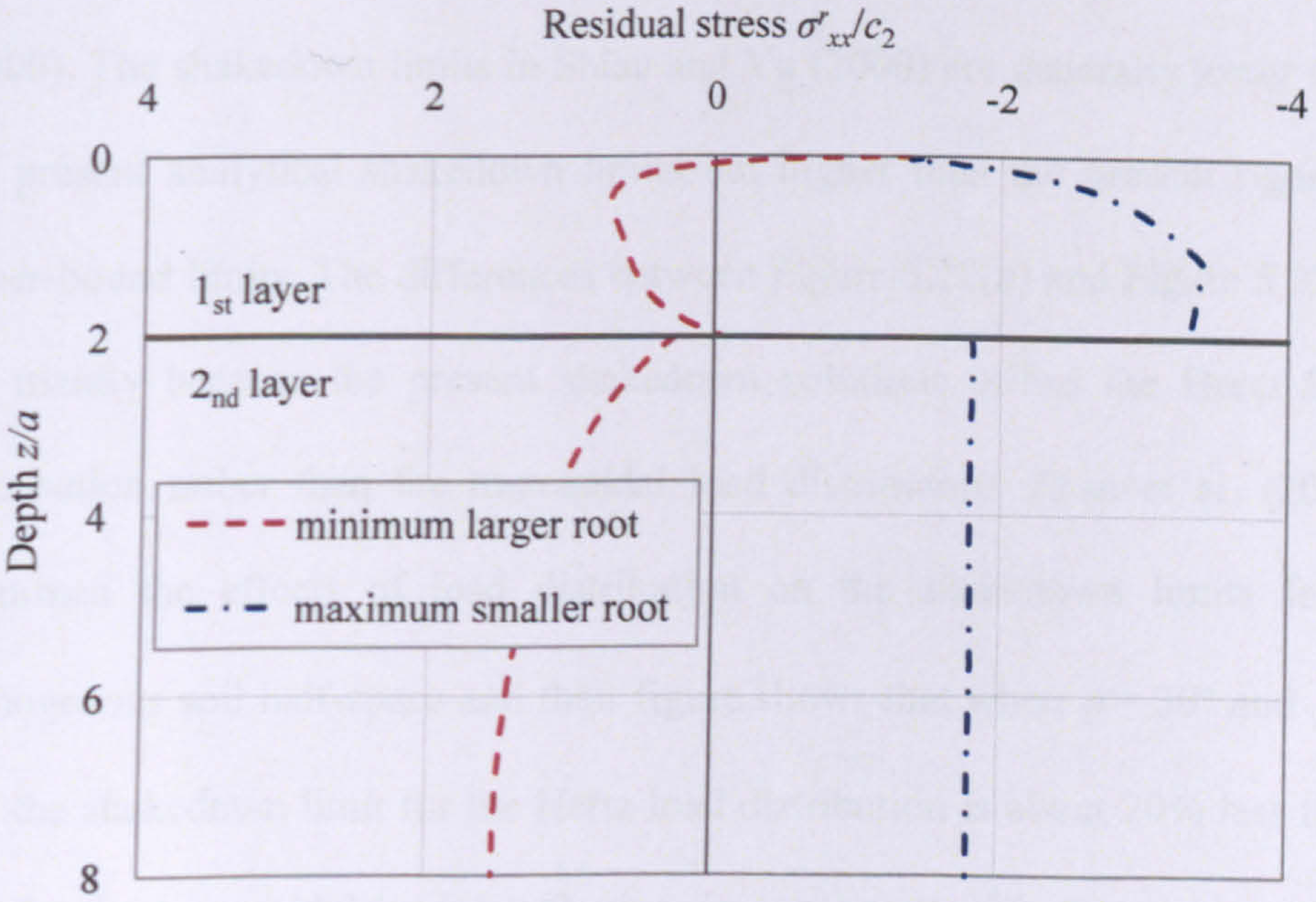

(c) $h_1/2a = 1$, $\phi_1 = 30°$, $\mu = 0.5$, $c_1/c_2 = 5$, $E_1/E_2 = 10$

Figure 5.21. Typical critical residual stress fields in 3D two-layered pavements

5.6 Comparison with other shakedown solutions

Shiau and Yu (2000) conducted lower-bound shakedown analysis of 2D layered pavements by using a numerical approach. The residual stress field is modelled by means of stress-based finite elements, satisfying the equilibrium conditions and the boundary conditions. Shiau and Yu (2000) show a plot of shakedown limits against stiffness ratio for a range of first layer thicknesses (see Figure 5.22(a)). The trapezoidal load distribution was utilised and the frictional coefficient was set to be 0.4.

For the purpose of comparison, the same material properties ($\phi_1 = 30°$, $\upsilon_1 = 0.3$, $\phi_2 = 0°$, $\upsilon_2 = 0.4$, $c_1/c_2 = 5$) and frictional coefficient are adopted for the present shakedown analysis. As shown in Figure 5.22, the present shakedown solutions are all maximised when $h_1/D = 5$, in agreement with that in Shiau and Yu (2000). The shakedown limits in Shiau and Yu (2000) are generally lower than the present analytical shakedown limits but higher than the present rigorous lower-bound limits. The differences between Figure 5.22(a) and Figure 5.22(c) are mainly because the present shakedown solutions utilise the Hertz load distribution rather than the trapezoidal load distribution. Zhao et al. (2008) examined the effects of load distribution on the shakedown limits for a homogenous soil half-space and their figure shows that when $\phi = 30°$ and $\mu = 0.4$, the shakedown limit for the Hertz load distribution is about 20% less than that for the trapezoidal load distribution, in agreement with the present study when $h_1/D = 5$.

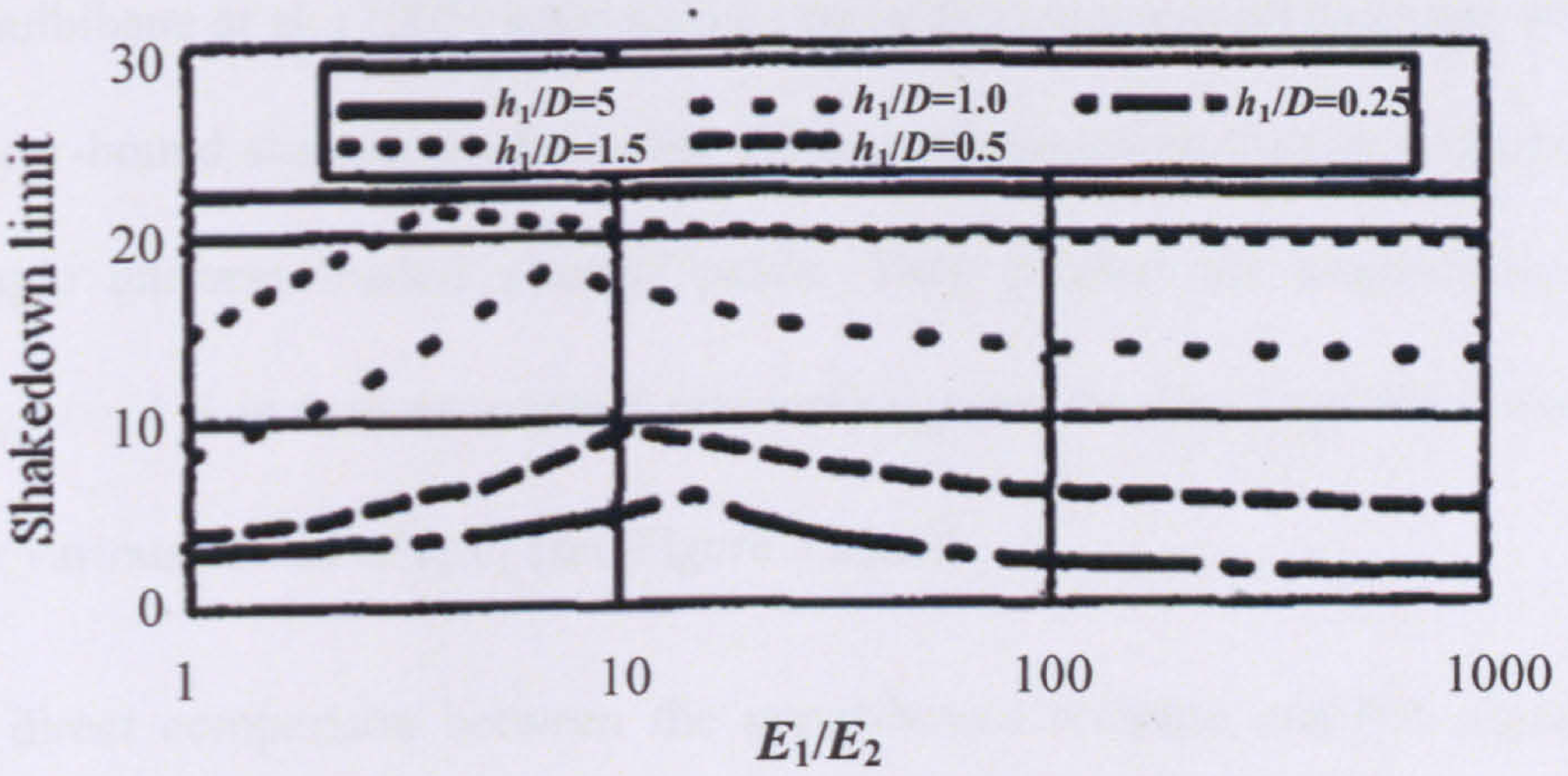

(a) Shiau and Yu (2000)

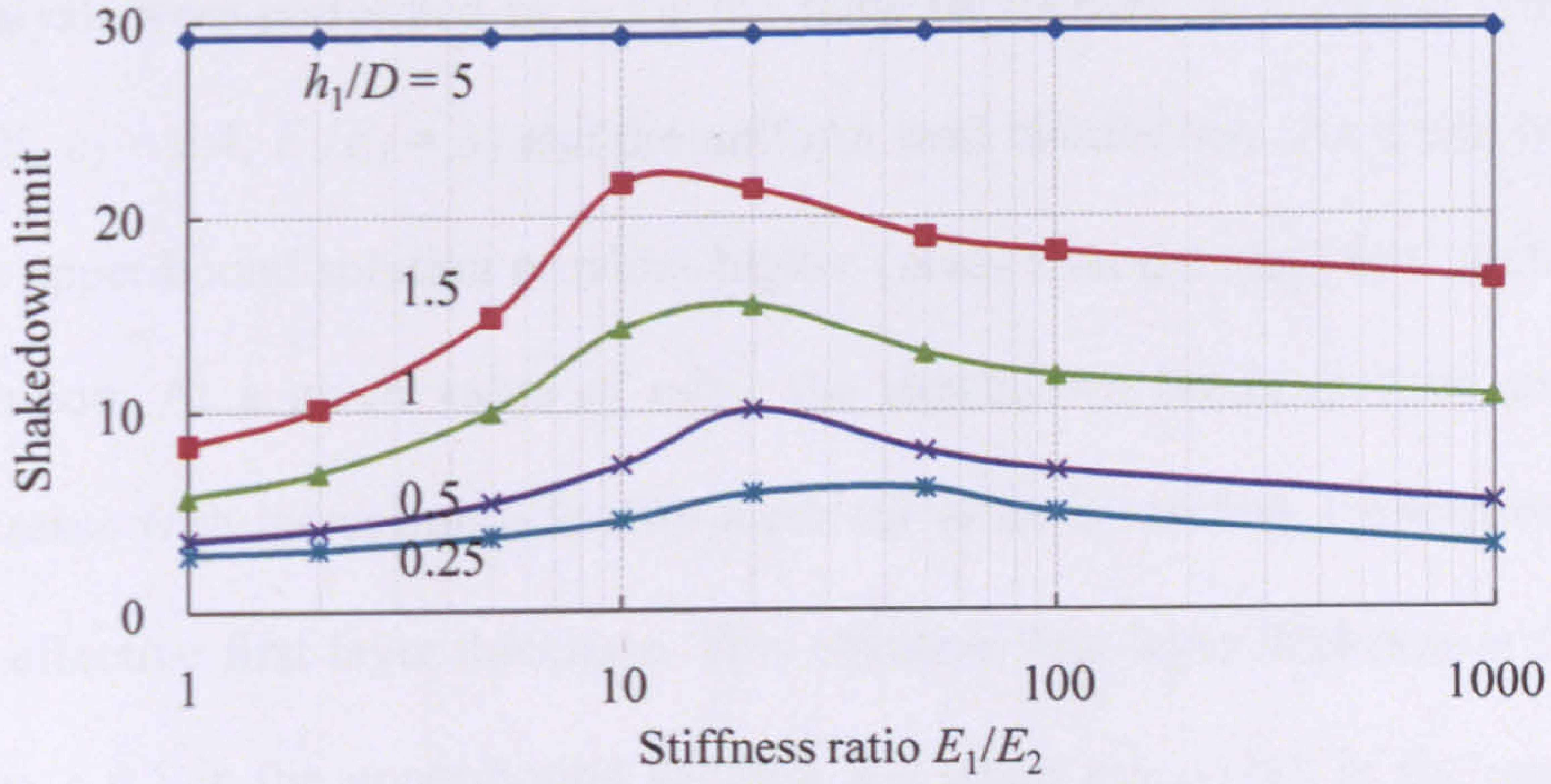

(b) Analyical shakedown solution

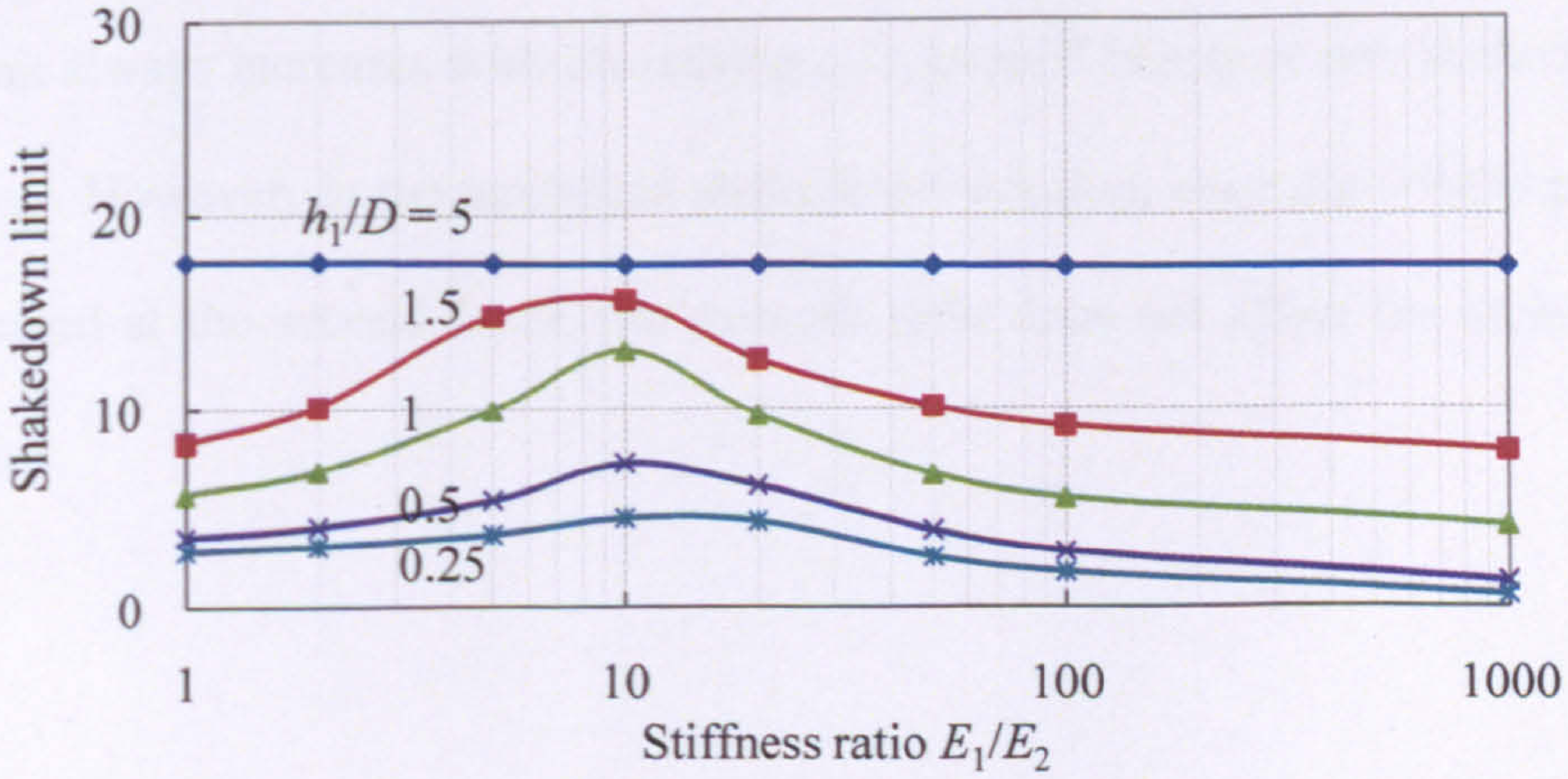

(c) Rigorous lower-bound solution

Figure 5.22. Comparison of 2D shakedown limits when $c_1/c_2 = 5$, $\phi_1 = 30°$, $\phi_2 = 0°$ and $\mu = 0.4$

Boulbibane et al. (2005) suggested a rutting development method and obtained upper-bound shakedown limits for 3D layered pavements when subjected to a single uniform loaded circular patch. They plotted the shakedown limits $\lambda_{sd}\bar{p}/c_2$ ($\bar{p}$ is uniform contact pressure) against the first layer thickness h_1/a for various values of c_2/c_1 (see Figure 5.23(a)).

A direct comparison between the upper-bound solution and the present 3D analytical shakedown solution is shown Figure 5.23. The present shakedown analysis were performed by using the same parameters ($\phi_1 = 20°$, $\upsilon_1 = 0.35$, $\phi_2 = 0°$, $\upsilon_2 = 0.4$, $E_1/E_2 = 3$) and the uniform load distribution. As it can be seen, the upper bound solution provides higher values than the analytical shakedown solution. At a given value of c_2/c_1, the shakedown limits in both solutions increase with increasing h_1/a until a critical value is reached, corresponding to an effective first layer thickness. This effective first layer thickness is 2 when $c_2/c_1 \geq 0.5$ in the upper-bound solution and when $c_2/c_1 \geq 0.3$ in the analytical shakedown solution. In addition, in the upper-bound solution, the shakedown limit always increases with decreasing c_2/c_1 even if failure occurs in the second layer. However, in the analytical shakedown solution, once the critical point is located at the second layer, the strength ratio does not affect the shakedown limit.

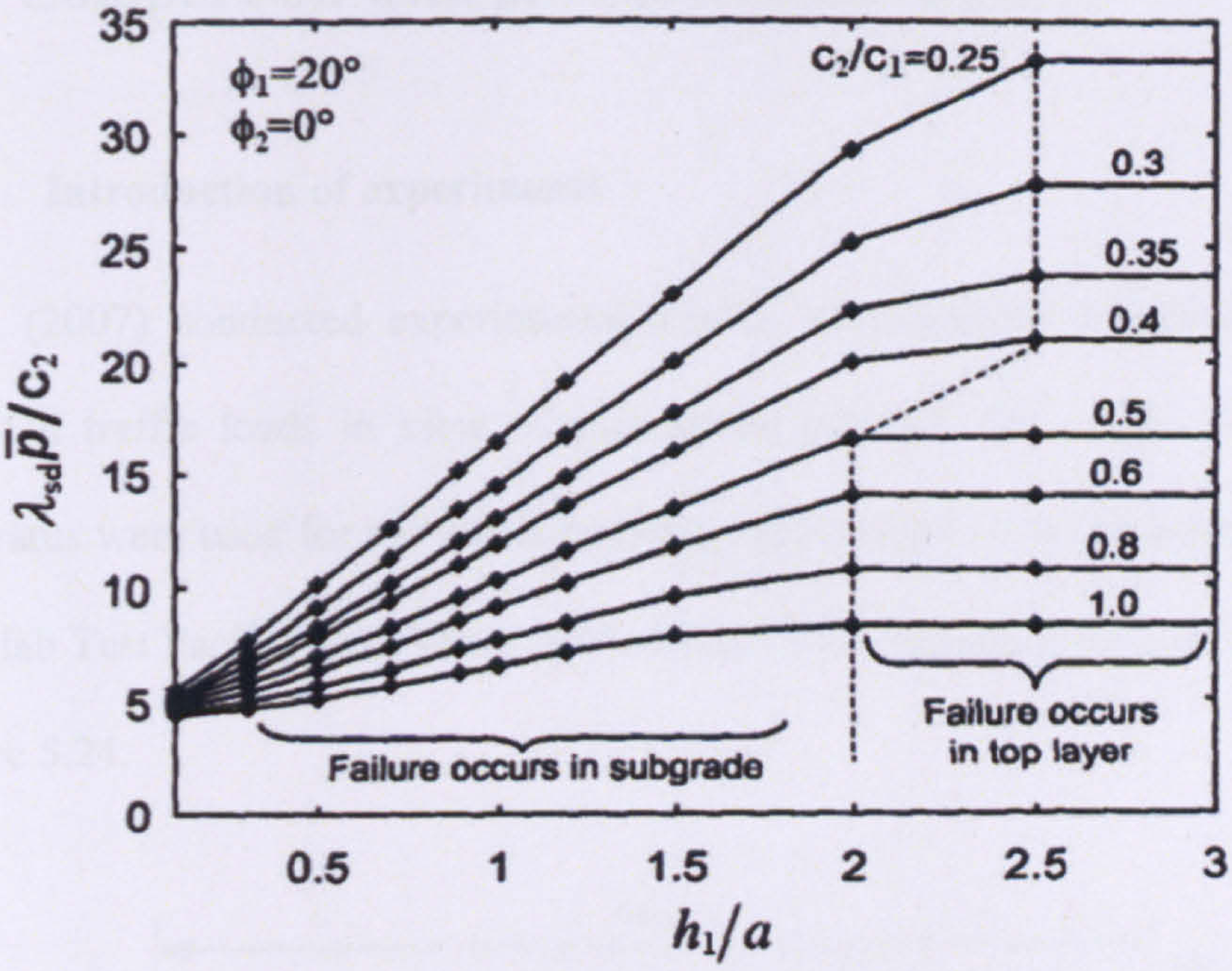

(a) Boulbibane et al. (2005)

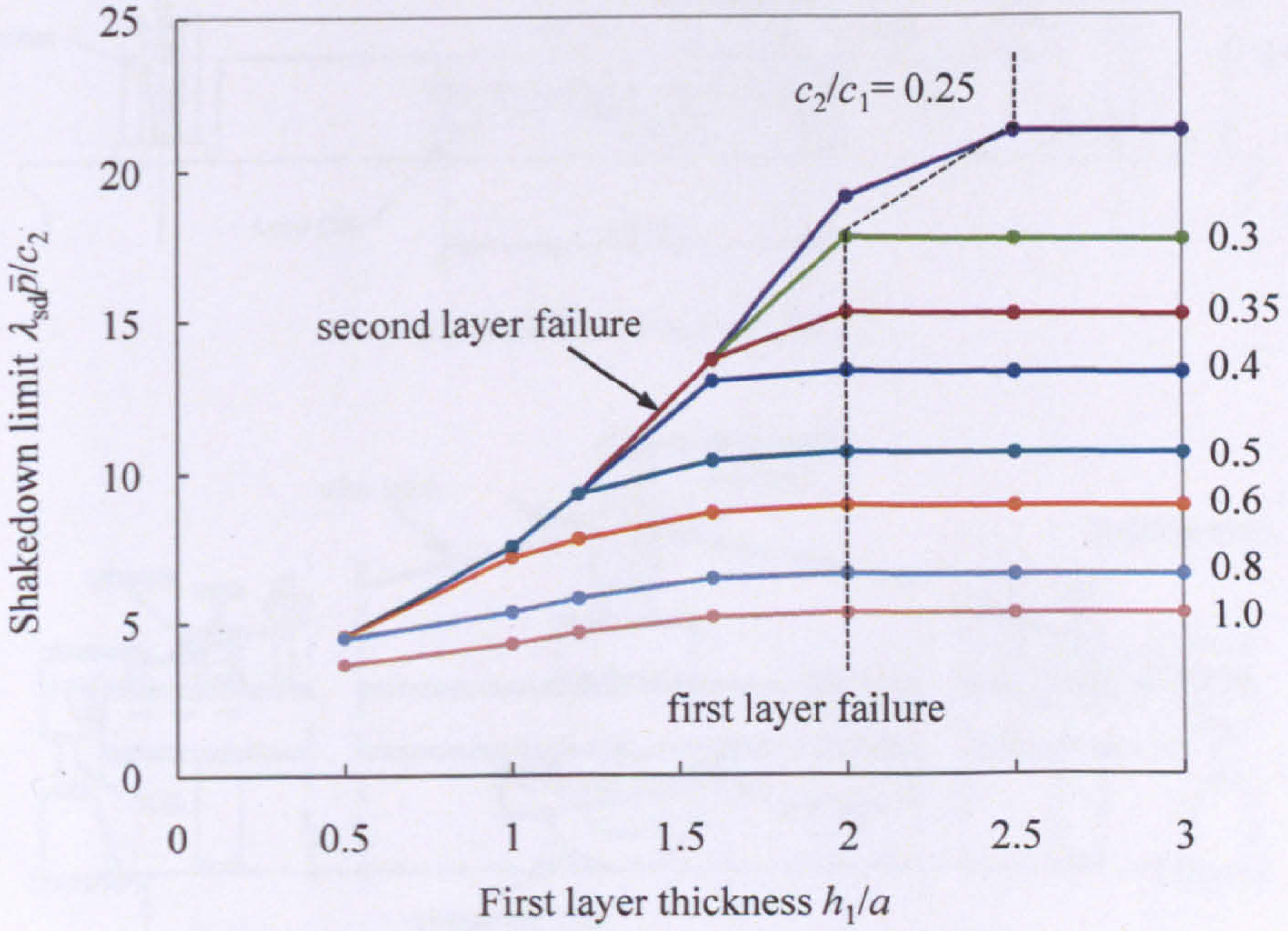

(b) Analytical shakedown solution

Figure 5.23. Comparison of 3D shakedown limits when $E_1/E_2 = 3$, $\phi_1 = 20°$, $\phi_2 = 0°$ and $\mu = 0$

5.7 Comparison with pavement experiments

5.7.1 Introduction of experiments

Juspi (2007) conducted experimental studies of pavement behaviour under repeated traffic loads in view of shakedown concept. Two types of testing apparatus were used for the wheel tracking experiments on layered pavements: the Slab Test Facility (STF) and the Pavement Test Facility (PTF), as shown in Figure 5.24.

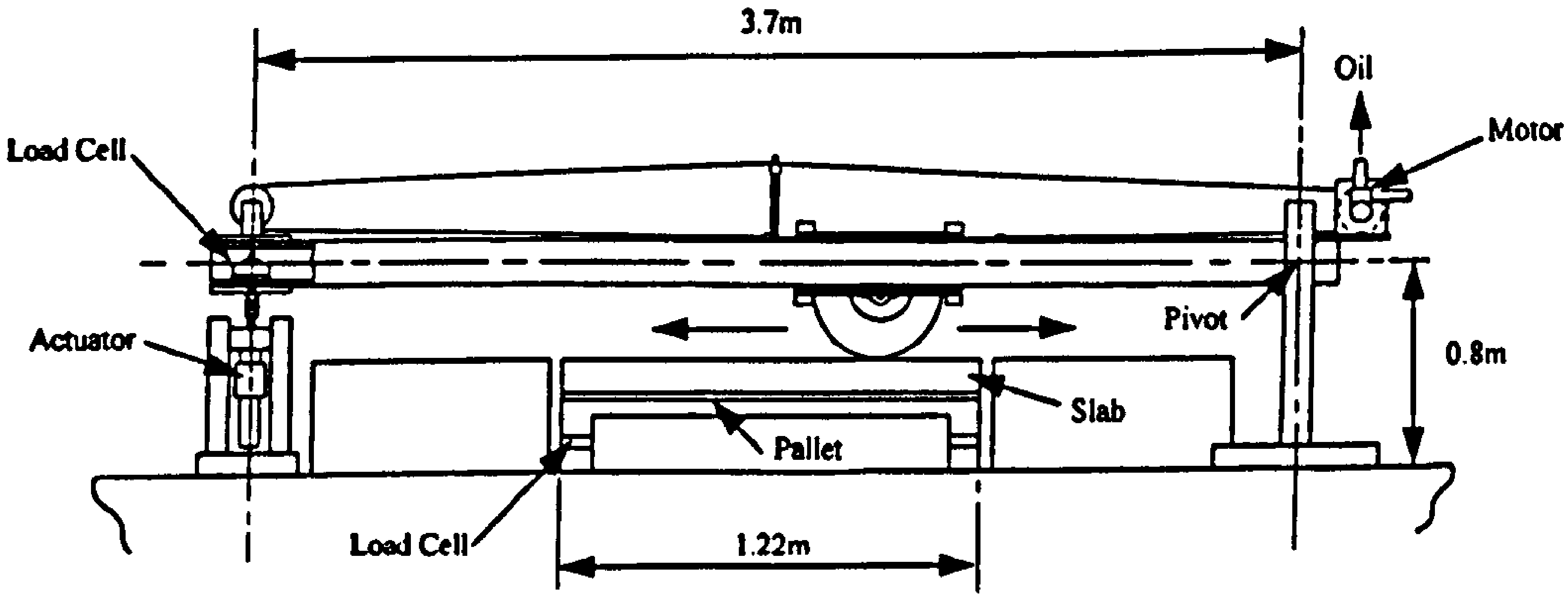

(a) Slab Test Facility (STF)

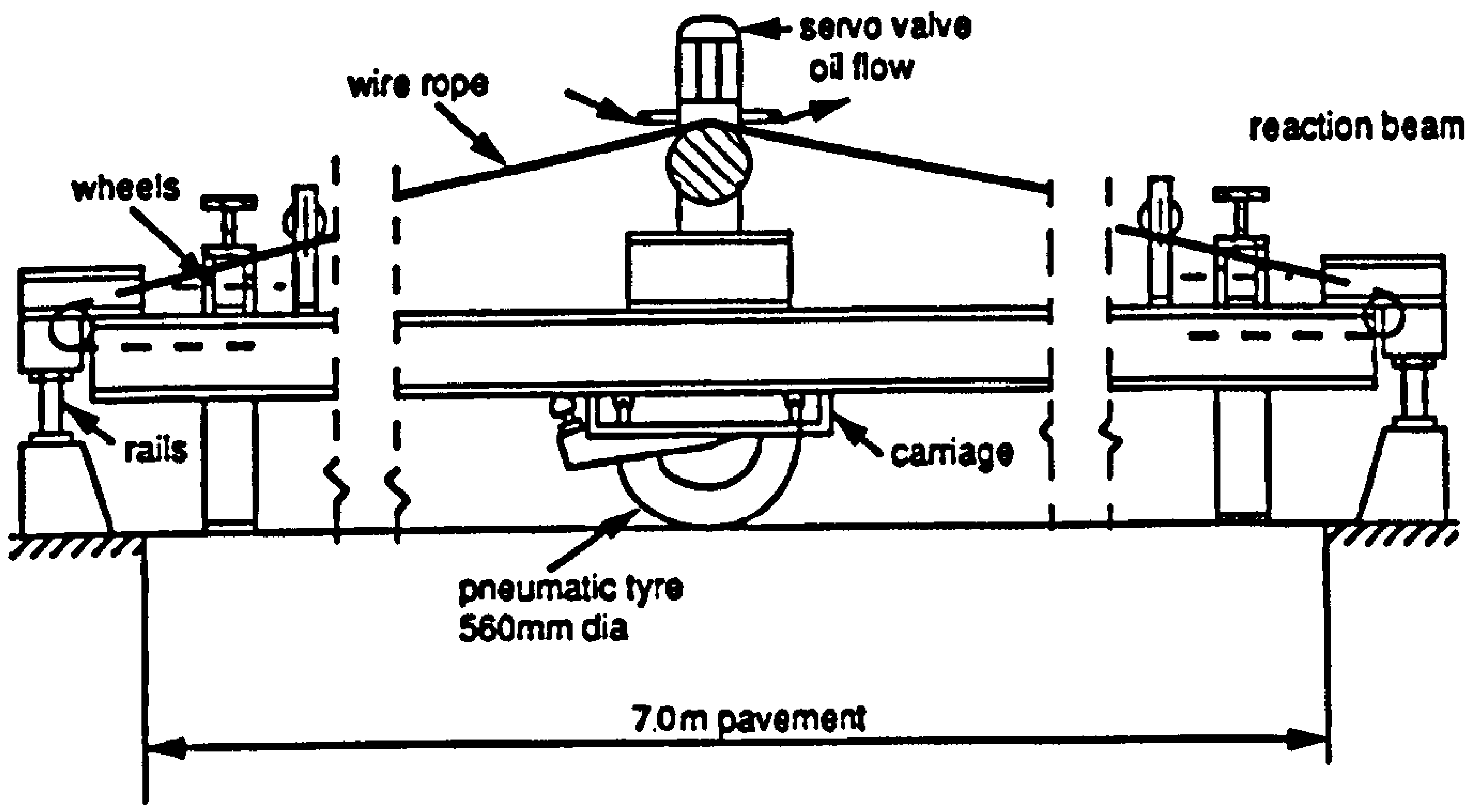

(b) Pavement Test Facility (PTF)

Figure 5.24. Wheel tracking apparatus

In the STF, specimens tested were 1m long × 0.6m wide × 0.18 m deep. In the PTF, four test sections (2.5m long × 1.25m wide each) were constructed in the test pit at the same time. A range of soil types were chosen for the experiments, including: silt, silty clay (Keuper Marl), sands (Portaway and Langford Fill) and crushed rocks (Carboniferous Limestone and Granite). Soil properties were obtained through standard monotonic load triaxial tests. The contact area between the pavement and the tyre was obtained by measuring the footprint of the static inked wheel on a graph paper placed over soil specimen. The tangential force required to rotate the wheel was also measured, and the ratio between the tangential force and the vertical force was 0.12 when operating on the Granite and 0.15 on the Limestone.

Juspi (2007) plotted vertical downward permanent deformations of specimens against the number of wheel passes for various contact pressures, as shown in Figure 2.15. The pavement behaviours due to different loading levels were then classified as shakedown status or non-shakedown status.

5.7.2 Numerical prediction of shakedown loads

For the problem studied here that the wheel ran repeatedly along a fixed path, the pavement was subjected to a 3D moving surface loads. 3D FE models were then established for each layered pavement. Table 5.1 shows material properties and layer thicknesses used in the FE models in which Poisson's ratios were set to be 0.4 for the silt and the Keuper Marl and 0.3 for the other materials. It was also assumed that the contact loads were limited to a circle of radius, a, calculated from $A = \pi a^2$ (A is the contact area measured in experiments). Both normal and shear loads are assumed in Hertz load distribution. The surface frictional coefficients μ were assumed to be 0.12 for Granite surface and 0.15 for Limestone surface.

Table 5.1. Summary of soil characteristics

Test reference	Layer	Material type	h (mm)	c (kPa)	ϕ (°)	υ	E (MPa)
Slab Test Facility (STF)							
Gr-PS	1	Granite	120	13	49	0.3	22
	2	Portaway Sand	60	8.5	36	0.3	26
Gr-Silt	1	Granite	120	13	49	0.3	22
	2	Silt	60	14	38	0.4	22
CL1-KM	1	Carboniferous Limestone 1	120	12	51	0.3	10
	2	Keuper Marl	60	44	0	0.4	2
Pavement Test Facility (PTF)							
CL2-KM	1	Carboniferous Limestone 2	450	16	55	0.3	46
	2	Keuper Karl	1050	44	0	0.4	2
CL2-LFS-KM	1	Carboniferous Limestone 2	450	16	55	0.3	46
	2	Langford Fill Sand	200	9.5	44	0.3	17
	3	Keuper Marl	850	44	0	0.4	2

Note: h = layer thickness, c = cohesion, ϕ = friction angle, υ = Poisson's ratio, E = Young's modulus.

5.7.3 Comparisons and discussion

A summary of the theoretical shakedown load limits $\lambda_{sd}p_0$ is presented in Table 5.2, together with experimental observations of pavement behaviours for different contact pressures. It can be seen that the theoretical shakedown load limits generally agree with experimental observations for two-layered pavements. For three-layered pavements, the theoretical prediction is well below the measured shakedown load. This difference could be caused by inaccurate measurements. Typically, the measurement on the ratio of shear to normal load might overestimate the surface frictional coefficient. Sensitive analyses were then conducted for the three-layered pavement by varying the frictional coefficient μ.

Table 5.2. Comparison of the experimental observations and the theoretical shakedown load limits

Test facility	Test reference	Maximum contact pressure p_0^* (kPa)	Shakedown?	Theoretical shakedown load limit $\lambda_{sd}p_0$ (kPa)
STF	Gr-PS	229	Yes	288
		339	No	
		404	No	
	Gr-Silt	218	Yes	290
		349	Yes	
		437	No	
		585	No	
	CL1-KM	212	Yes	239
		293	No	
		336	No	
PTF	CL2-KM	321	Yes	323
		381	No	
		500	No	
	CL2-LFS-KM	465	Yes	320
		615	No	
		650	No	
		680	No	

Table 5.3 summarises the predicted shakedown limits for a range of frictional coefficients from 0.15 to 0. It shows that the theoretical prediction increases markedly with decreasing frictional coefficient, and it agrees with the experimental observation when $\mu = 0$.

Table 5.3. Sensitive study on three-layered pavements

Contact pressure (kPa)	Shakedown?	Theoretical shakedown load limit (kPa)			
		$\mu = 0.15$	$\mu = 0.1$	$\mu = 0.05$	$\mu = 0$
465	Yes	320	362	415	480
615	No				

5.8 Design application

Shakedown limits calculated from the proposed numerical approaches can provide a means of practical pavement design. Given traffic load, contact pressure and contact area, a simple thickness design procedure is described below:

- Determine material properties for each layer: E, v, c, ϕ. (Asphalt properties are dependent on temperature and speed)
- Calculate shakedown load limits for different layer thickness combinations by using shakedown solution.
- Plot thickness design chart.
- Choose best thickness combination from the chart using the contact pressure and the shakedown load limit.

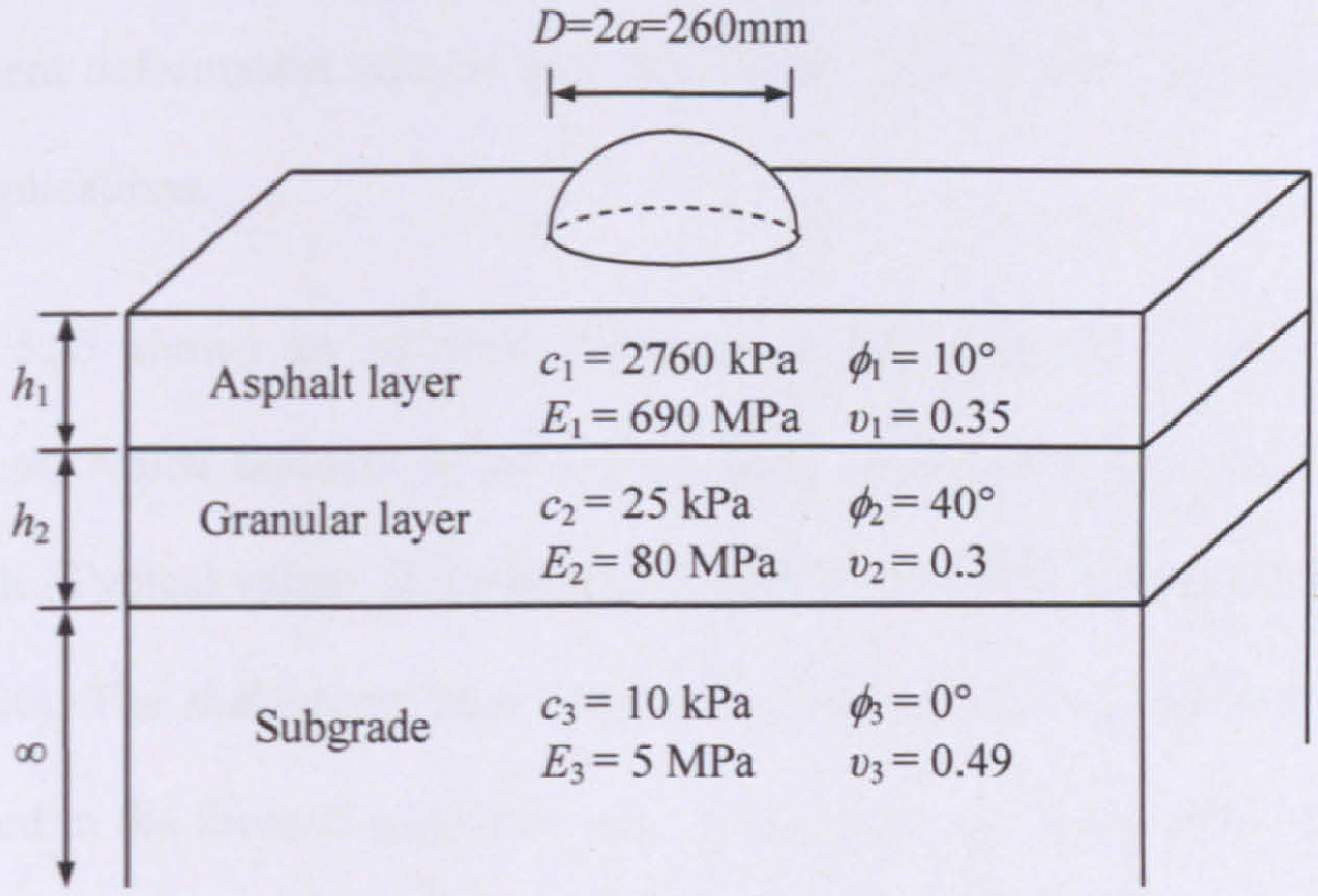

(a) pavement structures considered for design

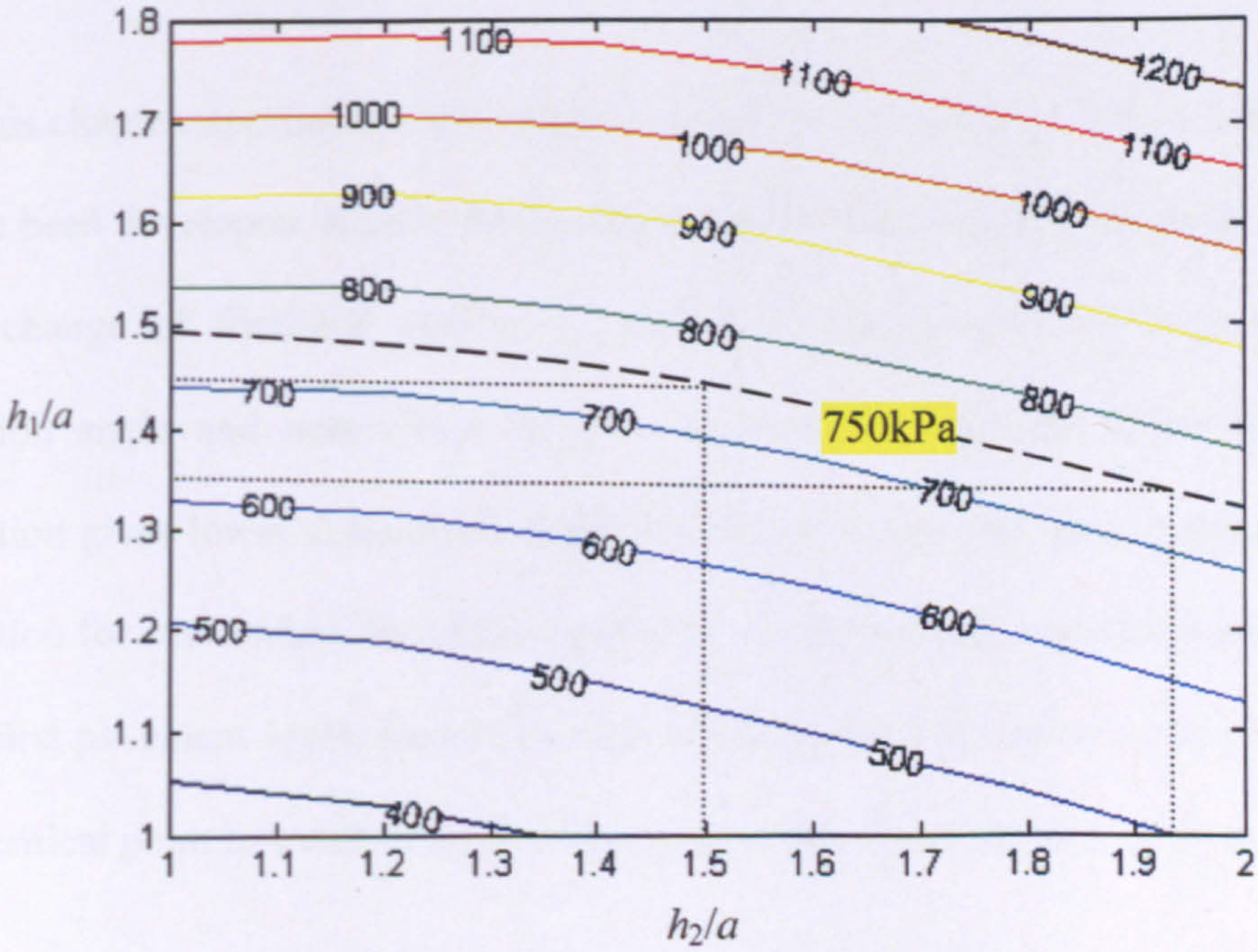

(b) Design chart

Figure 5.25. Example chart for the thickness design of a three-layered pavement

Pavement designed in this way will shakedown under design load so that the permanent deformation will be very small even under a very large number of load applications.

Figure 5.25 shows an example thickness design chart for a three-layered pavement, which consists of an asphalt layer, a granular layer and infinite subgrade. Typical values of asphalt parameters were taken from Boulbibane et al. (2000). The shakedown load limits in terms of pressure with unit kPa are presented in the form of a contour map. If the design pressure is 750 kPa, any thickness combination on this contour line can be chosen for design, such as $h_1/a = 1.45$ and $h_2/a = 1.5$ or $h_1/a = 1.35$ and $h_2/a = 1.94$.

5.9 Conclusions

In this chapter, approaches for shakedown analysis of multi-layered pavements have been developed. Results have shown that the shakedown limit varies with the change of frictional coefficient, material strength ratio, stiffness ratio, friction angle and normalised layer thicknesses. The rigorous lower-bound solution gives lower shakedown limits than those in the analytical shakedown solution for cases when the critical point lies on the surface or at the bottom of the first pavement layer. However, both solutions are identical for cases when the critical point lies within the first layer and at the top of the second layer.

The 3D shakedown limits are generally higher than the 2D shakedown limits. For the two-layered pavements with small surface traction, the critical point in the 3D model tends to initiate within the first pavement layer. However, the critical point in the 2D model tends to lie at the bottom of the first pavement layer.

Comparisons with recent numerical lower-bound solution (Shiau and Yu, 2000) and upper-bound solution (Boulbibane et al., 2005) have shown pleasing consistency. Comparisons with experimental data of Juspi (2007) have suggested the theoretical shakedown solutions provides a good estimation to the measured shakedown limits of layered pavements.

Design of pavements against excessive rutting using the shakedown theory can be carried out by choosing pavement materials and layer thicknesses to ensure that under a given design traffic load the pavement design will shakedown. An example chart has been used to illustrate the design process.

CHAPTER 6

CONCLUDING REMARKS

6.1 Conclusions

Shakedown analysis provides a load limit under which failure due to excessive plastic deformation can be prevented and therefore is a powerful tool for stability analysis of road pavement due to moving traffic loads.

FE analyses of soil half-space under moving surface loads have shown the shakedown and surface ratchetting phenomena owing to different loading levels. The non-associated plastic flow rule gives lower resistance to further yield than the associated plastic flow rule. Based on the fully-developed residual stress field, shakedown status of the soil half-space has been checked by means of Melan's lower-bound shakedown theorem. The results indicate that the FE calculated shakedown limits are generally consistent with the theoretical shakedown limits for 2D pavement models.

Two shakedown solutions have been presented for pavements subjected to 2D and 3D surface loads. The analytical shakedown solution is based on a residual stress field that may not satisfy the equilibrium condition, hence gives the necessary condition for shakedown. The lower-bound shakedown solution is based on a self-equilibrated critical residual stress field and provides rigorous lower-bound shakedown limits. The rigorous lower-bound solution is lower than the analytical shakedown solution for cases when the critical point lies on the surface or at the base of the first pavement layer.

Solutions for single-layered pavements which adopt analytical elastic stress fields can be used to benchmark numerical shakedown results. It has been found that the normalised shakedown limit increases with increasing soil friction angle ϕ but decreases with the rise of frictional coefficient μ. Moreover, when the critical point initiates on the pavement surface, the lower-bound shakedown limit is mainly controlled by the magnitude of shear force. In addition, Poisson's ratio υ also has slightly effect on the lower-bound shakedown limits.

In consideration of pavements with elliptical contact area, the shakedown limit can always be raised by decreasing the aspect ratio b/a ($b < a$) for subsurface failure cases. For surface failure cases, the lower-bound shakedown limit also rises with decreasing b/a when the friction angle is not zero.

In the application of layered pavements, shakedown solutions have been obtained by using elastic stresses calculated from FE analyses. The shakedown limits of layered pavements are not only dependent on the frictional coefficient and the material friction angle, but also on the strength ratio, stiffness ratio and normalised layer thicknesses h_i/D. Comparisons with experimental data have shown that the theoretical shakedown solution provides a good estimation for the experimental shakedown limits.

A pavement design approach against excessive rutting has been proposed using the shakedown theory. For the three-layered pavements with given material properties, pavement thickness design can be carried out by choosing thickness combinations to ensure that under a given design traffic load the designed pavement will shakedown.

Direct comparisons between 2D and 3D results suggest that the shakedown limit for 2D pavement model is generally lower than that for 3D pavement model. Their difference is of the most significant in the case of normal loading only and decreases with increasing frictional coefficient. For the two-layered pavements with small frictional coefficient, the critical point tends to lie within the first pavement layer in the 3D model rather than at the base of this layer in the 2D model.

The critical residual stress fields (i.e. the minimum larger root and the maximum smaller root) at the lower-bound shakedown limit constitute a region for the real residual stress field. Comparisons with FE results have shown that the compressive minimum larger root is close to the FE calculated residual stress field, particularly in the vicinity of the critical depth. In the layered pavement, the critical residual stress fields are discontinuous at the interface between two layers.

6.2 Suggestions for future research

Future work could be undertaken in the following aspects:

- The present shakedown analysis can be applied to railway foundations which have similar structures to the road pavements and have rolling stock running on its surface.
- The present shakedown solutions are based on the assumption of elastic-perfectly plastic pavement materials. In reality, these materials exhibit work hardening or softening behaviour. Further research will consider the effect of work hardening.
- FE analysis of soil half-space under moving surface loads can be extended to layered pavements and to work hardening material. Moreover, to reveal the real behaviour of pavement under moving wheel, a 3D FE model is required. Since the three-dimensional model will consume a lot of computation effort, modification should be made to the model dimensions and the boundary conditions.
- Unlike the numerical elastic-plastic analysis, solutions using shakedown theorems do not provide information about the deformation of pavements which is important in view of serviceability requirements. Further work along the line of Shiau and Yu (2000) is then required in order to predict the permanent deformation at the time when the shakedown state is reached.

REFERENCE

AASHTO (2002). *Guide for deisgn of new and rehabilitated pavement structures*. American Association of State Highway and Transportation Officials, America.

ARNOLD, G. K., DAWSON, A. R., HUGHES, D. A. B. and ROBINSON, D. (2003). The application of shakedown approach to granular pavement layers. *Journal of Transportation Research Board*, 1819(2), 194-200.

AUSTROADS (1992). *Pavement design: A guide to the structural design of road pavements*. Sydney, Australia.

BHARGAVA, V., HAHN, G. T. and RUBIN, C. A. (1985a). An elastic-plastic finite element model of rolling contact, part 1: analysis of single contacts. *Journal of Applied Mechanics*, 52, 67-74.

BHARGAVA, V., HAHN, G. T. and RUBIN, C. A. (1985b). An elastic-plastic finite element model of rolling contact, part 2: analysis of repeated contacts. *Journal of Applied Mechanics*, 52, 75-82.

BLEICH, H. (1932). Uber die bemessung statisch unbestimmter stahltragwerke unter beruschsichtigung der elastisch-plastischen verhaltens des baustoffes. *Journal of Bauingenieur*, 19, 261-269.

BONSE, R. P. H. and KUHN, S. H. (1959). Dynamic forces exerted by Moving Vehicles on a Road Surface. *Highway Research Board Bulletin*, 233, 9-29.

BOULBIBANE, M. and COLLINS, I. F. (2000). The calculation of shakedown loads for contact problems. *Key Engineering Materials*, 177-180, 763-774.

BOULBIBANE, M., COLLINS, I. F., WEICHERT, D. and RAAD, L. (2000). Shakedown analysis of anisotropic asphalt concrete pavements with clay subgrade. *Canadian Geotechnical Journal*, 37, 882-889.

BOULBIBANE, M. and PONTER, A. R. S. (2005). Extension of the linear matching method to geotechnical problems. *Computer Methods in Applied Mechanics and Engineering*, 194, 4633-4650.

BOULBIBANE, M., COLLINS, I. F., PONTER, A. R. S. and WEICHERT, D. (2005). Shakedown of unbound pavements. *International Journal of Road Materials and Pavement Design*, 6, 81–96.

BOULBIBANE, M. and PONTER, A. R. S. (2006). The linear matching method for the shakedown analysis of geotechnical problems. *International Journal for Numerical and Analytical Methods in Geomechanics*, 30, 157-179.

BOWER, A. F. (1989). Cyclic hardening properties of hard-drawn copper and rail steel. *Journal of the Mechanics and Physics of Solids*, 37, 455-470.

BOWER, A. F. and JOHNSON, K. L. (1989). The influence of strain hardening on cumulative plastic deformation in rolling and sliding line contact. *Journal of the Mechanics and Physics of Solids*, 37, 471-493.

BOWER, A. F. and JOHNSON, K. L. (1991). Plastic flow and shakedown of the rail surface in repeated wheel-rail contact. *Wear*, 144, 1-18.

BRETT, J. F. (1987). Stability and shakedown in pavement in pavement roughness change with age. *Proceeding of New Zealand Roading Symposium*, Welington, New Zealand, 695-704.

BROWN, S. F., BRUNTON, J. M. and STOCK, A. F. (1985). Analytical design of bituminous pavements. *Proceedings of the Institution of Civil Engineers*, Part 2, 79, 1-31.

BROWN, S. F. and BRUNTON, J. M. (1986). *An introduction to the analytical design of bituminous pavements (3rd Ed.)*, Internal Report, University of Nottingham.

BROWN, S. F. (1996). Soil mechanics in pavement engineering. *Geotechnique*, 46, 381-426.

BROWNE, A., LUDEMA, K. C. and CLARK, S. K. (1981). Contact between the tire and roadway. *In:* CLARK, S. K. (ed.) *Mechanics of pneumatic tires.* US Department of Transportation, National Highway Traffic Safety Administration.

BRYANT, M. D. and KEER, L. M. (1982). Rough contact between elastically and geometrically identical curved bodies. *Journal of Applied Mechanics*, 49, 345-352.

CHAN, F. W. K. (1990). *Permanent deformation resistance of granular layers in pavements.* PhD Thesis, University of Nottingham.

CHEN, H. F. and PONTER, A. R. S. (2001). Shakedown and limit analyses for 3-D structures using the linear matching method. *International Journal of Pressure Vessels and Piping*, 78, 443-451.

CHEN, H. F. and PONTER, A. R. S. (2005). The linear matching method for shakedown and limit analysis applied to rolling and sliding point contact problems. *Road Materials and Pavement Design*, 6, 9-30.

COLLINS, I. F. and CLIFFE, P. F. (1987). Shakedown in frictional materials under moving surface loads. *International Journal for Numerical and Analytical Methods in Geomechanics*, 11, 409-420.

COLLINS, I. F., WANG, A. P. and SAUNDERS, L. R. (1993a). Shakedown in layered pavements under moving surface loads. *International Journal for Numerical and Analytical Methods in Geomechanics*, 17, 165-174.

COLLINS, I. F., WANG, A. P. and SAUNDERS, L. R. (1993b). Shakedown theory and the design of unbound pavements. *Road and Transport Research*, 2, 28–39.

COLLINS, I. F. and BOULBIBANE, M. (1998). The application of shakedown theory to pavement design. *Metals and Materials International*, 4, 832-837.

COLLINS, I. F. and BOULBIBANE, M. (2000). Geomechanical Analysis of Unbound Pavements Based on Shakedown Theory. *Journal of Geotechnical and Geoenvironmental Engineering*, 126, 50-59.

COURANT, R. (1943). Variational methods for the solution of problems of equilibrium and vibrations. *Bulletin (New Series) of the American Mathematical Society*, 49, 1-23.

CRONEY, D. and CRONEY, P. (1991). *The design and performance of road pavements (2nd Ed.)*, McGraw-Hill Professional.

CROOK, A. W. (1957). Simulated gear tooth contacts: some experiments upon their lubrication and subsurface deformations. *Proceedings of the Institution of Mechanical Engineers*, 171, 187-214.

DE BEER, M., SADZIK, E. M., FISHER, C. and COETZEE, C. H. (2005). Tyre-pavement contact stress patterns from the test tyres of the Gautrans Heavy Vehicle Simulator (HVS) MK IV+. *The 24th Annual Southern African Transport Conference and Exhibition*, Pretoria, South Africa, 1-19.

FREITAG, D. R. and GREEN, A. J. (1962). Distribution of stresses on an unyielding surface beneath a pneumatic tire. *Highway Research Board Bullein*, 342, 14-23.

GIDEL, G., HORNYCH, P., CHAUVIN, J. J., BREYSSE, D. and DENIS, A. (2001). A new approach for investigating the permanent deformation behavior of unbound granular material using the repeated load triaxial apparatus. *Bulletin des Laboratoires des Ponts et Chaussées*, 233, 5-21.

HABIBALLAH, T. and CHAZALLON, C. (2005). An elastoplastic model based on the shakedown concept for flexible pavements unbound granular materials. *International Journal for Numerical and Analytical Methods in Geomechanics*, 29, 577-596.

HAHN, G. T. and HUANG, Q. (1986). Rolling contact deformation of 1100 aluminum disks. *Metallurgical and Materials Transactions A*, 17, 1561-1572.

HAM, G., RUBIN, C. A., HAHN, G. T. and BHARGAVA, V. (1988). Elasto-plastic finite element analysis of repeated, two-dimensional rolling-sliding contacts. *Journal of Tribology*, 110, 44-49.

HAM, G. L., HAHN, G. T., RUBIN, C. A. and BHARGAVA, V. (1989). Finite element analysis of the influence of kinematic hardening in two-dimensional, repeated, rolling-sliding contact. *Tribology Transactions*, 32, 311-316.

HAMILTON, G. M. (1963). Plastic flow in rollers loaded above the yield point. *Proceedings of the Institution of Mechanical Engineers*, 177, 667-675.

HAMILTON, G. M. (1983). Explicit equations for the stresses beneath a sliding spherical contact. *Proceedings of the Institution of Mechanical Engineers. Pt. C: Mechanical Engineering Science*, 197, 53-9.

HEARLE, A. D. and JOHNSON, K. L. (1987). Cumulative Plastic Flow in Rolling and Sliding Line Contact. *Journal of Applied Mechanics*, 54, 1-7.

HIGHWAYS AGENCY (2006). Pavement design (HD26), *Design manual for roads and bridge Vol.7: Pavement design and maintenance - pavement design and construction*. Stationery Office, London.

HIGHWAYS AGENCY (2009). Design guidance for road pavement foundations (Draft HD25), *Interim Advice Note 73/06 Revision 1*. Stationery Office, London.

HIMENO, K., KAMIJIMA, T., IKEDA, T. and ABE, T. (1997). Distribution of tire contact pressure of vehicles and its influence on pavement distress. *Eighth International Conference on Asphalt Pavements*, Seattle, Washington, 129-139.

HOWELL, M., HAHN, G. T., RUBIN, C. A. and MCDOWELL, D. L. (1995). Finite element analysis of rolling contact for nonlinear kinematic hardening bearing steel. *Journal of Tribology*, 117, 729-736.

HRENNIKOFF, A. (1941). Solution of problems of elasticity by the framework method. *Journal of Applied Mechanics*, 8, 169-175.

HUANG, Y. H. (1993). *Pavement analysis and design*, Prentice Hall.

HUHTALA, M., PIHLAJAMAKI, J. and PIENIMAKI, M. (1989). Effects of tires and tire pressures on road pavements. *Transportation Research Record*, 1227, 107–114.

JIANG, Y. and SEHITOGLU, H. (1994). An analytical approach to elastic-plastic stress analysis of rolling contact. *Journal of Tribology*, 116, 577-587.

JIANG, Y. and SEHITOGLU, H. (1996). Rolling contact stress analysis with the application of a new plasticity model. *Wear*, 191, 35-44.

JIANG, Y., CHANG, J. and XU, B. (2001). Elastic-plastic finite element stress analysis of two-dimensional rolling contact. *Hydraulic Failure Analysis: Fluids, Components, and System Effects*, 59-74.

JIANG, Y., XU, B. and SEHITOGLU, H. (2002). Three-dimensional elastic-plastic stress analysis of rolling contact. *Journal of Tribology*, 124, 699-708.

JOHNSON, K. L. (1962). A shakedown limit in rolling contact. *Proceedings of the Fourth US National Congress of Applied Mechanics*, Berkeley, California, 971–975.

JOHNSON, K. L. and JEFFERIS, J. A. (1963). Plastic flow and residual stresses in rolling and sliding contact. *Proceeding of the Institution of Mechanical Engineers: Fatigue in Rolling Contact*, 177, 54-65.

JOHNSON, K. L. (1985). *Contact mechanics*, Cambridge University Press.

JUSPI, S. (2007). *Experimental validation of the shakedown concept for pavement analysis and design.* Ph.D. thesis, University of Nottingham.

KAPOOR, A. and JOHNSON, K. L. (1992). Effect of changes in contact geometry on shakedown of surfaces in rolling/sliding contact. *International Journal of Mechanical Sciences*, 34, 223-239.

KOITER, W. T. (1960). General theorems for elastic-plastic solids. *In:* SNEDDON, I. N. A. H., R. (ed.) *Progress in solid mechanics.*

KÖNIG, J. A. (1987). *Shakedown of elastic-plastic structures*, Elsevier Science Ltd.

KRABBENHOFT, K., LYAMIN, A. V. and SLOAN, S. W. (2007). Shakedown of a cohesive-frictional half-space subjected to rolling and sliding contact. *International Journal of Solids and Structures*, 44, 3998-4008.

KULKARNI, S. M., HAHN, G. T., RUBIN, C. A. and BHARGAVA, V. (1990). Elastoplastic finite element analysis of three-dimensional, pure rolling contact at the shakedown limit. *Journal of Applied Mechanics*, 57, 57-65.

KULKARNI, S. M., HAHN, G. T., RUBIN, C. A. and BHARGAVA, V. (1991). Elasto-plastic finite element analysis of three-dimensional pure rolling contact above the shakedown limit. *Journal of Applied Mechanics*, 58, 347-353.

LEKARP, F., RICHARDSON, I. R. and DAWSON, A. R. (1996). Influences on permanent deformation behavior of unbound granular materials. *Transportation Research Record: Journal of the Transportation Research Board*, 1547, 68-75.

LEKARP, F. and DAWSON, A. (1998). Modelling permanent deformation behaviour of unbound granular materials. *Construction and building materials*, 12, 9-18.

LEKARP, F., ISACSSON, U. and DAWSON, A. R. (2000). State of the art. II: Permanent strain response of unbound aggregates. *Journal of Transportation Engineering*, 126, 76-83.

LI, H. X. and YU, H. S. (2006). A nonlinear programming approach to kinematic shakedown analysis of frictional materials. *International Journal of Solids and Structures*, 43, 6594-6614.

LI, H. X. (2010). Kinematic shakedown analysis under a general yield condition with non-associated plastic flow. *International Journal of Mechanical Sciences*, 52, 1-12.

LISTER, N. W. (1972). The transient and long term performance of pavements in relation to temperature. *Proceedings of the 3rd Inernational Conference for Structure Deisng of Aspalt Pavements*, London, 94-100.

MCDOWELL, D. L. and MOYAR, G. J. (1991). Effects of non-linear kinematic hardening on plastic deformation and residual stresses in rolling line contact. *Wear*, 144, 19-37.

MELAN, E. (1938). Der spannungsgudstand eines Henky-Mises schen Kontinuums bei Verlandicher Belastung. *Sitzungberichte der Ak Wissenschaften Wie (Ser. 2A)*, 147, 73.

MERWIN, J. E. and JOHNSON, K. L. (1963). An analysis of plastic deformation in rolling contact. *Proceedings of the Institution of Mechanical Engineers*, 177, 676-685.

MUHANNA, A. S., RAHMAN, M. S. and LAMBE, P. C. (1998). Model for resilient modulus and permanent strain of subgrade soils. *Transportation Research Record: Journal of the Transportation Research Board*, 1619, 85-93.

NUNN, M. (2004). *Development of a more versatile approach to flexible and flexible composite pavement design*, Transportation Research Laboratory, Report 615.

PONTER, A. R. S., HEARLE, A. D. and JOHNSON, K. L. (1985). Application of the kinematical shakedown theorem to rolling and sliding point contacts. *Journal of the Mechanics and Physics of Solids*, 33, 339-362.

PONTER, A. R. S. and ENGELHARDT, M. (2000). Shakedown limits for a general yield condition: implementation and application for a Von Mises yield condition. *EuropeanJournal of Mechanics. A. Solids*, 19, 423-445.

PONTER, A. R. S., CHEN, H. F., CIAVARELLA, M. and SPECCHIA, G. (2006). Shakedown analyses for rolling and sliding contact problems. *International Journal of Solids and Structures*, 43, 4201-4219.

POWELL, W. D., POTTER, J. F., MAYHEW, H. C. and NUNN, M. E. (1984). *The structural design of bituminous roads*, Transport and Road Research Laboratory, Report LR1132.

RAAD, L., WEICHERT, D. and NAJM, W. (1988). Stability of multilayer systems under repeated loads. *Transportation Research Board*, 1207, 181-186.

RAAD, L., WEICHERT, D. and HAIDAR, A. (1989a). Analysis of full-depth asphalt concrete pavements using shakedown theory. *Transportation Research Board*, 1227, 53-65.

RAAD, L., WEICHERT, D. and HAIDAR, A. (1989b). Shakedown and fatigue of pavements with granular bases. *Transportation Research Board,* 1227, 159-172.

RAAD, L. and WEICHERT, D. (1995). Stability of pavement structures under long term repeated loading. *In:* MROZ, Z. (ed.) *Inelastic Behaviour of Structures under Variable Loads.*

RADOVSKY, B. S. and MURASHINA, N. V. (1996). Shakedown of subgrade soil under repeated loading. *Transportation Research Record: Journal of the Transportation Research Board,* 1547, 82-88.

RAVINDRA, P. S. and SMALL, J. C. (2008). Shakedown analysis of road pavements. *The 12th International Conference of International Association for Computer Methods and Advances in Geomechanics,* Goa, India, 4432-4438.

RAVINDRA, P. S. (2008). *Shakedown analysis of road pavements - an experimental point of view.* Ph.D. thesis, University of Sydney.

SACKFIELD, A. and HILLS, D. A. (1983a). Some useful results in the classical Hertz contact problem. *The Journal of Strain Analysis for Engineering Design,* 18, 101-105.

SACKFIELD, A. and HILLS, D. A. (1983b). Some useful results in the tangentially loaded Hertzian contact problem. *The Journal of Strain Analysis for Engineering Design,* 18, 107-110.

SAKAE, C. and KEER, L. M. (1997). Application of direct method for a nonlinear-kinematic-hardening material under rolling/sliding line contact:

constant ratchetting rate. *Journal of the Mechanics and Physics of Solids*, 45, 1577-1594.

SANGREY, D. A., HENKEL, D. J. and ESRIC, M. I. (1969). The effective stress response of a saturated clay soil to repeated loading. *Canadian Geotechnical Journal*, 6, 241-252.

SEEDS, S. B. (2000). Flexible pavement design: summary of the state of the art. *Transportation Research Board, A3B05: Committee on Safety Data, Analysis, and Evaluation.*

SHARP, R. W. and BOOKER, J. R. (1984). Shakedown of pavements under moving surface loads. *Journal of Transportation Engineering, ASCE*, 110, 1-14.

SHIAU, S. H. and YU, H. S. (2000). Load and displacement prediction for shakedown analysis of layered pavements. *Transportation Research Record: Journal of the Transportation Research Board*, 1730, 117-124.

SHIAU, S. H. (2001). *Numerical methods for shakedown analysis of pavements under moving surface loads.* Ph.D. thesis, The University of Newcastle.

THOM, N. (2008). *Principles of pavement engineering*, Thomas Telford Publishing Ltd.

WERKMEISTER, S., DAWSON, A. R. and WELLNER, F. (2001). Permanent deformation behavior of granular materials and the shakedown concept.

Transportation Research Record: Journal of the Transportation Research Board, 1757, 75-81.

WERKMEISTER, S., DAWSON, A. R. and WELLNER, F. (2004). Pavement design model for unbound granular materials. *Journal of Transportation Engineering*, 130, 665-674.

WERKMEISTER, S., DAWSON, A. R. and WELLNER, F. (2005). Permanent deformation behaviour of granular materials. *Road Materials and Pavement Design*, 6, 31-52.

WONG, J. Y. (2001). *Theory of ground vehicles*, Wiley-Interscience.

XU, B. and JIANG, Y. (2002). Elastic-plastic finite element analysis of partial slip rolling contact. *Journal of Tribology*, 124, 20-26.

YANG, S. R. and HUANG, W. H. (2007). Permanent deformation and critical stress of cohesive soil under repeated loading. *Transportation Research Record: Journal of the Transportation Research Board*, 2016, 23-30.

YU, H. S. and HOSSAIN, M. Z. (1998). Lower bound shakedown analysis of layered pavements using discontinuous stress fields. *Computer Methods in Applied Mechanics and Engineering*, 167, 209-222.

YU, H. S. (2005). Three-dimensional analytical solutions for shakedown of cohesive-frictional materials under moving surface loads. *Proceedings of the Royal Society A: Mathematical, Physical and Engineering Science*, 461, 1951-1964.

YU, H. S. (2006). *Plasticity and geotechnics*, Springer.

YU, H. S. (2011). *Recent advances in pavement soil mechanics*, British Geotechnical Association Talk, Institution of Civil Engineers, London.

YU, M., MORAN, B. and KEER, L. M. (1993). A direct analysis of two-dimensional elastic-plastic rolling contact. *Journal of Tribology*, 115, 227-236.

ZHAO, J., SLOAN, S. W., LYAMIN, A. V. and KRABBENHØFT, K. (2008). Bounds for shakedown of cohesive-frictional materials under moving surface loads. *International Journal of Solids and Structures*, 45, 3290-3312.